博士論文

Interaction Force Distribution on the Contact Area during the Sliding and Vibration of Droplets

（液滴の滑りと振動における接触面での力分布）

Nguyen Thanh Vinh

グェン タン ヴィン

Table of contents

Chapter 1 Introduction ---------- 4
1.1 Objective 4
1.2 Background 5
1.2.1 Background study on the sliding mechanism of droplet 5
1.2.2 Background study on the sliding mechanism of droplet 7
1.2.3 Relationship between droplet sliding and vibration 7
1.3 Originality and significance 8
1.4 Thesis structure 8
Chapter 2 Background theory ---------- 10
2.1 Droplets on a horizontal substrate 10
2.2 Sliding of a droplet on a tilted substrate 12
2.3 Vibration of a droplet on a substrate 15
2.3.1 Resonant frequencies 15
2.3.2 Viscous damping 16
Chapter 3 Sensor fabrication and evaluation ---------- 17
3.1 Sensor design and sensing principle 17
3.1.1 Sensor design 17
3.1.2 Sensing principle 19
3.1.3 FEM simulation 19
3.2 Sensor fabrication 21
3.2.1 Fabrication process 21
3.2.2 Surface hydrophobicity treatment 22
3.2.3 Fabrication results 22
3.3 Fabrication result of the cantilever array 23
3.4 Fabrication of a cantilever used for sensor calibration 24
3.5 Sensor calibration of the MEMS-based two axis sensor 25
3.5.1 Calibration method 25
3.5.2 Calibration of the load cell and the cantilever 25
3.5.3 Sensor calibration setup 27
3.5.4 Calibration result 28
Calibration result for two-axis force sensors 28
Calibration result for the cantilever used in measurement of the droplet vibration 33
3.6 Sensor resonant frequency 33
Measurement of the resonant frequency of the two-axis force sensor 33
Measurement of the resonant frequency of the cantilever 36

Chapter 4 Experiments on the droplet sliding ---------- 38
4.1 Experimental preparation 38
4.1.1 Experiment description 38
4.1.2 Preparation of liquid samples 38
Surface tension measurement 39
Viscosity measurement 41
4.1.3 Experimental setup 41
4.1.4 Image processing 41
Volume calculation 44
4.2 Measurement results for the droplet sliding 45
4.2.1 Normal and shear forces during the sliding of the droplets 45
Droplet sliding on the sensor with flat surface 45
Droplet sliding on the sensors with a micropillar array 49
Experimental results for all fabricated sensors and prepared liquid samples. 53
4.2.2 Effects of the droplet volume, micropillar density and liquid viscosity on the interaction forces . 59
Effect of the droplet volume 59
Effect of micropillar array density 62
Effect of the liquid viscosity 65
4.2.3 Comparison between the measured normal force over the contact area and the normal force estimated from the high speed camera images 67
4.2.4 Comparison between the measured shear force and the frictional force of the droplets 70
4.3 Vibration during sliding of the droplets on micropillar arrays 74
4.3.1 Sliding induced vibration of droplet 75
Effect of the micropillar array pitch on the frequency of the vibration 81
Effect of the liquid viscosity on the frequency of the vibration 82
Chapter 5 Experiments on droplet vibration ---------- 86
5.1 Experimental setup and liquid samples preparation 86
Experimental setup 86
Liquid samples preparation 86
5.2 Experimental results 87
Normal force distribution along the contact diameter of a droplet during vibration 87
Effect of the droplet volume on the vibration frequency 91
Effect of the liquid viscosity on the vibration decay and its application in viscosity measurement 92
Effect of the droplet volume on the decay rate of the vibration 93
Chapter 6 Conclusion ---------- 100
Interaction forces during the sliding of a droplet 100
Interaction forces during the vibration of a droplet 101

Appendix ---------- 103
Appendix 1 Experimental results 104
Comparison of the normal force during the vibration of droplet 120
Rolling motion of a glycerol droplet 127
Appendix 2 Chemicals 128
References ---------- 129
Publications ---------- 135
Acknowledgment ---------- 137

Chapter 1 Introduction

1.1 Objective

The objective of this study is to directly measure the interaction force distribution on the contact area during the sliding and vibration of liquid droplets on a rigid substrate using MEMS-based force sensors as shown in **Fig. 1.1**. From the measurement results of this study, it is expected to achieve profound understanding of the dynamical interactions between a droplet and the substrate during the sliding and vibration. In this study, the surfaces of the substrates are decorated with micrometer-size hydrophobic pillar array to improve the mobility of the droplet. This surface modification allows the sliding of small droplets on the surface as well as induces the droplet levitation to enhance the vibration of the droplet. The interaction forces in this study refers to the forces in normal and shear direction acting on a single micropillar of the surface.

For the droplet sliding, this study aims to clarify the following issues:

- How the droplet interacts with the micropillars during the sliding. How the interaction forces distribute over the contact area.
- How the interaction forces during the sliding of a droplet on a micropillar array differ from those during the sliding of a droplet on a flat surface.
- How the interaction forces depends on the droplet volume, micropillar density and liquid viscosity.
- The relationship between the shear force acting at a single micropillar and the total frictional force during the sliding of the droplet.
- Moreover, in this study, it is found that during the sliding of the droplets on the micropillar arrays, vibration of the droplets over a high frequency range (kHz order) was observed. This study also aims to clarify the relationship between the frequency of this sliding-induced vibration and the droplet volume, micropillar density and liquid viscosity.

For the droplet vibration, this study aims to clarify the following issues:

- How the normal force distributes over the contact area during the resonance vibration of the droplet.

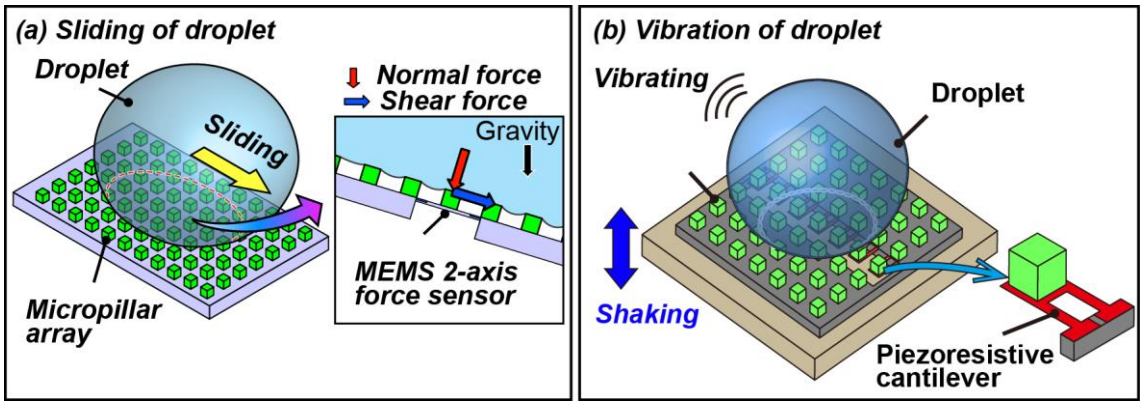

Fig. 1.1 Conceptual illustration of this study. The interaction forces during the sliding and vibration of a droplet are measured using MEMS-based sensor. (a) Copyright 2014 Elsevier, (b) Copyright 2015 IEEE.

- How the frequency of the vibration depends on the droplet volume.
- How the liquid viscosity can be estimated from the output of the sensor.

1.2 Background

Dynamical interactions between a droplet and a rigid surface such as sliding and vibration can be found in many natural and industrial processes. For example, a raindrop adhered to a glass window or an umbrella if large enough will run down by the gravity. Many biological surfaces such as plant leaves, animal skins are self-cleaned by dust removal during the sliding of water droplets on the surfaces [1-9]. In the context of industrial and engineering, the dynamic motions of the droplets are involved in microfluidic systems [10-16]; droplet directional transportation [15, 17-25], realization of water repellent surface coating [2, 3]. Understanding of the mechanism of these dynamic behaviors is therefore important in these applications which have been topics for numerous study.

1.2.1 Background study on the sliding mechanism of droplet

Sliding behavior of droplets on a rigid surface has been investigated from both theoretical, numerical [26-44] and experimental [45-67] approaches.

During the sliding of the droplet, the interaction between the droplet and the substrate at the receding edge plays a critical role in controlling the motion of the droplet. As one of the most basic theoretical references, de Gennes, P. G et al. [34, 35, 42, 44] proposed a model of the contact line during the receding of the contact line for a single defect problem using spring analogy. From this model, it is possible to achieve the analysis on the contact angle hysteresis of a droplet sliding on strong dilute defects, which was experimentally verified by D. Quere, et al. [45, 47].

For a highly viscous droplet sliding on a non-wetting surface, Mahadevan, L. et al. [33] addressed a

scaling argument and predicted that the droplet rather rolls than slides on the surface and the small viscous droplet would roll faster than a large one. The prediction was experimentally verified, again, by D. Quere, et al. [59].

Besides, for theoretical analysis, N. Savva et al. [32] studied the motion of a droplet on inclined heterogeneous substrates using 2D model based on the long-wave approximation of the Stokes equations. U. Thiele et al. [41] studied the pining and depining of a droplet from substrates by two types of heterogeneity: hydrophobic defect in font and hydrophilic one at the back of the droplet.

Various numerical study on the sliding of droplet was also carried out. Mognettti, B. M et al. [28, 31] used a lattice Boltzmann algorithm to numerically study the dynamics of droplets moving on substrates that are either hydrophobic or superhydrophobic. Their results demonstrate that the velocity profile varies from quadratic to linear with the height, indicating crossover from sliding to rolling motion. The rotational velocity was also shown to increase with viscosity. Moreover, they also provided the results on mechanism for the depinning of the receding contact line on a superhydrophobic surface.

Thampi. S. P et al. [27] numerically investigated the sliding and rolling motion of a droplet and argued that the rolling motion dominates when droplet shape close to a circle and viscosity contrast between the droplet and the surrounding fluid is large.

Tretyakov, N. et al. [26] used molecular dynamics simulations to investigate the motion of the droplets on a saw-tooth shaped textured surface while the vibration is applied to the surface and showed that surface texture can cause additional rotation pattern inside the droplet depending on the fineness of the surface corrugation.

For experimental approach, most of the study related on the sliding or motion of the droplet are based on observation. Most common technique to investigate the macro motion of the droplet is high speed image inquiry. The shape and motion of the droplets sliding on a substrate can be captured by a high speed camera and from these image, the sliding velocity and dynamic contact angles of the droplet can be obtained. This technique has been used in various study [46, 49, 51, 52, 54, 61, 68, 69]. In some of these studies, particle image velocimetry (PIV) was also utilized to investigate the inner motion of the droplet during sliding [49, 61].

Another observation method is to capture the detachment of liquid at the receding edge using transparent substrates to understand the depinning mechanism of the contact line [65, 66]. However, this technique is only applicable for relatively slow processes such as evaporation of the droplet. Beside, scanning electron microscope (SEM) and environmental scanning electron microscope (ESEM) were also utilized to visualize the interaction between receding contact line and the substrate [48, 64] by which local interaction of the droplet and the surface defect can be observed. This technique is superior in spatial resolution but again, has a disadvantage of the time resolution which is not enough to capture the fast dynamical depinning motion of the liquid from the defects of the substrate.

From the aspect of analysis based on force measurement, several attempts have been made to directly measure the interaction forces between a sliding droplet and the substrate. Generally, the total frictional

force of a droplet sliding on a tilted substrate can be calculated from the tilted angle of the substrate and the acceleration of the droplet obtained by observation. For a small droplet which cannot be moved by gravity, a cantilever-based measurement method is proposed [58]. By dragging the droplet using the cantilever, the frictional force is calculated from the deflection of the cantilever. Beside, centrifugal force based measurement method was also provided to measurement the lateral adhesion force of the droplet to a substrate [70]. However, by conventional measurement methods, it is only possible to obtain the total frictional force between a droplet and a substrate, the local frictional force and its distribution over the contact area between the droplet and the substrate still remain unclarified.

1.2.2 Background study on the sliding mechanism of droplet

Study on the vibration of the droplet dates back to 19th century with a paper of Rayleigh, L. [71] which discusses on the capillary phenomena of jets. Recently, the droplet vibration has regained significant attention due to its importance in many applications such as vibration-based droplet manipulation [19, 20, 72-75], inkjet printing[76], droplet vibration-based contact angle measurement [77], vibration induced droplet ejection [78].

Various measurement methods have been used to probe the vibration of the droplets. In most common method, the high speed image inquiry is used to capture the oscillating shape of the droplet [72-75, 79-82]. Recently, more advanced methods were also proposed using atomic force microscopy (AFM) [83], optical deflection [84, 85] or PIV based observation [86].

In terms of vibration generation method, in most of conventional study, mechanical vibration (vibrator, loud speaker and so on) was used. In some other studies, electrowetting was used to induce the vibration of the droplet.

From observations mentioned above, it is possible to obtain the shape oscillation of the droplet during vibration as well as the inner flow inside the droplet. Nevertheless, the normal force distribution along the contact area of the droplet, which is an important factor controlling the motion of the droplet, has not been measured.

Moreover, in the context of droplet vibration based sensing, vibration of the droplet provides the information related to surface tension and viscosity of the liquid, which can be very useful in droplet based sensing. However, conventional methods to measure the droplet vibration rely on sophisticated equipment such as high speed camera or AFM, thereby developing simple sensors based on the droplet vibration is still challenging.

1.2.3 Relationship between droplet sliding and vibration

In term of macro motion direction, the sliding of the droplet is the motion in lateral direction parallel to the substrate while that of the vibration is the motion mainly in normal direction perpendicular to the substrate. These two motions differ in the flow inside droplet. However, it has been shown that vibration of the droplet can induce the sliding motion [19, 20, 72-75]. Moreover, as shown later in this thesis, the sliding of the droplet on a micropillar array also induces vibration of the entire droplet. In some specific

applications such as droplet manipulation using surface roughness gradient, it is necessary to deal with both sliding and vibration behaviors of the droplet.

1.3 Originality and significance

The most original point of this work is the proposed measurement method using MEMS-based force sensors. As mentioned above, conventional methods to investigate the dynamical interaction between a droplet and a substrate mainly rely on the observation using a high speed camera, a microscope or an SEM. Each of the methods has both advantage and disadvantage in term of time resolution or spatial resolution. However, none of the conventional study was able to directly measure the interaction forces locally between the droplet and a microstructure of the substrate. To reveal the dynamic of droplets on a substrate, a quantitative measurement of these local interaction forces is necessary because the macro motion of the droplet are controlled by these local interactions.

The advantages of the MEMS-based force sensors proposed in this study make it possible to realize the direct measurement of the local interaction forces during the sliding and vibration of the droplet. These advantages include:

- Miniaturized size due to MEMS-based fabrication technique: total sizes of the sensors are from several tens to 120 μm
- High force sensing resolution based on piezoresistor effect of micrometer-size sensing structure: The sensors are able to detect a force of less than 0.12 μN.
- High time resolution due to the measurement method based on monitoring electrical voltages. The sensors themselves are able to measure the vibration up to 10 kHz
- Multiple axis: For the measurement of the droplet sliding, the sensors are able to measure not only normal force but also shear force simultaneously

Based on this measurement method, the following results are expected to be obtained in this study:

- Normal shear force distribution over the contact area of a sliding droplet on a micropillar array.
- Fluctuation of the interaction forces caused by the sliding-induced vibration of the droplet.
- Normal force distribution along the contact area during the vibration of a droplet.

Moreover, the effects of droplet volume, liquid viscosity and the micropillar density on the interaction forces are also investigated.

1.4 Thesis structure

This thesis is organized as followed.

Chapter 1 Introduction

- Objective of this thesis.

- The background study on the sliding and vibration of the droplet.
- The original point and significance of this study.

Chapter 2 Background theory

- Background theory related to mechanism of the droplet resting on a horizontal substrate
- Background theory related to sliding of the droplet.
- Background theory related to the resonance vibration of the droplet.
-

Chapter 3 Sensor fabrication and evaluation

- Sensor design, sensing principle and simulation results.
- Fabrication process and fabrication result of the sensors.
- Force calibration of the sensor.
- Resonant frequency measurement of the sensors.
-

Chapter 4 Experiments on the droplet sliding

- Experimental description, preparation of the liquid samples and measurement of surface tension and viscosity of the liquid samples
- Experimental setup.
- Image inquiry and processing
- Comparison of the interaction forces during a sliding of a droplet on a flat surface and a micropillar array.
- Effect of droplet volume, micropillar density and viscosity on the interaction forces.
- Comparison of the measured normal and shear forces and those obtained from high speed camera images.
- Results on the sliding induced vibration of the droplet.

Chapter 5 Experiments on droplet vibration

- Experimental setup and liquid preparation.
- Normal force distribution during the vibration of a droplet.
- Relationship between droplet volume and the 2^{nd} mode resonant frequency of the droplets.
- Relationship between the liquid viscosity and the attenuation rate of the droplet vibration. Application for measurement of the liquid viscosity based on droplet vibration using the proposed sensor array.

Chapter 6 Conclusion

Chapter 2 Background theory

This chapter reports the theory background on the static and dynamic interaction between a droplet and a solid substrate. The analysis on the contact angle of a droplet on a horizontal substrate is first introduced. Then the analysis on the sliding and vibration of a droplet is provided.

2.1 Droplets on a horizontal substrate

When a droplet is deposited on a smooth rigid substrate, the shape of the droplet is determined by the balance of gravitational energy and surface energy. The equilibrium contact angle of the droplet is given by the well-known Young-Dupre equation [7, 8, 87]:

$$\cos\theta_0 = \frac{\gamma_{SV} - \gamma_{SL}}{\gamma_{LV}} \qquad (2.1)$$

where γ_{SV}, γ_{SL} and γ_{LV} are the solid-vapor, solid-liquid and liquid-vapor interface free energy as shown in **Fig. 2.1 (a)**. This relation is obtained from either the force balance in the lateral direction at the edge of the contact area or the minimization of net surface free energy of the systems.

In case of a droplet on a rough surface, for example a surface decorated with microstructure array **Fig. 2.1 (b)**, the droplet can contact surface in two state: the Cassie state where the droplet sitting on the top of the microstructures and the Wenzel state where the droplet wets both the microstructures and the base of the substrate. It has been shown that the droplet in Cassie state can obtain a very high contact angle exceeding the maximum value of contact angle a droplet can obtain on a smooth surface. The contact angle of the droplet in Cassie state is given as [88]:

$$\cos\theta_{Cassie} = f_1 \cos\theta_0 - f_2 \qquad (2.2)$$

where θ_0 is the contact angle of the droplet on a smooth surface which has the same chemical properties with that of the micropillar; f_1 and f_2 is the fractions of the solid-liquid contact area and liquid-vapor contact area under the droplet base. When the solid is smooth, f_1 becomes 1 and f_2 becomes 0 and the

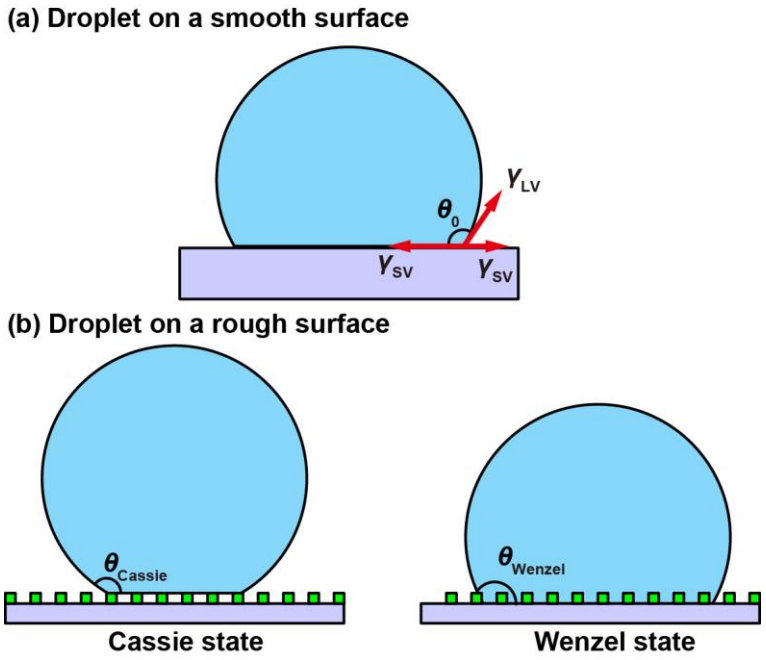

Fig. 2.1 Contact angle of a droplet on a smooth and a rough hydrophobic surface.

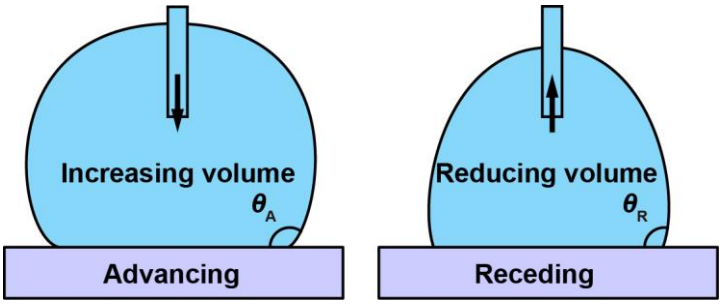

Fig. 2.2 Advancing and receding contact angles.

contact angle become θ_0. The relationship in **Eq. (2.2)** indicates that the contact angle of the droplet would increases if the solid-liquid area fraction decreases. In the other words, by reducing the microstructure size or density, it is able to obtain high contact angle, which is the design principle of a superhydrophobic surface. However, reducing the density also lets to the transit of the droplet to Wenzel state once the liquid between the microstructure touches the substrate base.

Beside the equilibrium contact angle, one important factor needed to be considered when analyzing the dynamics of the droplet is the contact angle hysteresis. Surfaces in reality is not completely smooth nor chemical heterogeneous, therefore the contact angle of a droplet on the surfaces is not unique, but can vary

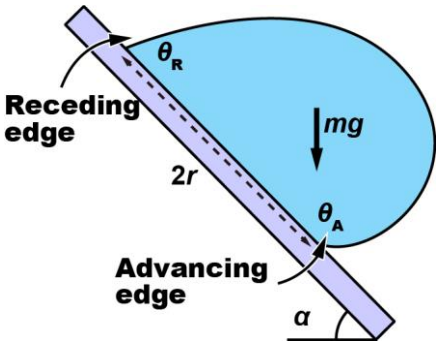

Fig. 2.3 Sliding of a droplet on a smooth surface.

in a range between the advancing and receding contact angle (the contact angle of advancing or receding liquid) as shown in **Fig. 2.2**. The contact angle hysteresis is defined as the difference between the advancing and receding contact angle. Contact angle hysteresis is important to evaluate the adhesion of the droplet to a surface. The larger the contact hysteresis is, the stronger the droplet adheres to the substrate.

Contact angle hysteresis often depends on the equilibrium contact angle, the higher the equilibrium contact angle usually results in a lower contact angle hysteresis.

2.2 Sliding of a droplet on a tilted substrate

A droplet on a tilted surface would slide if the gravitational force exceeds the frictional force of the droplet. The driving force to move the droplet forward is the component of gravity parallel to the surface $mg\sin\alpha$ where α is the tilted angle as shown in **Fig. 2.3**. Meanwhile the frictional force holding the droplet is the contact angle hysteresis induced adhesion of the droplet to the substrate in the lateral direction. For a smooth surface, this frictional force F_S can be approximately calculated as followed [63]:

$$F_S = \pi r(\cos\theta_R - \cos\theta_A) \quad (2.3)$$

Where r is the radius of the contact area, assuming the contact area is a circle. From these results, the sliding angle (the minimum tilted angle of the substrate when the droplet starts to slide), can be estimated as:

$$\sin\alpha = \frac{\pi r(\cos\theta_R - \cos\theta_A)}{mg} \quad (2.4)$$

Because the advancing and receding contact angles are determined by the nature of the liquid and the substrate, not by the droplet volume, **Eq. (2.4)** states that a larger droplet would slide at smaller tilted angle than that of a small one. Moreover, the lower the contact angle hysteresis is the smaller the sliding angle of

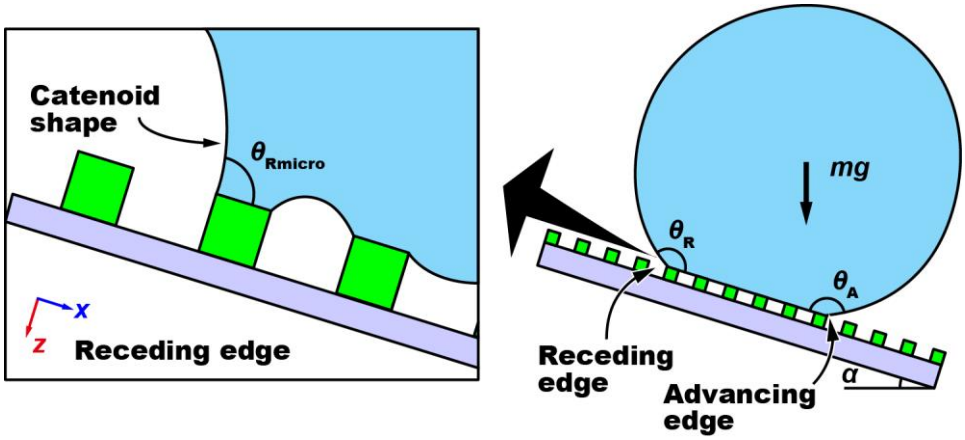

Fig. 2.4 Sliding of a droplet on a rough hydrophobic surface.

a droplet can be obtained. For the droplet sliding on a smooth surface, the advancing and receding contact angles can be obtained easily from captured images and the estimation of the frictional force is not difficult.

However, for a droplet on a rough surface in Cassie state, estimation of the frictional force becomes complicated since the droplet contacts with discrete microstructures. The first issue is that the apparent contact angle which is obtained from low resolution image of a camera and the contact angle at micro scale are not the same [67] as shown in **Fig. 2.4**. Achieving this dynamic micro contact angle is not easy by current observation technique based on microscopes. A method using ESEM was proposed to visualize the micro contact angle at the receding edge of the droplet very recently [48].

The second issue is that when the liquid recedes from each individual micropillar, a catenoid shaped liquid leg is developed. The interaction forces between the droplet and the micropillar depends on the three dimensional shape of this liquid leg. As mention previously, the ESEM images can provide the picture of the liquid leg, however, in only two dimensions. Thus the calculation of the interaction forces from ESEM images is still difficult.

A theoretical analysis on the development of the liquid leg attached to a single microstructure was proposed by de Gennes, P. G. and colleagues [34, 35, 42, 45] based on the spring model. As depicted in **Fig. 2.5**, the problem deals with a dilute system of defects (micropillar) with an assumption that the defects are far from each other. The interval between two micropillar and the width of a micropillar are ***p*** and ***w***, respectively. The liquid droplet is assumed to be much larger than the defect and the curvature of the liquid legs that be pulled back by the defect becomes almost zero which is similar to the case of a menisci on a thin fiber. Therefore the shape of the liquid leg can be described by the following equation [35]:

$$y \approx \frac{w}{2}\cosh\left(\frac{2x}{w}\right) \qquad \textbf{(2.5)}$$

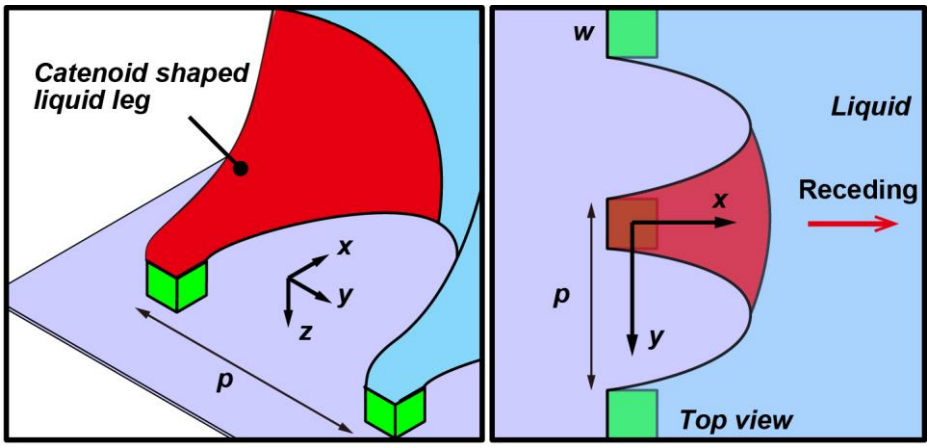

Fig. 2.5 Detachment of liquid from dilute defects at the receding edge.

where ***x*** and ***y*** are the coordinates as shown in **Fig. 2.5**. Here "≈" means scale as or in the same order with.

If we look at the ***y***-axis direction, the deformation of the liquid is largest at ***y*** = ***p***/2, therefore the maximum deformation of the liquid leg in x_{MAX} direction is obtained by solving the Eq. **(2.5)** under the assumption ***p*** is much larger than ***w***. The result is

$$x_{MAX} \approx \frac{w}{2} \ln\left(\frac{2p}{w}\right) \qquad (2.6)$$

Moreover, the force per micropillar scales as $F \approx w\gamma_{LV}$; therefore we obtain the relationship between the force and the displacement ***x*** which is quoted as:

$$F \approx \frac{\gamma_{LV}}{\ln\left(\frac{2p}{w}\right)} x \qquad (2.7)$$

This relationship between the force and the displacement indicates that the liquid leg behaves as a spring with the stiffness ***k*** is quoted as:

$$k \approx \frac{\gamma_{LV}}{\ln\left(\frac{2p}{w}\right)} \qquad (2.8)$$

Next the elastic energy ***U*** per micropillar is obtained from the stiffness ***k*** and the maximum deformation described in **Eq. (2.6)**. The result is quoted as:

$$U = \frac{1}{2} k x_{MAX}^2 \approx w^2 \gamma_{LV} \ln\left(\frac{2p}{w}\right) \qquad (2.9)$$

This elastic energy is balanced by the surface energy induced by the contact angle hysteresis; from which

the contact angle hysteresis can be estimated as followed:

$$\cos\theta_R - \cos\theta_A \approx \frac{w^2}{p^2}\ln\left(\frac{2p}{w}\right) \quad (\mathbf{2.10})$$

The relationship in **Eq. (2.15)** was experimentally investigated by Reyssat M. et al. [45].

In this study, the analysis on the spring-like behavior of the liquid leg developed at the receding of the droplet will be used to interpret the results related to the sliding-induced vibration of the droplet. The volume of the liquid leg can be estimated as:

$$V = \pi \int_0^{x_{\mathrm{Max}}} y(x)^2\,dx = \pi \int_0^{x_{\mathrm{Max}}} \left(\frac{w}{2}\cosh\left(\frac{2x}{w}\right)\right)^2 dx \quad (\mathbf{2.11})$$

Using the estimation of $x_{\mathbf{Max}}$ in **Eq. (2.6)**, we obtained:

$$V \approx w^3\left(2\ln\left(\frac{2p}{w}\right) + \sinh\left(2\ln\left(\frac{2p}{w}\right)\right)\right) \approx wp^2\left(1 + \frac{2\ln\left(\frac{2p}{w}\right)}{\left(\frac{2p}{w}\right)^2}\right) \quad (\mathbf{2.12})$$

Again, by assuming that $\boldsymbol{p}$ is much larger than $\boldsymbol{w}$, then volume of the liquid leg scales as:

$$V \approx wp^2 \quad (\mathbf{2.13})$$

2.3 Vibration of a droplet on a substrate

In this section, the basic theoretical results on resonant frequencies and damping factor of the vibration of a sessile droplet will be reported.

2.3.1 Resonant frequencies

The resonance frequencies of a free or levitated droplet with completely spherical shape are quoted as [89]:

$$f_{\mathrm{n}}^2 = \frac{n(n-1)(n-2)\gamma_{\mathrm{LV}}}{4\rho\pi^2 R^3} \quad (\mathbf{2.14})$$

where $\boldsymbol{\rho}$, $\boldsymbol{R}$ are the density of the liquid and the radius of the spherical droplet. n = 2, 3, 4.. is mode number.

The frequencies are fixed by liquid surface tension and the mass of the droplet. This relation shows that the frequency at a certain mode is proportional to the square root of the droplet mass.

For a sessile droplet which are similar to those in this study, the frequencies are not perfectly the same with **Eq. (2.14)** due to the effect of the solid-liquid contact area. The contact angle dependence of the frequencies are described in [84] as followed:

$$f_n^2 \approx \frac{n^3 \gamma_{LV}}{m} \frac{(\cos^3\theta - 3\cos\theta + 2)}{\theta^3} \qquad (2.15)$$

where θ is the contact angle and m is the droplet mass.

If we assume that the contact angle of a droplet on a substrate does not depend on the droplet volume; then the frequency of one mode are still proportional to square root of the droplet mass.

2.3.2 Viscous damping

Similarly to the frequencies, the damping of the vibration of a perfect spherical droplet was reported in previous research [90]. The result is quoted as:

$$\Gamma \approx \frac{n^2 \mu}{m^{2/3} \rho^{1/3}} = \frac{n^2 \mu}{\rho V^{2/3}} \qquad (2.16)$$

where Γ and μ are the damping constant associated with the exponential decay of the vibration amplitude and the viscosity of the droplet, respectively. The result shows that damping constant is proportional to the viscosity of the liquid.

In case of a sessile droplet, the bulk viscous damping coefficient is dependent on the contact angle. The modified result with consideration of the effect of the contact angle is quoted as:

$$\Gamma \approx \frac{n^2 \mu}{\rho V^{2/3}} \left(\frac{\cos^3\theta - 3\cos\theta + 2}{\theta^3} \right)^{2/3} \qquad (2.17)$$

where θ, R and n are the contact angle, the radius of droplet when it does not deform and the vibration mode number. For a certain vibration mode of droplets with the same volume, if the contact angle does not depend on the viscosity of the liquid then we obtain the same linear relationship between the damping constant and the viscosity as for a spherical shaped droplet.

Chapter 3 Sensor fabrication and evaluation

In this chapter, the design, fabrication and calibration of MEMS-based force sensors used in this study are presented. In the first section, the design and geometrical parameters of the sensor will be provided, followed by the sensing principle which is supported by FEM simulation results. In the next section, the fabrication process of the sensor is described and the fabrication results with SEM images of the sensors is reported. Then, the calibration method and calibration results of all fabricated sensor are presented. Finally, the resonant frequency measurement for each sensor is reported.

3.1 Sensor design and sensing principle

3.1.1 Sensor design

The top view conceptual sketch of the entire device is shown in **Fig. 3.1**. The device consists of a micropillar array and a MEMS-based sensor at the center. The surface area of the entire device and the micropillar are 10 mm × 6 mm and 10 mm × 5 mm, respectively. The MEMS-based sensor in this paper was designed to directly measure the normal force and shear force acting on the surface of a micropillar. To realize the detection of both normal and shear force, a piezoresitive silicon structure beneath the micropillar is proposed as a sensing element as shown in **Fig. 3.2(a)**. The basic idea in this sensor design is to utilize the piezoresistive effect of silicon: when a piezoresistive silicon beam deforms, its electrical resistance will change [91, 92], which also means that by monitoring the resistance of the beam, it is possible to detect the force acting on the beam.

The design parameters of the sensor are given in **Fig. 3.2(b)**. The size of a micropillar is 30 μm by 30 μm by 30 μm, which is fixed in this study. The pitch of the micropillar array is varied in the range of 75 μm to 175 μm. In the design of the sensing elements, the silicon structure consists of four silicon beams supporting a square pad at the center on which the micropillar is formed. Two piezoresistors are formed at the root of two opposite beams, while the remaining area of the silicon structure is deposited with Cr/Au which functions as electrical wires. Basically, the thinner the silicon structure is, the higher the sensitivity

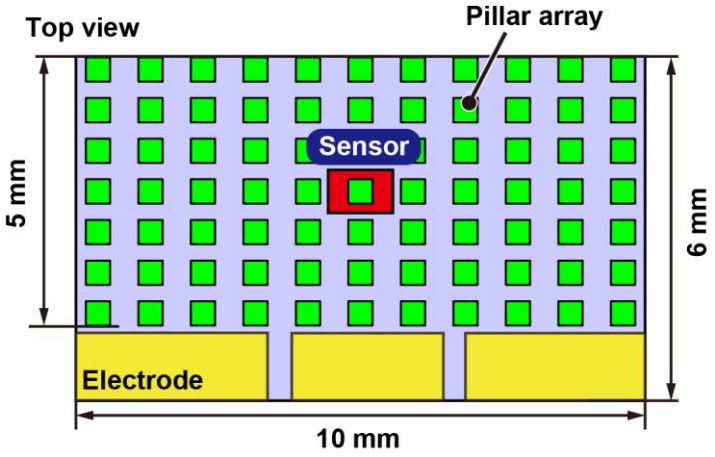

Fig. 3.1 The design and geometrical parameters of a sensor chip.

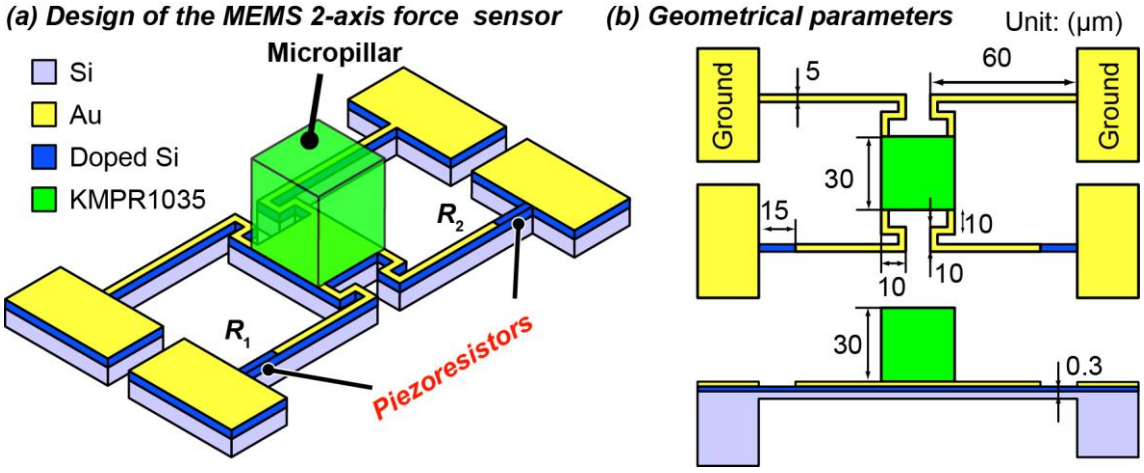

Fig. 3.2 The design and geometrical parameters of a two-axis MEMS-based sensor.
Reproduced from [93], Copyright 2014 Elsevier.

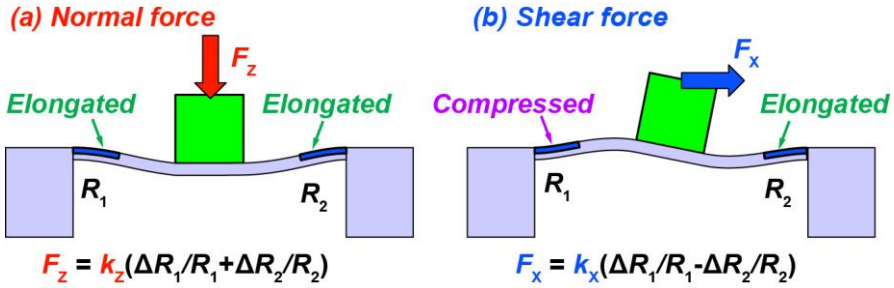

Fig. 3.3 Sensing principle of the proposed two-axis force sensor.
Reproduced from [93], Copyright 2014 Elsevier.

of the sensor can be obtained. However, for extremely thin silicon beam, for example less than 100 nm,

relatively complicated fabrication process is required. In this paper, the thickness of the silicon structure is chosen to be 300 nm, for which a well-established fabrication process is already reported [93, 94]. The width and the length of each silicon beam are 5 μm and 60 μm, respectively. The length of two piezoresistors was 15μm.

3.1.2 Sensing principle

The sensing principle of the sensor is illustrated in FIGURE. When a normal force is applied to the surface of the micropillar, the silicon structure underneath the micropillar will be pressed down causing a positive strain of both two piezoresistors. Depending on the doping-type of the piezoresistors, their resistances will both increase or decrease. Thus, the applied normal force can be detected from the average value of the resistance changes of the two piezoresistors.

On the other hand, when a shear force is applied to the micropillar surface, the micropillar will slightly rotate due to a torque caused by the shear force. As a result of this rotation, one piezoresistor is elongated, whereas the other is compressed. Therefore, the resistance of one piezoresistor decreases, whereas that of the other increases, hinting that the shear force can be detected from the difference in the resistance changes of two piezoresistors.

In summary, since the silicon structure deforms in different manners when normal or shear force is applied, from the resistance changes of the two piezoresistors, normal and shear force can be independently back-calculated.

3.1.3 FEM simulation

To confirm the sensing principle, finite element model simulations were carried out using software COMSOL MultiPhysics (COMSOL). The model used in the simulations is shown in **Fig. 3.4(a)**, which has the same geometrical dimensions with those in the sensor design. Materials properties used in the simulations are given in **Table 3.1**. The model was meshed using the free tetrahedral-type element as shown in **Fig. 3.4(b)**. Number of the element was 332,283. For boundary conditions, the free end of all four Si beams are fixed. A force of 1 μN was applied to the surface of the pillar in *z*-axis direction or *x*-axis direction. The positive directions of the forces are the same with that of *z*-axis and *x*-axis, respectively. Moreover, the resonant frequencies of the sensor is also investigated.

The simulation results are shown in **Fig. 3.5**. The deformation and strain in *x*-axis direction, which determined the resistance change of the sensing beams, are shown in **Fig. 3.5**(a) and **Fig. 3.5**(b) for normal force and shear force, respectively. As expected, when the normal force is applied, both piezoresistors are elongated, and the average strain over the surface of each piezoresistor were approximately 0.5 μstrain. On the other hand, when the shear force is applied, one piezoresistor is elongated while the other is compressed and the average strains over the surface of the two piezoresistors were approximately 0.2 μstrain and -0.2 μstrain, respectively. This result agrees with the sensing principle described previously.

Fig. 3.6 shows the results on the resonant frequencies of the sensor. Two first resonant frequencies of the sensor were 15.1 kHz and 27.2 kHz, and the corresponding deformation modes are shown in **Fig. 3.6(a)**

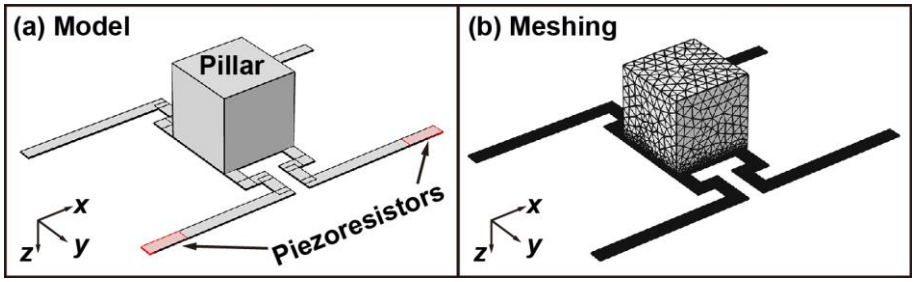

Fig. 3.4 (a) Model used in FEM simulation. (b) Meshing of the model.

Table 3.1 Properties of materials used in the simulations.

Material properties	Silicon (Sensing structure)	KMPR1035 (Micropillar)
Density	2329 kg/m^3	1200 kg/m^3
Young's modulus	170 GPa	2 GPa
Poisson ratio	0.28	0.22

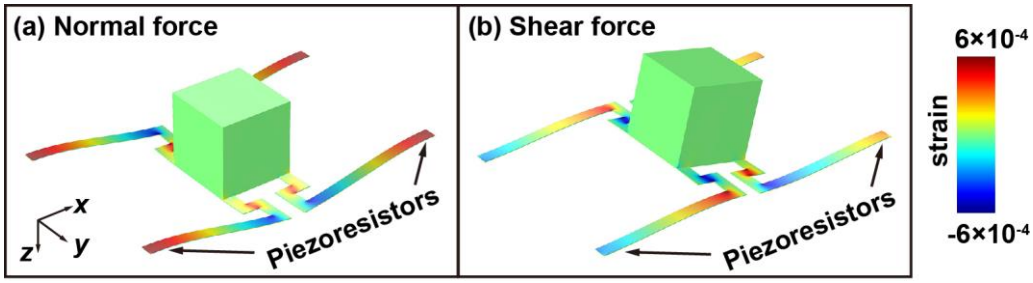

Fig. 3.5 Simulation results. The strain in *x*-axis direction when (a) a normal force is applied and (b) a shear force in *x*-axis is applied to the pillar surface.

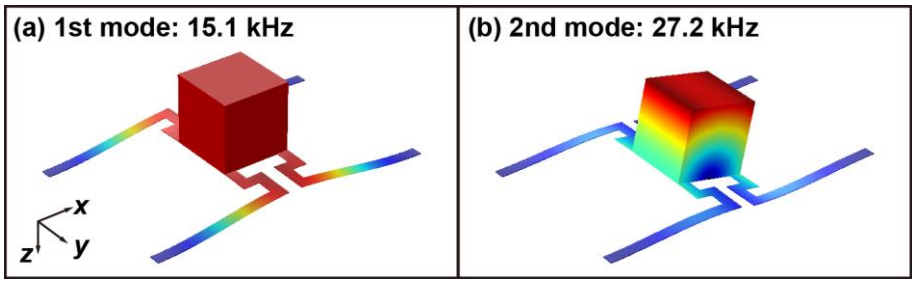

Fig. 3.6 Simulation results. The first (a) and second (b) resonant modes of the sensor.

and **Fig. 3.6(b)**, respectively. The lowest resonant frequency corresponds to the vibration in the normal (*z*-axis) direction. The result indicates that this sensor design is able to detect the high frequency component of the normal and shear forces up to 15 kHz.

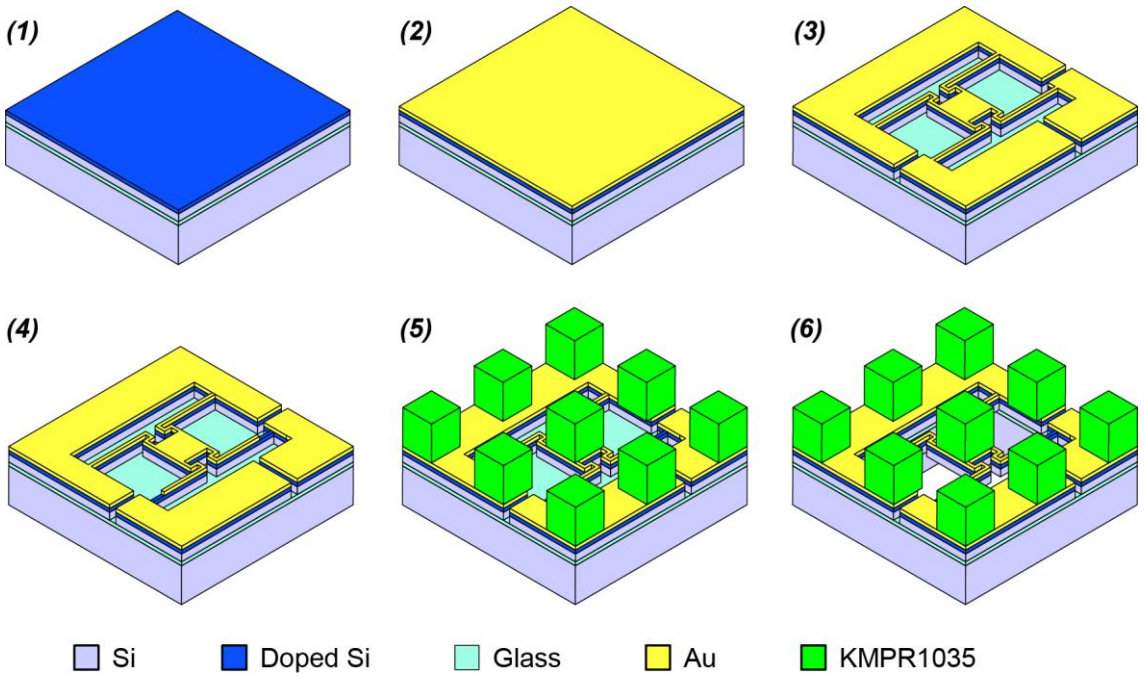

Fig. 3.7 Fabrication process of the sensor. Reproduced from [93], Copyright 2014 Elsevier.

3.2 Sensor fabrication

3.2.1 Fabrication process

The fabrication process of the sensor is shown in **Fig. 3.7**. In the first step, the device Si layer of a Si-On-Insulator (SOI, thickness: 0.3/0.4/300 μm) wafer was doped using ion implantation. Then, an Au/Cr layer (thickness: 30 nm/3 nm) was deposited onto the device Si layer using electron beam-induced evaporation. After the Au/Cr layer was patterned using wet etching, the device Si layer was etched using inductively coupled plasma-RIE (ICP-RIE) to form the sensing Si structure. In the next step, the Au/Cr layer was patterned again to reveal the piezoresistors at the roots of two Si beams. The micropillar array was then formed by spin-coating and patterning a layer of KMPR1035 (MicroChem Co., US; 3000 rpm for 60 s) photoresist on the device Si layer. Micropillar arrays with different pitches were formed using glass-masks that have different square patterns. Afterwards, the handle Si layer was deposited with an Al layer as a mask for ICP-RIE etching. After the Al layer was patterned, the device Si layer was etched using ICP-RIE to create a through-hole under the sensing Si structure. In this etching step, the micropillar array was covered by an AZP 4620 photoresist layer (MicroChem Co., Us). Then, the SiO_2 layer was removed by HF vapor etching. After that the wafer was dipped in acetone for 15 minutes before being removed from the aluminum disk of the ICP-DRIE. Finally, the wafer was left in IPA for one day, to remove all the vacuum oil and photoresist on the micropillar array.

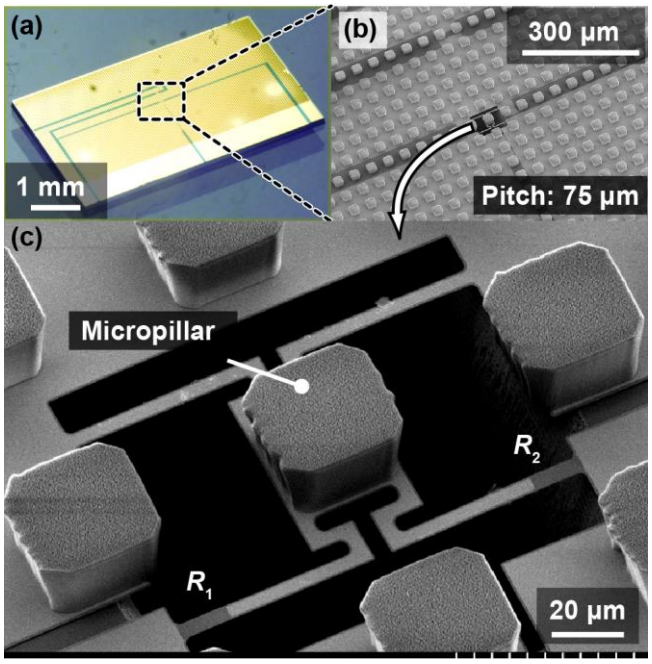

Fig. 3.8 Photograph and SEM images of the fabricated sensor with the pillar pitch of 75 µm. Reproduced from [93]**,** Copyright 2014 Elsevier.

3.2.2 Surface hydrophobicity treatment

The fabricated device was first cleaned using O_2 plasma (Compact Etcher, SAMCO Inc.) under 50 W for 5 minutes. This process also induces the hierarchical structure of the micropillar array by creating a nano-grass structure on the surface of the micropillars. Finally, a thin layer of C_4F_8 was deposited on the device as a hydrophobic coating. The coating was carried out inside the vacuum chamber of ICP-DRIE.

3.2.3 Fabrication results

A photograph and SEM images of a fabricated sensor having a 75 µm-pitch micropillar are shown in **Fig. 3.8**. The two piezoresistors formed at the root of two silicon beams are shown in **Fig. 3.8(c)**. It is also confirmed that nano-grass structure is formed on the surface of the micropillars as a side result of the O_2 plasma cleaning. This nano-grass structure actually improves the hydrophobicity of the micropillar array as shown in previous research [48]. The entire surface areas of the sensor device and micropillar array were 10 mm × 6 mm and 10 mm × 5 mm, respectively. The initial resistances of the two piezoresistors were approximately 750 Ω.

As described previously, in this study, the pitch of the micropillar array is varied to investigate the effect of pillar density on the interaction forces between a sliding droplet and a micropillar. Sensors having micropillar array with different pitches are fabricated as shown in **Fig. 3.9**. All the sensors have the same sensing Si structure but the pitches of the micropillar array were varied as 75, 100, 125, 150 and 175 µm. Moreover, a sensor without pillar array (flat surface) was also fabricated for comparison.

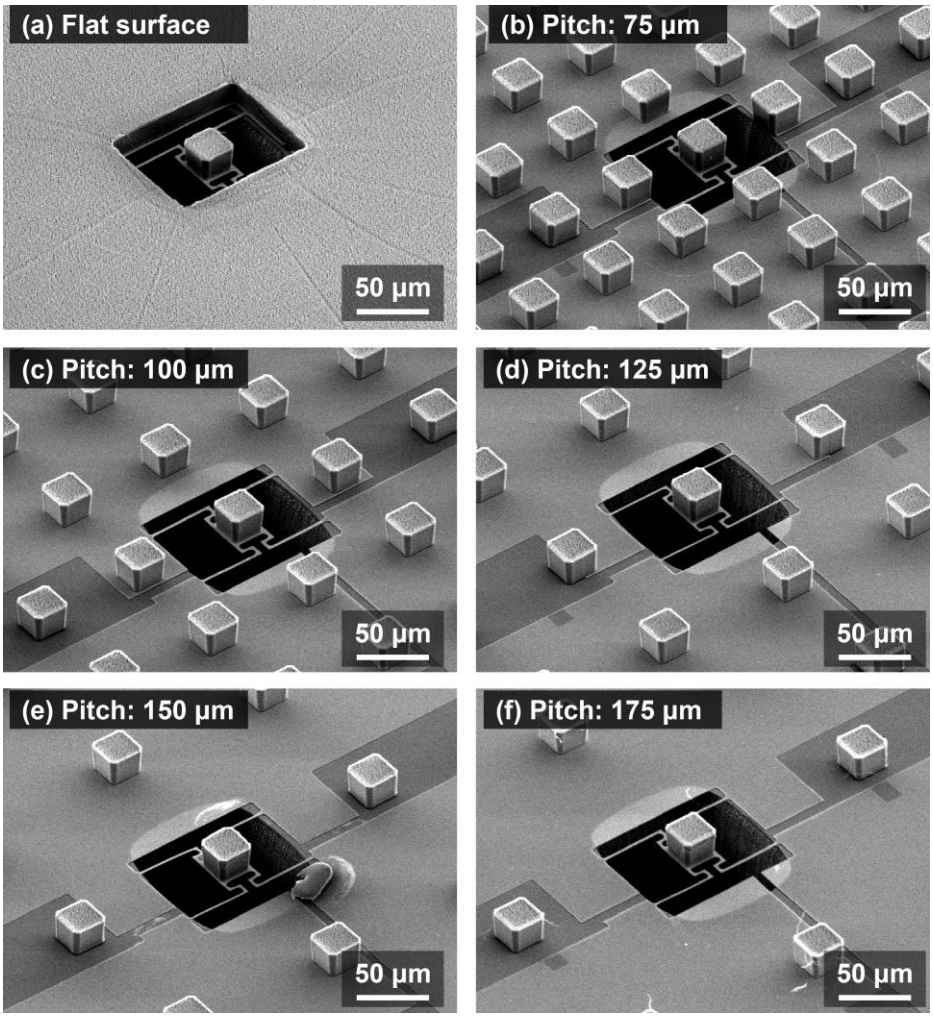

Fig. 3.9 SEM images of the fabricated sensors with flat surface (a) and the micropillar pitch of 100, 125, 150 and 175 μm (b-f).

Each fabricated sensor chip was then attached to a printed circuit board (PCB) using kapton both-side tape and the electrodes of the chip were connected to the Cu patterns of the PCB using a wire-bonder (USW-5Z60K, Ultrasonic Engineering Co.).

3.3 Fabrication result of the cantilever array

The fabrication process of the cantilever array designed for the measurement of droplet vibration is the same with that of the two axis-MEMS based sensor described in previous section. The fabrication result is shown in **Fig. 3.10**. An array of thirteen cantilevers were fabricated. Each of the cantilever has a micropillar sitting on the surface. The micropillars in this sensor design have the same size with that of the two-axis sensors reported in previous section. The pitch of the micropillar array is 75 μm. The micropillar array of the sensor was also cleaned with O_2 plasma before deposited with C_4F_8 for hydrophobic treatment.

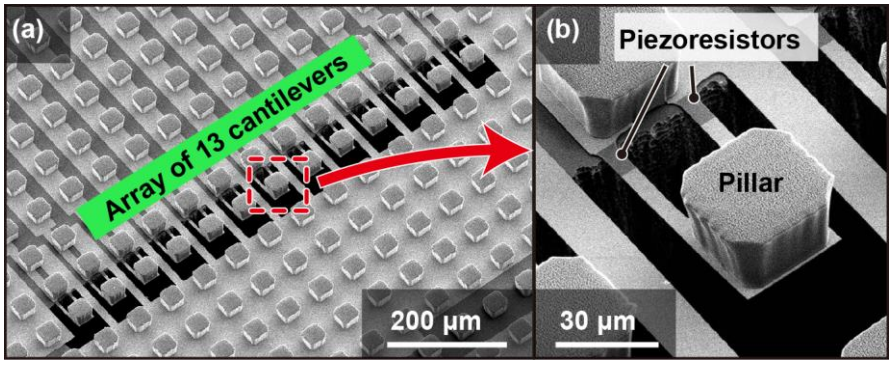

Fig. 3.10 SEM images of the fabricated cantilever array used for measurement of the droplet vibration. Copyright 2015 IEEE.

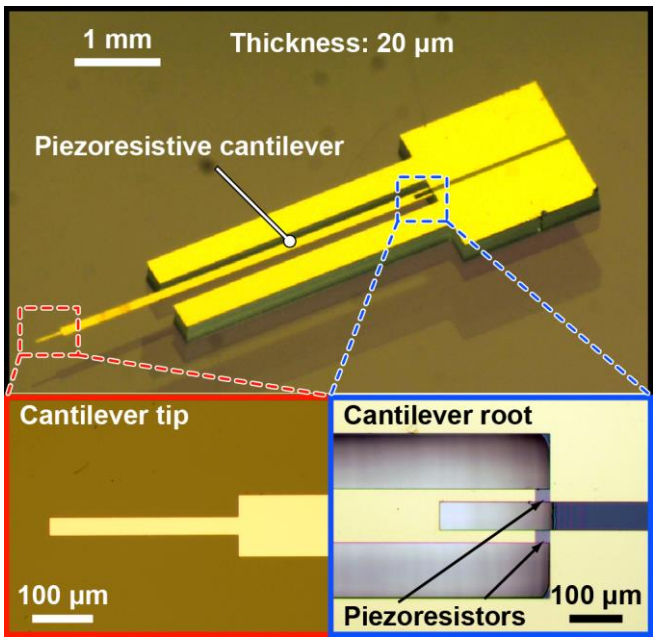

Fig. 3.11 Photographs of fabricated cantilever used for sensor calibration. Reproduced from [93], Copyright 2014 Elsevier.

3.4 Fabrication of a cantilever used for sensor calibration

The fabricated sensors in this study are designed to measure the forces of several μN. Therefore, it is not easy to calibrate the sensors using commercially available force gauges which have sensing resolution of several tens μN order. Therefore, a MEMS-based cantilever was fabricated to apply and measure the force acting on the micropillar. The fabrication process for the cantilever is basically similar with that for the

sensors described previously, except for the doping process and the micropillar array formation step. For the doping step, instead of ion implantation, the wafer is doped by rapid thermal infusion method [95] using n-type dopant (OCD P-59230, Tokyo Ohka Industries, Co.). This method is suitable for doping only one wafer. Moreover, the micropillar formation step was not necessary in the fabrication process of the cantilever.

Photographs of the fabricated cantilever is shown in **Fig. 3.11**. The thickness of the cantilever is 20 μm and the width of the cantilever tip is 30 μm, which is the same with the width of the micropillar. The length of the cantilver was 4 mm. Two walls along the cantilever were formed from the device Si layer to protect the cantilever during the calibration process.

3.5 Calibration of the MEMS-based two axis sensor

In this section, the calibration method and calibration result for all fabricated sensors will be provided.

3.5.1 Calibration method

As mentioned previously, the sensor in this study is calibrated using a reference MEMS-based piezoresistive cantilever shown in **Fig. 3.11** as a force probe. The cantilever itself is calibrated using a commercial load cell (LVS-5GA, Kyowa Co., Japan) which has a sensing resolution of several tens μN order. The reference cantilever is designed to have the sensitivity in between that of the sensor and the load cell to improve the accuracy of the calibration.

3.5.2 Calibration of the load cell and the cantilever

First, the load cell was calibrated by testing it with different known weights ranging from 0 to 5 mN. The output of the load cell is the voltage difference before and after the weights are placed on the load cell. The calibration result of the load cell is shown in **Fig. 3.12**. A linear relationship between the output of the load cell and the applied force was confirmed and the sensitivity of the load cell was calculated from the slope of the fitting line to be 263.8 (V/N).

In the next step, the fabricated reference cantilever is calibrated using the load cell. A setup of the calibration is shown in **Fig. 3.13(a)**. The cantilever was first attached to a piezo-stage (P-753.11C, PI Polytech), which can move in three dimensions independently within the range of ±15 μm. The cantilever tip was first brought in contact with the load cell, and then, the piezo-stage was moved in the normal direction to apply a force to the cantilever. The applied force was calculated from the output of the load cell. During the calibration, the resistance of the cantilever was measured using a Wheatstone brigde circuit. The output of the Wheatstone brigde circuit was amplified by 1,000 times using AIN 217 (Texas Instrument Inc., US) before being measured by a scope-coder (DL850, Yokogawa Meters & Instruments Co.). The resistance change of the cantilever was calculated from the output voltage of as followed [93, 96]:

$$\frac{\Delta R}{R} = 4\frac{\Delta V_{\text{out}}}{V_{\text{cc}}} \qquad (3.1)$$

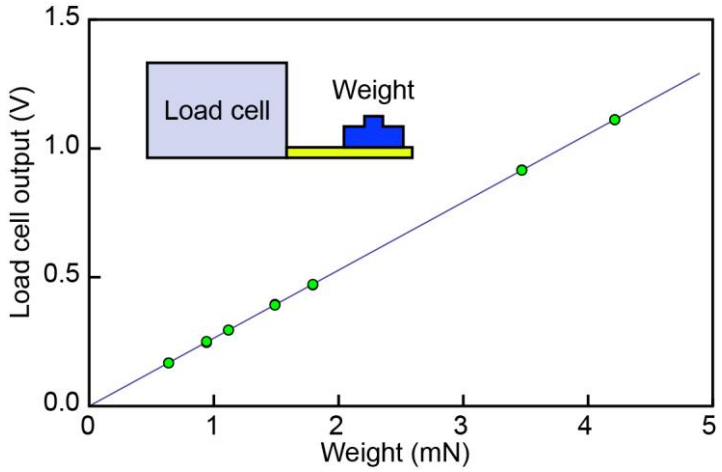

Fig. 3.12 Calibration result of the load cell (LVS-5GA, Kyowa Co., Japan).

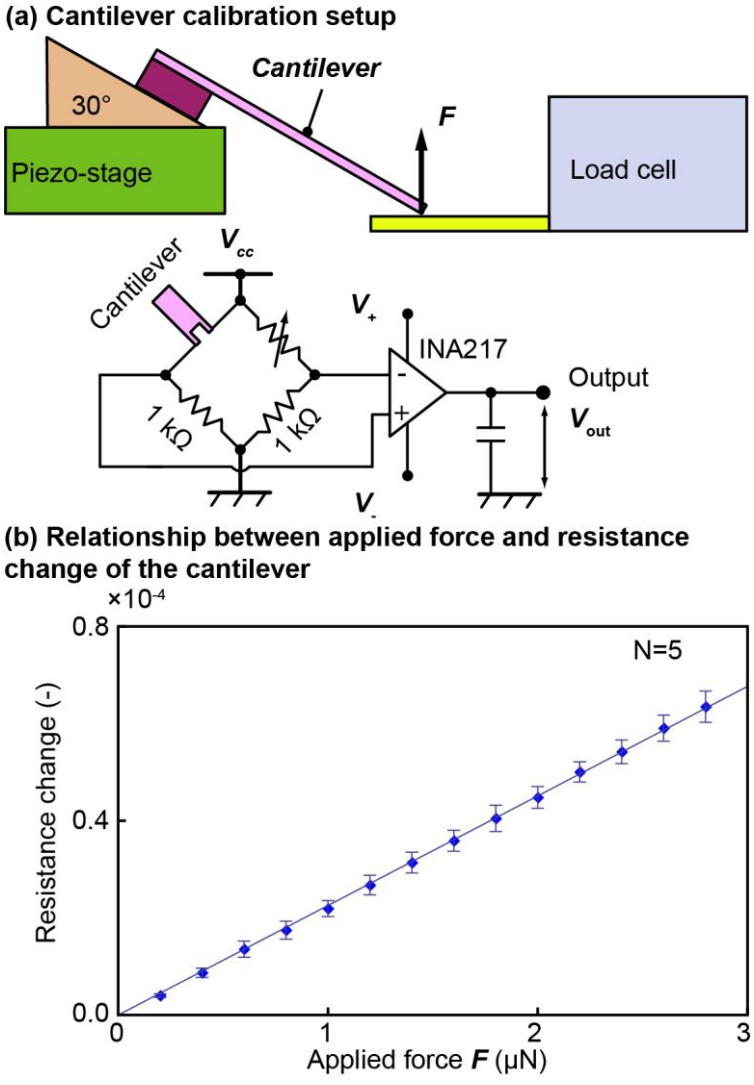

Fig. 3.13 Calibration setup and calibration result of the cantilever.

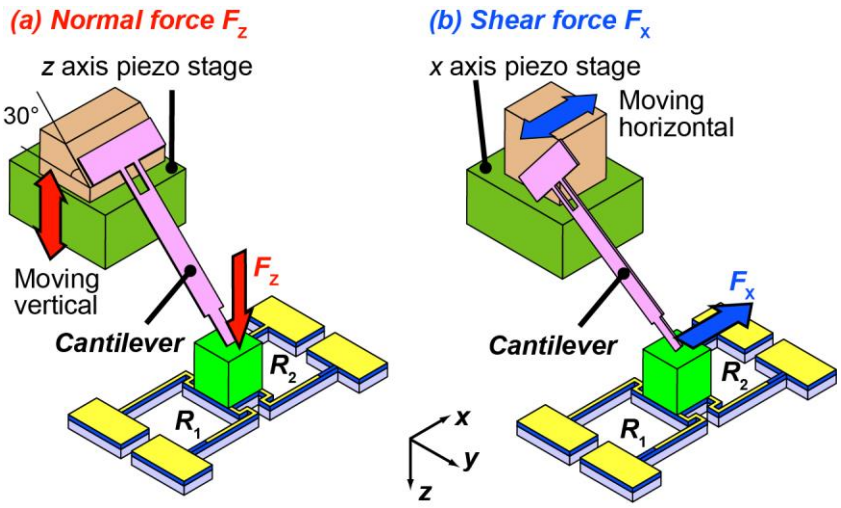

Fig. 3.14 Setups for the calibration of the two-axis force sensor in normal (a) and shear (b) directions. Reproduced from [93], Copyright 2014 Elsevier.

where V_{cc} was 1 V during the experiment.

The calibration result of the cantilever is shown in **Fig. 3.13(b)**. The resistance change of the cantilever was confired to be proportional to the applied force. The sensitivity of the cantilever was obtained to be 0.23×10^{-3} (μN^{-1}).

3.5.3 Sensor calibration setup

The fabricated 2-axis sensors were calibrated using setup shown in **Fig. 3.14**. This setup was similar to the setup that was used to calibrate the cantilever. Here, the load cell was replaced by the sensor. First, the cantilever was attached to a stage made from 3D printer with a 30° slanting angle to the horizon. The stage was then attached to the *xyz*-piezo-stage to control the displacement of the cantilever in the vertical and lateral directions. As shown in **Fig. 3.14(a)**, in the normal force calibration, the cantilever tip was pressed on the micropillar of the sensor in the normal direction by moving the piezo-stage in *z*-axis. The alignment of the cantilever tip and the micropillar was carried out by using a microscope (Keyence, VH-5910). The force applied to the micropillar was calculated from the resistance change of the cantilever as:

For the shear force calibration, as shown in **Fig. 3.14 (b)**, the cantilever was rotated by 90° about its length axis such that the cantilever could detect the force acting in the *x*-axis direction. First, the cantilever was pressed onto the upper surface of the micropillar by moving the *z*-axis piezo-stage. The cantilever was then moved in the lateral direction by the *x*-axis piezo-stage to apply a shear force to the micropillar. The initial pushing force in the normal direction was applied to prevent the cantilever tip from slipping on the pillar when the shear force was applied. Similar to the normal force calibration, the applied shear force was calculated from the resistance change of the cantilever. Because the cantilever is perpendicular to shear force, the shear force.

The piezo-stage was moved by applying a voltage from a function generator in triangular shape at 0.3 Hz.

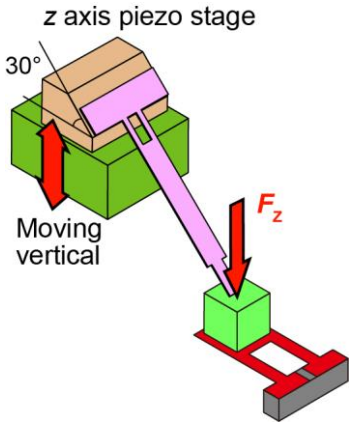

Fig. 3.15 Set up for calibration of the cantilever array.

The displacement of the piezo-stage was controlled by adjusting the amplitude of the applied voltage. Obviously, the displacement of the piezo-stage and that of the micropillar was not the same due to the deformation of the cantilever. The voltage of the piezo-stage was adjusted so that the force acting on the micropillar became several μN order. For this condition, the displacement amplitudes of the piezo-stages were approximately 10 μm and 6 μm in calibration of normal and shear forces, respectively.

The setup for calibration of the cantilever array used in measurement of the droplet vibration is shown in **Fig. 3.15**, which is similar to that of the normal force calibration of the two-axis sensors.

3.5.4 Calibration result

Calibration result for two-axis force sensors

The calibration results of the sensors with 75, 100, 125, 150 and 175 μm are shown in **Fig. 3.17** to **Fig. 3.21**. Overall, for all sensors, when the normal force $\boldsymbol{F_Z}$ is applied, the resistances of both piezoresistors $\boldsymbol{R_1}$ and $\boldsymbol{R_2}$ decreased. Meanwhile, when a shear force $\boldsymbol{F_Z}$ is applied, the resistance of $\boldsymbol{R_1}$ increased while that of $\boldsymbol{R_2}$ decreased. These behaviors of the two piezoresistors when normal and shear forces were applied are well agreed with the sensing principle and FEM simulation results provided in Section **3.1**. Moreover, the change in resistances $\boldsymbol{R_1}$ and $\boldsymbol{R_2}$ were proportional to the applied forces which indicates that the applied forces can be back-calculated from the resistance changes of the two piezoresistors. In details, the proportional coefficients between the resistance changes of $\boldsymbol{R_1}$ and $\boldsymbol{R_2}$ and the applied normal and shear forces for each sensor are obtained by fitting the plot points in each graph with a linear function. From these results, matrixes showing relationships between the resistance changes of the two piezoresistors of each sensor and the applied forces can be obtained as shown in **Eq. (3.2)** to **Eq. (3.7).** The variation in the value of these matrixes is thought to be caused by the variation in the width of the sensing beams of the fabricated sensors. In our sensor design with long narrow beams as sensing elements, the sensitivity of the sensor largely depends on the beams width. In fact, as described in the fabrication process, the sensing beams of all sensors are patterned using wet-etching of Au/Cr layer. During this step, depending on the

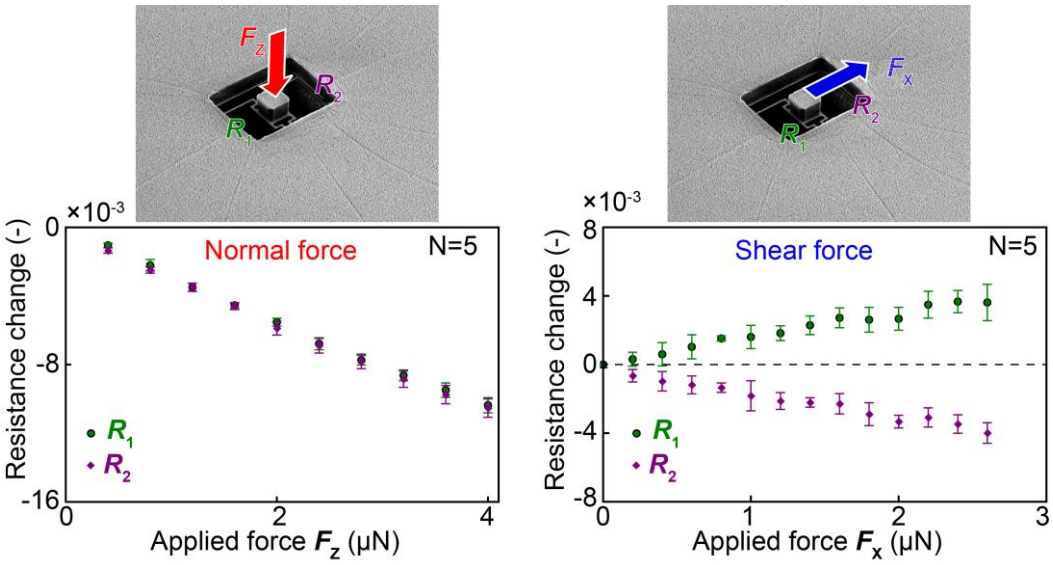

Fig. 3.16 Calibration result for the sensor that has a flat surface.

$$\begin{pmatrix} \Delta R_1 / R_1 \\ \Delta R_2 / R_2 \end{pmatrix}_{(-)} = 10^{-3} \times \begin{pmatrix} -2.7 & 1.5 \\ -2.8 & -1.6 \end{pmatrix} \begin{pmatrix} F_Z \\ F_X \end{pmatrix}_{(\mu N)} \quad \textbf{(3.2)}$$

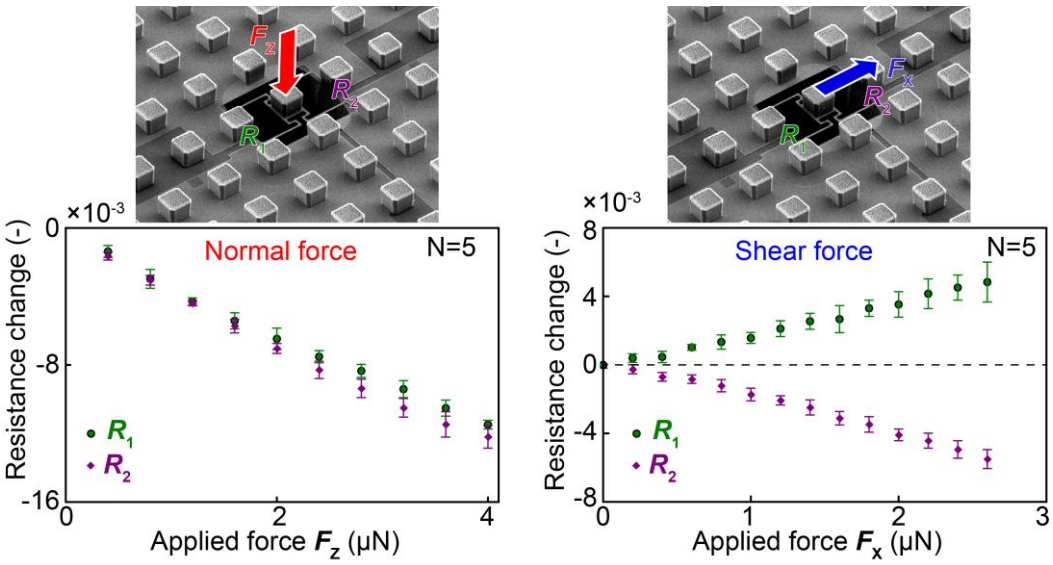

Fig. 3.17 Calibration result for a sensor with a micropillar array that has 75 μm-pitch.

$$\begin{pmatrix} \Delta R_1 / R_1 \\ \Delta R_2 / R_2 \end{pmatrix}_{(-)} = 10^{-3} \times \begin{pmatrix} -3.0 & 1.8 \\ -3.3 & -2.0 \end{pmatrix} \begin{pmatrix} F_Z \\ F_X \end{pmatrix}_{(\mu N)} \quad \textbf{(3.3)}$$

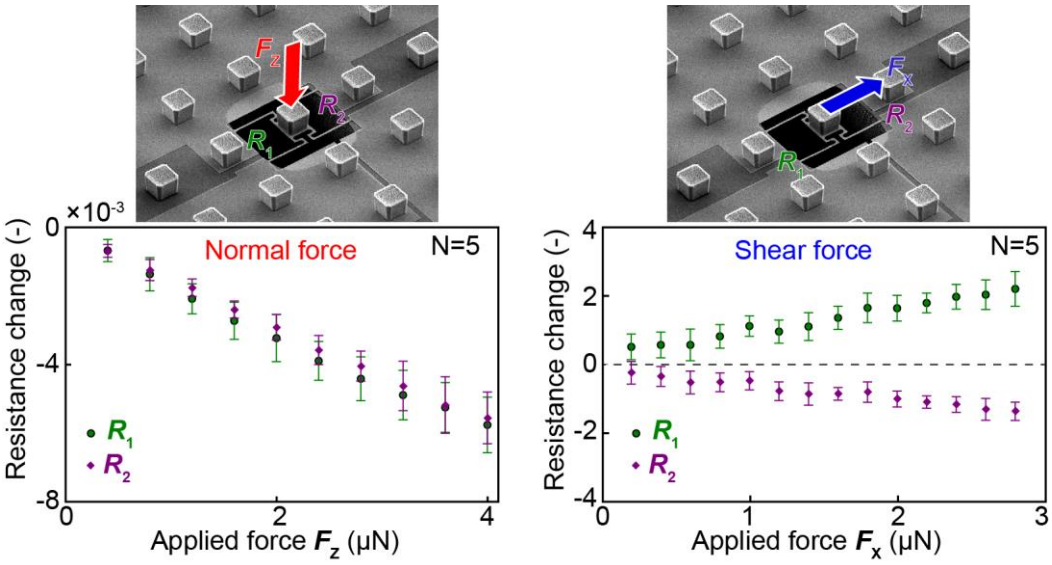

Fig. 3.18 Calibration result for the sensor with a micropillar array that has 100 μm-pitch.

$$\begin{pmatrix} \Delta R_1 / R_1 \\ \Delta R_2 / R_2 \end{pmatrix}_{(-)} = 10^{-3} \times \begin{pmatrix} -1.5 & 0.8 \\ -1.4 & -0.5 \end{pmatrix} \begin{pmatrix} F_Z \\ F_X \end{pmatrix}_{(\mu N)} \quad \textbf{(3.4)}$$

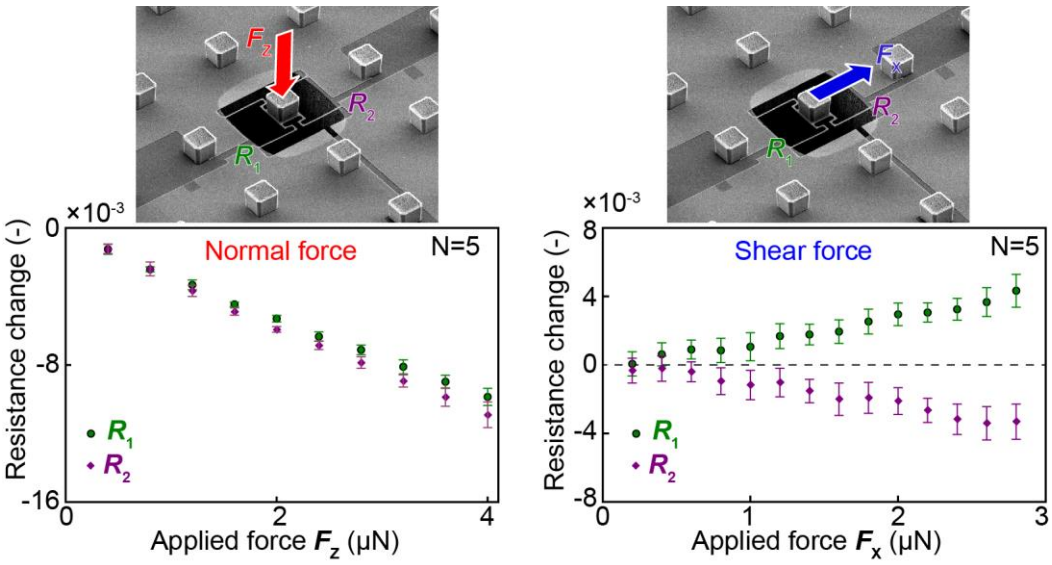

Fig. 3.19 Calibration result for the sensor with a micropillar array that has 125 μm-pitch.

$$\begin{pmatrix} \Delta R_1 / R_1 \\ \Delta R_2 / R_2 \end{pmatrix}_{(-)} = 10^{-3} \times \begin{pmatrix} -2.6 & 1.4 \\ -2.8 & -1.2 \end{pmatrix} \begin{pmatrix} F_Z \\ F_X \end{pmatrix}_{(\mu N)} \quad \textbf{(3.5)}$$

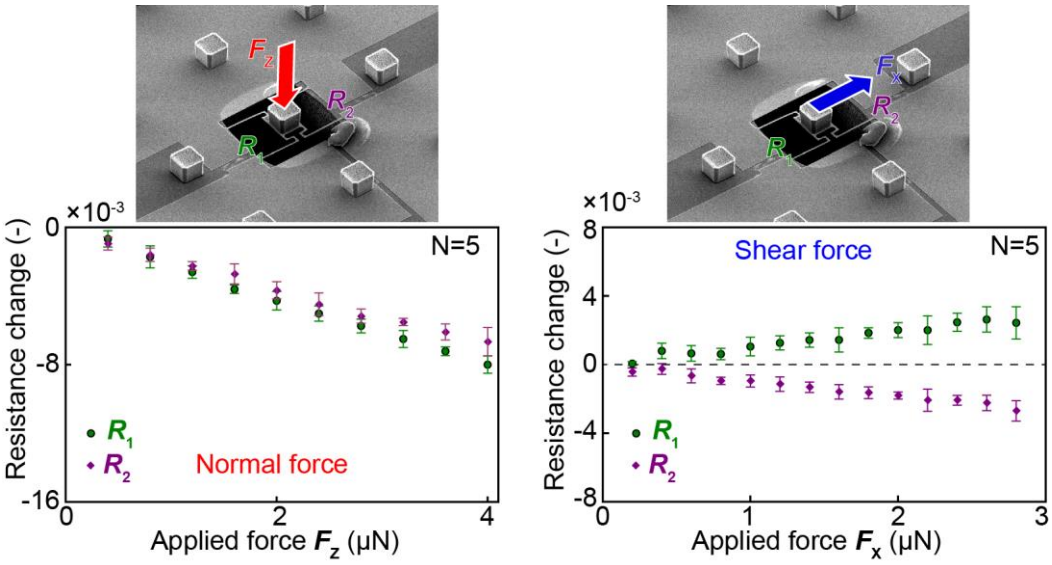

Fig. 3.20 Calibration result for the sensor with a micropillar array that has 150 μm-pitch.

$$\begin{pmatrix} \Delta R_1 / R_1 \\ \Delta R_2 / R_2 \end{pmatrix}_{(-)} = 10^{-3} \times \begin{pmatrix} -2.0 & 1.0 \\ -1.7 & -0.9 \end{pmatrix} \begin{pmatrix} F_Z \\ F_X \end{pmatrix}_{(\mu N)} \quad \textbf{(3.6)}$$

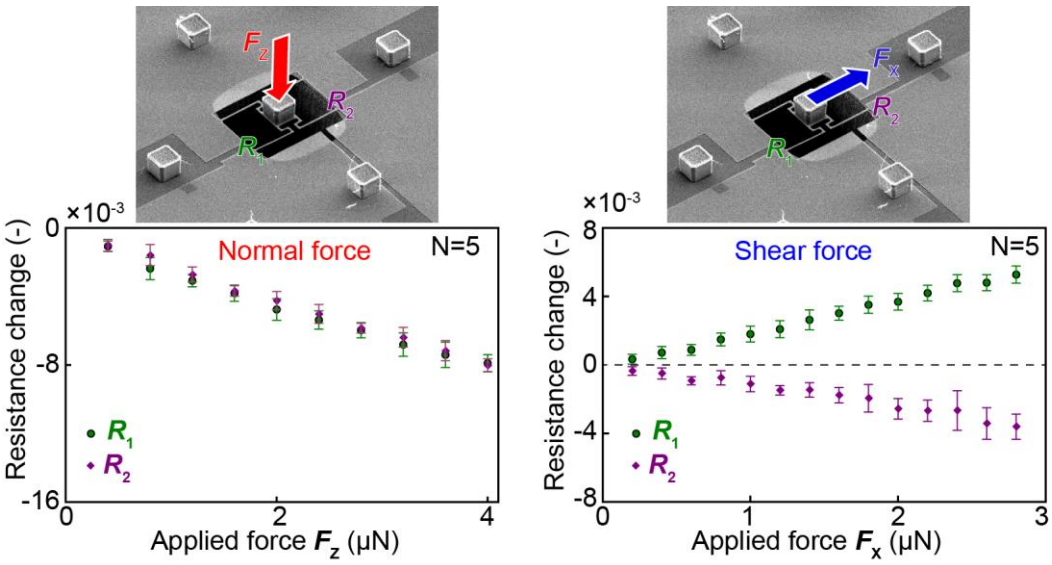

Fig. 3.21 Calibration result for the sensor with a 175μm pitch micropillar array.

$$\begin{pmatrix} \Delta R_1 / R_1 \\ \Delta R_2 / R_2 \end{pmatrix}_{(-)} = 10^{-3} \times \begin{pmatrix} -2.1 & 1.9 \\ -2.1 & -1.2 \end{pmatrix} \begin{pmatrix} F_Z \\ F_X \end{pmatrix}_{(\mu N)} \quad \textbf{(3.7)}$$

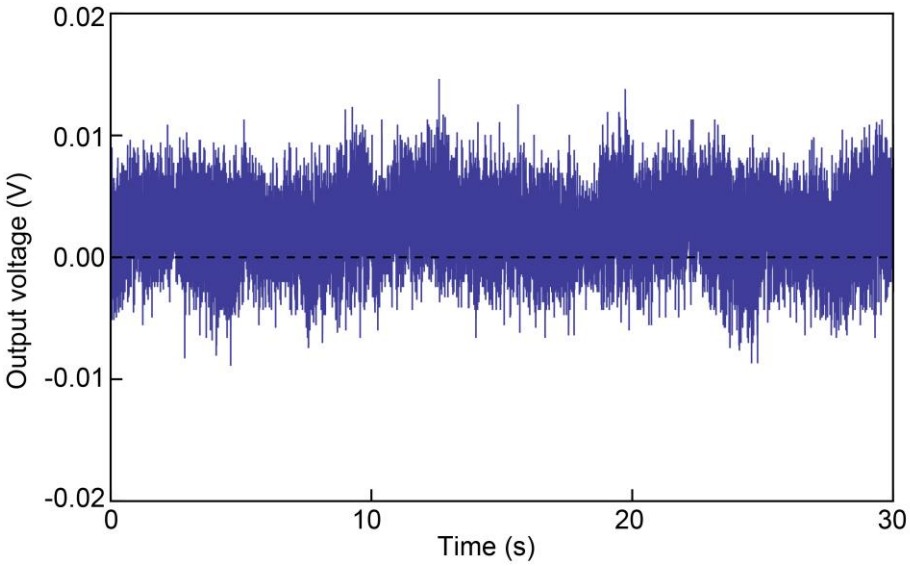

Fig. 3.22 A typical output voltage of a sensor. The noise level is less than 20 mV corresponding to a resistance change of 8×10^{-5}.

Table 3.2 Sensing resolution of the fabricated sensors.

Sensor	Normal force resolution	Shear force resolution
Flat surface	0.03 μN	0.05 μN
75 μm-pitch	0.03 μN	0.04 μN
100 μm-pitch	0.06 μN	0.12 μN
125 μm-pitch	0.03 μN	0.06 μN
150 μm-pitch	0.04 μN	0.08 μN
175 μm-pitch	0.04 μN	0.05 μN

position of the beam on the wafer, the etching rate varied resulting in a variation of the sensing beam width. Nevertheless, using the inverse-matrix of the matrix in each equation, the applied force in normal and shear direction can be calculated. Moreover, the sensing resolutions of each sensor can also be estimated from the noise level of the measuring system. Particularly, for our measuring systems, the noise level is less than 20 mV as shown in **Fig. 3.22**. This voltage is equivalent to a minimum detectable resistance change of $\pm8\times10^{-5}$ using the relationship in **Eq. (3.1)**. Inversely calculating from this minimum detectable resistance change, we obtain the sensing resolution of each sensor as shown in **Table 3.2**. The results show that our sensors are able to detect a normal force of less than 0.06 μN and a shear force of less than 0.12 μN. Because the maximum force acting on a micropillar having an edge length of 30 μm is in order of several μN, the proposed sensors therefore are sensitive enough for measuring the target forces.

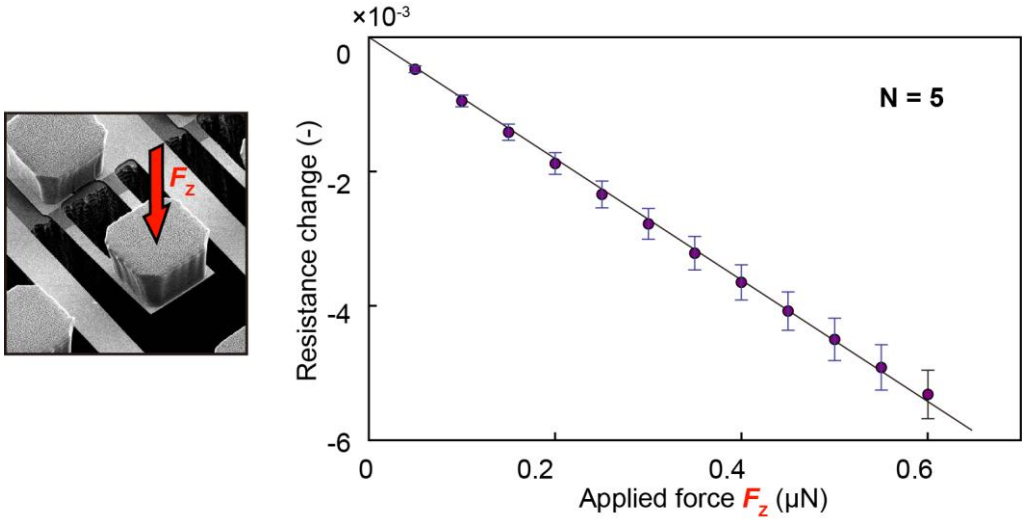

Fig. 3.23 Calibration result of one cantilever in the cantilever array used for measurement of the droplet vibration. Copyright 2015 IEEE.

Calibration result for the cantilever used in measurement of the droplet vibration

The calibration result of a cantilever used in measurement of the droplet vibration is shown in **Fig. 3.23**. A linear relationship between the resistance change of the cantilever and the applied normal force was obtained. Fitting the relationship yields

$$\frac{\Delta R_{\mathrm{Can}}}{R_{\mathrm{Can}}} = 9.05\times10^{-3} F_{\mathrm{Z}} \qquad (3.8)$$

where $\boldsymbol{R_{\mathrm{Can}}}$ is the resistance of the cantilever. The unit of $\boldsymbol{F_{\mathrm{Z}}}$ in the equation is (μN).

Because as mention previously, the measurement setup of in this study can detect a resistance change of $\pm8\times10^{-5}$ (-), the sensing resolution of the cantilever is obtained from the relationship shown in Eq. **(3.8)** to be 8.8 nN. The sensitivity of the cantilever approximately 3 times higher than the sensitivity regarding to the normal force of a two-axis force sensor because of the free edge of the cantilever.

3.6 Sensor resonant frequency

Measurement of the resonant frequency of the two-axis force sensor

The resonant frequency of fabricated two axis force sensors was measured using an experimental setup shown in **Fig. 3.24**. The sensor was vibrated in the vertical direction using a vibrator (Brüel & Kjær, Mini-shaker Type 4810). A network analyzer was used to apply the driven voltage to the vibrator through an amplifier. The vibration frequency was swept in the range of 10 Hz to 20 kHz or 30 kHz, depending on the resonant frequency of the sensor. A heterodyne interferometer was used to measure the velocity of

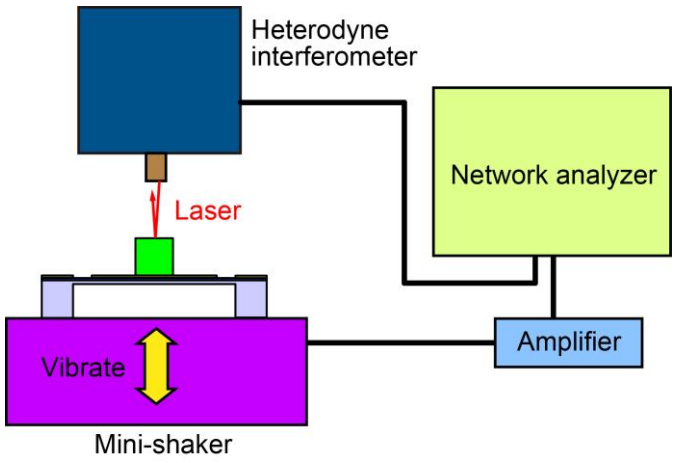

Fig. 3.24 Experimental setup to measure the resonant frequency of the fabricated sensor.

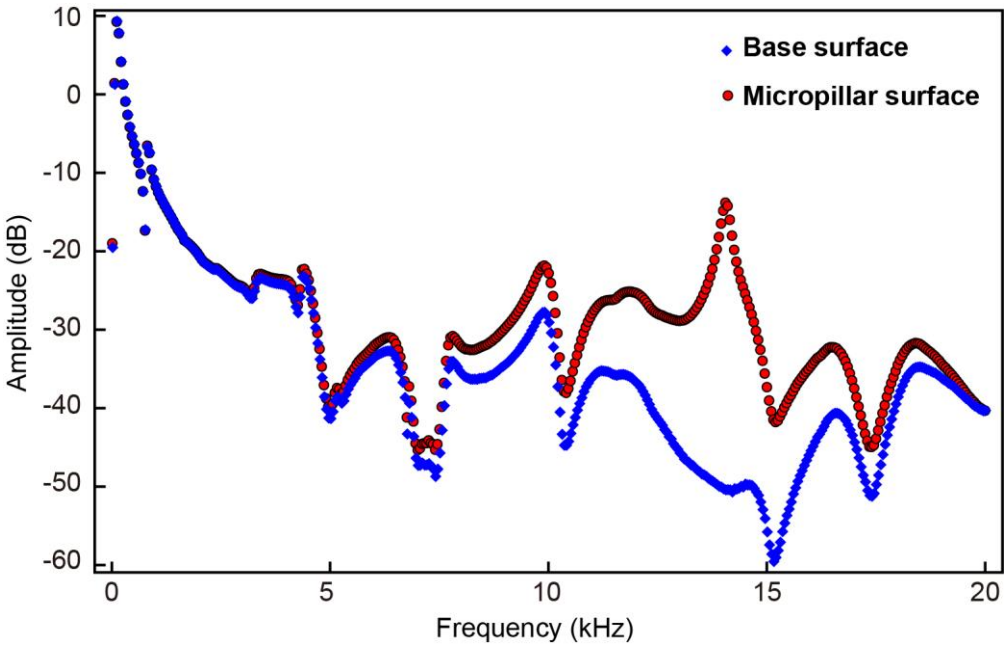

Fig. 3.25 Vibration amplitude of the micropillar and the base surface when the sensor was subjected to vibration from 1 to 20 kHz.

vibration of the micropillar and that of the sensor base as reference. The ratio between these two vibration velocities presents the effective vibration amplitude of the sensing element. The raw outputs of the heterodyne interferometer for the vibration of the micropillar surface and the sensor base surface are shown in **Fig. 3.25** . The obtained spectrum of the frequency responses of all sensors are shown in **Fig. 3.26**. The vertical axis in each graph shows the effective vibration amplitude mentioned above. The first resonant frequency of each sensor can be easily extracted from the peak of the vibration amplitude. **Fig. 3.27** shows

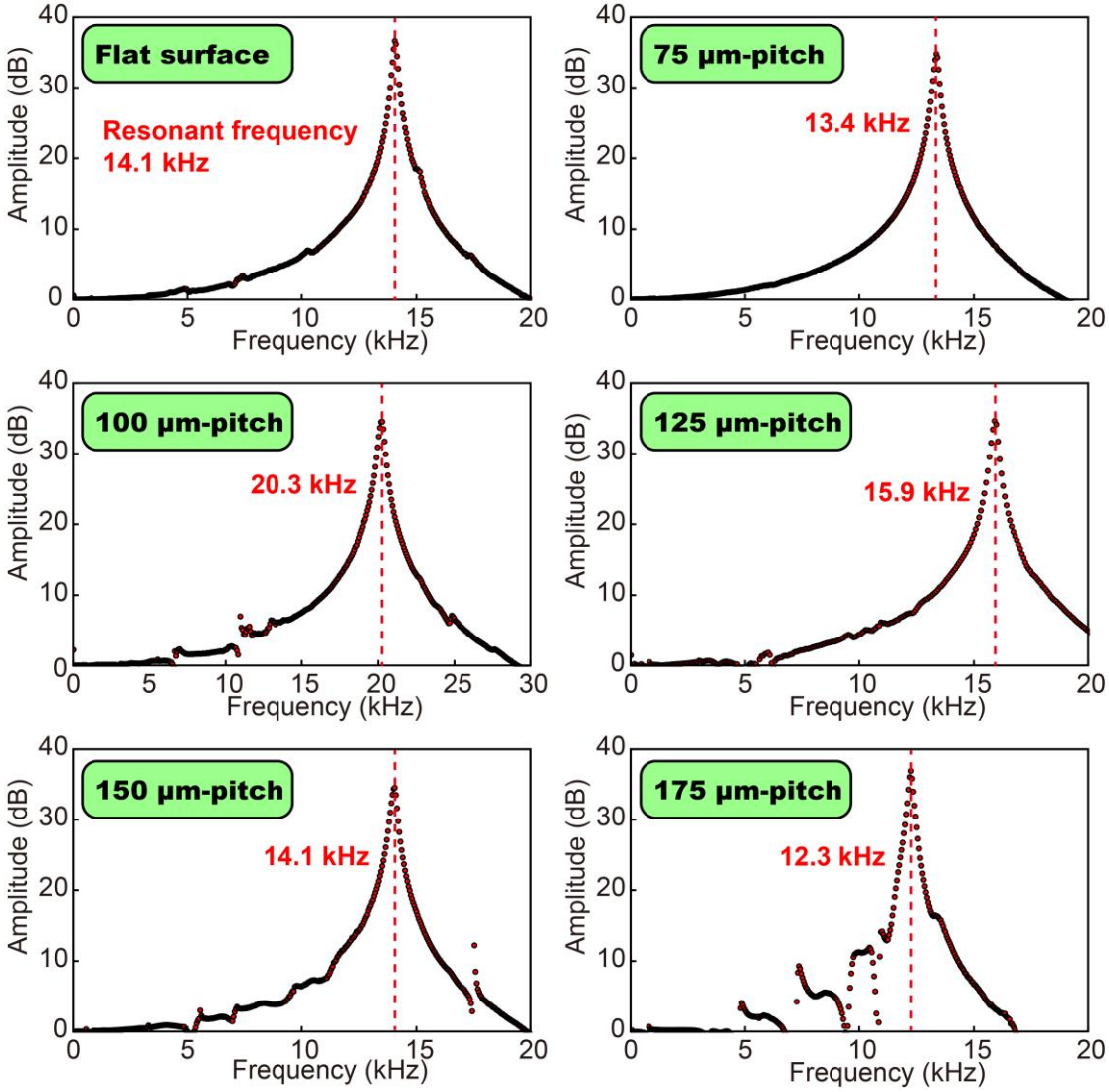

Fig. 3.26 Responses of the sensors when vibration in vertical direction was applied.

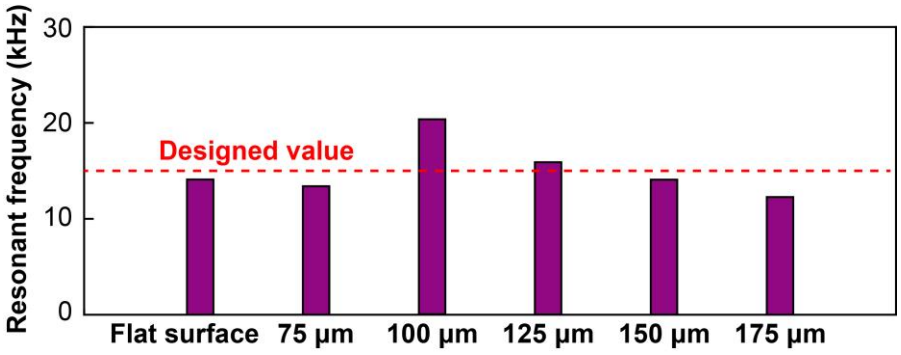

Fig. 3.27 First resonant frequency of the fabricated sensors. The designed value was the resonant frequency obtained by FEM simulation in **Section 3.1.3**.

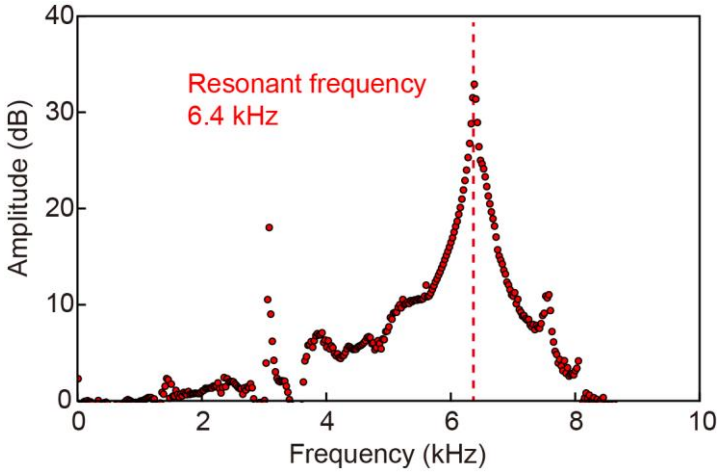

Fig. 3.28 Vibration amplitude of the micropillar and the base surface when the cantilever was subjected to vibration from 1 to 10 kHz.

the first resonant frequencies of the fabricated sensors in comparison with designed value. All the measured resonant frequencies are in the same order with the design value and are larger than 12 kHz. This result mentions that the fabricated sensors are able the measure a force that varies at the frequency up to more than 12 kHz.

Measurement of the resonant frequency of the cantilever

The resonant frequency of the cantilever used in measurement of the droplet vibration was also measured using the same experimental setup shown in **Fig. 3.24**. The result is shown in **Fig. 3.28**, from which the first resonant frequency of the cantilever was obtained to be 6.4 kHz, which is smaller than that of the two-axis sensors due to the smaller spring constant of the cantilever that is cantilever structure is generally more flexible than both fixed ends beam. Because in the droplet vibration experiment, the first resonant frequency of the vibration as shown later in Chapter 5 is less than several hundred Hz, the cantilever is able to detect the force during this vibration of the droplets.

3.7 Surface treatment evaluation

The effect of the surface treatment is evaluated by measuring the contact angle of a small droplet deposited on the surface. Here, effect of O_2 plasma cleaning and C_4F_8 coating are the subjects to investigate.

The result is shown in **Fig. 3.29** for the case of a micropillar that has 75 μm-pitch. For the untreated micropillar array, the contact angle was 102 degree. For a micropillar array that is only cleaned with O_2 plasma the contact angle was 90 degree because the surface was made hydrophilic by the O_2 plasma cleaning. In case of the micropillar array that is coated with C_4F_8, the contact angle is 140 degree, which indicates the hydrophobicity enhancement by the microstructure and coating. Finally, for the micropillar array that was first cleaned with O_2 plasma then coated with C_4F_8, the contact angle was 150 degree, which was highest among four samples. This

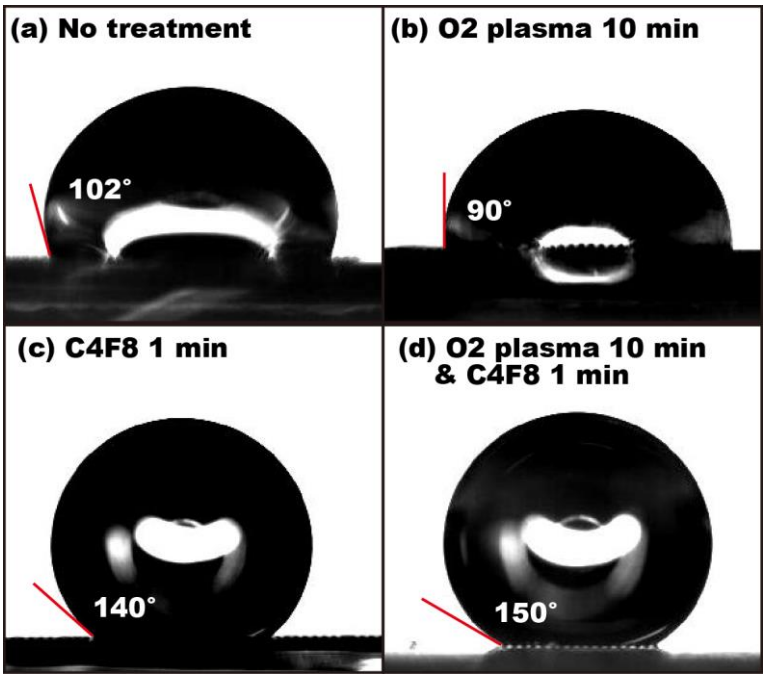

Fig. 3.29 Effect of the surface treatment on the static contact angle.

increase in the contact angle is thought to be a result of the nanostructures on the surface of each micropillar.

Chapter 4 Experiments on the droplet sliding

This chapter reports on measurement of the interaction forces during the sliding of liquid droplets with different volume and viscosity on the fabricated sensors. First, a brief description of the experiments in this study is introduced. Then, the preparation of liquid samples and their surface tension and viscosity measurement are reported. Next, the experiment setup and the image inquiry method are described. The following section provides the experiment results on the interaction forces measured by the sensors and the effects of droplet volume, liquid viscosity on the measured normal and shear forces are discussed.

4.1 Experimental preparation

4.1.1 Experiment description

Fig. 4.1 depicts the outline of the experiments to investigate the interaction forces during the sliding of droplets on the fabricated sensors. The droplets are first deposited on the micropillar array at the location nearby but not in contact with the sensing micropillar. Then the micropillar array was tilted slowly until the droplets slide through the sensor. The interaction forces between the droplet and the sensor in normal and lateral direction $\boldsymbol{F}_{\mathbf{Z}}$ and $\boldsymbol{F}_{\mathbf{X}}$ are measured by monitoring the resistances of the sensors.

In this study, as shown in GIF the effect of micropillar density and liquid viscosity as well as droplet volume on the interaction forces $\boldsymbol{F}_{\mathbf{Z}}$ and $\boldsymbol{F}_{\mathbf{X}}$ are investigated. For the viscosity, five types of liquid samples with different viscosity in the range of 1 to 1000 mPa·s are prepared as described in the next section. To investigate the effect of droplet volume, for each type of liquid sample, droplets having volume in the range of 2 μL to 50μL were tested. Moreover, these experiments are carried out for all fabricated sensors that have micropillar arrays with different pitches to investigate the effect of the micropillar density.

4.1.2 Preparation of liquid samples

In this study, liquid samples that have different viscosity were used to investigate the effect of viscosity on the interaction forces during the sliding of droplets. To create liquid samples that have similar surface tension but largely different viscosity, water-glycerol mixtures are often chosen. The surface tension of water and glycerol are 72 and 63 mN/m, respectively, whereas their viscosity are approximately 1000 times

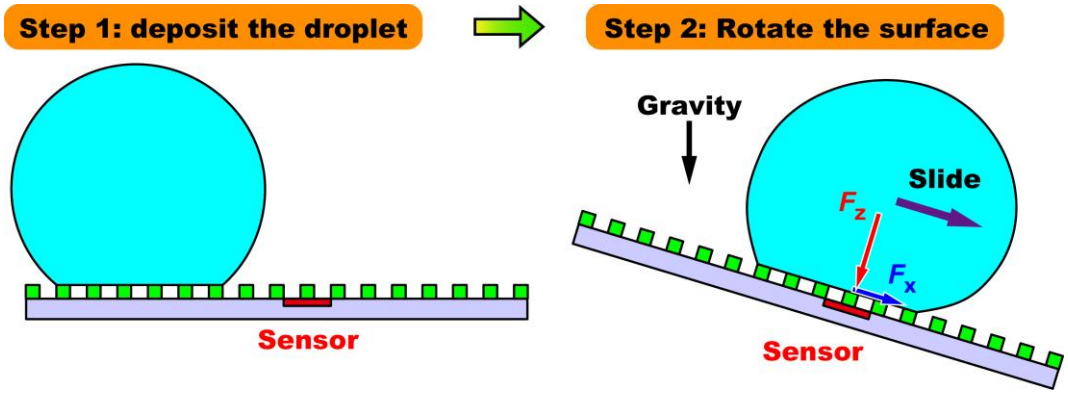

Fig. 4.1 Overview of the experiments in this study.

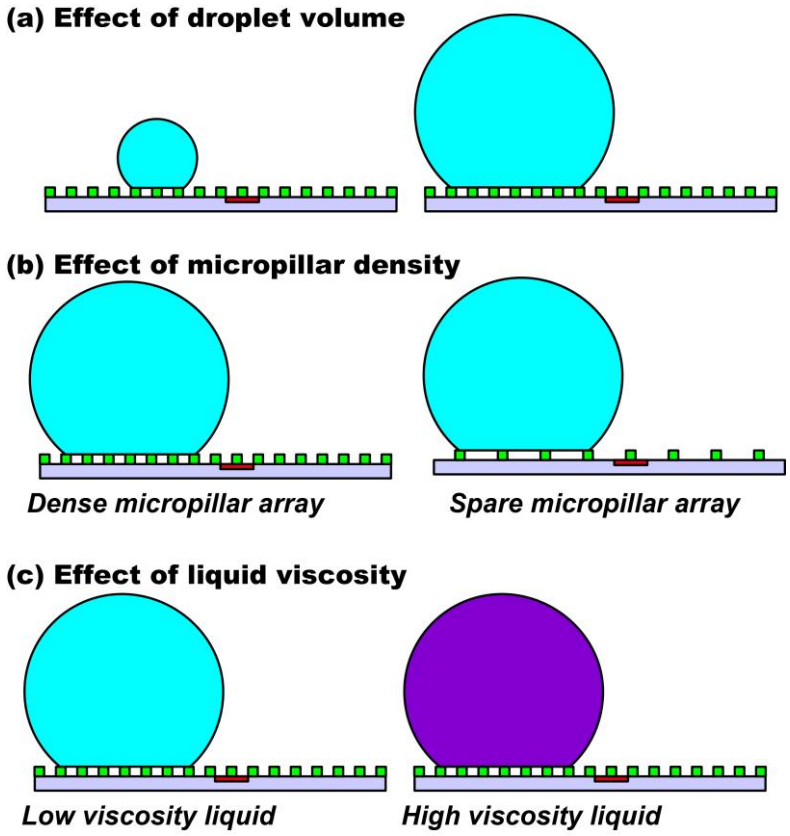

Fig. 4.2 Parameters to study in this study.

different. In this study, following liquid sample are prepared for the experiments. Hereafter, "G1W1", "G3W1" and "G9W1" are used to name the prepared liquid sample that has glycerol/water mixture ratio of 1:1, 3:1 and 9:1, respectively.

Surface tension measurement

The surface tension of liquid samples was measured using Wilhelmy plate method with an experimental

Table 4.1 Liquid samples prepared for the experiments.

Liquid name	Glycerol : water ratio	Density (kg/m^3)
Water	0:1	1000
G1W1	1:1	1126
G3W1	3:1	1195
G9W1	9:1	1235
Glycerol	1:0	1260

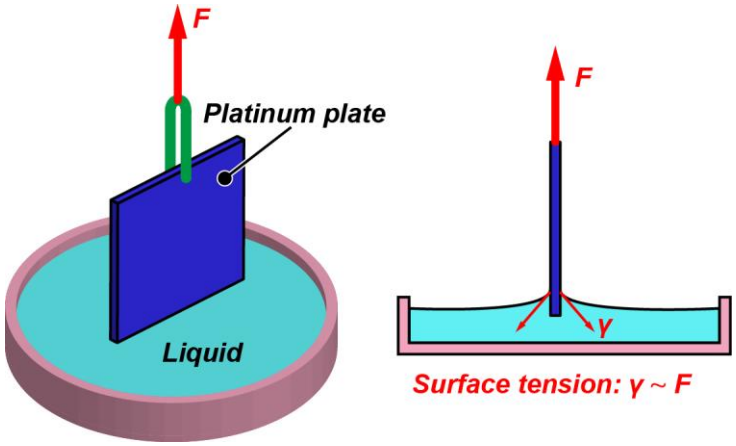

Fig. 4.3 Experimental setup to measure the surface tension of liquid samples.

Table 4.2 Measured surface tension of the liquid samples.

Liquid	Water	G1W1	G3W1	G9W1	Glycerol
Surface tension (mN/m)	72	68	66	64	63

setup shown in **Fig. 4.3**. The liquid sample inside a petri dish was brought in contact with a platinum plate by moving the petri dish in vertical direction. When the liquid wets the plate, surface tension will pull the plate down. This force ***F*** caused by the surface tension was measured using an electrical balance. First, the pulling force $\boldsymbol{F_0}$ for DI water was measured. Next, for every liquid sample, similarly, the pulling force ***F*** is measured.

The surface tension of liquid samples is calculated by from the ratio $\boldsymbol{F/F_0}$ as followed:

$$\gamma = \frac{F}{F_0}\gamma_{\text{Water}} \tag{4.1}$$

here, the surface tension of DI water is assumed to be 72 mN/m.

Table 4.3 Measured viscosity of the liquid samples at 23°C.

Liquid	Water	G1W1	G3W1	G9W1	Glycerol
Viscosity (mPa·s)	0.97±0.005	6.78±0.005	42.7±0.25	176±0.5	1020±2.5

The measured surface tension of all liquid samples are shown in **Table 4.2**. Among the prepared liquid samples, the surface tension of water is largest and surface tension of a glycerol/water mixture decreases as the percentage of glycerol increases. Nevertheless, the surface tension of prepared liquid samples does not vary much and are high in comparison with other liquid such as ethanol or common silicon oils. The liquid sample that have high surface tension are favorable in the experiments because droplet of low surface tension liquid cannot sit on the micropillar array and hardly can be moved by gravity.

Viscosity measurement

The viscosity of liquid samples was measured using an electromagnetically spinning viscometer (Kyoto Electronics Manufacturing Co., EMS-1000) at 23℃ which is the same with temperature during the experiments. Each measurement was repeated for 4 times. The results are shown in **Table 4.3**.

4.1.3 Experimental setup

A conceptual sketch of the experimental setup is shown in **Fig. 4.4**. The fabricated sensor was attached to a 3D-printed connector which is affixed to a rotational stage (Sigma Koki Co., Japan, SGSP-40YAW). The connector was designed so that the position of the sensor was the same with the rotational center of the stage. The rotational stage was also attached to a *xyz*-stage to control the position of the sensor in three dimension. During the experiment, droplets were first deposited on micropillar array placed along horizontal. After that, the micropillar array was tilted by the rotational stage at a constant speed (1.25 degree/sec) until the droplets slide through the sensor. The resistances of the sensors were connected to a Wheatstone brigde circuit which converts the resistance change into voltage change. This voltage is then amplified and measured by a scope-coder as described in **Section 3.5.3**. The sampling rate of the measurement was 200 kHz. Moreover, the sliding motion of the droplet was captured using a high speed camera (PHOTRON Inc., Japan, SA-XTKY03) at the record rate of 2000 frames per second. The outputs of the sensor and the motion of the droplet were synchronized by a trigger switch that terminates both the recordings of the scope-coder and the high-speed camera at the same moment. Photographs of the experimental setup are shown in **Fig. 4.5**.

4.1.4 Image processing

For the recording of the droplet motion, a line sensor telecentric lens (VS Technology, Japan, VS-LTC2-70/FSN) was used with the high speed camera. The pixel resolution of captured images is 1024×1024. Each pixel corresponds to a length of approximately 10 μm and the width of the image is 10.2 mm. A typical snapshot captured by the high speed camera is shown in **Fig. 4.6**. The pitch of micropillar array in the snapshot was 175 μm. From the captured image, the geometrical information such as volume,

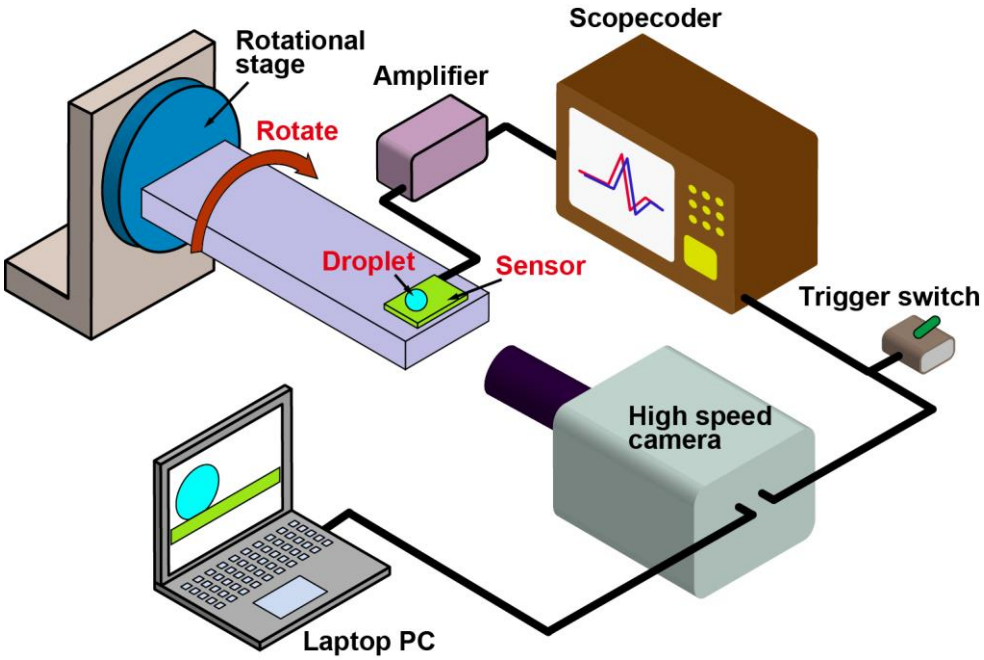

Fig. 4.4 Conceptual illustration of the experimental setup to measure the interaction forces during sliding of droplets on the fabricated sensors.

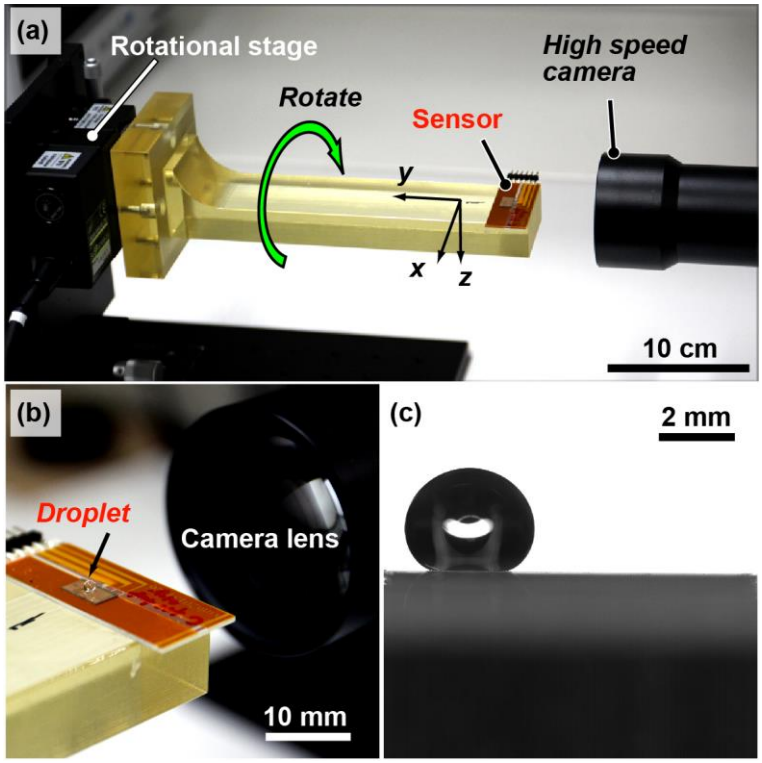

Fig. 4.5 Photographs of the experimental setup and a snapshot taken by the high speed camera. Reproduced from [93], Copyright 2014 Elsevier.

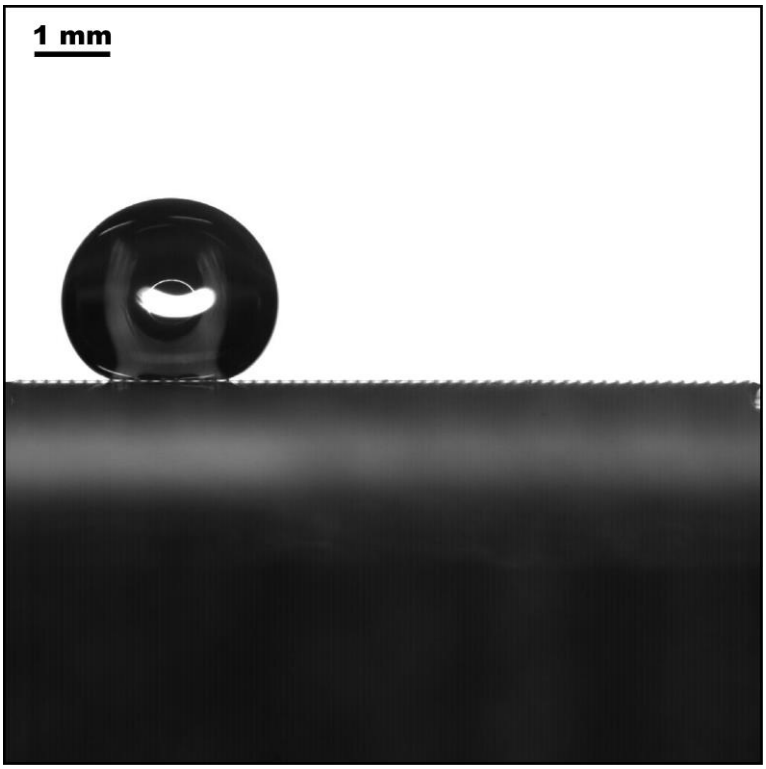

Fig. 4.6 A typical snapshot taken by the high speed camera.

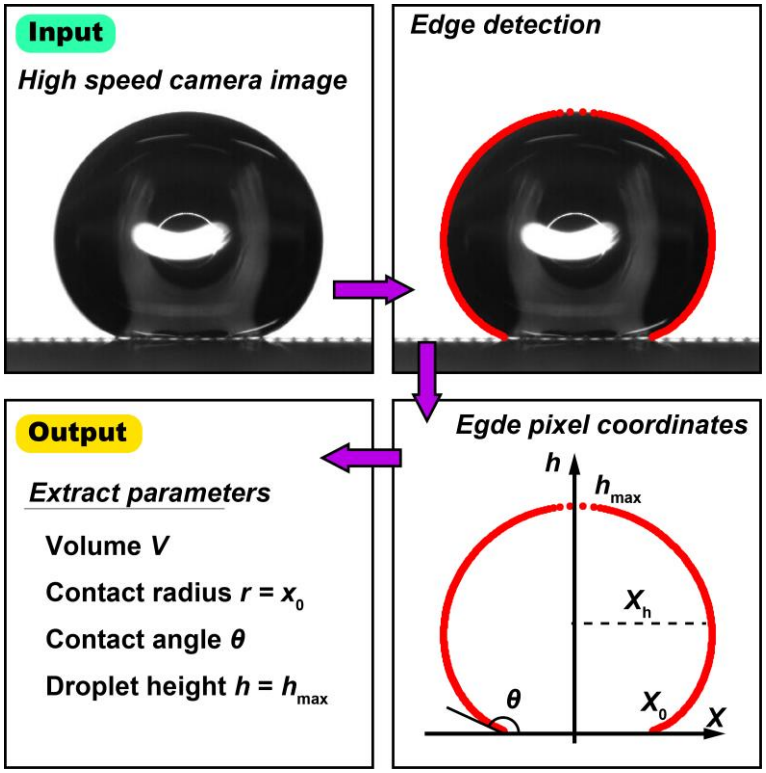

Fig. 4.7 Image processing to extract the profile and geometrical information of the droplet sitting on the horizontal substrate.

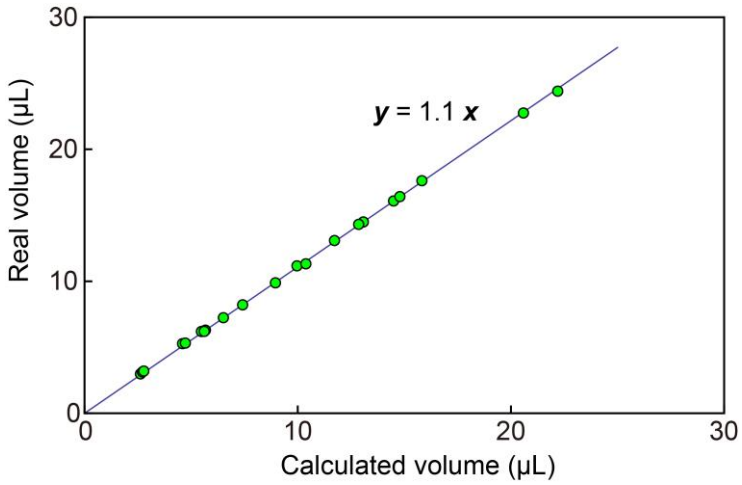

Fig. 4.8 Evaluation of the image processing. The calculated volume obtained from the image processing is compared with the real volume obtained by measuring the weight of the droplet.

contact diameter, contact angle of droplet can be extracted using a process shown in **Fig. 4.7**. The image processing was carried out using software Mathematica (WolframAlpha Research). The height and contact radius of the droplet can be immediately extract as x_0 and h_{max} as shown in **Fig. 4.7**. The calculation of the droplet volume and contact angle are described as followed.

Volume calculation

First the profile $h(x)$ of the droplet was extracted using EdgeDetect function of Mathematica. From the profile of the droplet, the volume can be calculated by assuming that the droplet is rotational symmetric using the following equation.

$$V = \sum_0^{h_0} \pi x_h^2 \tag{4.2}$$

Here x_h is the radius of the profile at the height h. Because the calculation is carried out on pixel coordinates, the volume is sum of the area, not the integration of the area. Of course, the unit of the calculated volume is pixel × pixel × pixel, and from the real length of a pixel, it is possible to convert the unit of the volume into μL.

The accuracy of this calculation was also evaluated by comparing the calculated volume with the weight of the droplet. In this evaluation experiment, the weight of the droplets was measured by the load cell mentioned in **Section 3.5.3**. A sensor was first placed on the load cell, then water droplets with different volume were deposited on the sensor. The weights of the droplets were calculated from the output of the load cell, while the droplets themselves were captured by the high speed camera. Volume of each droplet is obtained from its weights by assuming the density of water is 1000 kg/m^3.

The relationship between calculated volume and the real volume of the droplets are shown in **Fig. 4.8**. The calculated volume is shown to be proportional to the real volume which indicates the validation of the calculation. The error is due to the assumption that the droplet rotational symmetric which does not hold

true in the case of a droplet sitting on micropillar array. This also explains the result that the real volume is slightly larger than the calculated volume.

4.2 Measurement results for the droplet sliding

4.2.1 Normal and shear forces during the sliding of the droplets

In this section, the measured normal and shear forces during the sliding of a water droplet on the sensor with flat surface and that with a 175 μm-pitch pillar array are reported. The volume of the droplets in both experiments was 16 μL.

Droplet sliding on the sensor with flat surface

The result of the droplet sliding on the sensor with a flat surface is shown in **Fig. 4.9**. As shown in **Fig. 4.9 (a)**, the initial contact angle of the droplet was 138 degree which is relative large in comparison with a normal smooth surface. This high contact angle was obtained by the roughness of the KMPR 1035 photoresist after the etching with O_2 plasma as mentioned in **Section 0**. However, as shown in **Fig. 4.9** (b), the droplet did not easily slide on the sensor surface. In fact, the tilted angle $\boldsymbol{\alpha}$ of the surface for the droplet to start sliding was 68 degree. The apparent advancing and receding contact angles $\boldsymbol{\theta_A}$ and $\boldsymbol{\theta_R}$ of the droplet when sliding were 154.3 and 75.3 degree, respectively. The contact angle hysteresis $\boldsymbol{\theta_A - \theta_R}$ was 79 degree.

The graph in **Fig. 4.9** shows the normal and shear forces obtained from the output of the sensor during the sliding of the droplet. Here, the normal force and shear force $\boldsymbol{F_Z}$ and $\boldsymbol{F_X}$ are defined as the forces from the droplet acting on the pillar in the directions that are perpendicular and parallel to the surface of the pillar, respectively. The positive direction of the forces were also defined to be the same with those of the ***z***-axis and ***x***-axis shown in **Fig. 4.9 (b).** From the interaction force, the contact mechanism of the droplet can be described as shown in **Fig. 4.10**. When the advancing edge of the droplet began to contact with the micropillar of the sensor, both the normal and shear forces became negative, indicating that the micropillar was slightly pulled upward and backward. The maximum absolute value of the pulling force in the normal direction and shear direction were 0.68 and 0.67 μN, respectively.

As the droplet moved forward, the micropillar entered the contact area and the normal force increased to be positive while the shear force returned to zero. This result means that inside the contact area, the pillar was merely pushed downward by the liquid pressure and no significant shear force acting on the micropillar was detectable. Because in our experiment, the sliding of the droplet was in the beginning stage (the first several millimeters). During this stage, the sliding velocity of the droplet was small (typically less than 0.1 m/s) and hence, the effect of the viscosity can be neglected which agrees with the measured shear force inside the contact area. Meanwhile, the normal force inside the contact area was always positive and decreased as the droplet moving forward. This behavior of the normal force is thought to be caused by the difference in the liquid pressure along the droplet. As mentioned previously, the advancing and receding contact angles of the droplet were significantly different (154.3 and 75.3 degree). At the receding edge, the

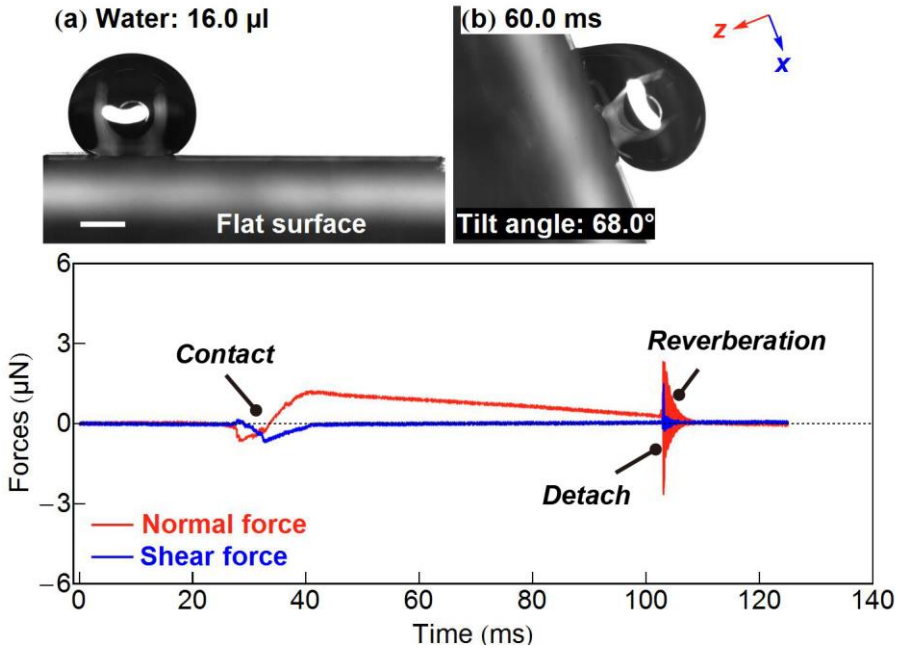

Fig. 4.9 Interaction forces between a droplet and the sensor with a flat surface.
(a) Initial shape of the droplet. Scale bar is 1 mm. (b) Snapshot of the high speed camera during the sliding.

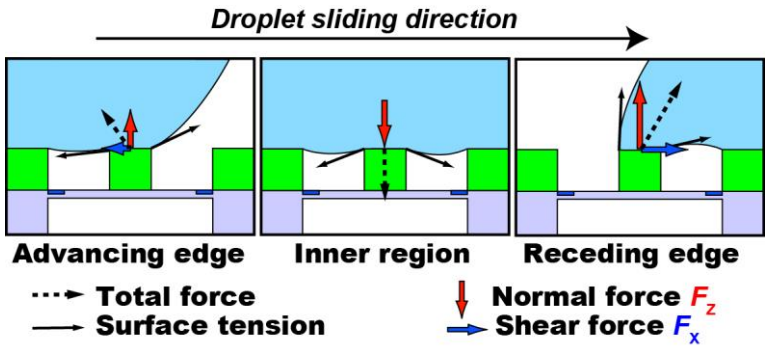

Fig. 4.10 Contact mechanism of the droplet with the micropillar.

contact angle was small, meaning that the mean curvature radius of the liquid surface was large in comparison with that at the advancing edge. Because the Laplace pressure is inversely proportional to the mean curvature radius, the Laplace pressure at the receding edge became smaller than that at the advancing edge. This pressure difference at advancing and receding edges reflects in the gradient of the normal force as shown in the graph. It is worth noticing that the difference in the pressure at the advancing and receding edge is caused by gravity. It is the portion of the droplet weight parallel to the sensor surface that causes the deformation of the droplet and the difference in the contact angles at advancing and receding edges when the sensor surface was tilted. In the case of the a droplet on a flat surface, the tilt angle α required for the

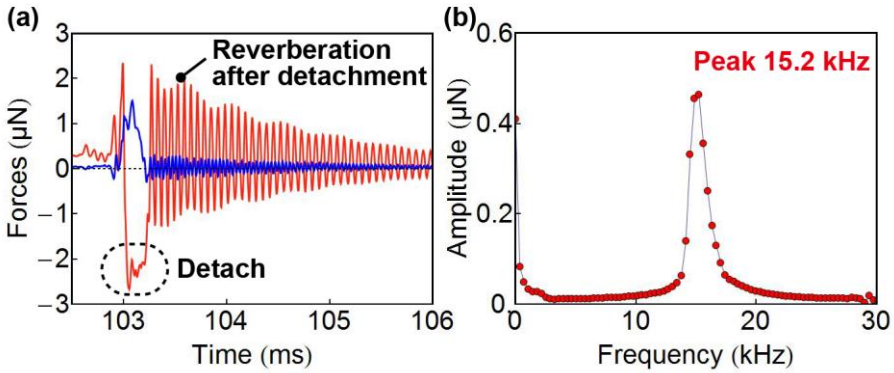

Fig. 4.11 (a) A close view of the interaction forces at the receding edge of the droplet.
(b) Fourier spectra of normal force during the sensor reverberation after the detachment from the droplet trailing edge.

droplet to move was large (68 degree) due to the low receding contact angle resulting in a significant gradient of the pressure along the contact area. A close view of the interaction between the droplet and the micropillar at the receding edge are shown in **Fig. 4.11** (a). It can be confirmed that the micropillar was again pulled upward when contacting with the receding edge of the droplet. However, the shear force indicates that the pillar is pulled forward, which is opposite to the direction of the shear force when the pillar contacted with advancing edge of the droplet. Moreover, the maximum absolute values of both normal and shear forces are also larger than those at the advancing edge, which is, again, a result of the difference between advancing and receding contact angle as shown in **Fig. 4.10**. At the receding edge, the maximum values of the pulling force in normal and shear direction were 2.67 and 1.51 μN, respectively. Because the contact angle was large at the advancing edge, the normal force and the shear force pulling the micropillar backward were small. On the other hand, since the receding contact angle was small, the normal force and the shear force pulling the micropillar forward at the receding edge of the droplet became large, in comparison with those at the advancing edge. The behaviors of the normal and shear forces also indicate that the friction of during the sliding of the droplet was mainly caused by the adhesion of the droplet to the sensor surface at the receding edge.

As also shown in **Fig. 4.11** (a), after detachment of the droplet, the micropillar rebounded back causing the reverberation of the sensor signal. The frequency of the reverberation was obtained from the Fourier transformation spectrum of the normal force to be 15.2 kHz (**Fig. 4.11** (c)), which is close to the first resonant frequency of the sensor (14.1 kHz) shown in **Fig. 3.26**.

Next, the frictional force $\boldsymbol{F}_S$ of the droplet is analyzed from the images of the high speed camera. **Fig. 4.12** shows the snapshots of the droplet sliding motion and the sliding distance extracted from the image sequence. By tracking one point on the edge of the droplet profile using software Tema (Image Systems Motion Analysis, Sweden), the sliding of the droplet can be obtained. Here, the sliding distance was defined as the distance of the droplet from its location at the moment $\boldsymbol{t}$ = 0 ms. The result show that in the

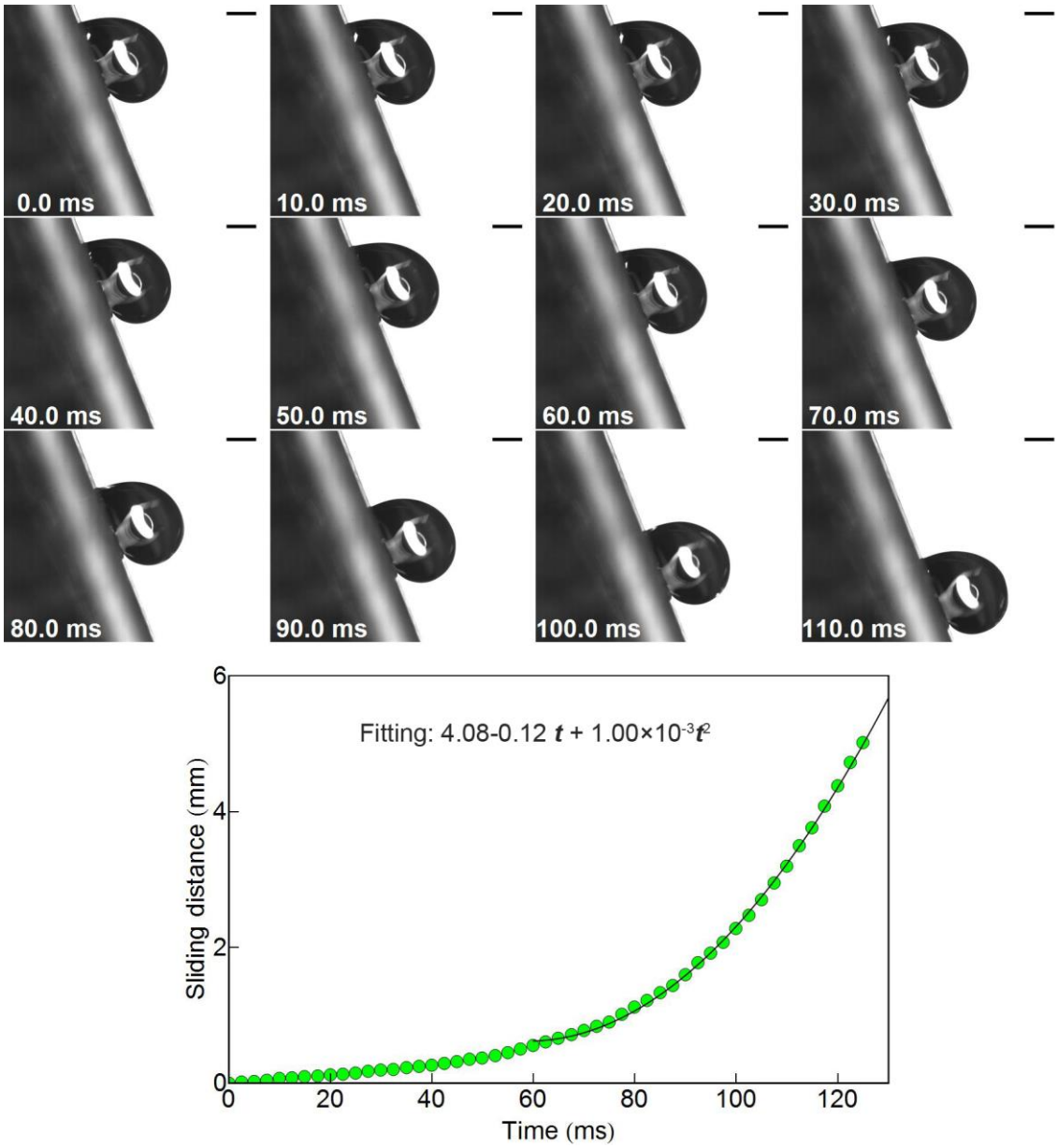

Fig. 4.12 Snapshots of the high speed camera showing the sliding motion of the droplet on the sensor with a flat surface and the sliding distance obtained by tracking the droplet. Scale bar in each snapshot is 1 mm.

beginning (t < 60 ms), the sliding velocity of the droplet was relatively small and then suddenly increased. For t > 60 ms the sliding droplet can be fitted by a function of t and t^2 which mean that the acceleration of the droplet was almost constant for this duration. From the fitting fuction the accerlation of the droplet was calculated to be a = 2 m/s^2. The frictional force, thus, can be obtained using following equation:

$$F_S = m(g\sin\alpha - a) \tag{4.3}$$

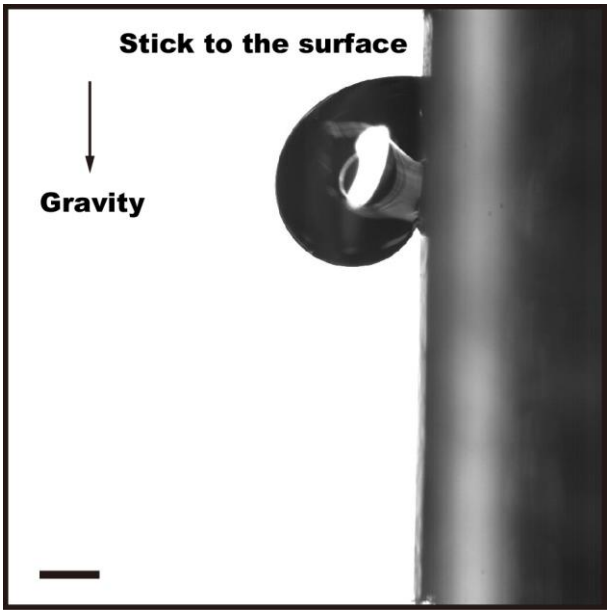

Fig. 4.13 A 14 μL water droplet did not slide on the sensor with a flat surface even when the surface was tilted at almost 90 degree from horizon. Scale bar is 1 mm.

Using m = 16 mg and α = 68 degree, we obtain F_S = 113.4 μN.

Because the flat surface of the sensor was sticky, a small droplet could not slide even when the sensor was tilted at 90 degree from horizon as shown in **Fig. 4.13**. Therefore, sliding experiment using small droplets (less than 15 μL) could not be carried out. Moreover, a large droplet, when tilting the surface, the advancing of the droplet moved and contacted with micropillar of sensor before the droplet started to slide because of the limited distance from the initial advancing edge of the droplet and the micropillar of the sensor. For those reasons, sliding experiments for droplets with various volume on the sensor having a flat surface could not be conducted.

Droplet sliding on the sensors with a micropillar array

The experimental results in the case of a water droplet sliding on a micropillar array that has 175 μm-pitch are shown in **Fig. 4.14**. The initial contact angle of the droplet was 153 degree, which was larger than that of a droplet on a flat surface shown in **Fig. 4.9 (a)**. Moreover, the sliding angle of the droplet was 7.8 degree, which was much smaller than that in the case of the flat surface. This low sliding angle indicates the hydrophobicity of the surface was dramatically enhanced by the micropillar array. The advancing and receding of the droplet was 141 and 170 degree, respectively. The contact angle hysteresis was thus 29 degree which, again, was much smaller than that in the case of a droplet sliding on the flat surface. This low contact angle hysteresis is the reason why the droplet could slide on the micropillar array at very low tilt angle as demonstrated for many pillar-typed superhydrophobic surfaces.

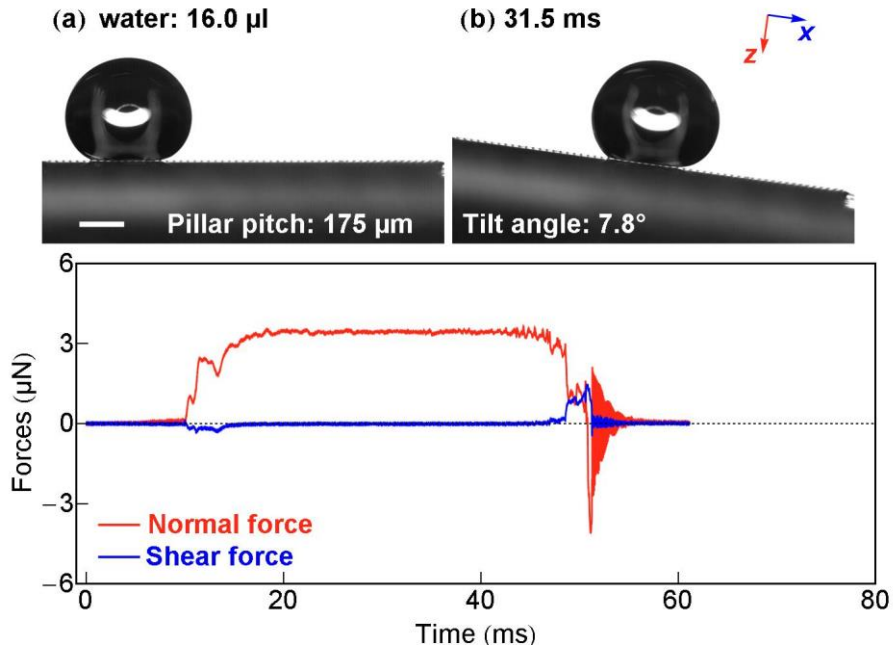

Fig. 4.14 Interaction forces between a 16 µL-water droplet and the sensor with a 175 µm- pitch micro pillar array. (a) Initial shape of the droplet. Scale bar is 1 mm. (b) Snapshot of the high speed camera during the sliding of the droplet.

The graph in **Fig. 4.14** shows the interaction forces during the sliding of the water droplet. During the sliding of the droplet, the interaction between the droplet and the micropillar exhibited some similar properties with those in the case of the droplet sliding on a flat surface. First, the when the droplet contacted with pillar at the advancing edge, the pillar was slightly pulled backward. The normal force at the advancing edge was almost zero due to the large advancing contact angle and the droplet simply laid down on the pillar. At the receding edge, similar to the case of a flat surface, the micropillar was pulled upward and forward by the droplet. The maximum absolute value of the pulling forces in normal and shear directions were 4.1 and 1.4 µN, respectively. The result shows that the pulling force in shear direction was the in the same order with that in the case of the sensor with a flat surface (1.51µN). However, the pulling force in normal direction were large than that in the case of a droplet sliding on the sensor with a flat surface despite of the fact that the receding contact angle was much larger in the case of droplet sliding on the micropillar array. The meaning of this result is that the actual interaction forces between the droplet and the surface cannot be simply calculated from the apparent (macroscopic) contact angle. Especially, for a surface with microstructures, the details of the microscopic contact angles around each microstructure are required in order to calculate the interaction forces between the liquid and the microstructure. This task is not easy for the low resolution observation, in fact, it is necessary to obtain the profile of the liquid portion that is close to the surface (in the order of the microstructure size, which is normally several ten µm or less). The measurement method in this study providing the direct interaction forces between the droplet and a

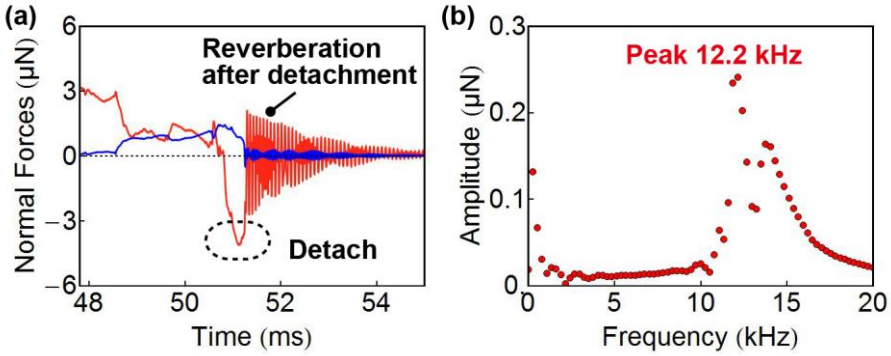

Fig. 4.15 (a) A close view of the interaction forces at the receding edge of the droplet. (b) Fourier transformation spectrum of the normal force during the sensor reverberation after the detachment from the droplet trailing edge.

single microstructure of the surface therefore is advantageous to investigate how a droplet locally adheres to a surface.

Another important property of the interaction between the droplet and the micropillar array can be seen from the result was that the normal force was almost the same over the inner region of the contact area. As mentioned previously in the case of a droplet sliding on the sensor with a flat surface, the large difference between the advancing and receding contact angles led to the gradient of the normal force along the diameter of the contact area. Conversely, in the case of a droplet sliding on the micropillar array, due to a small contact angle hysteresis, there was little difference between the mean curvature radii and hence the pressure at advancing and receding edges of the droplet. This results in a relatively constant value of the normal force along the contact area as shown in **Fig. 4.14**.

Furthermore, it is also important to notice that there was a fluctuation in the normal force acting on the micropillar when it was close to the receding edge. This fluctuation was not observed in the case of a droplet sliding on the flat surface as shown in **Fig. 4.9,** which indicates that the interaction between the droplet and the micropillar array might cause the vibration of the droplet during sliding**.** In section **0** , a discussion on the fluctuation of the normal force and its relation to the vibration of the droplet during sliding will be provided in details.

Fig. 4.15 shows a close view of the interaction forces between the droplet and the sensor at the receding edge. It was also observed that after detaching from the droplet, the sensor rebounded resulting in the reverberation of the normal and shear forces. From the Fourier transformation spectrum, the reverberation frequency was obtained to be 12.2 kHz which was approximately the same with the sensor first resonant frequency (12.3 kHz) shown in **Fig. 3.26**.

Next, the sliding distance and the frictional force during the sliding of the droplet is discussed. Snapshots of the high speed camera showing the sliding motion of the droplet are provided in **Fig. 4.16**. Moreover, by tracking the droplet, the sliding distance was obtained as shown in the graph. The result shows that the

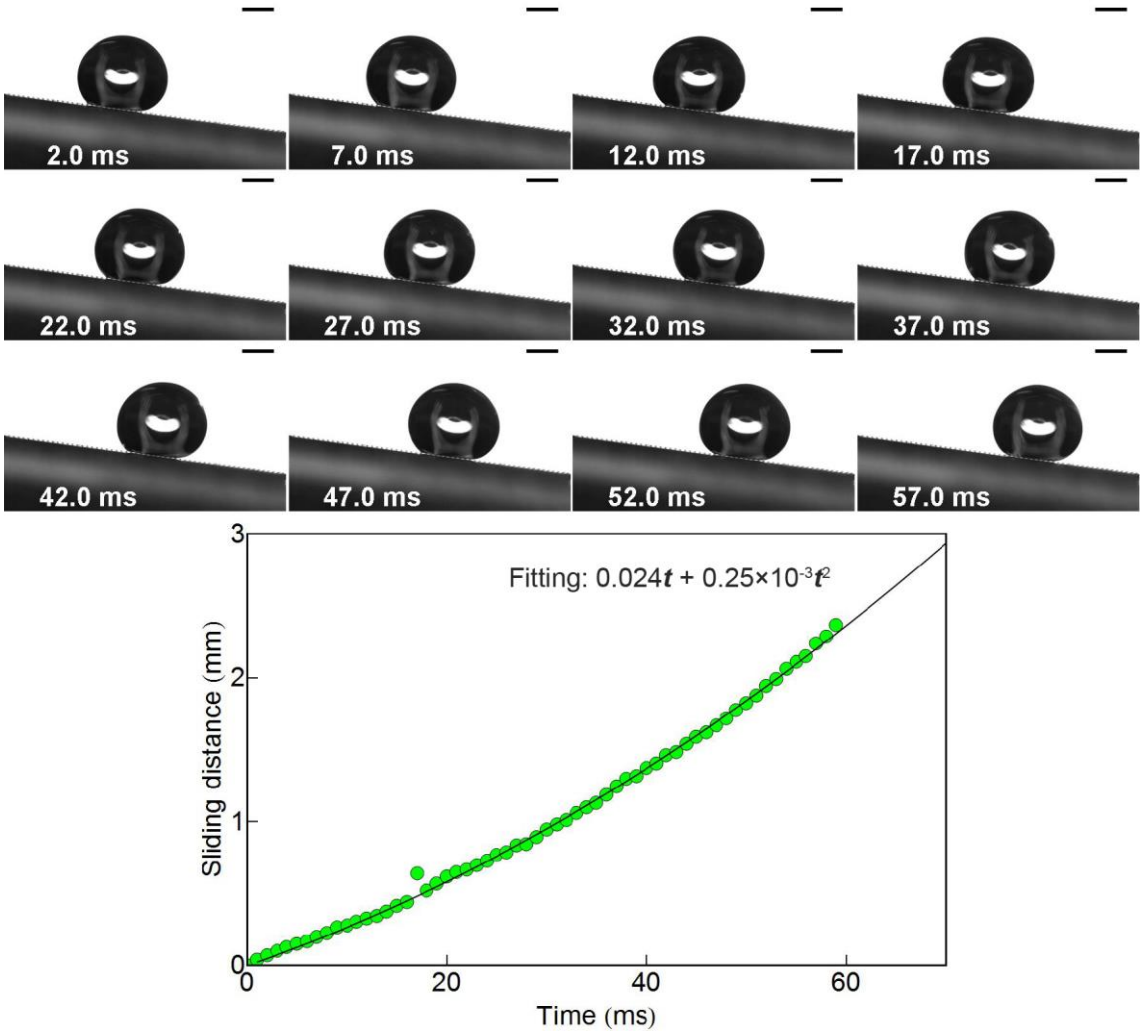

Fig. 4.16 Snapshots of the high speed camera showing the sliding motion of the droplet sliding on the 175 μm-pitch micropillar array. The graph shows the sliding distance of the droplet.

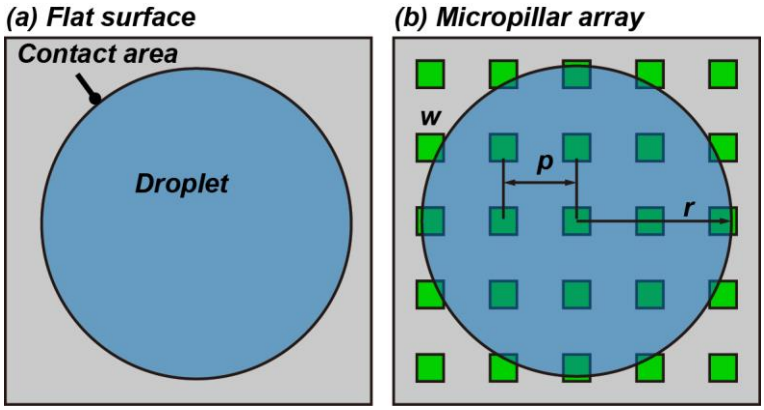

Fig. 4.17 Top view of the contact line between a droplet and a flat surface (a) and a micropillar array (b).

droplet was sliding at a constant acceleration $\boldsymbol{a}$ = 0.5 m/s^2. As shown previously, in the case of the droplet sliding on the flat surface, the sliding acceleration of the droplet was small in the beginning then rapidly increased as the velocity increased. Here, in the case of a droplet sliding on the micropillar array, the sliding distance can be well-fitted to a function of $\boldsymbol{t}$ and $\boldsymbol{t}^2$ from the beginning of the sliding, meaning that the acceleration was almost constant during the sliding. From the acceleration and the tilt angle of the surface $\boldsymbol{\alpha}$ = 7.8 °, the frictional force was calculated to be $\boldsymbol{F}_S$ = 21.3 μN using Equation **(4.3)**, which was one fifth of the frictional force during the sliding of the droplet on a flat surface. This result demonstrates that the frictional force was significantly reduced by the micropillar. The reducing mechanism can be simply explained by taking account of the actual length of the contact line at the receding of the droplet. For surface with a micropillar array, because of the droplet only contacted with the micropillars during the sliding, the actual length of the contact line can be approximated as followed:

$$L_{\text{Pillar}} \approx \frac{w}{p} L_{\text{Flat}} \tag{4.4}$$

where $L_{\text{FLAT}} \approx 2\pi r$ is the length of the contact line of a droplet on a flat surface with a contact radius *r*; *w* and *p* are the width and pitch of the micropillars (**Fig. 4.17**). As described previously, the maximum pulling force in shear direction at the receding edge of the droplets in two case were approximately the same, indicating that the force per unit length during the receding of a droplet is constant. Therefore, as the pitch of the micropillar array increases, the actual length of the contact line decreases and the total frictional force decreases. In the case of the micropillar with 30 μm-width and 175 μm-pitch, the actual length of the contact line is $L_{\text{Pillar}} \approx \frac{30}{175} L_{\text{Flat}}$. This ratio between the actual lengths of the contact line in the case of the micropillar with that in the case of a flat surface was approximately equal to the ratio between the total frictional forces of the droplets in these two cases.

Experimental results for all fabricated sensors and prepared liquid samples.

The measurement results for droplets of the same liquid sliding on sensors with micropillar arrays having different pitches (75, 100, 125, 150, 175 μm) **Fig. 4.18** to **Fig. 4.22**. In these figures, the liquid was water. Moreover, measurement results for droplets of different liquid samples (water, G1W1, G3W1, G9W1, glycerol) sliding on the same sensor are shown in **Fig. 4.23** to **Fig. 4.26**. For each pair of sensor and liquid sample, experiment results of a large droplet (more than 12 μL) and a relatively small droplet (3-5 μL) are provided. The experimental results for other pairs of sensor and liquid samples are shown in **Fig. A. 1** to **Fig. A. 11** in **Appendix 1**.

Overall, for all sensors and liquid sample, common behaviors of the interaction forces during the sliding of droplets are followings:

- When the micropillar contacts with the droplet at its advancing edge, the micropillar was pulled upward and backward to the droplet by the surface tension.

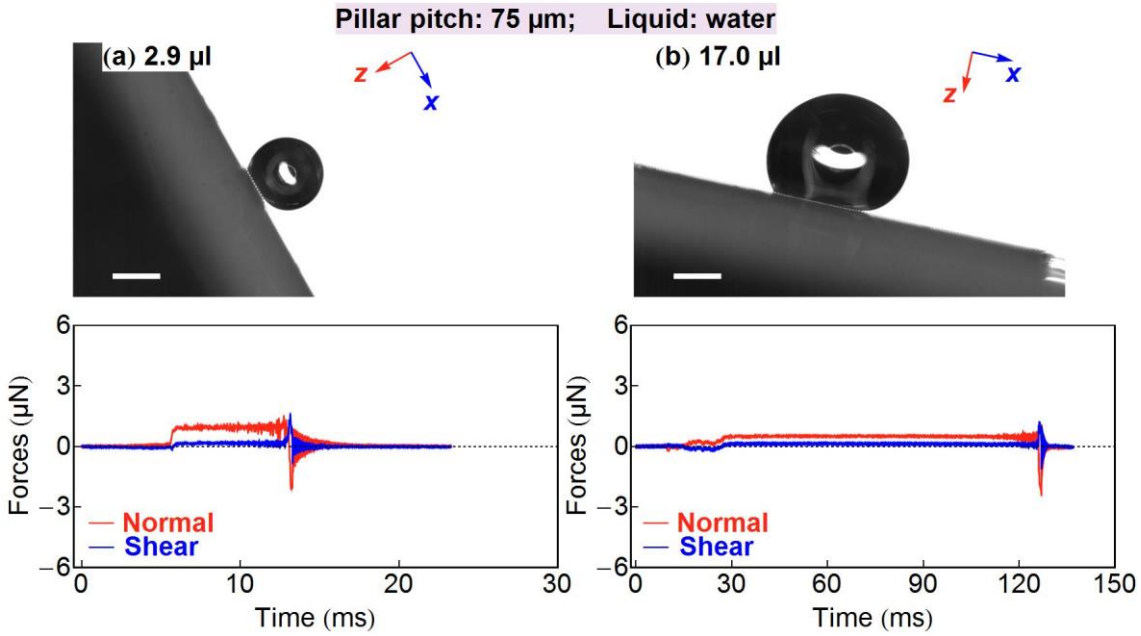

Fig. 4.18 Interaction forces during the sliding of a 2.9 μL-water droplet and 17 μL-water droplet on the sensor with a 75 μm- pitch micro pillar array. Scale bar is 1 mm.
The sliding angles are 61 degree and 12 degree, respectively.

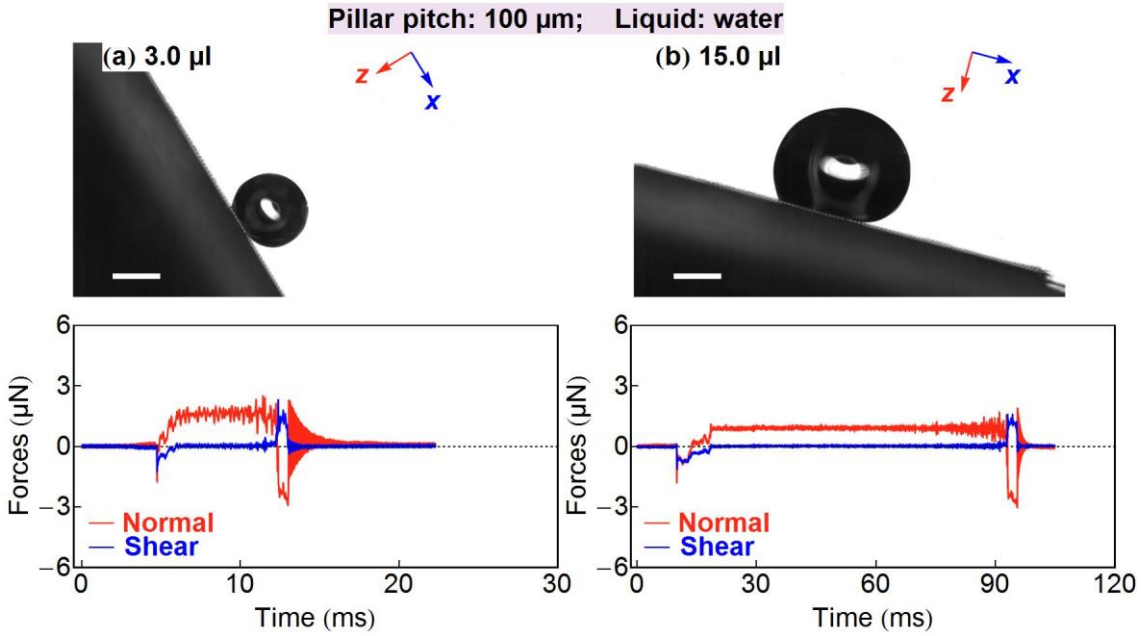

Fig. 4.19 Interaction forces during the sliding of a 3.0 μL water droplet and 15 μL water droplet on the sensor with a 100 μm-pitch micropillar array. Scale bar is 1 mm.
The sliding angles are 58 degree and 15 degree, respectively.

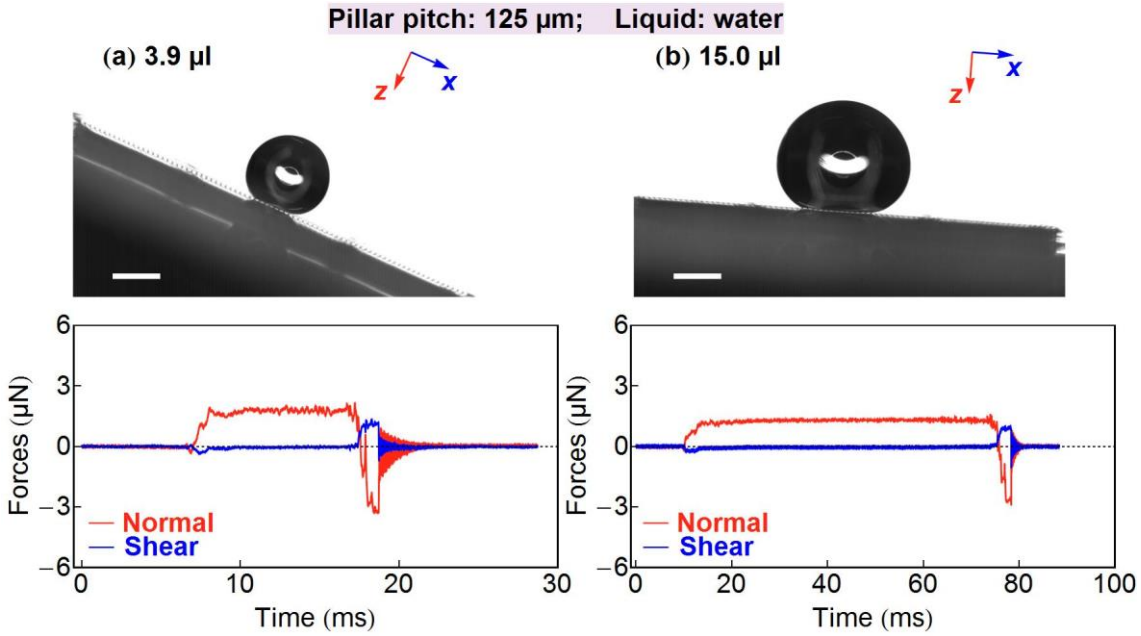

Fig. 4.20 Interaction forces during the sliding of a 3.9 μL water droplet and 15 μL water droplet on the sensor with a 125 μm-pitch micropillar array. Scale bar is 1 mm.
The sliding angles are 24 degree and 4.2 degree, respectively.

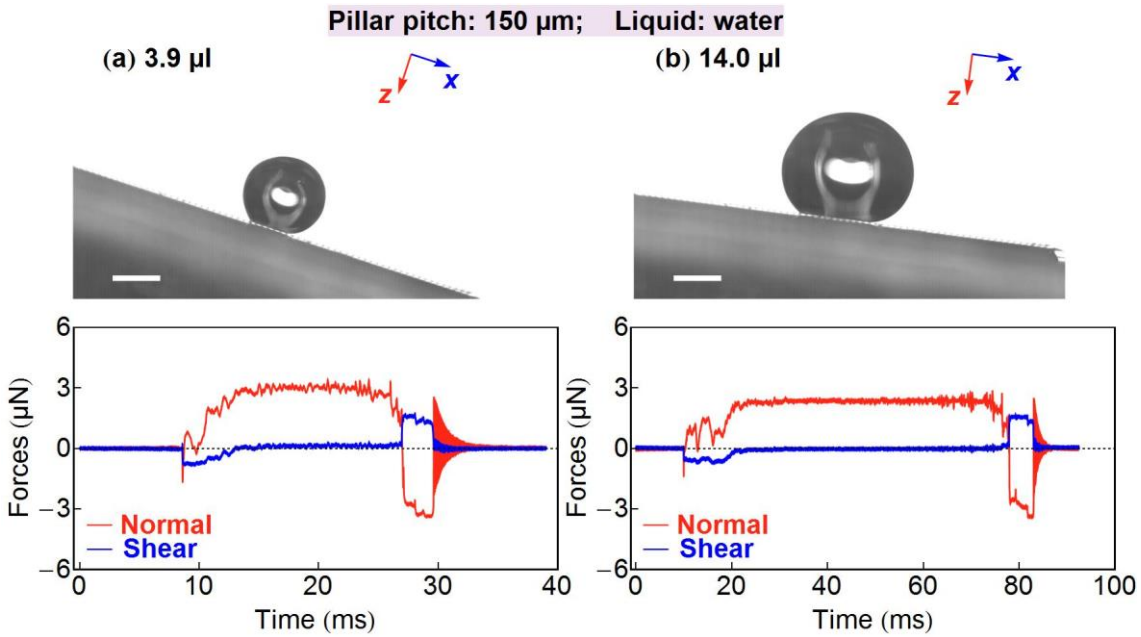

Fig. 4.21 Interaction forces during the sliding of a 3.9 μL water droplet and 14 μL water droplet on the sensor with a 150 μm-pitch micropillar array. Scale bar is 1mm.
The sliding angles are 18 degree and 7.4 degree, respectively.

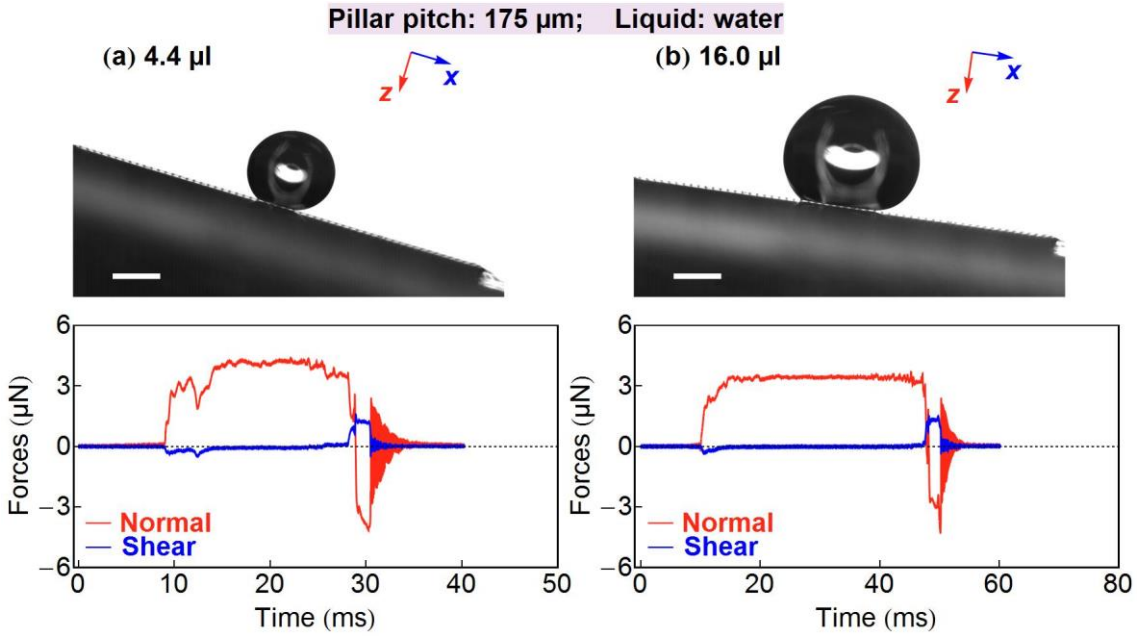

Fig. 4.22 Interaction forces during the sliding of a 4.4 μL water droplet and 16 μL water droplet on the sensor with a 175 μm-pitch micropillar array. Scale bar is 1 mm. The sliding angles are 17 and 8.1 degree, respectively.

- When the micropillar was in the inner region of the normal force became positive indicating that the micropillar was pushed downward by the liquid pressure. Meanwhile, the shear force became almost zero, meaning that the friction over the inner region of the droplets were small. Some liquid samples used in the experiments, for example glycerol, have relatively high viscosity. However, because the droplets in the experiments were in the beginning stage of the sliding when the sliding velocities of the droplets were small, the effect of viscosity on the friction over the inner region of the contact area was not obviously observed. The normal force over the inner contact area also stable meaning that the pressure were the same over the inner contact area.
- When the micropillar contact with the receding edge of the droplet, the micropillar was pulled upward again and forward to the droplet. The maximum pulling forces (absolute value) at the receding edge in normal and shear directions are both larger than those at the advancing edge due to the contact angle hysteresis. From these properties of normal and shear forces along the contact diameter, it is the adhesion of the droplet and the micropillar at the receding edge. In this small velocity state, the effect found that during the sliding of droplets at small velocity, the frictional force was most contributed by of surface tension dominates that of viscosity.
- The average value of the normal force over the inner region of the contact area increased as the volume of droplet decreased indicating the role of Laplace pressure on the normal force over the inner region of the contact area.

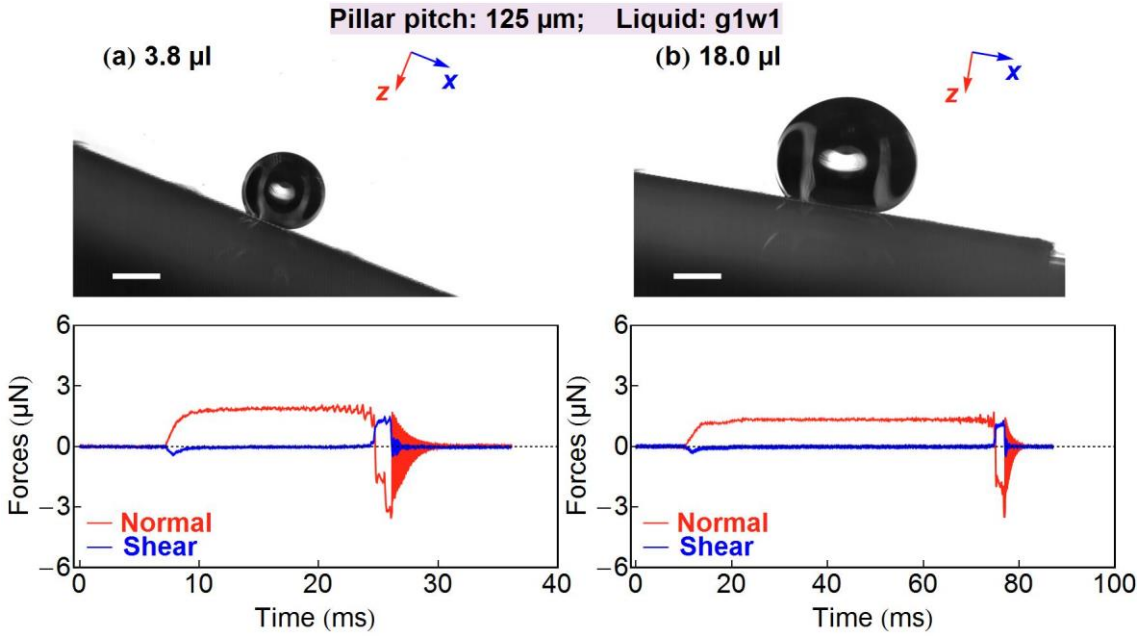

Fig. 4.23 Interaction forces during the sliding of a 3.8 μL G1W1 droplet and 18 μL G1W1 droplet on the sensor with a 125 μm pitch micro pillar array.

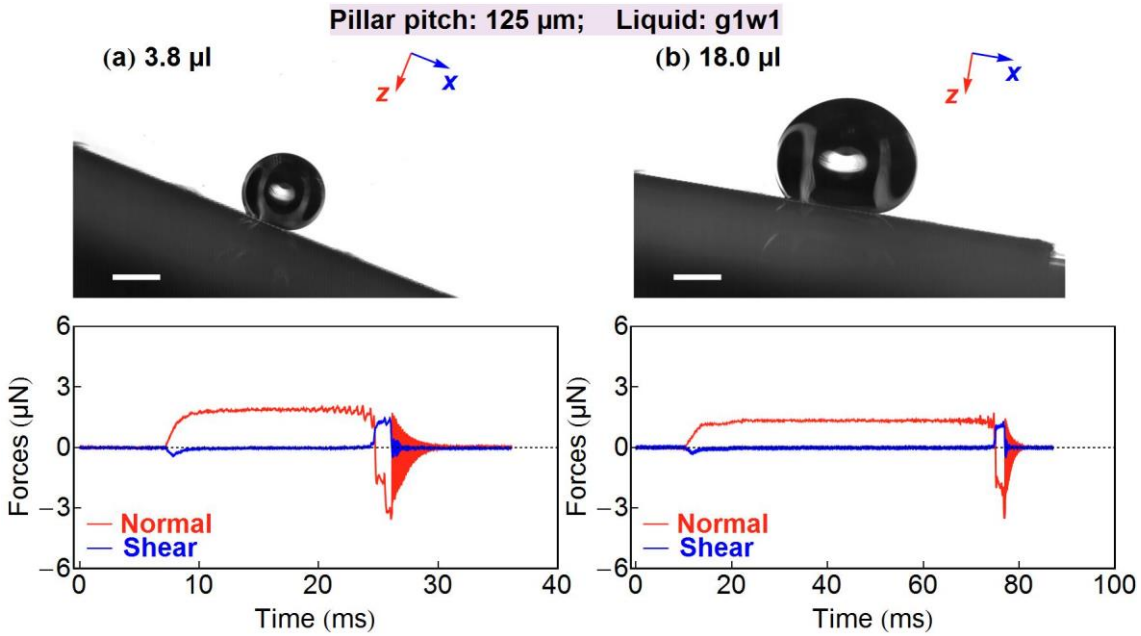

Fig. 4.24 Interaction forces during the sliding of a 3.3 μL G3W1 droplet and 18 μL G3W1 droplet on the sensor with a 125 μm pitch micro pillar array.

- After the detachment of the droplet from the micropillar, the micropillar rebounded causing the reverberation of the sensor output signal. The frequency of the reverberation of each sensor was

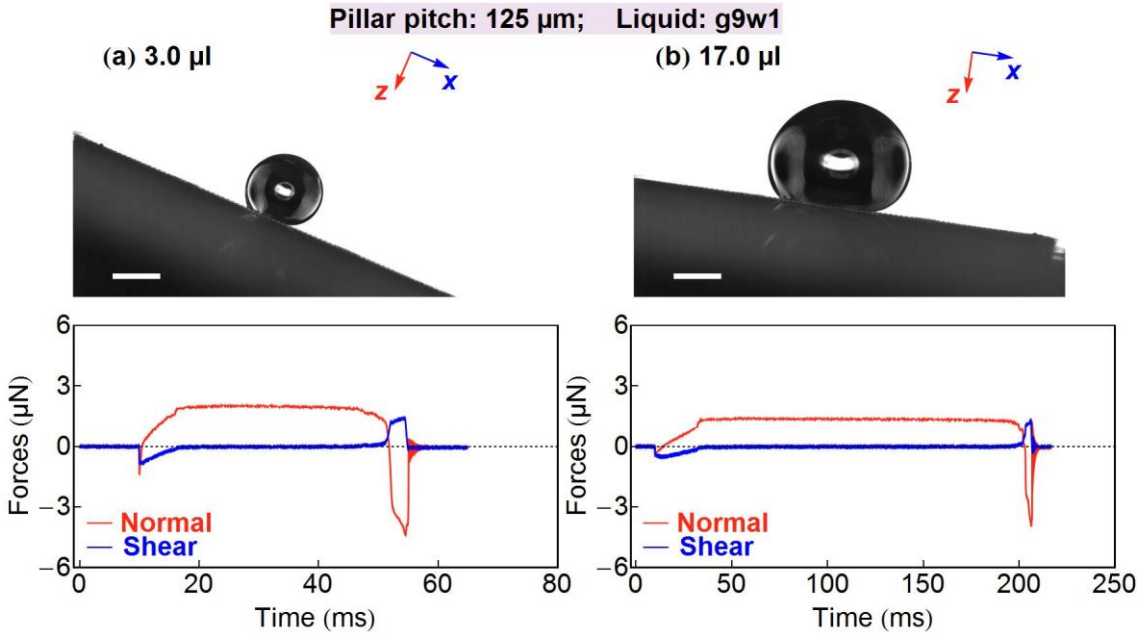

Fig. 4.25 Interaction forces during the sliding of a 3.0 μL G9W1 droplet and 17 μL G9W1 droplet on the sensor with a 125 μm pitch micro pillar array.

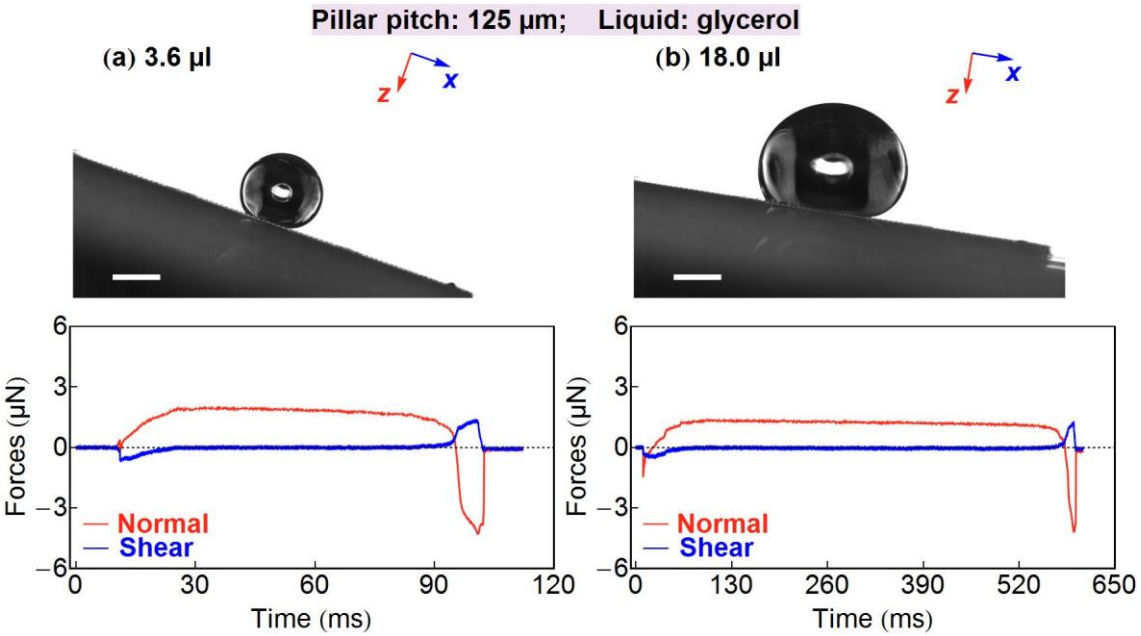

Fig. 4.26 Interaction forces during the sliding of a 3.6 μL glycerol droplet and 18 μL glycerol droplet on the sensor with a 125 μm pitch micro pillar array.

confirmed to be approximately the same with the first resonant frequency of the sensor.

- On the same micropillar, a larger tilt angle was required to let a smaller droplet to slide. Because the

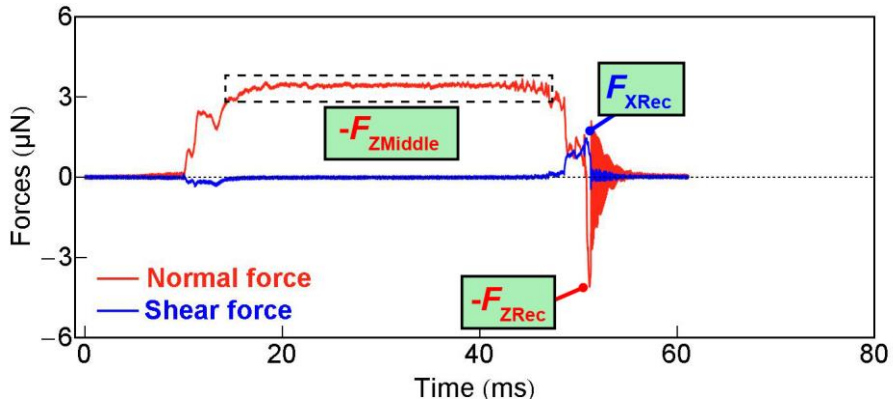

Fig. 4.27 Definition of the forces that will be focused in the analysis.

force driving the droplet to slide was the component of gravity parallel to the sensor surface. Smaller droplet has smaller weight and therefore a lager tilt angle is needed to drive the droplet to slide.

- During the sliding of the droplets of liquids with low viscosity (for example water or G1W1), fluctuation of the normal force acting on the micropillar was observed, especially over the region close to the receding edge of the droplet. The amplitude of these fluctuations decreased as the viscosity of the droplet increased. The relationship between the frequency of these fluctuations and the pitch of the micropillar array and the viscosity of the sensor will be discussed in details in the next section.

4.2.2 Effects of the droplet volume, micropillar density and liquid viscosity on the interaction forces

In this section, effects of three parameters: droplet volume, pitch of the micropillar array and the liquid viscosity on the interaction forces during the sliding of droplets are discussed. In these analysis, the specific force values will be focused are defined in **Fig. 4.27**. The first value is the average normal force over the inner region of the contact area, defined as $\boldsymbol{F}_{\mathbf{ZMidlle}}$, from which it is possible to understand how the pressure inside droplet depends on the parameters above. Moreover, the absolute value of maximum pulling forces at the receding edge of the droplet in normal and shear directions, defined as $\boldsymbol{F}_{\mathbf{ZRec}}$ and $\boldsymbol{F}_{\mathbf{XRec}}$, will also be analyzed to clarify the local interaction at receding edge, which is an important factor controlling the sliding motion of the droplets.

Effect of the droplet volume

The effect of the droplet volume on the interaction forces, for example in the case of water droplets sliding on the sensors having 75 μm-pitch and 125 μm-pitch micropillar arrays, are shown in **Fig. 4.28** and **Fig. 4.29**. The result shows that as the droplet volume increased, the average normal force over the inner region of the contact are $\boldsymbol{F}_{\mathbf{ZMidlle}}$ decreased. This tendency of $\boldsymbol{F}_{\mathbf{ZMidlle}}$ indicates that the force acting on the

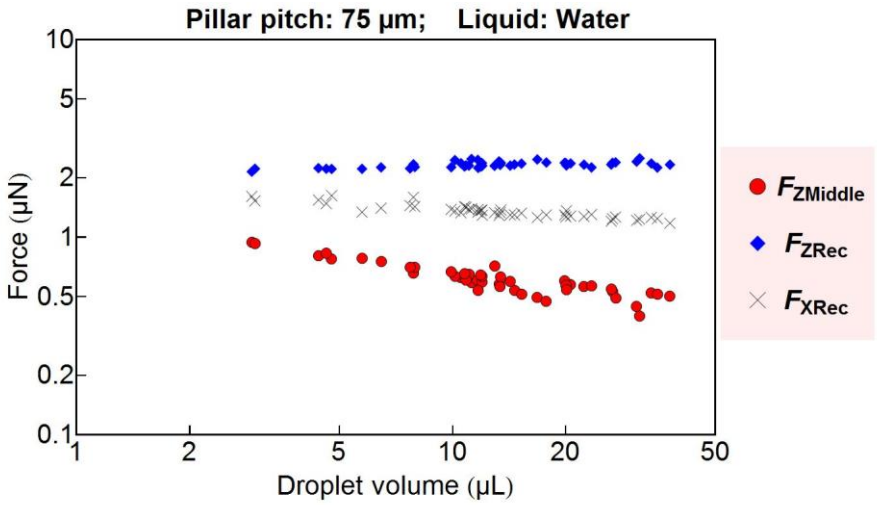

Fig. 4.28 Effect of droplet volume on the average normal force over the contact area and the maximum pulling forces at the receding edge in the case of water droplets sliding on 75 μm-pitch micropillar array.

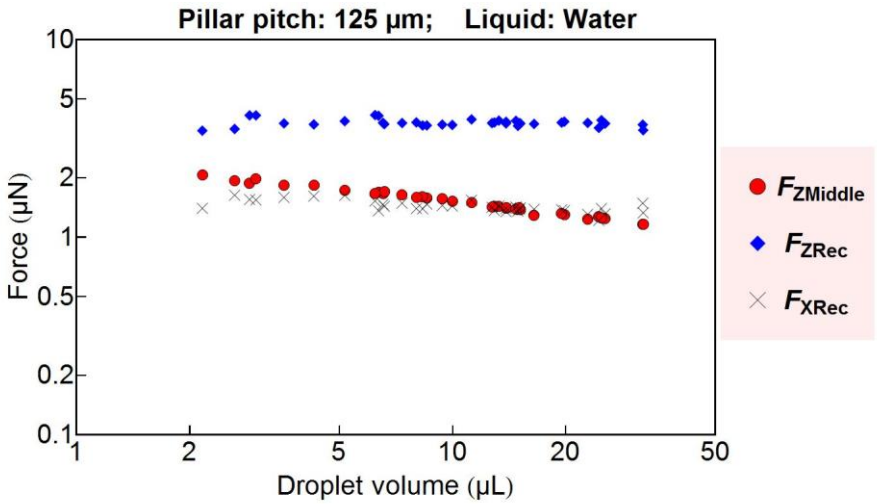

Fig. 4.29 Effect of droplet volume on the average normal force over the contact area and the maximum pulling forces at the receding edge in the case of water droplets sliding on 75 μm-pitch micropillar array.

micropillar over the inner region of the contact area are dominant by Laplace pressure which increases as the size of the droplet decreases. Meanwhile, the maximum pulling forces at the receding edge in both normal and shear directions $\boldsymbol{F}_{\mathbf{ZRec}}$ and $\boldsymbol{F}_{\mathbf{XRec}}$ did not show significant dependence on the size of the droplet. This result indicates that the interaction between the micropillar and droplet at the receding edge is local, which is determined only by the liquid bridge adhered to the pillar not the entire shape or volume of the droplet. The result also means that for a droplet sliding on a micropillar array, it is possible to evaluate the

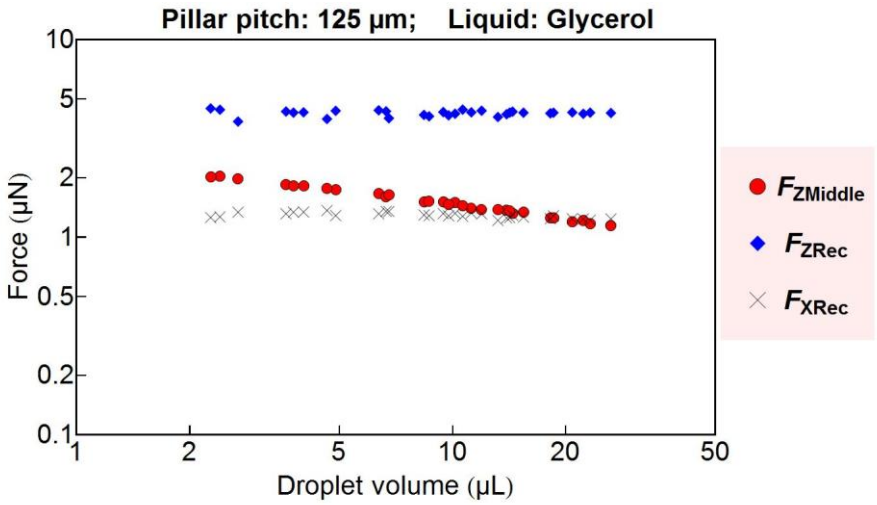

Fig. 4.30 Effect of droplet volume on the average normal force over the contact area and the maximum pulling forces at the receding edge in the case of glycerol droplets.

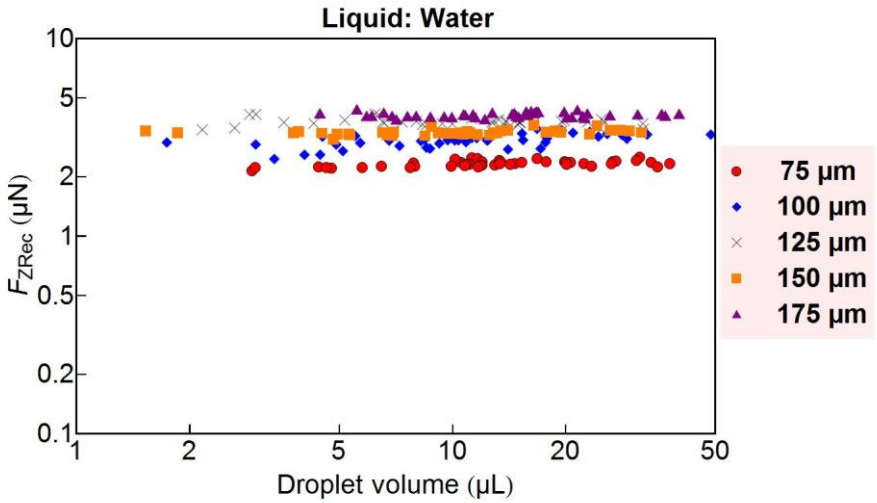

Fig. 4.31 Effect of the micropillar array pitch on the maximum pulling force at the receding edge in normal direction. The plot legend indicates the pitches of the micropillar arrays.

total force acting on the receding edge of the droplet as sum of the force acting on each individual micropillar.

The effect of the droplet volume on the interaction forces mentioned above holds true for all micropillar arrays with different pitches and all liquid samples. For example, **Fig. 4.30** shows the effect of droplet volume on the on the interaction forces for glycerol droplets, which also demonstrates that the average normal force inside the contact area decreased as the volume of the droplet increased and the maximum pulling forces at the receding edge did not depend on the droplet size. For other sensors and liquid samples, the results are shown in **Fig. A. 12** to **Fig. A. 17** in **Appendix 1**.

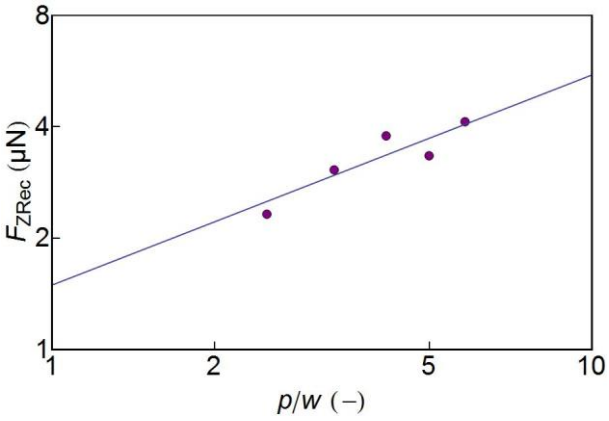

Fig. 4.32 Relationship between the maximum pulling force in the normal direction at the receding edge of the droplet and the ratio of pillar interval per pillar width. The line indicates the fitting of points to function $y = ax^b$ with a = 1.49, b = 0.57.

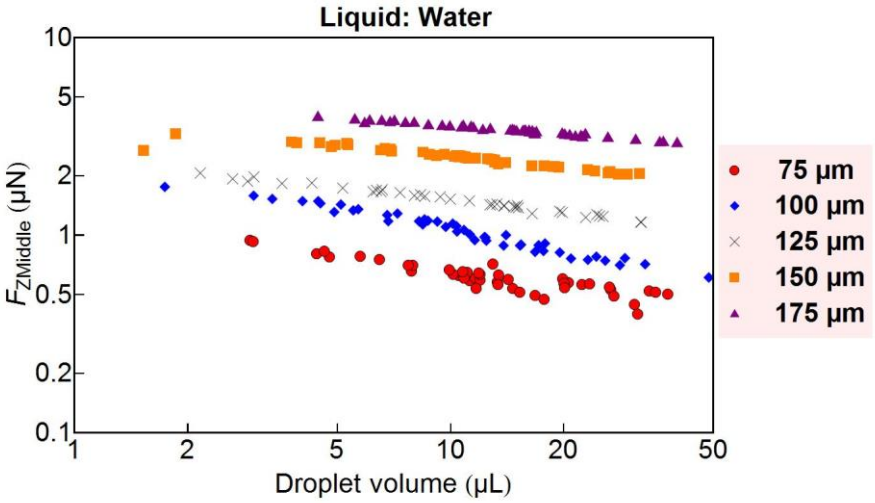

Fig. 4.33 Effect of the micropillar array pitch on the average normal force over the contact area in case of water droplets. The plot legend indicates the pitches of the micropillar arrays.

Of course, the local interaction between the micropillar and the liquid bridge depends on the geometrical parameters of the micropillar array such as the shape and size of a micropillar and the pitch between two adjacent micropillars. The effect of the micropillar array pitch will be discussed in the next section.

Effect of micropillar array density

The effect of the micropillar pitch on the maximum pulling force in the normal direction at the receding edge of the droplet $\boldsymbol{F_{ZRec}}$ is shown in **Fig. 4.31**. It is shown that $\boldsymbol{F_{ZRec}}$ increases as the interval of the pillar increases. Since the volume of the droplet does not affect the value of $\boldsymbol{F_{ZRec}}$, we can take the average value

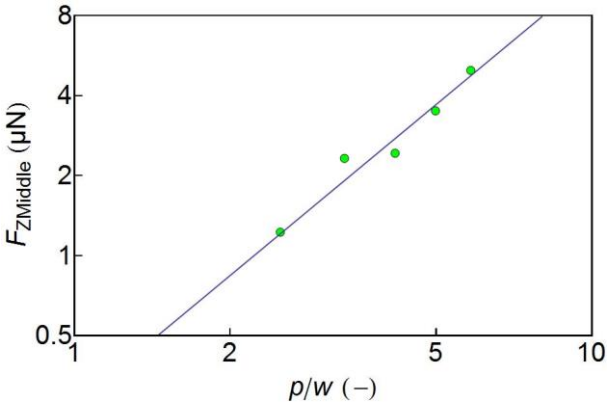

Fig. 4.34 Relationship between the average normal force inside the contact area for droplets of 1 μL and the ratio of the pillar interval per pillar width. The line indicates the fitting result of the data by a function $y = 0.28x^{1.61}$.

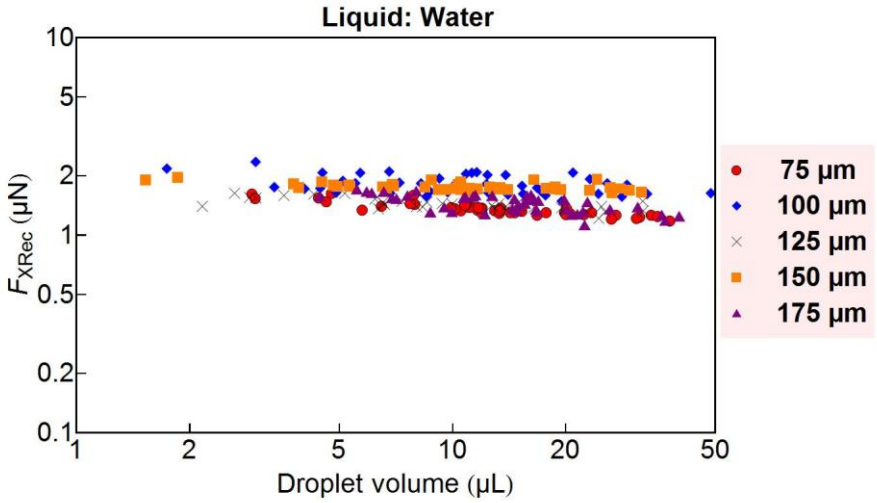

Fig. 4.35 Effect of the micropillar array pitch on the maximum pulling force at the receding edge in shear direction. The plot legend indicates the pitches of the micropillar arrays.

of F_{ZRec} from the values for droplets with different volume. The result, as depicted in **Fig. 4.32,** shows that the maximum pulling force at the receding edge of the droplet is a weak function of the ratio p/w, where p, w are the pitch of the micropillar array and the micropillar pitch. This result suggests that the deformation of the local liquid bridge at the receding edge is more distorted when the micropillar array becomes sparser causing the larger maximum pulling force in the normal direction.

The effect of the micropillar interval on the average normal force over the inner region of the contact area, for example, in the case of water droplets is shown in **Fig. 4.33**. It is clear that for droplets with the same volume, the normal force inside the contact area increase as the pitch of the micropillar array increases, which is quite obvious because the number of micropillar over unit area decreases when the pitch of the

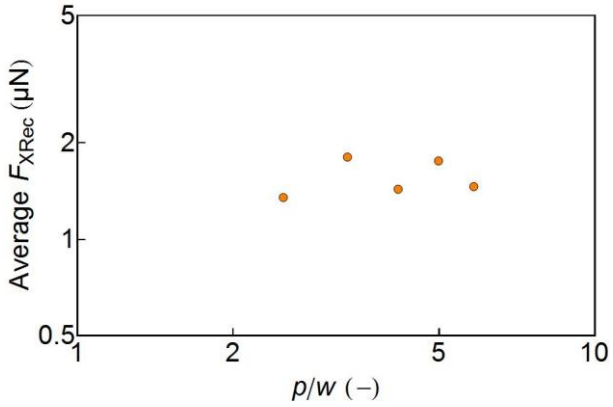

Fig. 4.36 Average maximum pulling force at the receding edge in shear direction plotted again ***p*/*w***.

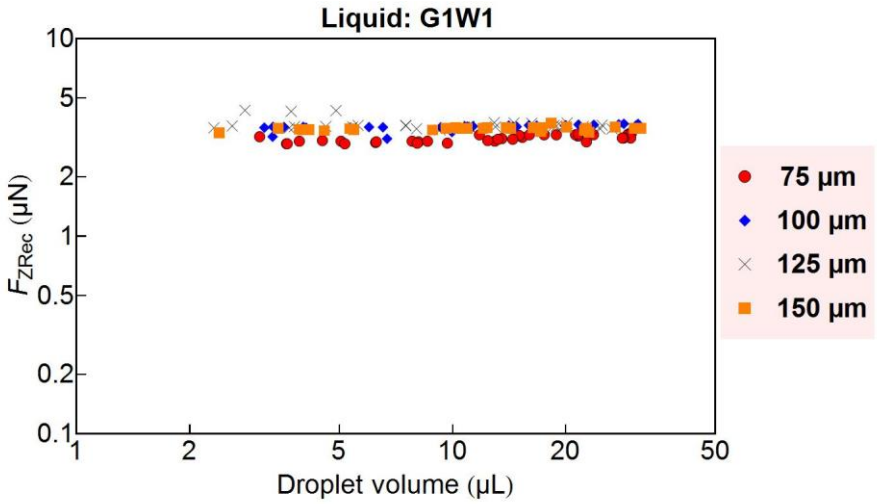

Fig. 4.37 Effect of the micropillar array pitch on the maximum pulling force at the receding edge in shear direction in case of G1W1 liquid sample. The plot legend indicates the pitches of the micropillar arrays.

micropillar array increases as followed:

$$N \approx \frac{1}{p^2} \tag{4.5}$$

If we fit the data with the function $\boldsymbol{F_{ZMiddle} = aV^b}$ where $\boldsymbol{V}$ (μL) is the droplet volume, then we obtain the relationship between $\boldsymbol{a}$ and the ratio $\boldsymbol{p/w}$ as shown in **Fig. 4.34**. It is worth noticing that the coeffient $\boldsymbol{a}$ represents the average normal force for the droplet of 1 μL, for which the effect of gravity can be neglected. By fitting the relationship between $\boldsymbol{a}$ and $\boldsymbol{p/w}$, we obtain $\boldsymbol{a = 0.28\ (p/w)^{1.61}}$. The exponentiation coefficient

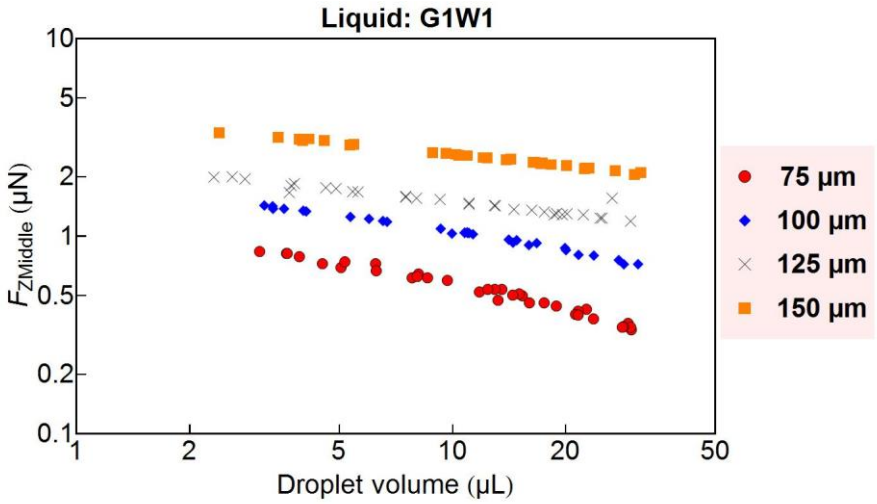

Fig. 4.38 Effect of the micropillar array pitch on the average normal force over the inner region of the contact area in case of G1W1 liquid sample. The plot legend indicates the pitches of the micropillar arrays.

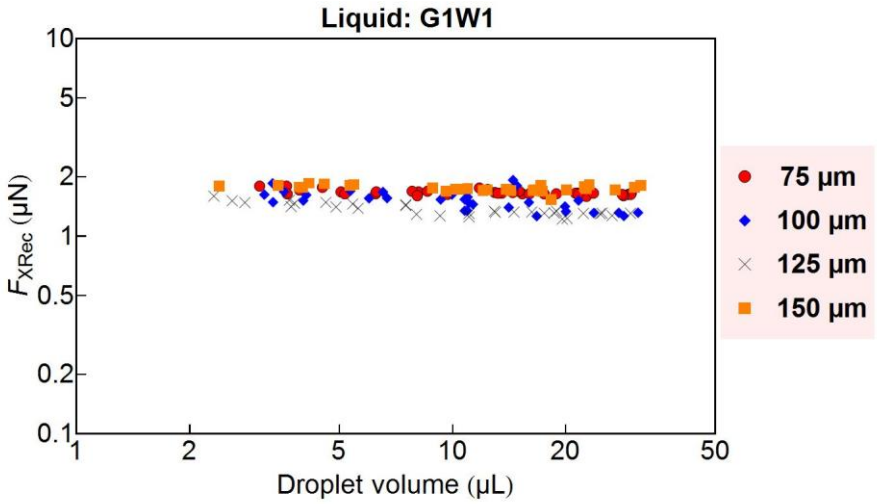

Fig. 4.39 Effect of the micropillar array pitch on the maximum pulling force at the receding edge in shear direction in case of G1W1 liquid sample. The plot legend indicates the pitches of the micropillar arrays.

1.61 is slightly different from that in Eq. **(4.5)**, which is thought to be caused by the dependence of the pulling force in normal direction at the receding edge of the droplet on the pitch of the micropillar array.

For the maximum pulling force in the shear direction $\boldsymbol{F}_{\mathbf{XRec}}$ at the receding edge of the droplet, as shown in **Fig. 4.35**, the pitch of the micropillar array does not show clear effect. There were variations of $\boldsymbol{F}_{\mathbf{XRec}}$ as the volume of the droplet varied, however, the average value $\boldsymbol{F}_{\mathbf{XRec}}$ over droplets with different volume, as

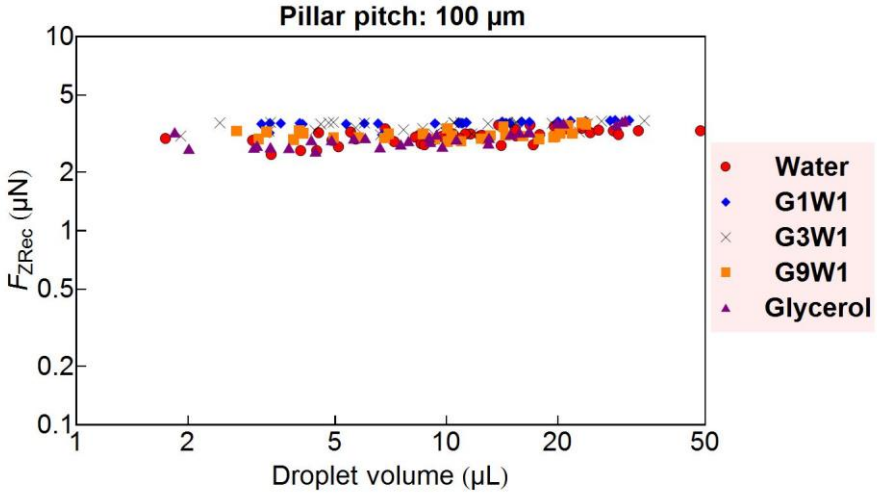

Fig. 4.40 Effect of the liquid viscosity on the maximum pulling force at the receding edge in normal direction in case of G1W1 liquid sample. The plot legend indicates the liquid samples.

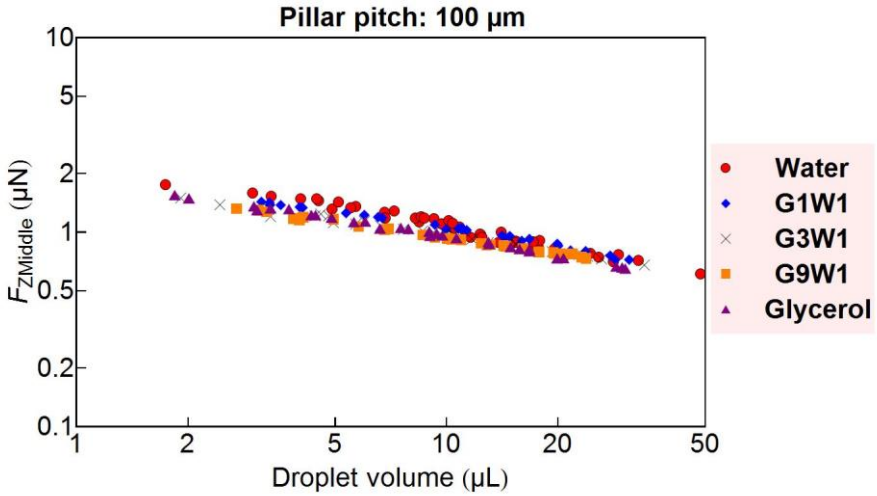

Fig. 4.41 Effect of the liquid viscosity on the average normal force over the inner region of the contact area in case of 100 μm-pitch micropillar array. The plot legend indicates the liquid samples.

shown in **Fig. 4.36** did not obviously depend on the density of the micropillar.

In cases of other liquid samples, the relationship between the pitch of the micropillar and interaction forces were similar with that in the case of water mentioned above. For example, **Fig. 4.37**, **Fig. 4.38** and **Fig. 4.39** shows the effect of the micropillar pitch on $\boldsymbol{F}_{\mathbf{ZRec}}$, $\boldsymbol{F}_{\mathbf{ZMiddle}}$, and $\boldsymbol{F}_{\mathbf{XRec}}$ respectively.

Effect of the liquid viscosity

The effects of liquid viscosity on the interaction forces during the sliding of droplets, for example, in the

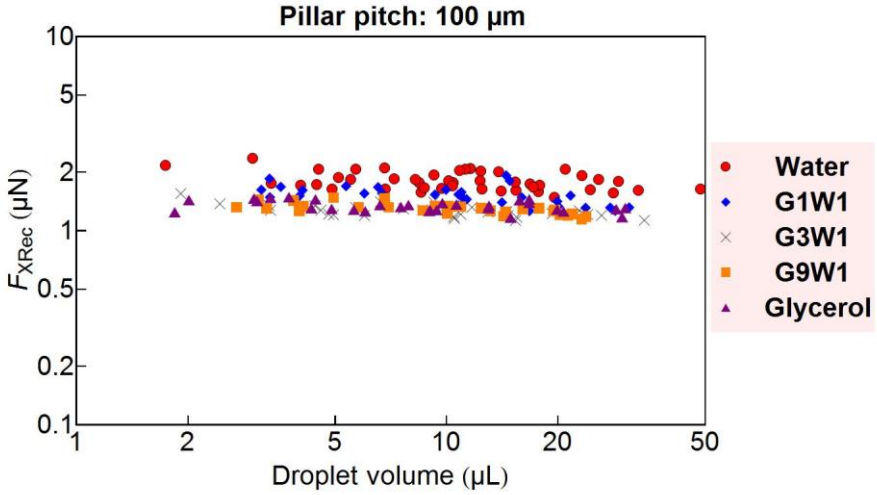

Fig. 4.42 Effect of the liquid viscosity on the maximum pulling force at the receding edge in shear direction in case of 100 µm-pitch micropillar array. The plot legend indicates the liquid samples.

case of the micropillar with 100 µm- pitch, are shown in **Fig. 4.40**, **Fig. 4.41** and **Fig. 4.42**. The results show that the interaction forces during the sliding of the droplets did not vary much when the viscosity changed. It should be reminded that the sliding of droplets in the experiment was in the beginning state (first several millimeters), in which surface tension is still dominant over the viscosity. Because the surface tension of prepared liquid samples are not different much (from 63 mN/m for glycerol to 72 mN/m for water), the interaction forces during the sliding of droplets were not affected significantly by the type of liquid samples. Only slight differences in the value of the average normal force inside the contact area and the maximum pulling force in shear direction at the receding edge (**Fig. 4.41** and **Fig. 4.42**) were observed, which are thought to be a result of the difference in surface tension of liquid samples.

4.2.3 Comparison between the measured normal force over the contact area and the normal force estimated from the high speed camera images

This section presents the comparison between the average measured normal force acting on a micropillar inside the contact area of a droplet and normal force estimated from the shape of the droplet extracted from high speed camera images.

Inside the contact area of the droplet the liquid pressure can be estimated from capillary pressure and hydrostatic pressure as shown in **Fig. 4.43** by the following equation:

$$P = P_{\text{capillary}} + P_{\text{hydrostatic}} \tag{4.6}$$

where $\boldsymbol{P_{\text{capillary}}}$ and $\boldsymbol{P_{\text{hydrostatic}}}$ are the capillary pressure or pressure jump and the hydrostatic pressure presenting the effect of the droplet weight. The capillary pressure is determined by the mean curvature radius of the droplet whereas the hydrostatic pressure is determined by the height of the droplet.

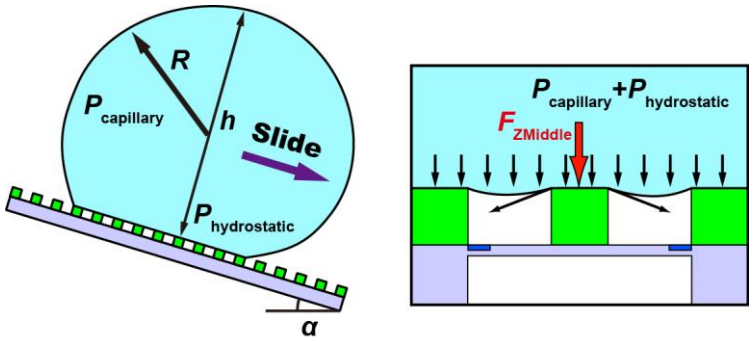

Fig. 4.43 Normal force acting on a micropillar inside the contact area of the droplet is resulted from the liquid pressure.

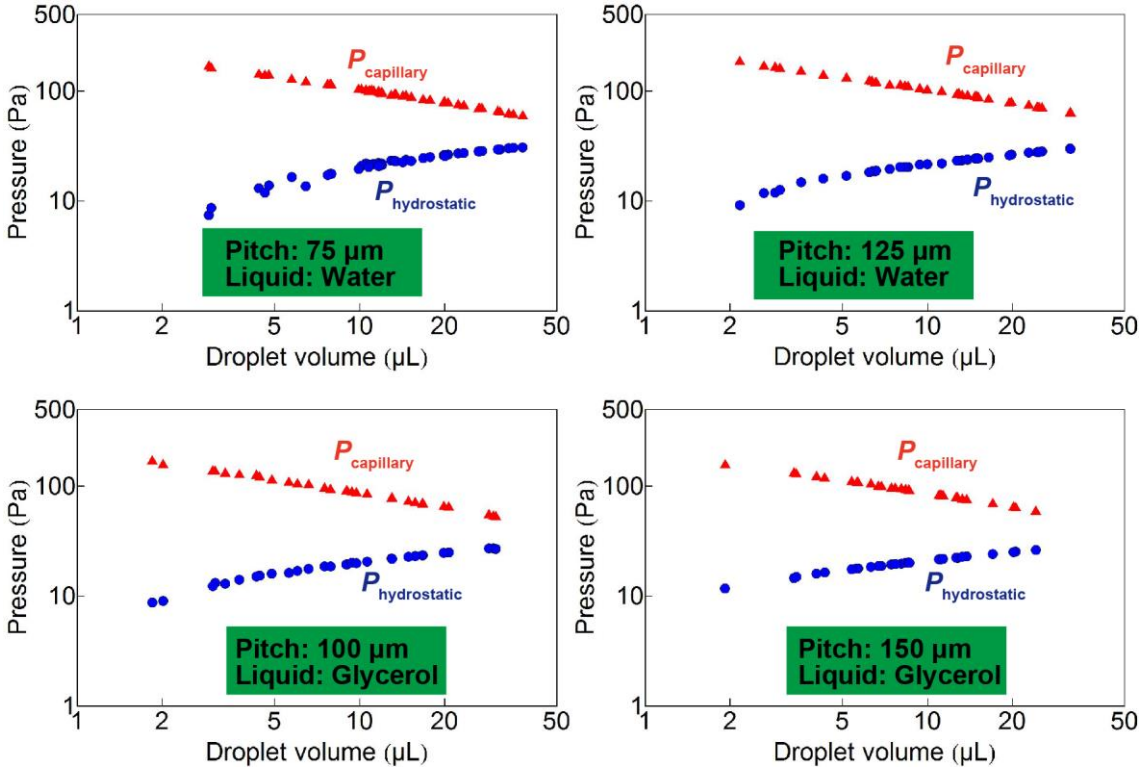

Fig. 4.44 Capillary pressure and hydrostatic pressure of the droplets during the sliding.

The values of $\boldsymbol{P}_{\mathbf{capillary}}$ and $\boldsymbol{P}_{\mathbf{hydrostatic}}$ can be calculated as followed:

$$P_{\text{capillary}} = \frac{2\gamma}{R} \tag{4.7}$$

$$P_{\text{hydrostatic}} = \rho g h \cos\alpha \tag{4.8}$$

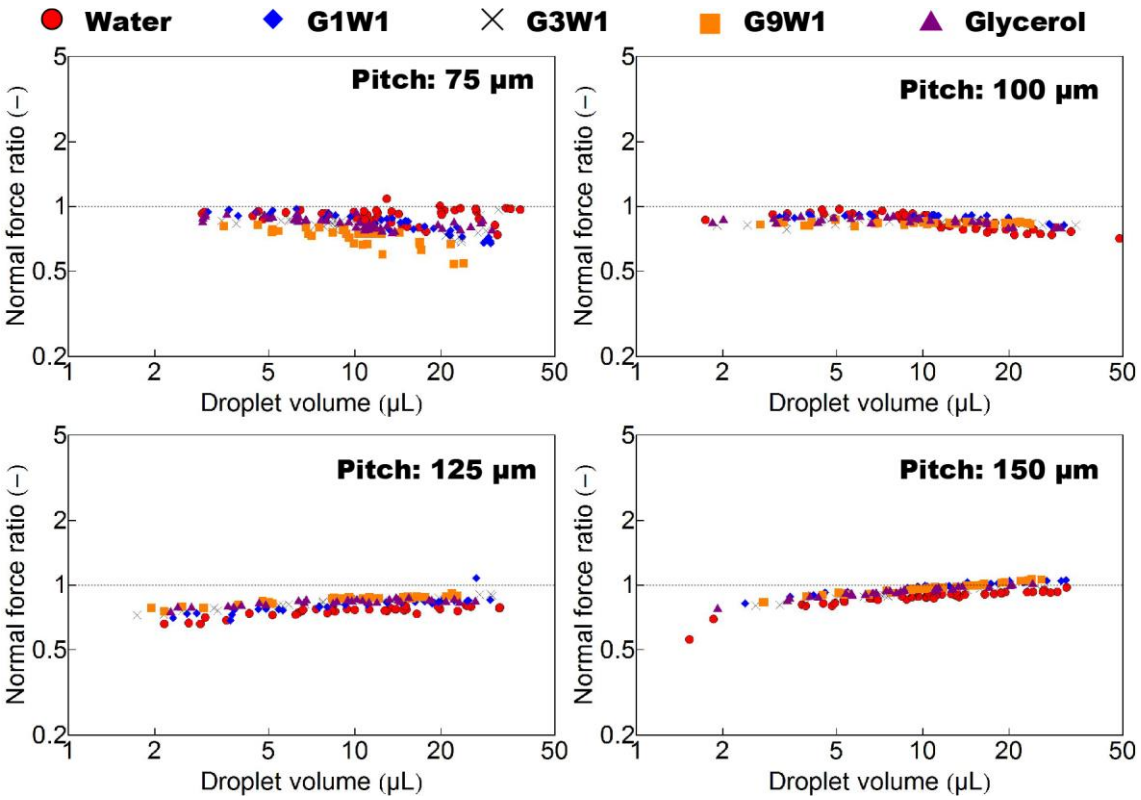

Fig. 4.45 Ratio between the measured normal force and the force obtained by high speed camera images.

where γ, R are the liquid surface tension and curvature radius of the droplet at its apex, respectively; ρ, g, h, α are the liquid density, gravitational acceleration, droplet height and sliding angle, respectively. The geometrical parameters of the droplet and the sliding angle can be obtained from the high speed camera images, from which it is possible to calculate the liquid pressure P.

It has been known that for small droplet whose radius is smaller than capillary length, the capillary pressure dominates over gravity. This relationship can be confirmed by comparing $P_{capillary}$ and $P_{hydrostatic}$ as shown in **Fig. 4.44**, for example, for water droplets sliding on micropillar with pitches of 75 and 125 μm and glycerol droplets sliding on micropillar with pitches of 100 and 150 μm. The result indicates that as the size of the droplet decreases, the capillary pressure increases and the hydrostatic pressure decreases. Moreover, for droplets used in the experiment, the capillary pressure is larger than the hydrostatic pressure.

On the other hand, the measured normal force acting on a micropillar $F_{ZMiddle}$ is equivalent to the following liquid pressure

$$P_{Measure} = \frac{F_{ZMiddle}}{p^2} \tag{4.9}$$

where p is the pitch of the micropillar array. By comparing $P_{Measure}$ and P, we can evaluate the accuracy of the measurement. **Fig. 4.45** shows the calculated ratios $P_{Measure}/P$ for all tested liquid types and micropillar arrays having the pitches of 75, 100, 125 and 150 μm. The result demonstrates that these ratios were approximately 1, which indicates that the measured normal forces over the contact area of the droplet were approximately the same with those estimated from the size and shape of the droplet.

4.2.4 Comparison between the measured shear force and the frictional force of the droplets

This section presents the comparison between the measured shear force acting on a single micropillar and the frictional force of the droplet obtained from high speed camera images. The frictional forces of the droplets during the sliding were calculated from the tilt angle of the sensor and the accelerations of the droplets.

First, sine of the sliding angles of the droplets (the tilt angle of sensor at which the droplet started to slide) are presented in **Fig. 4.46**. Each graph shows the results for droplets of the same liquid sample sliding on micropillar array with different pitches. It is clear that the sliding angle of a droplet decreases as the volume of the droplet increases. Moreover, for droplets of the same liquid sample with the same volume, the sliding angle increases as the density of the micropillar array increases.

The frictional force F_S during the sliding of the droplets is then calculated from the sliding angle α and the sliding acceleration a of the droplet using following relationship:

$$F_S = m(g\sin\alpha - a) \tag{4.10}$$

where m is mass of the droplet which can be calculated from its volume, and g is gravitational acceleration. The calculation of the sliding acceleration of the droplet was similar to that described in Section 4.2.2. By tracking the droplet in images of the high speed camera, the sliding distance was obtained and from the sliding distance, the sliding acceleration was calculated.

The calculated frictional forces are shown in **Fig. 4.47**. Each graph in the figure presents the results for each liquid sample and different pitches of the micropillar array. Different from the results related to the sine of the sliding angle, the frictional force of a droplet increases as the droplet volume increases. This is because for a larger droplet, more micropillars pulling the droplet back and the frictional force becomes larger. As shown in previous section, during the sliding of droplets in our experiment, shear force acting on the micropillars at the receding edge of the droplet is the dominant factor determining the friction of the droplet. The number of the micropillar at the receding edge of the droplet increases as the size of the droplet increases or the density of the micropillar array increases. This estimation also agrees with the fact that the frictional force of the droplets with same volume increases as the pitch of the micropillar array decreases which can be confirmed in each graph.

For the viscosity of the droplet, its effect on the frictional force of the droplets is shown in **Fig. 4.48**. In the figure, each graph presents the frictional forces of droplets of different liquid samples sliding on the

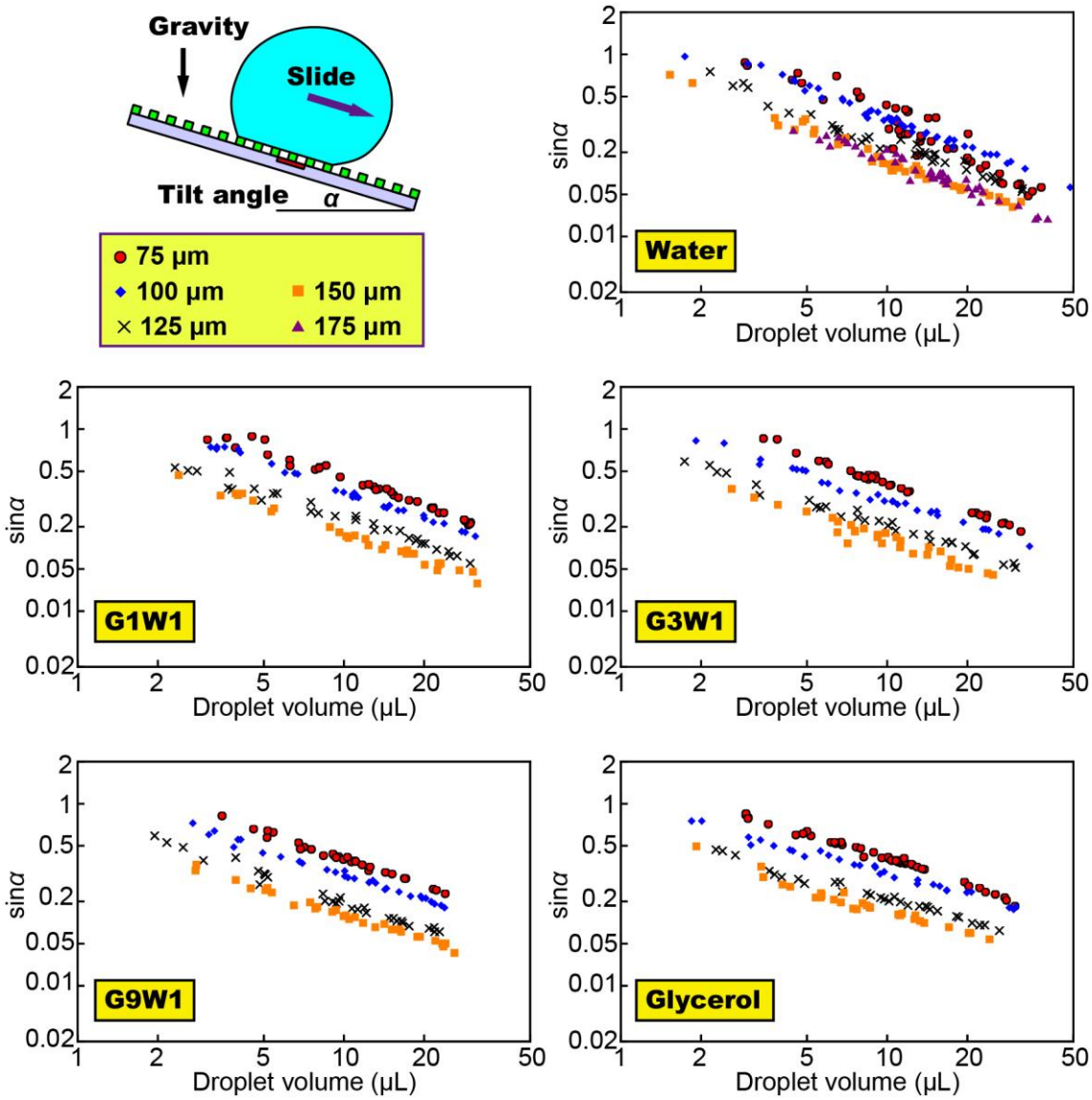

Fig. 4.46 Relationship between the droplet volume and the sliding angle of the droplets. Each graph shows the results for droplets of the same liquid sample sliding on micropillar arrays with different pitches.

same micropillar array. A common tendency can be found in the relationship of the frictional force and the liquid viscosity is the frictional force increases as the viscosity increases. However, if we compare the effect of the viscosity and that of the micropillar array density, one can find that the viscosity has less effect on the frictional forces of the droplet. This is, again, due to the fact that the droplets were sliding at relatively low velocity. When the sliding velocity of the droplets increases, one can expect to see the effect of viscosity more clearly. Because of the limitation in the size of the sensors in this study, experiments on the high velocity regime could not be carried out.

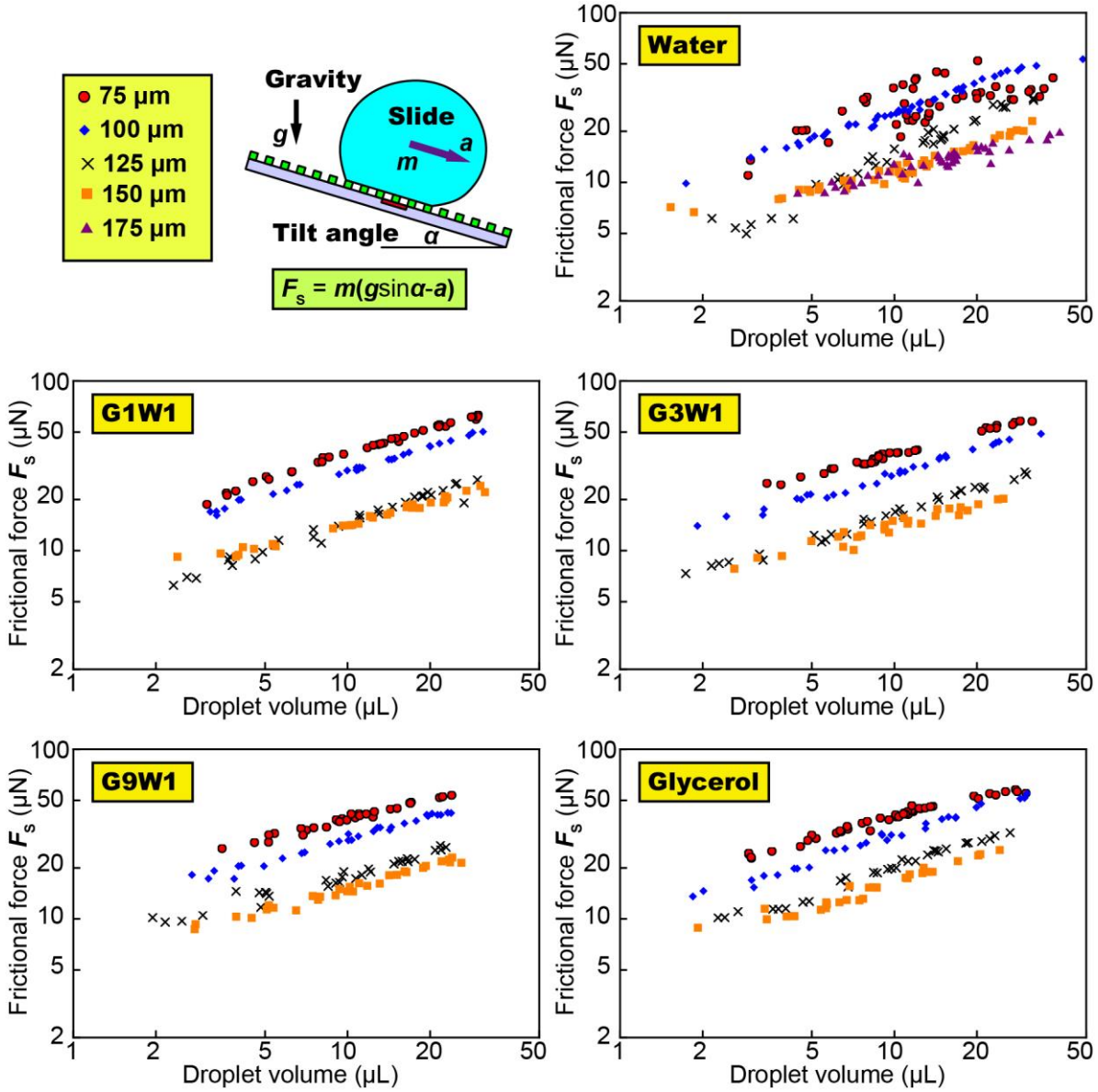

Fig. 4.47 Frictional force during the sliding of the droplets. Each graph shows the results for droplets of the same liquid sample sliding on micropillar arrays with different pitches.

From the total frictional force, the average frictional force contributed by one micropillar is estimated. Assuming that the contact area of the droplet maintains circle during the sliding, the number of micropillar at the receding edge of the contact area can be estimated as by following equation:

$$N_{\mathrm{Rec}} \approx \frac{\pi r}{p} \tag{4.11}$$

where ***r*** is the radius of the contact area, and ***p*** is the pitch of the micropillar array. This estimation is based on the assumption that on every length of ***p*** of the contact line, there is one micropillar. The contact radius

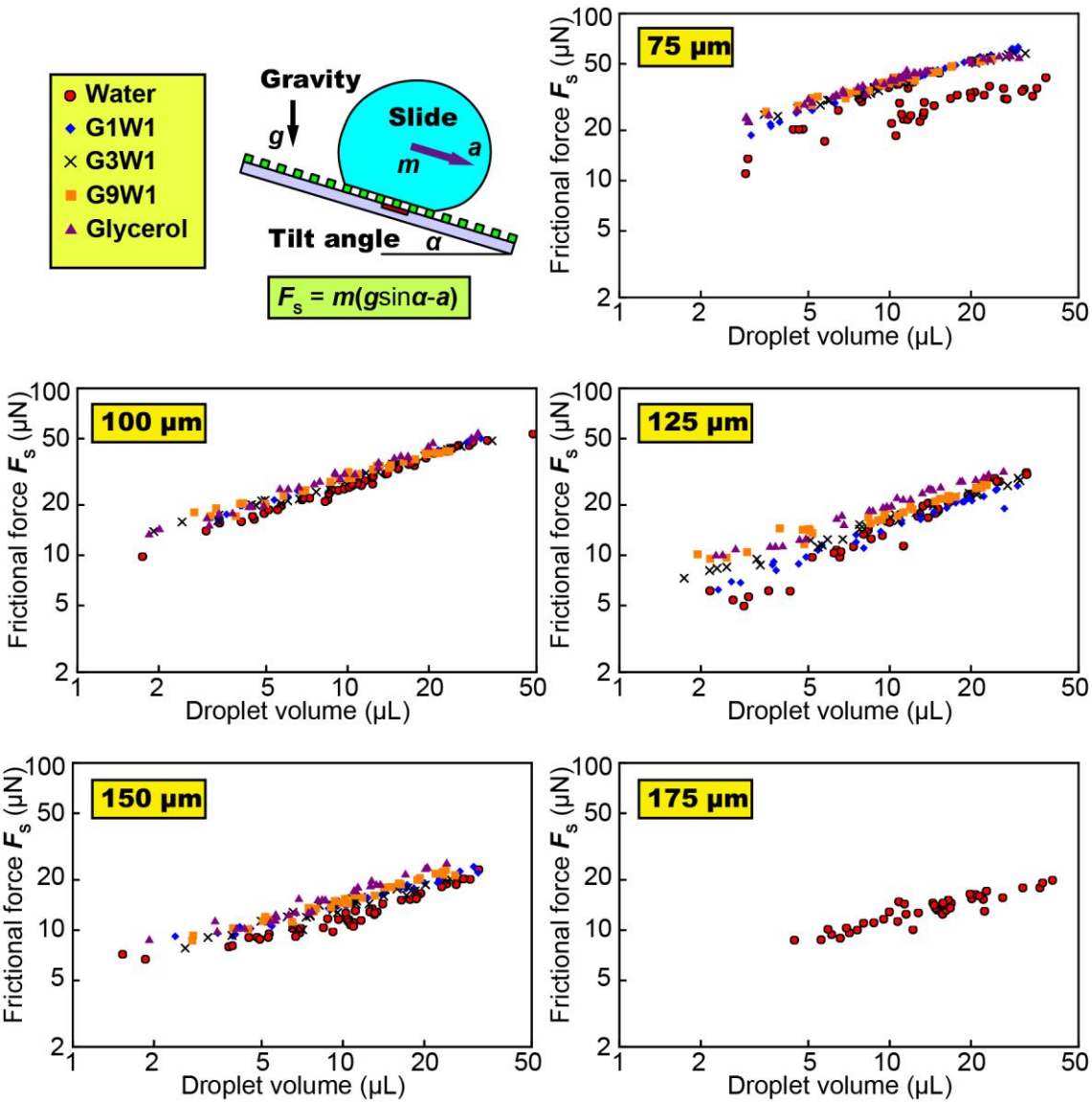

Fig. 4.48 Relationship between the droplet volume and the frictional force during the sliding of the droplets.

of the contact area was obtained from the image of the high speed camera. Because the friction of the droplet is mainly caused by the adhesion of the droplet at the receding edge of the contact area, the frictional force on a single micropillar is:

$$F_{\mathrm{SAverage}} = \frac{F_{\mathrm{S}}}{N_{\mathrm{Rec}}} \tag{4.12}$$

where $\boldsymbol{F}_{\mathbf{S}}$ is the total frictional force acting on the droplet described above.

On the other hand, the average shear force $\boldsymbol{F}_{\mathbf{XAverage}}$ acting on a micropillar can be obtained by from the

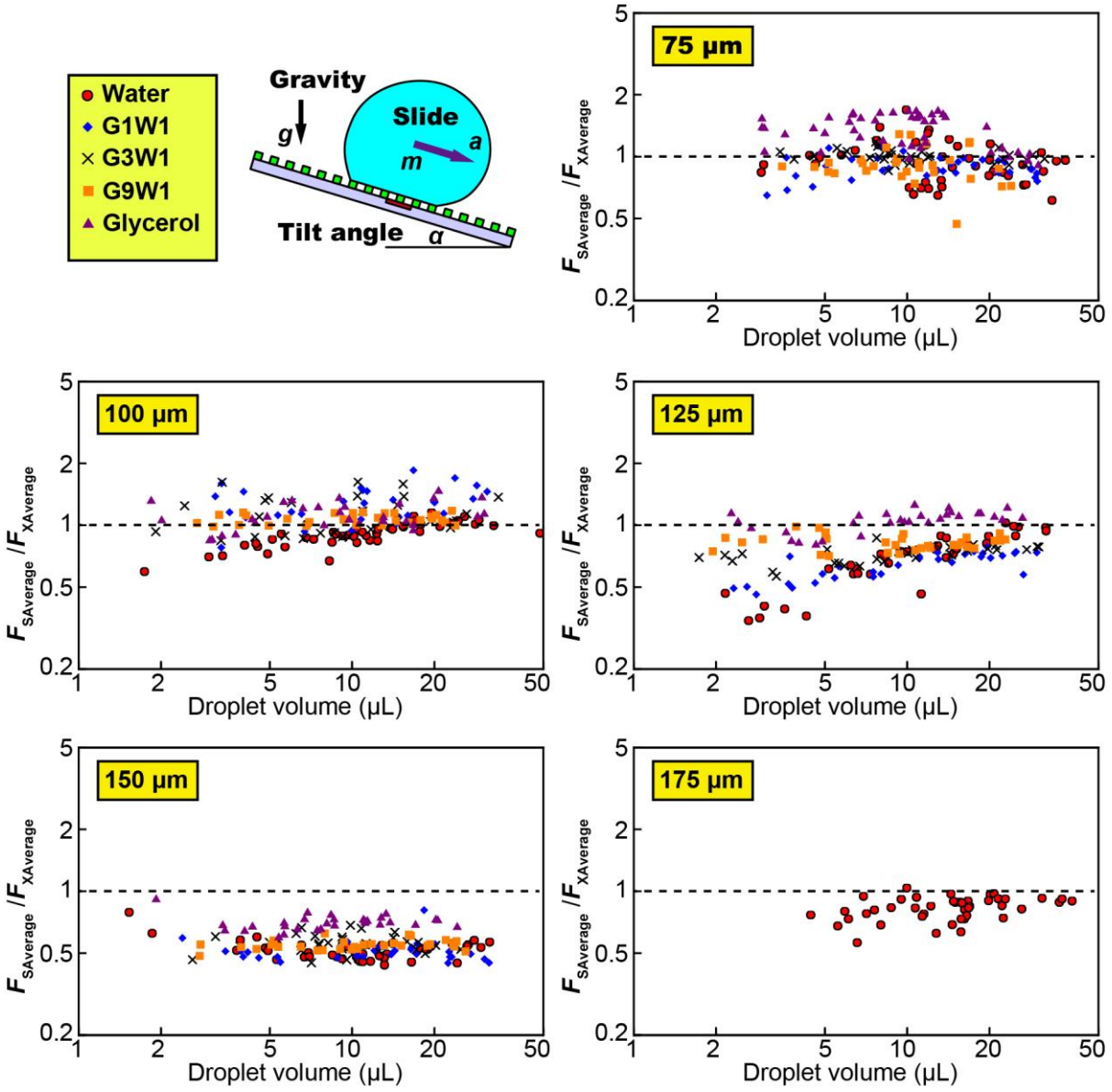

Fig. 4.49 Ratio of the average frictional force acting on the micropillar calculated from the frictional force of the droplet and that measured by the sensor.

output of the sensor.

Next we will compare the values of $F_{SAverage}$ and $F_{XAverage}$. **Fig. 4.49** shows the ratio $F_{SAverage}/F_{XAverage}$ plot against volume of the droplet for droplets of different liquid types sliding on the same micropillar. The results show that the ratio for does not depend on the volume of the droplet even the total frictional force increased as the volume of the droplet increased. Moreover, the ratio $F_{SAverage}/F_{XAverage}$ for all sensor and liquid samples overall are not very different from 1, which indicates the strong correlation between the measured shear force acting on a micropillar and the frictional force of the droplet. The variation of the ratio from 1 may come from an error of the estimation of $F_{SAverage}$. During the sliding, the contact area, of

course, would deform and have eclipse shape rather than circle. The shape of the ellipse depend on the contact angle and the size of the contact area. Moreover, due to the discrete micropillar array, the number of the micropillar at the receding edge of the droplet should be more than the number estimated by **Eq. (4.11)** and the actual frictional force should be larger than that estimated by **Eq. (4.12)**. Therefore, the ratio of the estimated frictional force over the measured shear force for one micropillar were often smaller than 1, for example in the case of the micropillar array that has 150 μm-pitch. Furthermore, the result also indicates that the ratio $\boldsymbol{F}_{\mathbf{SAverage}}/\boldsymbol{F}_{\mathbf{XAverage}}$ is greater for liquid having higher viscosity, which agrees with the result shown in **Fig. 4.48**: the friction of more viscous liquid sample is larger than that of less viscous liquid sample, which implies the small effect of viscosity dissipation on the friction of the droplets.

4.3 Vibration during sliding of the droplets on the micropillar arrays

This section discusses the sliding induced vibration of the droplet and the effect of the micropillar array pitch and liquid viscosity on the frequency of the vibration. It should be clear that this "sliding induced" vibration of the droplet differs from the resonance vibration of the droplet which will be discussed in the next chapter.

4.3.1 Sliding induced vibration of droplet

It was mentioned in previous section, when a water droplet sliding on a micropillar array, a fluctuation in the output of the sensor was seen, especially when the sensor was close to the receding edge of the droplet. In order to evaluate the frequency spectrum of the vibration, Discrete Fourier Transform (DFT) was conducted for the normal force over the inner region of the contact area. Moreover, DFT was also conducted for the normal force just before the droplet contact the micropillar as noise lever. The duration of the noise lever was the same with that of the normal force during the contact of the sensor with the inner region of droplet base.

Fig. 4.50 and **Fig. 4.51** show the results for the cases of 2.9 and 17 μL water droplets sliding on the micropillar array with 75 μm-pitch. The zoom views ((b) in each Figure) show the normal forces during the last approximately 10 ms before the micropillar contacting the receding edge of the droplet. The result confirms the high frequency (several kHz) fluctuation of the normal forces in both cases. The DFT spectrum corresponding to the normal force over the inner region of the contact area of the droplets (shown in purple color in **Fig. 4.50** (a) and **Fig. 4.51** (a)) are shown in **Fig. 4.50** (d) and **Fig. 4.51** (d). Comparing to the spectrum of the noise lever, it is clear that the normal force during the sliding of the droplet includes fluctuations over a high frequency band around 10 kHz. Moreover, the frequency band of these fluctuations were the similar for two droplets which had significantly different size (2.9 and 17 μL) which indicates the independence of the vibration frequency on the volume of the droplet.

Furthermore, effect of the sliding velocity on the frequency of the vibration was also investigated. As shown in **Fig. 4.52**. Three 10μL water droplets were first deposited at different distances from the sensor so that when the droplets slide through the sensor, their sliding velocities were different. The closer the initial

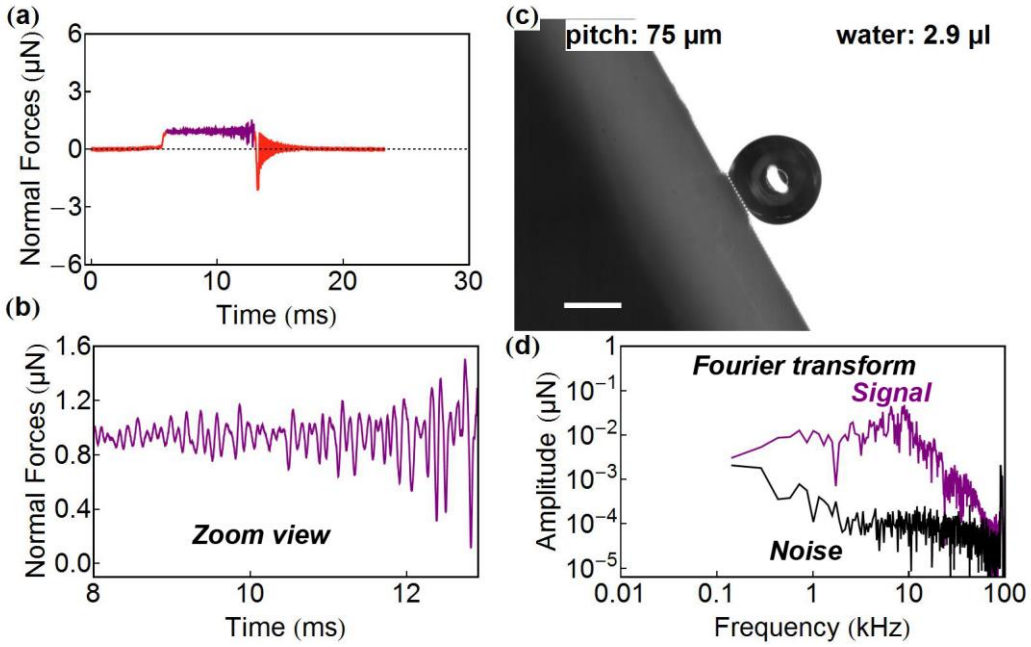

Fig. 4.50 Result for 2.9 μL water droplet sliding on 75 μm-pitch micropillar array (a) Normal force (b) a close view of the normal force, (c) snap shot of the droplet during sliding, scale bar 1 mm (d) Fourier transform spectrum of the normal force.

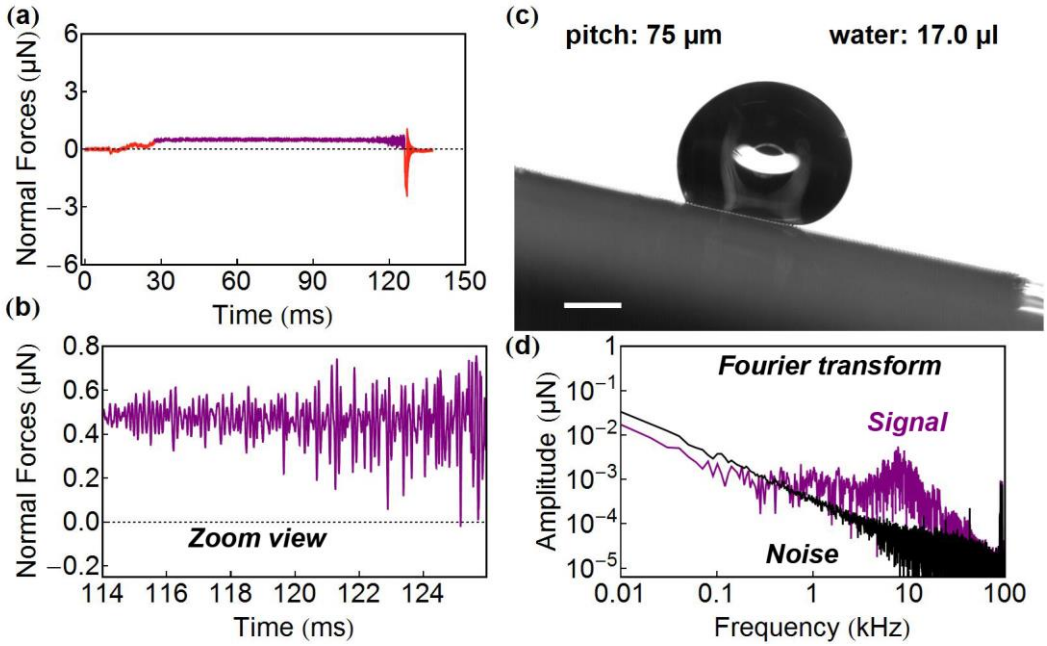

Fig. 4.51 Result for 17 μL water droplet sliding on 75 μm-pitch micropillar array (a) Normal force (b) a close view of the normal force, (c) a snap shot of the droplet during sliding, scale bar 1 mm (d) Fourier transform spectrum of the normal force and noise lever.

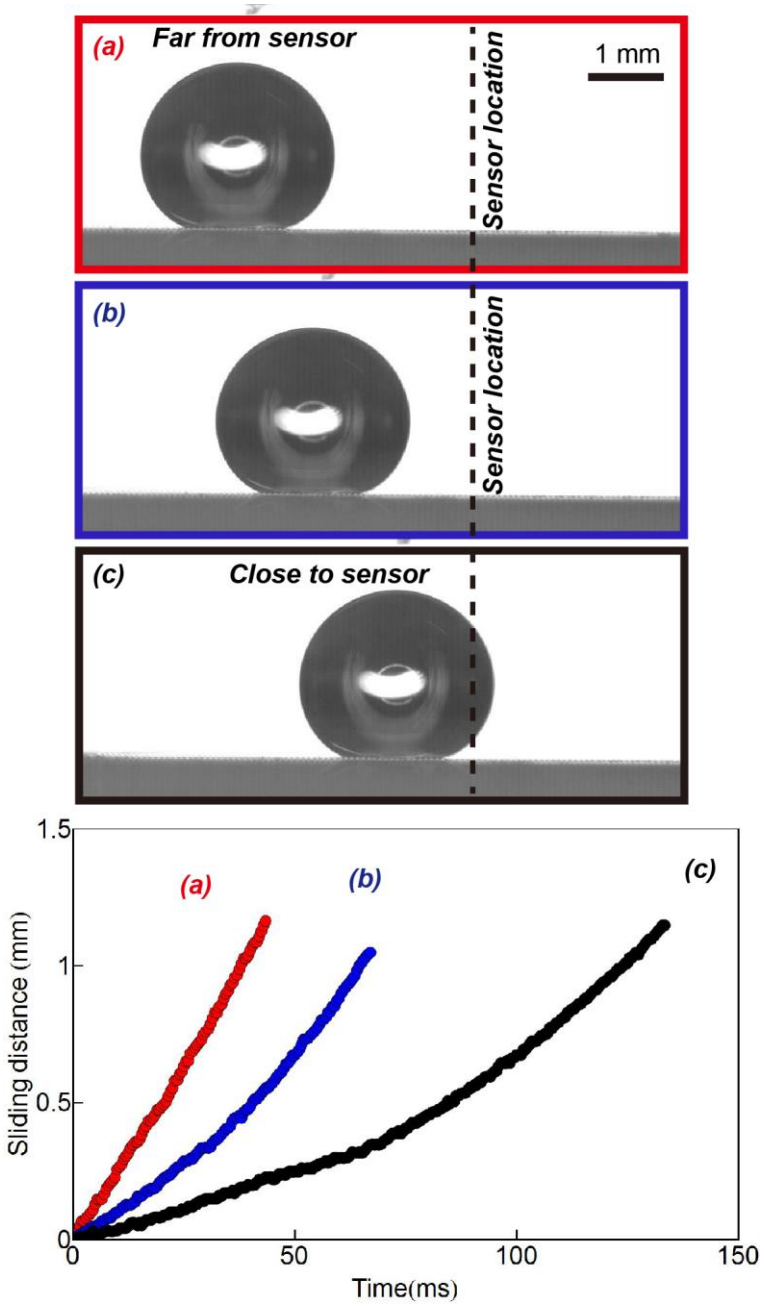

Fig. 4.52 Initial locations and the sliding distances of three water droplets having the same volume. The pitch of the micropillar is 75 μm.

location of the droplet to the sensor, the smaller the droplet velocity when it slides through the sensor.

From the sliding distances, the average sliding velocities of three droplet were calculated to be 3, 10 and 25 (mm/s), respectively. Nevertheless, as shown in **Fig. 4.53**, the frequency spectra of normal forces during the sliding of three droplet are similar with the vibration over the frequency range around 10 kHz. These properties of the frequency spectra give a hint that the fluctuation in the normal force during the sliding of a

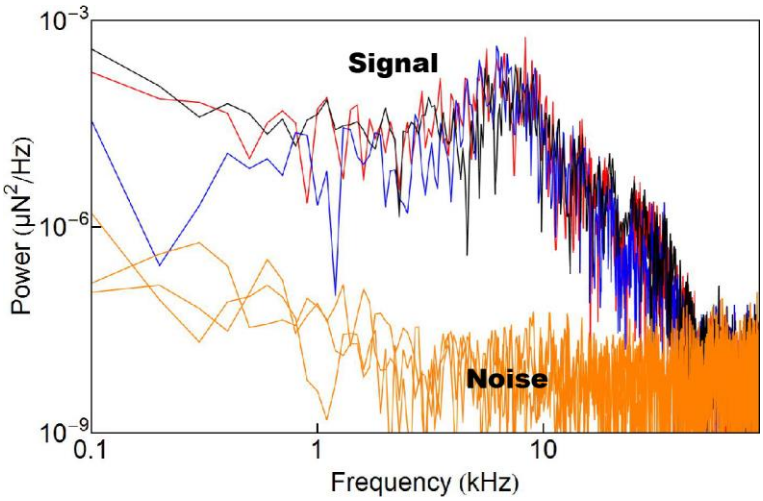

Fig. 4.53 Frequency spectrum of normal forces and noise lever during the sliding of the three water droplets having the same volume, but different sliding velocities.

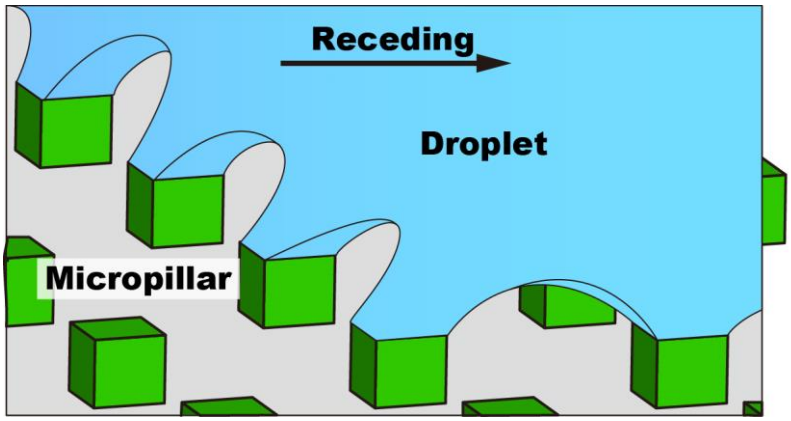

Fig. 4.54 Liquid legs developed at the receding edge of the droplet during sliding.

droplet is not caused by the macro sliding motion of the droplet, but rather by the local detachment of the liquid legs from each micropillar. A schematic illustration of the development of these liquid legs at the receding edge of the droplet is shown in **Fig. 4.54**. These liquid legs can be modeled using a spring-mass system as shown in **Fig. 4.55**. During the sliding of the droplet, the liquid moves forward and pulls the liquid legs from the micropillars at the receding edge. Since the liquid adheres to the micropillar, the pulling force induces the deformation of the liquid legs until the elastic force exceeds the adhesion force. Elastic energy stored in the deformation of the liquid legs releases after the detachment of each liquid leg causing the vibration propagating to the entire droplet. The detachment mechanism of the liquid leg at the receding edge of a sliding droplet can be also confirmed in images obtained by the high speed camera. **Fig. 4.56** shows detachment of a liquid leg during sliding of a droplet on a 175 μm-pitch micropillar array. The record rate in this case was 40000 fps. From the images, one can easily confirm the development and the

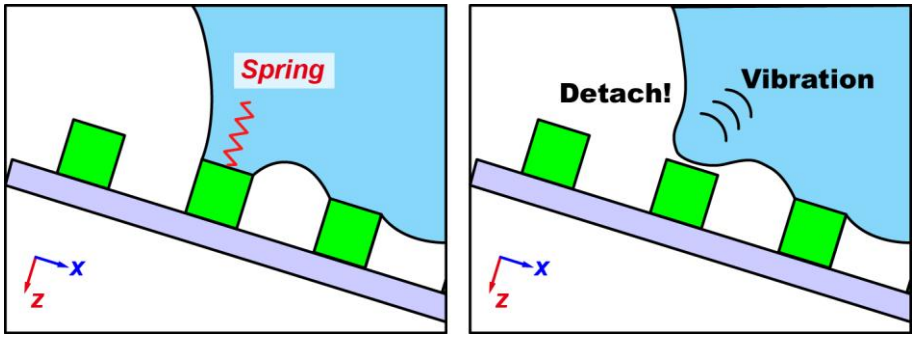

Fig. 4.55 Liquid leg detachment induced vibration.

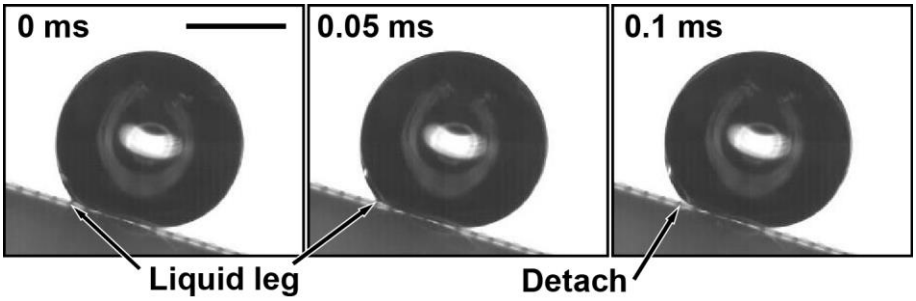

Fig. 4.56 Snapshots of the high speed camera showing the detachment of a liquid leg from the micropillar. Scale bar is 1 mm.

detachment of the liquid leg from micropillar at the receding edge of the droplet.

Since the detachment of the liquid leg induces the release of the elastic energy stored as the spring-mass model, the frequency of the vibration propagating to the entire droplet is determined by the vibration frequency of this spring-mass model. As shown in **Chapter 2**, the spring constant of the liquid leg in relationship with the pitch of the micropillar is:

$$k \approx \frac{\gamma}{\ln(\frac{2p}{w})} \tag{4.13}$$

where p and w are the pitch of the micropillar array and the width of the micropillar, respectively. If we ignore the effect of viscosity, the resonant frequency of the sping-mass model is:

$$f \approx \sqrt{\frac{k}{m}} \tag{4.14}$$

where m is the mass of the liquid leg, scaling as $m \approx wp^2$. Thus, we obtained the relationship between the

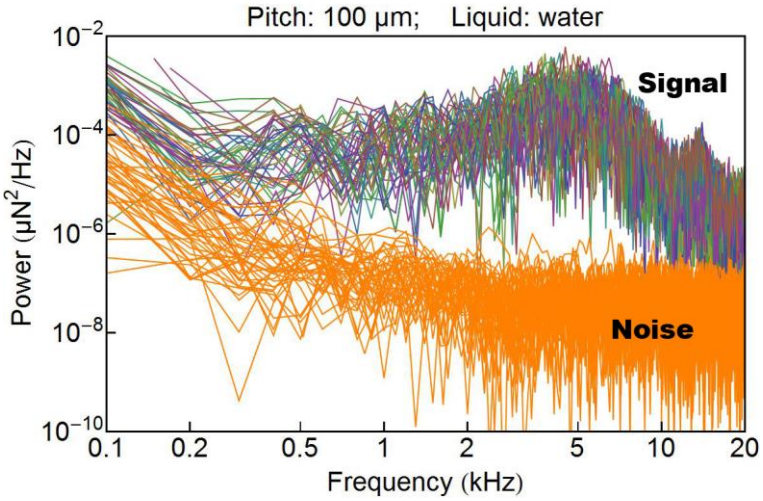

Fig. 4.57 Frequency spectra of the normal force and noise during the sliding of water droplets with different volumes on the micropillar array of 100 µm-pitch. Each line in the graph represents the spectrum for one droplet.

resonant frequency of the liquid leg and the pitch of the micropillar as followed:

$$f \approx \sqrt{\frac{\gamma}{wp^2 \ln\frac{2p}{w}}} \qquad (4.15)$$

which indicates that the frequency of the vibration reduces as the pitch of the increases. This relationship between the vibration frequency and the pitch of the micropillar array will be verified later in this section. **Eq (4.15)** also predicts that the frequency of the sliding-induced vibration of the droplets does not depend on the droplet volume nor the sliding velocity of the droplet; which agrees with previously mentioned results (**Fig. 4.50**, **Fig. 4.51** and **Fig. 4.53**).

A further analysis on the effect of the droplet volume is presented in **Fig. 4.57**. The graph shows the frequency spectra for all tested water droplets having volumes ranging from 2 to 40 µL sliding on the 100 µm-pitch micropillar array. The result demonstrates that the spectra for all the droplet have the similar shape, thus, we can derive the "average spectrum" from those of droplets with different volume for the same liquid type and micropillar array. The results for other liquid samples and micropillar arrays are shown in **Fig. A. 18** to **Fig. A. 22** of **Appendix 1**.

The calculation of the average spectrums is described as followed:

- For each individual experiment, for example, a droplet of volume $\boldsymbol{V_i}$ of the liquid type $\boldsymbol{j}$, sliding on the micropillar array with the pitch $\boldsymbol{p_k}$, an interpolation function $\boldsymbol{g_{ijk}}$ (order 1) is obtained from the frequency spectrum of normal force (discrete data).
- For all the droplets of the same liquid type sliding on the same micropillar array, the average

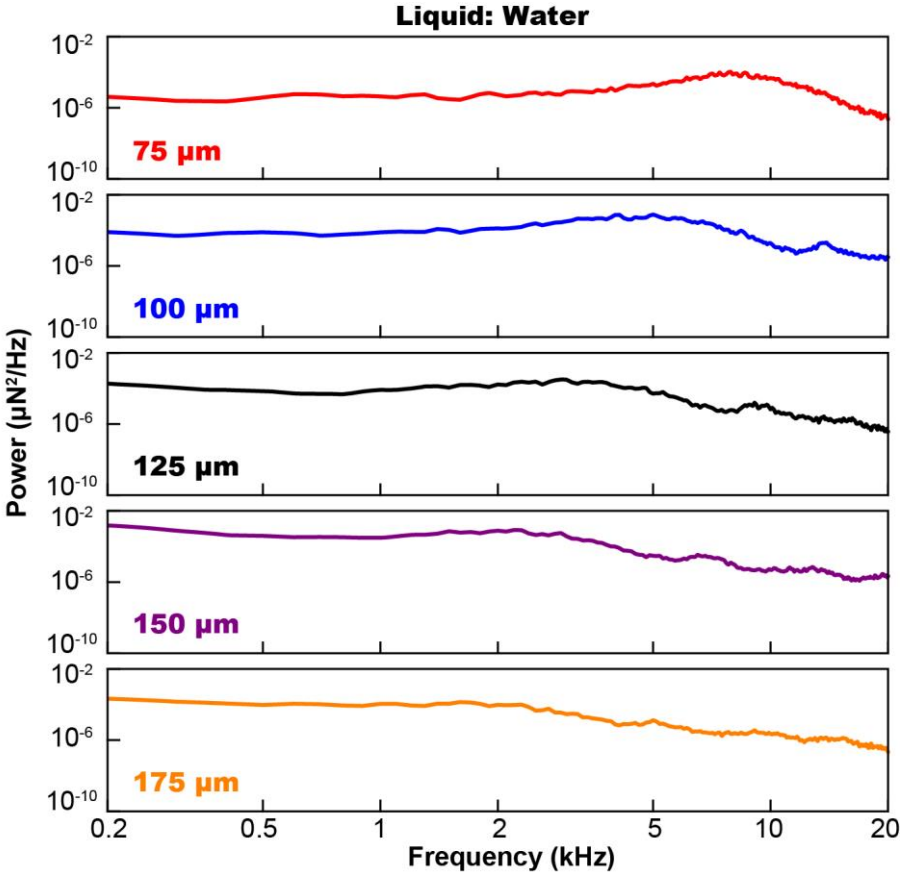

Fig. 4.58 The average spectrum of the normal force during the sliding of the water and G1W1 droplets on the micropillar arrays of different pitches.

spectrum function is g_{jk} obtained as following:

$$g_{jk} \approx \frac{1}{N_{jk}} \sum_{i=1}^{N_{jk}} g_{ijk} \tag{4.16}$$

where N_{jk} is the number of the droplets of liquid type j, tested on the micropillar array with the pitch p_k.

Effect of the micropillar array pitch on the frequency of the vibration

Fig. 4.58 shows the average spectra of the normal force in cases of, for example, water droplets sliding on the micropillar arrays. From the results, it is shown that as the pitch of the micropillar array increases, the frequency spectrum of the normal force shift toward the low frequency region. In other words, the frequency of the fluctuation in the normal force of the sensor decreases as the pitch of the micropillar increases which agrees with tendency described by the **Eq. (4.15**). Each spectrum is not sharp but exhibits large amplitude over a range of frequency. Because during the sliding of the droplets, at the receding edge,

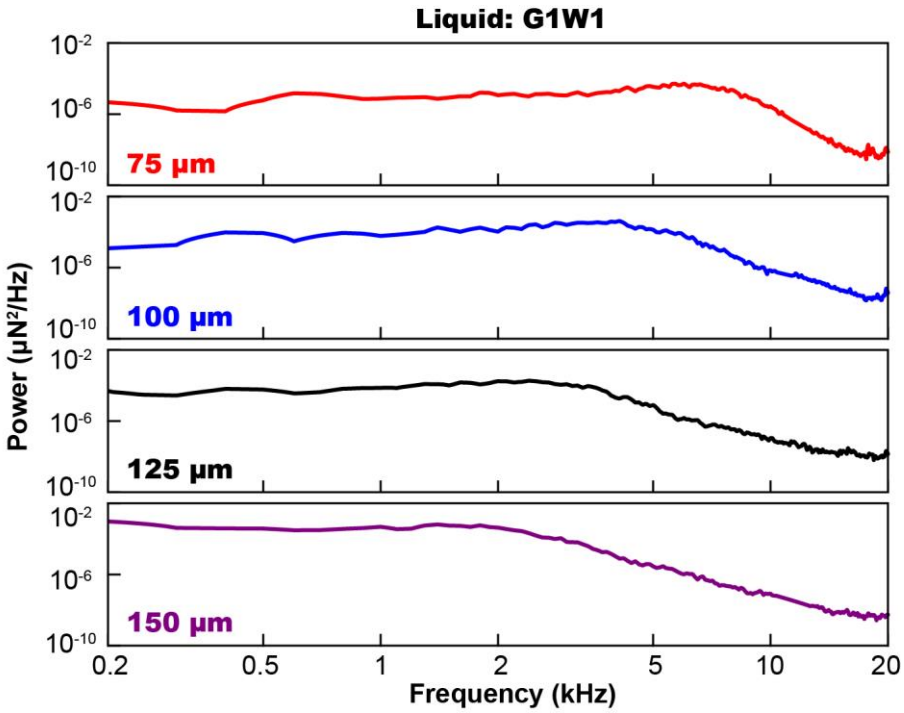

Fig. 4.59 The average spectrum of the normal force during the sliding of the G1W1 droplets on the micropillar arrays of different pitches.

the liquid does not detach from one by one micropillar but simultaneously from multiple micropillars. The vibrations caused by the detachments of the liquid from multiple micropillars interact resulting in a band of the frequency over which the large amplitude of the vibration is found. Nevertheless, the effect of the pitch of the micropillar array was clearly observed in the shift of spectrum. For other liquid types, the similar relationship between the pitch of the micropillar array and the spectrum of the vibration are obtained as shown in **Fig. 4.59** for the case of G1W1.

Effect of the liquid viscosity on the frequency of the vibration

Fig. 4.60 shows the average spectra of the normal forces during the sliding of droplets of different liquid types on the same micropillar arrays which have the pitches of 75, 100 and 125 µm, respectively. The result also indicates that there is a shift in the frequency and the amplitude of the vibration toward lower frequency region as the viscosity of the liquid increases. Moreover, the vibration amplitude significantly reduced as the viscosity of the droplet increases, which implies the damping effect of the viscosity on the vibration. As shown previously in **Fig. 4.55**, the vibration of the droplets during the sliding is caused by the detachment of the liquid legs from the micropillars at the receding edge of the droplets. The detachment of the liquid legs releases the stored elastic energy that will then propagate as surface wave causing the vibration of the entire droplet. In the propagation of the vibration, viscosity plays the role damping: the higher the viscosity is, the lower the vibration amplitude is. This explains why the amplitude of the normal

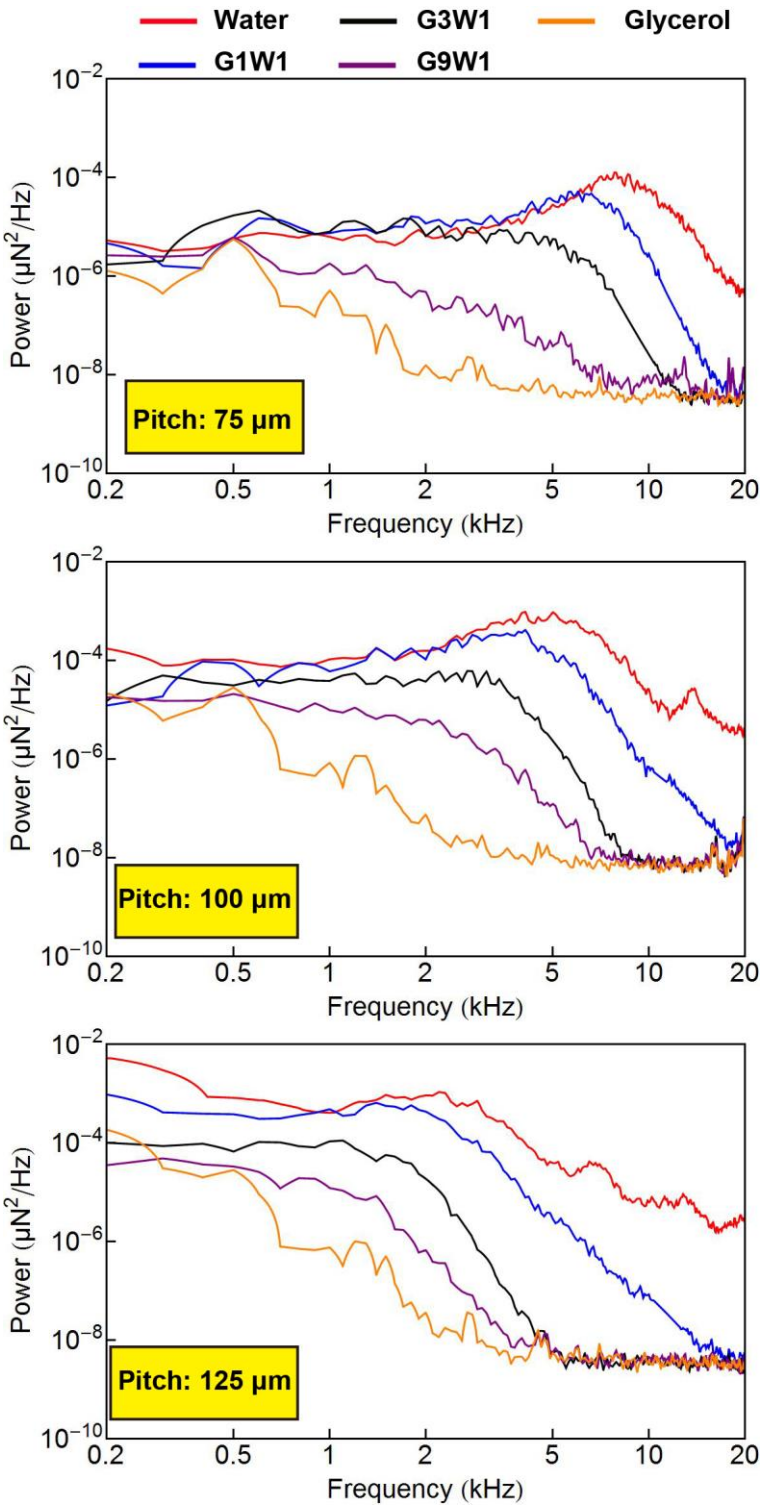

Fig. 4.60 The average spectrum of the normal force during the sliding of droplets of different liquid types on the 75 μm-pitch micropillar array.

force decreases as the viscosity of the liquid increases.

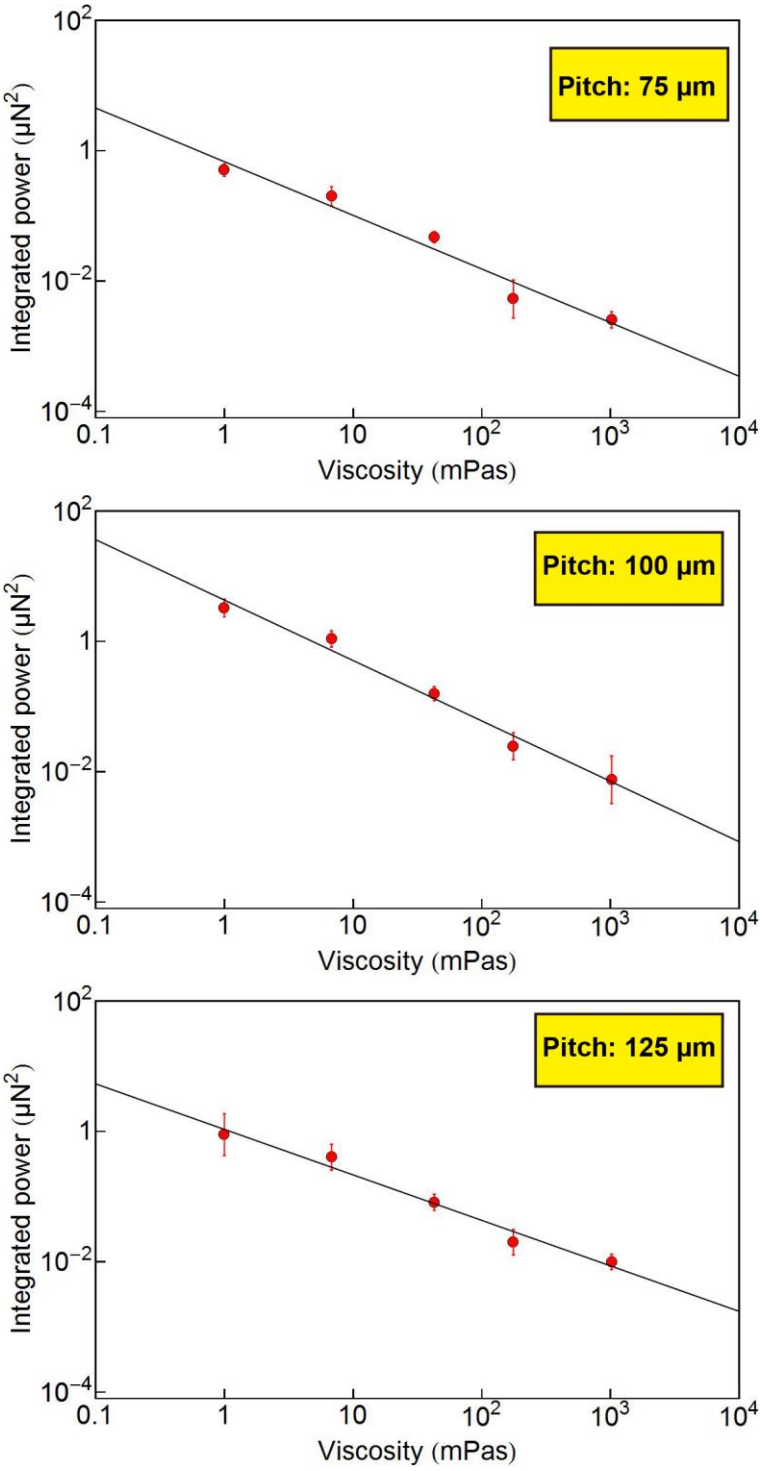

Fig. 4.61 Relationship between the liquid viscosity and the integrated power of the normal force spectrum.

We can further quantitatively investigate the effect of liquid viscosity from the aspect of vibration energy. Since the frequency spectrum obtained by Fourier transform also presents the power density of the

vibration, integration of this spectrum presents the energy of the vibration. **Fig. 4.61** shows the relationship between the liquid viscosity and the integrated power obtained from the DFT spectra. Each graph shows the result for different liquid types and the same micropillar array. It is clear that as the viscosity of the liquid increases, the integrated power decreases, indicating that the decrease in the vibration energy. The results also demonstrate the possibility of estimating liquid viscosity from the output of the sensor during the sliding of the droplets.

Chapter 5 Experiments on droplet vibration

This chapter reports on measurement of the interaction forces in normal direction during the virbation of liquid droplets on the fabricated cantilever array. First, the experimental setup and preparation are described. Then, the results on the normal force distribution during the vibration of a water droplet is reported. Next, the relationship between liquid viscosity and the decay rate of the vibration is discussed and the ability of the proposed cantilever array to measure the viscosity of small droplet is demonstrated. Finally, the tapping induced vibration of the droplets are investigated.

5.1 Experimental setup and liquid sample preparation

Experimental setup

The experimental setup to investigate the vibration of liquid droplet on the fabricated cantilever array is shown in **Fig. 5.1**. The fabricated sensor array was first attached to the piezo-stage which was used in the calibration of the sensors. Droplets were then deposited onto the cantilever array using a glass-tube connected to a syringe. A function generator was used to apply a sine wave voltage to the piezo-stage to induce a periodical displacement of the piezo-stage in vertical direction. The frequency of the voltage and thus, the frequency of the piezo-stage vibration were controlled by the function generator.

Similarly to the experiments on droplet sliding, the resistance changes of the cantilever array were measured by Wheatstone bridge circuits and a scopecoder at the sampling rate of 2 kSps. Moreover, the motion of the droplet was captured by the high speed camera at 2 kfps.

Liquid sample preparation

The liquid samples using in the experiment on droplet vibration were water and water-glycerol solutions with mixture ratios varying in the range of glycerol 17% to glycerol 75%. The viscosity of the liquid samples was measured using the EMS viscometer as described in **Section 4.1**. The measured viscosity of all liquid samples are given in **Table 5.1**.

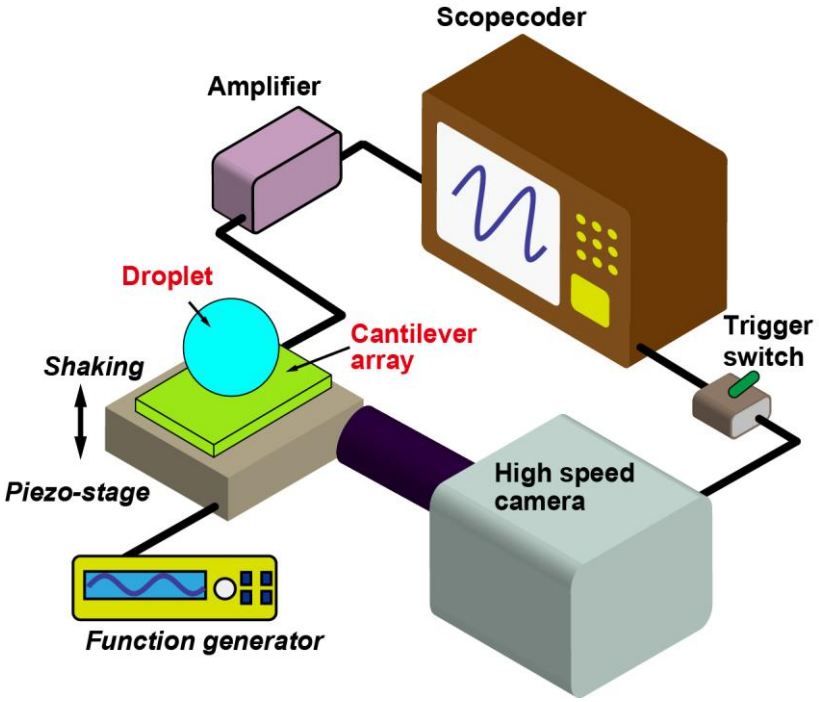

Fig. 5.1 Experimental setup to investigate the vibration of droplets. Copyright 2015 IEEE.

Table 5.1 Measured viscosity of the liquid samples at 23°C.

Water - glycerol solution	Viscosity (mPa·s)
Water	0.97
Glycerol 17%	1.9
Glycerol 25%	2.4
Glycerol 33%	3.0
Glycerol 50%	6.8
Glycerol 75%	42.7

5.2 Experimental results

Normal force distribution along the contact diameter of a droplet during vibration

The normal distribution during the vibration of a water droplet was measured the cantilever array. A water droplet was deposited on the cantilever array so that the base diameter of the droplet was supported by exact thirteen fabricated sensor. The position of the droplet was adjusted manually by dragging the droplet using the glass tube.

As shown in **Fig. 5.2**, there were thirteen pillar under the base diameter of the droplet. Moreover, as shown later, when the droplet vibrated, all the resistance of the cantilever changed; therefore, we can be sure that the droplet base diameter was supported by exact thirteen micropillars of the cantilever array. The

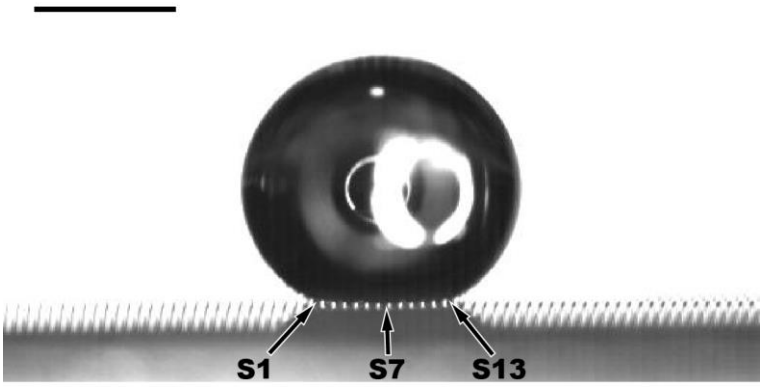

Fig. 5.2 A snap shot of the high speed camera showing the droplet on the cantilever array. There were exact 13 cantilevers underneath the base diameter of the droplet. Scale bar is 1 mm.

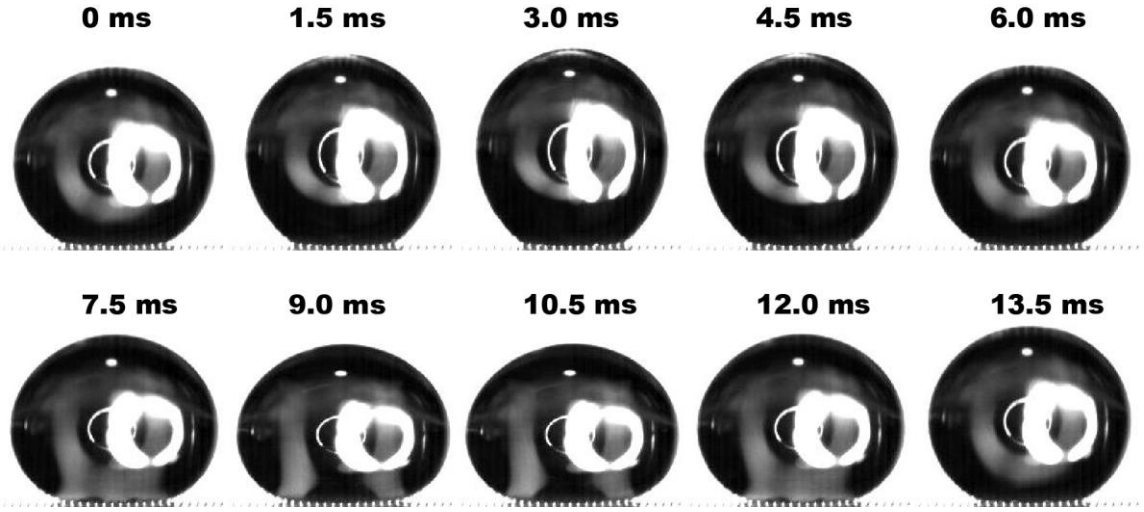

Fig. 5.3 Snapshots of the high speed camera showing the vibration of the droplet

cantilevers are marked as S1 to S13 as shown in **Fig. 5.2**.

First, the resonant frequency of the droplet was obtained by manually sweeping the frequency of the piezo-stage while monitoring the output of the cantilever. In this case the resonant frequency of the droplet was found to be 75.7 Hz, which is corresponding to the 2^{nd} mode of the droplet oscillation. The motion of the droplet when vibrating at 75.7 Hz is shown in **Fig. 5.3**. It is confirmed that the droplet vibrated in the mode $n = 2$ (Eq. **(**2.14)) with mainly the motion in vertical direction. Notice that the time in each snapshot was relative with the time of the first snapshot $\boldsymbol{t} = 0$ ms.

The normal change at cantilever S1 in response to the vibration of the piezo-stage is shown in **Fig. 5.4**. The vibration amplitude of the piezo-stage was approximately 2 μm. As we can see from the results, when the vibration of the piezo-stage started, the normal force at S1 also gradually increased its vibration amplitude and became stable approximately 1 second after the beginning of the vibration. The zoom view

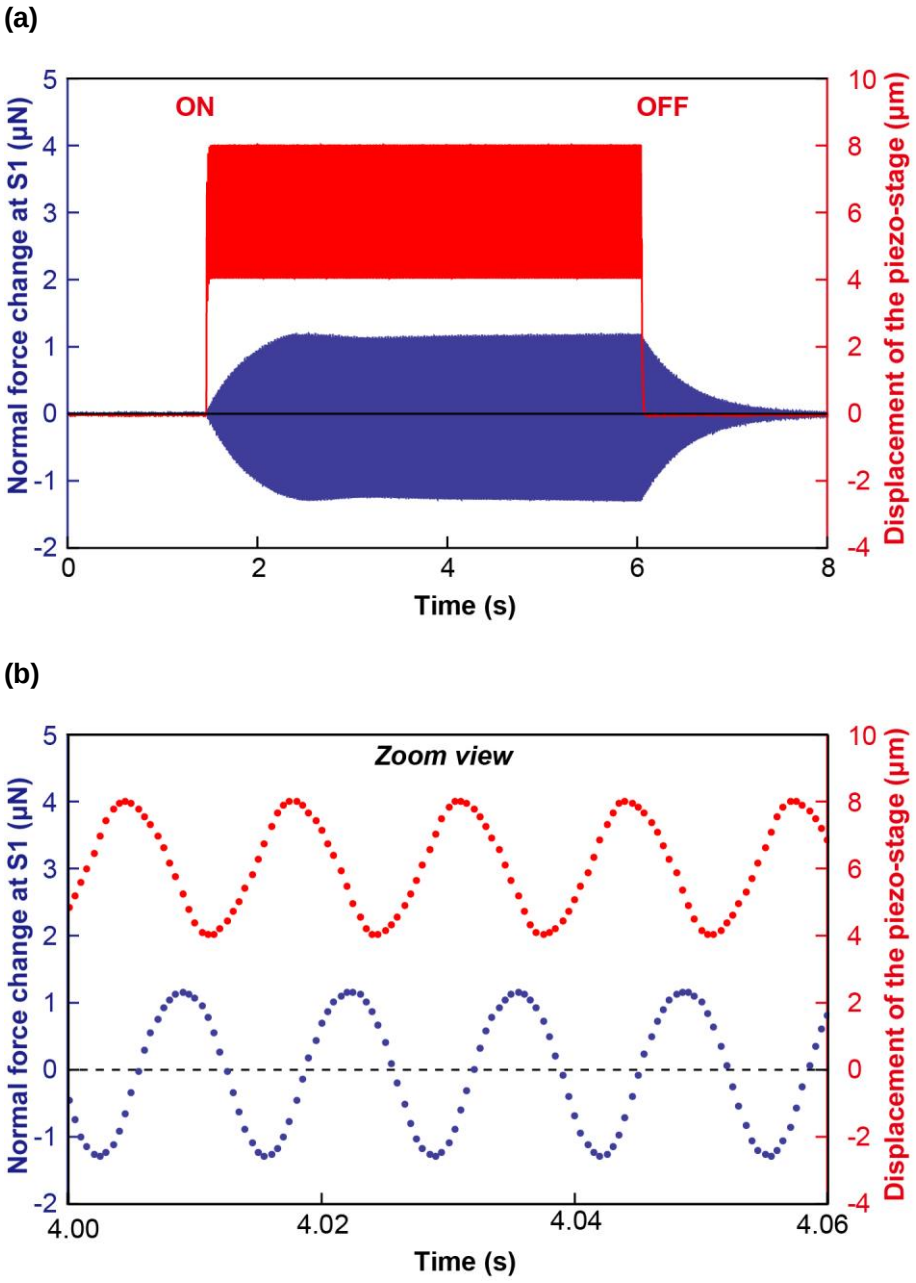

Fig. 5.4 Normal force change at the position of cantilever S1 in response to vibration of the piezo-stage.

of the vibrations in **Fig. 5.4 (b)** shows that the normal force at S1 also changed periodically at the same frequency of the piezo-stage vibration. A slight delay can be found between the vibration of the piezo-stage and the change of the normal force at S1.

When the piezo-stage is turned off, the amplitude of the normal force change at S1 slowly decreased and became almost zero after 2 seconds. The delay in responses and slowly decay of normal is thought to be caused by the low viscosity of the water droplet.

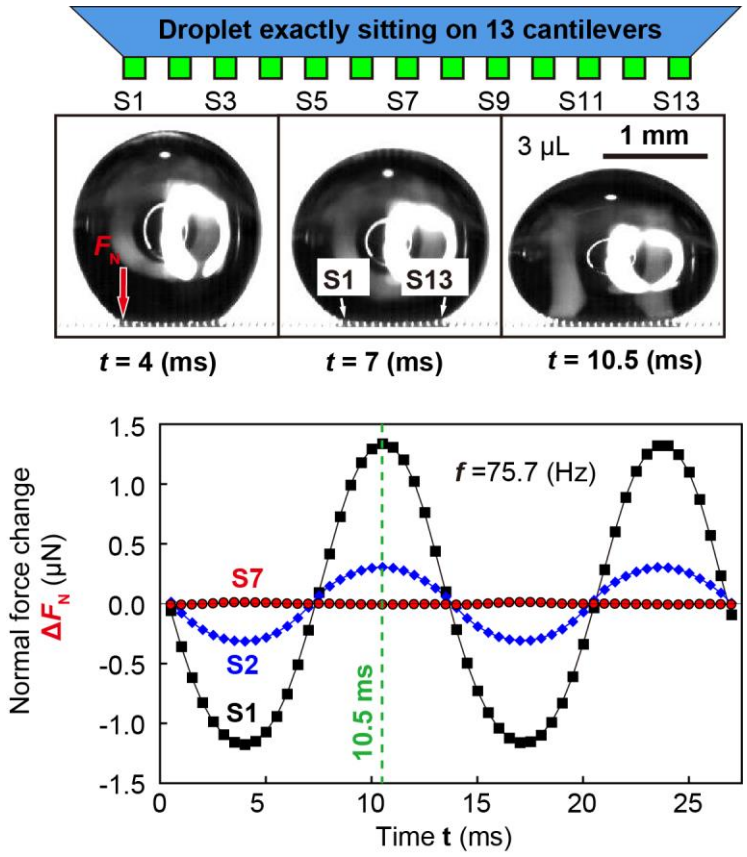

Fig. 5.5 Normal force change at sensor S1, S2 and S7 during two periods of the vibration.

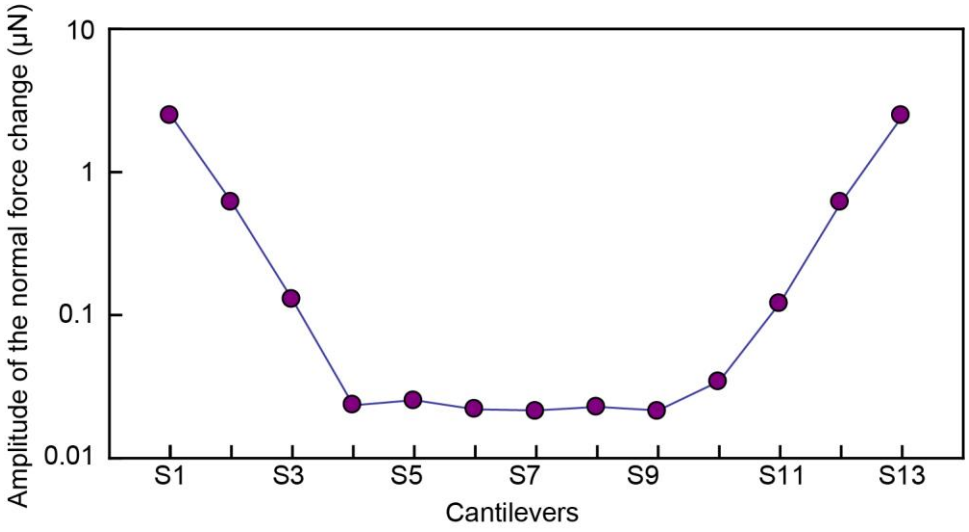

Fig. 5.6 The amplitude of the normal force change at each sensor.

The normal force changes at cantilevers S1, S2 and S7 are shown in **Fig. 5.5**. Here the positive direction of the normal is defined to be the same direction of gravity, which means that when the normal force is positive, the sensor is pushed downward and vice versa. The normal force changes and the synchronized

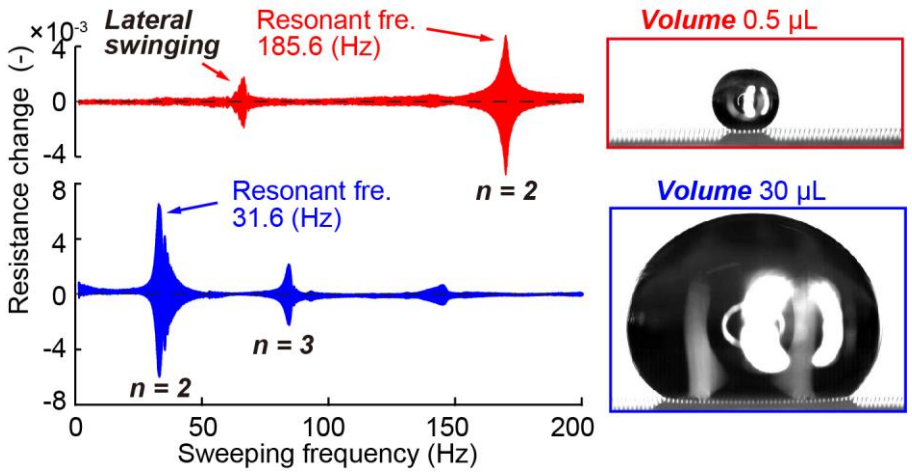

Fig. 5.7 Resonant frequency of 0.5 µL and 30 µL water droplets.

images shows that, when the droplet move upward or downward, the micropillar close to the edge of the contact area were also pulled upward or downward, respectively. Moreover, the amplitude of the normal force change at all cantilevers were not the same but depends on the location of the cantilever.

From the change in normal force at each cantilever, the amplitude (peak to peak) can be easily obtained and is shown in **Fig. 5.6**. It is clear that, the normal force change is largest at the edge of the droplet contact area (S1 and S13) and decreases as getting closer to the center of the contact area (S7). In fact, the amplitude of the normal force change at S1 was approximately 117 times larger than that at S7. This result suggests that for the measurement of the droplet vibration using cantilevers, the optimized location of the sensor should be on the periphery of the contact area between the droplet and the substrate.

Effect of the droplet volume on the vibration frequency

The resonant frequency of water droplets with different volume was investigated by sweeping the frequency of the piezo-stage vibration. By measuring the resistance change of a cantilever at the edge of the contact area (at which the normal force is largest as proven above), it is possible to detect the resonant frequency of the droplet. **Fig. 5.7** shows the result for water droplets with volume of 0.5 µL and 30 µL. The frequency was swept in the range of 1 to 200 Hz. It is shown that the droplets exhibit multiple resonant modes which has been shown in previous research. At the second mode of the vibration related to the vibration of the droplet in vertical direction, the output of the cantilever was largest.

The relationship between the droplet volume and the resonant frequency at mode n = 2 () of the droplet is shown in **Fig. 5.8**. The result confirms that as the volume of the droplet increases, the frequency of the vibration decreases. The resonant frequencies at mode n = 2 of 0.5 µL and 30 µL water droplets were 31.6 and 185.6 Hz, respectively. Moreover, by fitting the data with the function $\boldsymbol{f = aV^b}$, where $\boldsymbol{f}$ is frequency

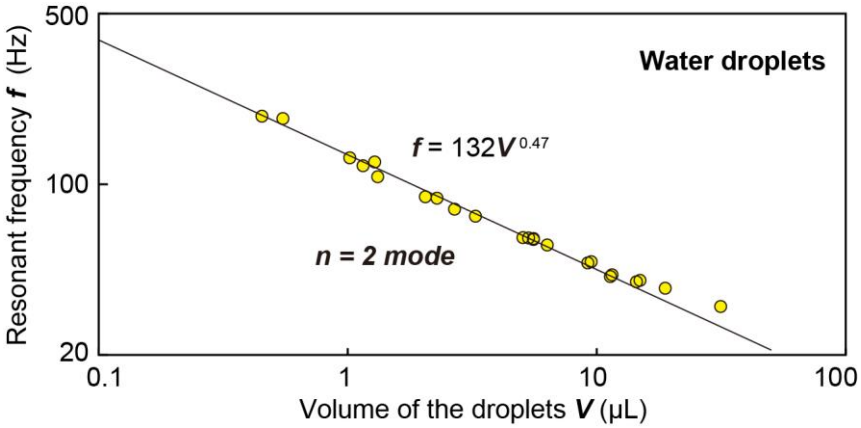

Fig. 5.8 Resonant frequency of 0.5 μL and 30 μL water droplets.

and V is droplet volume, we obtain: $f = 132\ V^{-0.47}$, which indicates that the frequency is inversely proportional to the square root of the volume. This result is in good agreement with the theoretical estimation (theoretical slope -0.5) provided in Eq. **(**2.14) in Chapter **2**.

Effect of the liquid viscosity on the vibration decay and its application in viscosity measurement

As shown in **Fig. 5.4 (a),** a water droplet slowly attenuated after the piezo-stage was turned off. The relationship between the liquid viscosity and the attenuation rate of the droplet vibration was investigated using liquid samples shown in Table 5.1. In the experiment, the volume of droplets were all 3 μL. For each droplet, the droplet was vibrated at the mode n = 2 resonant frequency obtained beforehand by sweeping the frequency of the piezo-stage as shown previously. Then the piezo-stage was turned off to let the vibration of the droplet attenuate. The output of the cantilever on the periphery of the contact area was used because it has largest output among the cantilever array.

The results for water (viscosity 1 mPa·s) and glycerol 33% solution (viscosity 3 mPa·s) droplets are shown in **Fig. 5.9**. It is clear that vibration of more viscous droplet attenuates faster due to the viscosity induced damping. To quantitatively clarify the relationship between the liquid viscosity and the attenuation of the droplet vibration, the attenuation rate β (-) of each droplet vibration was obtained by fitting the decay of the cantilever output with a function $y = \alpha E^{-\beta t}$ where t (s) is time.

The relationship between liquid viscosity and the attenuation rate β (-) is shown in **Fig. 5.10**. The result shows that the attenuation rate of a droplet increases almost linearly with the increase of the liquid viscosity. Therefore, by measuring the attenuation rate of the cantilever output, it is possible to estimate the viscosity of a droplet. This method to measure the liquid viscosity benefits an advantage of small volume required of liquid sample (in the experiment, 3 μL droplets were demonstrated), which is highly desirable in point-of-care testing and droplet-based sensing. In point-of-care sensing, only limited amount liquid sample is available. Moreover, in droplet-based sensing, it is advantageous when using small droplet to utilize the effect of surface area over the droplet volume.

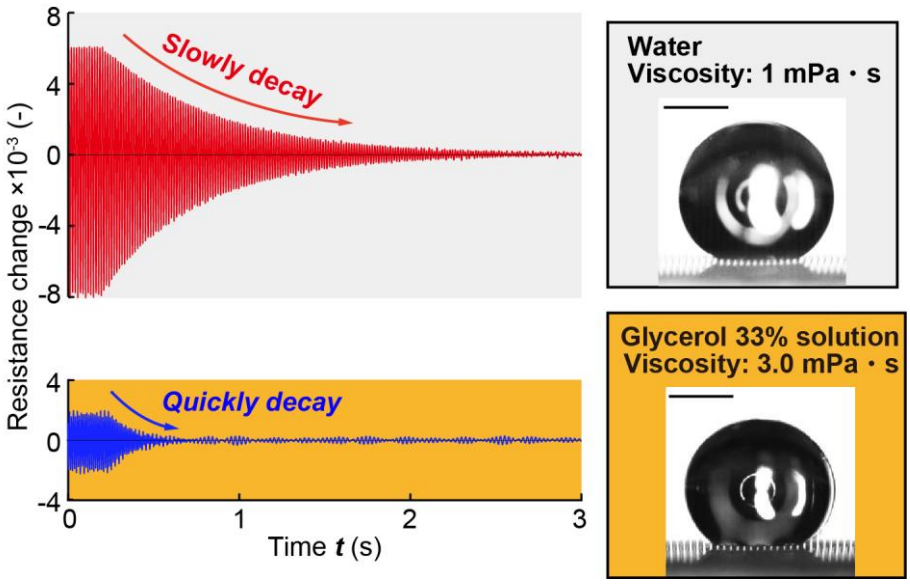

Fig. 5.9 Attenuation of the droplet vibration after the vibration of the piezo-stage was turned off for droplets of water and glycerol 33% solution. Scale bar is 1 mm. Copyright 2015 IEEE.

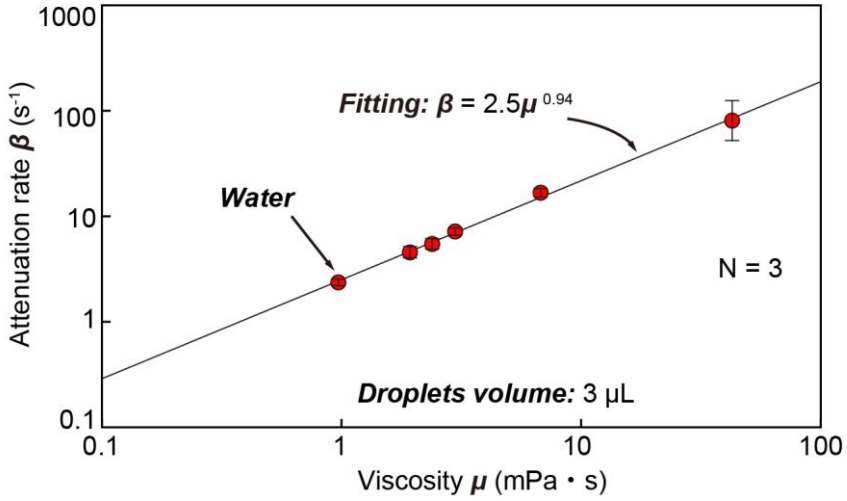

Fig. 5.10 Relationship between liquid viscosity and the attenuation rate of the droplet vibration after the vibration of the piezo-stage was turned off. Copyright 2015 IEEE.

Therefore, the viscosity measurement method based on the droplet vibration proposed in this study is expected to be useful in point-of-care testing and droplet-based sensing.

Effect of the droplet volume on the decay rate of the vibration

As one can notices from **Eq. (2.16)**, theoretically, beside viscosity, the volume of the droplet is also a factor

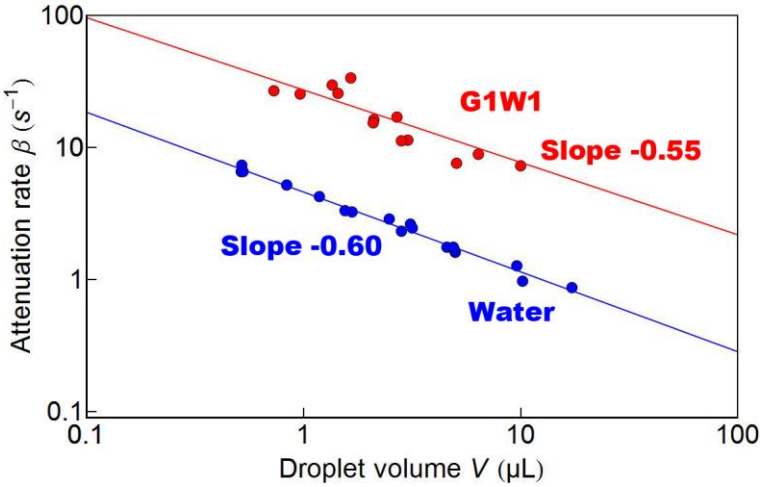

Fig. 5.11 Relationship between the droplet volume and the attenuation rate of the droplet vibration.

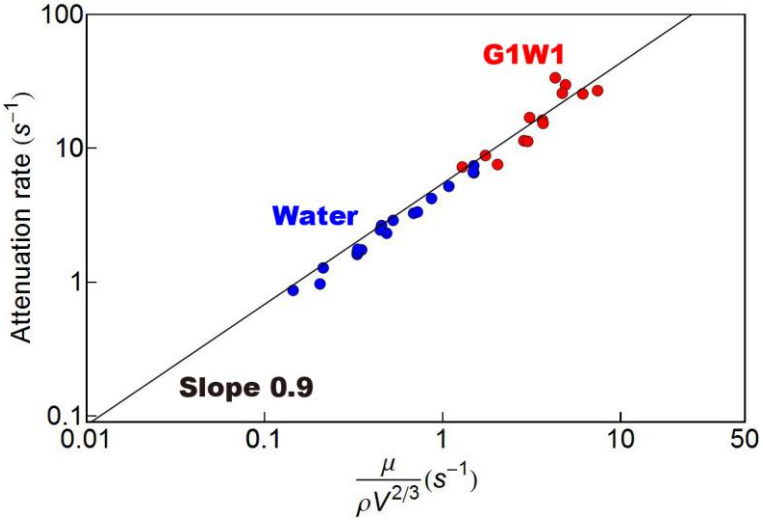

Fig. 5.12 Relationship between the droplet volume and the attenuation rate of the droplet vibration.

that determines the damping of the droplet free vibration. To confirm this relationship, water and G1W1 (glycerol/water 50% solution) droplets with different volume were tested. The relationship between the droplet volume and the attenuation rate of the vibration is shown in **Fig. 5.11**. The results show that when the volume of the droplet increases, the attenuation rate of the vibration decreases, agreeing with **Eq. (2.16)**. By fitting the data, we obtain the slopes for water and G1W1 to be -0.6 and -0.55, respectively, which are in the order with theoretical value (-0.67) obtained from **Eq. (2.16)**. Moreover, the results also indicate that the attenuation rate of the vibration of a water droplet is smaller than that of a G1W1 droplet having the same volume. However, if we combine all the factors: viscosity, density and volume as shown in **Eq. (2.16)**, a relationship between this combination and the attenuation rate is obtained as shown in **Fig. 5.12**. Despite of the difference in viscosity, results for both water and G1W1 show a good agreement with theoretical

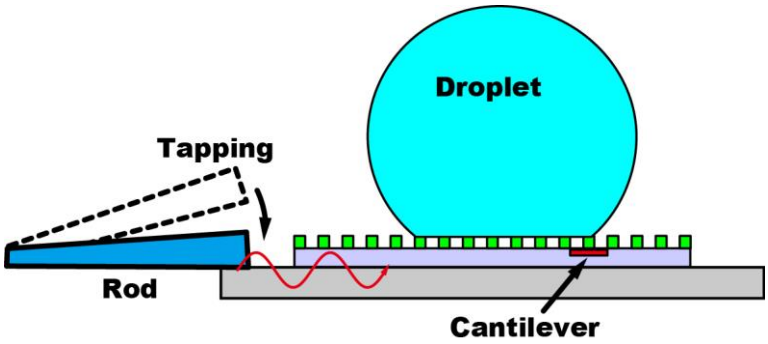

Fig. 5.13 Conceptual sketch of the experimental setup to investigate tapping induced vibration of the droplets.

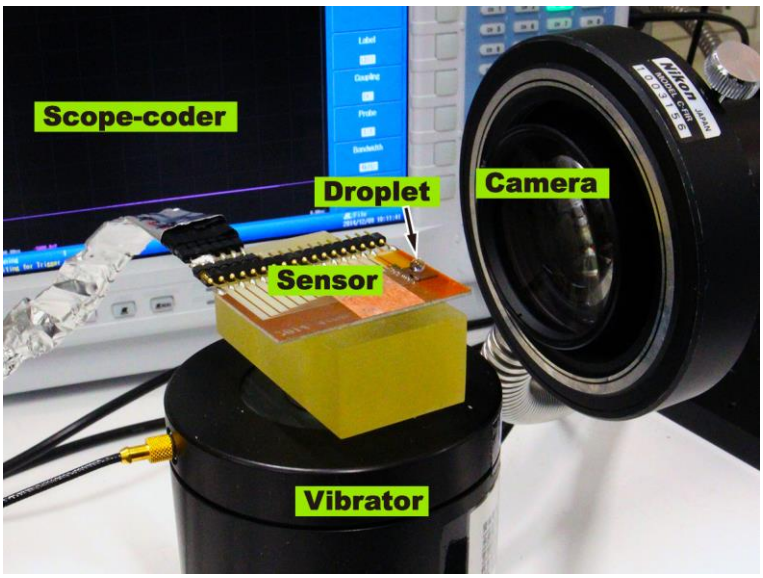

Fig. 5.14 A photograph of the experiment to investigate the tapping induced vibration of the droplet.

prediction. The slope of the fitting line is 0.92 which is also close to theoretical value 1.

In summary, it has been experimentally demonstrated that the attenuation rate of the droplet vibration is affected by the viscosity and droplet volume. Nevertheless, for a droplet with known volume, the viscosity of the liquid can be estimated from the attenuation rate of the cantilever output.

Tapping induced vibration of the droplet

In the previous experiments, the vibration of the droplet was induced by shaking the substrate using a piezo-stage which allows us to obtain the vibration at a single frequency. In this section, the tapping induced vibration of the droplet as shown in **Fig. 5.13** is investigated. By gently tapping the substrate, the

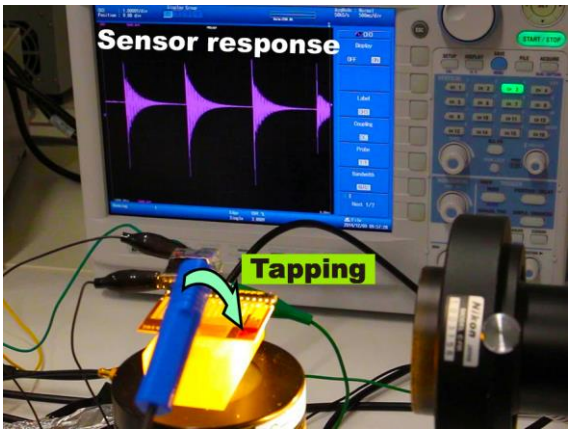

Fig. 5.15 A photograph showing the real time measured signal of the cantilever for each tapping.

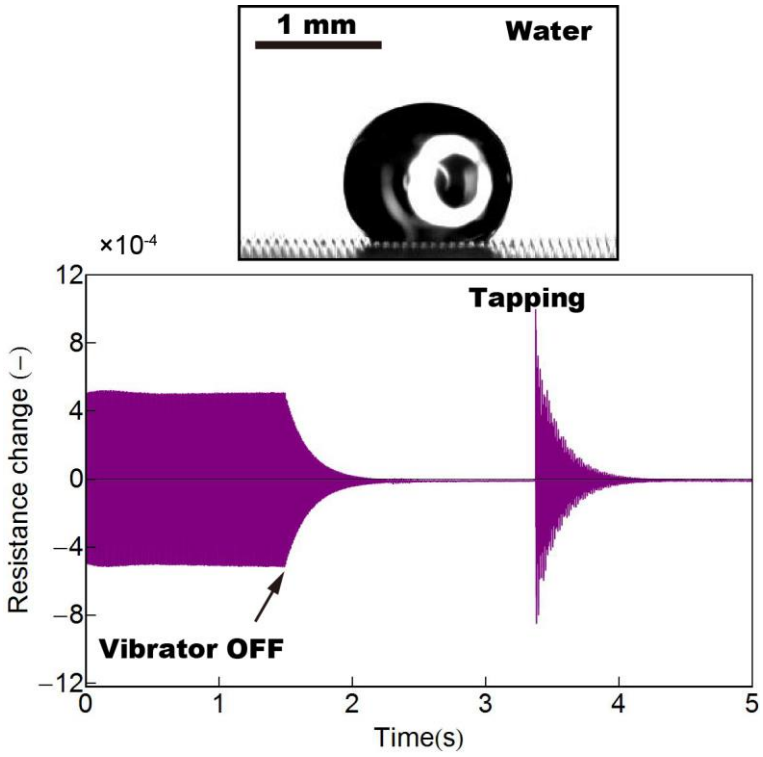

Fig. 5.16 Responses of the cantilever when tapping and when shaking the substrate by the vibrator.

vibration wave resulted from the tapping will propagate through the substrate to the droplet which in turn will absorb this propagated energy and vibrate. The experimental setup used to investigate this tapping induced vibration of the droplet is shown in **Fig. 5.14** and **Fig. 5.15**. The cantilever at the edge of the droplet was used to measure the signal since it has largest response as mentioned previously. Moreover, the resonant vibration of the droplet was also measured in comparison by shaking the substrate using a vibrator (Brüel & Kjær, Mini-shaker Type 4810) as has been done in previous experiment. **Fig. 5.16** shows the responses of the cantilever when tapping the substrate and when shaking the substrate by the vibrator in the

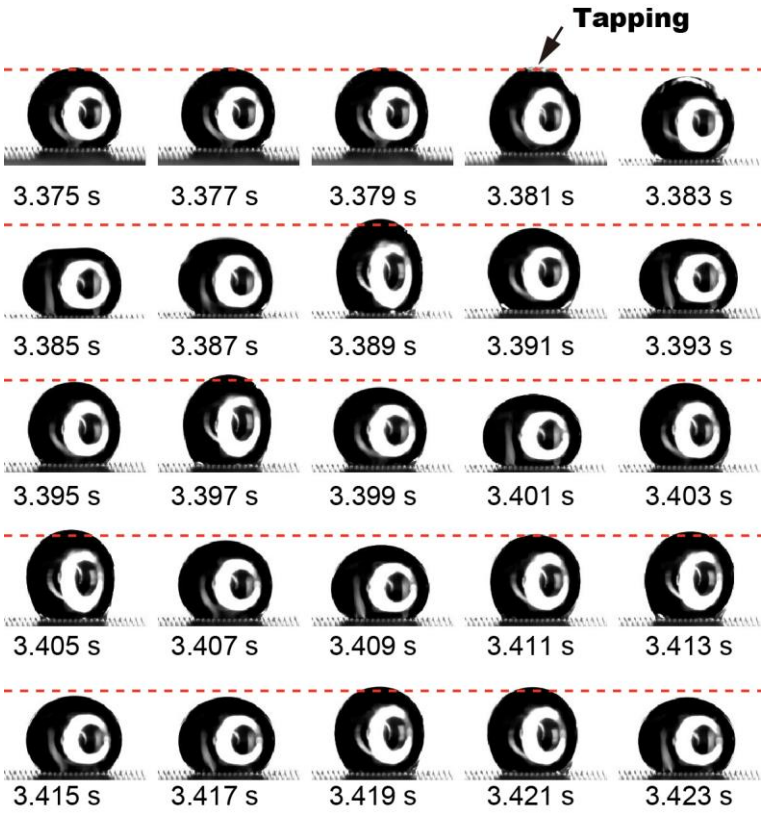

Fig. 5.17 Snapshots of the high speed camera showing the motion of the droplet when tapping is induced.

case of a 1.1 μL water droplet. The frequency of the vibrator was 131 Hz, which was the n = 2 mode resonance frequency of the droplet.

It can be confirmed from the graph that both tapping and shaking by the vibrator can induce the vibration of the droplet. The tapping induced vibration immediately decays just after the tapping. Snapshots of the high speed camera showing the motion of the droplet when tapping the substrate are presented in **Fig. 5.17**. The red dashed lines show the initial position of the droplet apex. At around t = 3.381 s, the substrate was tapped and the droplet started to vibrate. Agreeing with the sensor output shown in **Fig. 5.16**, the vibration of the droplet gradually decayed just after the tapping.

Next, let us compare the attenuation rate of the tapping induced vibration and the forced vibration by shaking the substrate using the vibrator (hereafter, is called “forced vibration”). The decays of the two vibrations are shown in **Fig. 5.18**. Here the outputs of the cantilever were first normalized and then matched the original time when the vibrations started to decay. The result demonstrates that, the frequency and the attenuation rate of both signal were approximately the same. The sensor output for the tapping induced vibration shows a fluctuation from that for the forced vibration applied by the vibrator. This result indicates that the tapping induced vibration of the droplet includes not only n = 2, but also other modes of the droplet resonant vibration.

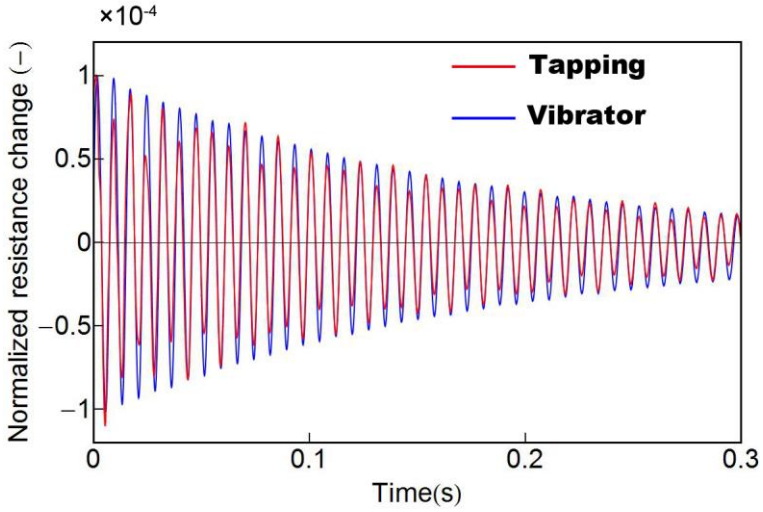

Fig. 5.18 Decay of the tapping induced vibration and the forced vibration by shaking the substrate using the vibrator.

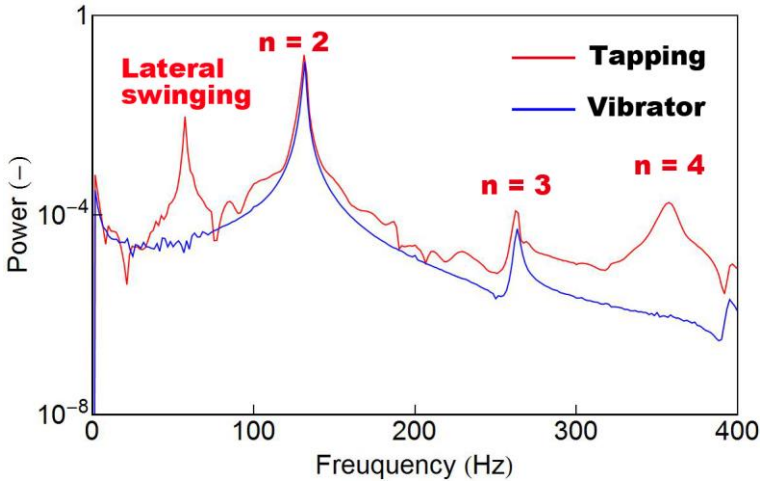

Fig. 5.19 Frequency spectrum of the tapping induced vibration and the forced vibration of the droplet.

The frequency spectrum of the two vibration shown in **Fig. 5.18** are shown in **Fig. 5.19**. The frequency of forced vibration is relatively sharp with only one peak at $n = 2$ frequency. On the other hand, the frequency spectrum of the tapping induced vibration consists of several peaks corresponding to multiple modes of the vibration. Beside $n = 2$ mode, the $n = 3$, 4 modes and lateral swinging can be found in the frequency spectrum of the tapping induced droplet vibration.

However, as shown in **Fig. 5.18**, the vibration at frequency of $n = 2$ resonant mode is dominant even in the tapping induced vibration of the droplet. Therefore, we observed the similar attenuation rates of the tapping induced vibration and forced vibration. This result implies that, in actual applications such as viscosity measurement based on droplet vibration, the external vibrator may not needed to induce the droplet

vibration. Instead, the vibration of the droplet can be simply induced by tapping the substrate and thus, the sensing system can be easily made simple and portable.

The experimental results for a G1W1 droplet are shown in **Appendix 1**.

Chapter 6 Conclusion

In this study, MEMS based force sensors were proposed to measure the interaction force distribution on the contact area during the sliding and vibration of liquid droplets on a solid substrate. The proposed MEMS based sensors were shown to have many advantages such as miniaturized size, high sensitivity, high time resolution, by which, the dynamic interaction forces between a single microstructure of the substrate and the droplet could be directly measured. This study has provided a quantitative clarification of the liquid-solid interaction force distribution on the contact area of a droplet during the sliding and vibration, which could not be obtained by the conventional methods based on observation. It was shown that, the measured interaction forces on the contact area can provide the information related to the dynamical behaviors of the droplet as well as the liquid properties and surface roughness of the substrate. Most importantly, the proposed sensors were able detect the delicate vibration of the droplet during the sliding on a textured surface. From the frequency and magnitude of this sliding induced vibration, information on the surface roughness and liquid viscosity could be obtained. Moreover, the proposed sensor were also able to measure the resonant vibration of droplets, from which the liquid viscosity could be estimated. Therefore, MEMS based force sensors in this study are useful tools not only for the studying the dynamical behavior of droplets but also for the liquid evaluation and sensing applications.

In details, the following results are obtained in this study:

Interaction forces during the sliding of a droplet

Normal and shear forces acting on a micropillar during the sliding of the droplets in the first several millimeters of sliding distance were measured, from which the distribution of these forces along the contact area of the droplets were obtained. It is experimentally shown that the micropillar is pulled upward when contacting with both advancing and receding edges of the contact area which is caused the vertical component of the surface tension. Inside the contact area, the micropillar is pushed down by the liquid pressure. For the interaction in shear direction, the micropillar is pulled backward and forward when contacting with the advancing and receding edges of the contact area, respectively. The forces at the

receding edge are larger than those at the advancing edge due to the difference in contact angle of the droplet at these edges. Inside the contact area, the shear force is small indicating that for the first several millimeters of sliding distance, the frictional force of the droplet is mainly caused by the adhesion of the droplet to substrate at the receding edge.

A comparison between the interaction forces during the sliding of a droplet on a flat surface and those during the sliding of a droplet on a micropillar array is reported. The most significant difference between these two cases is the gradient of the normal force along the contact area found in the case of flat surface. The gradient is suggested to be a result of the large difference in curvature at advancing and receding edge of the droplet caused by the large contact angle hysteresis of a droplet on a flat surface.

Effects of droplet volume, pillar density and liquid viscosity on the interaction forces is investigated. Increasing the volume leads to the reduction of the normal inside the contact area of the droplet due to the decrease of Laplace pressure as the droplet becomes larger. The normal force on a micropillar also increase if the pitch of the micropillar increases. The maximum absolute values of the normal and shear forces at the receding edge of the droplets do not depend on the volume of the droplet, which indicates that interaction between the droplet and a micropillar at the receding edge is determined by the local geometrical parameters such as size and interval of the micropillars. It is also shown that as the pitch of the micropillar array increases, the maximum normal force at the receding edge increases while the maximum shear force does not vary significantly. Viscosity shows a little effect on the value of the average value of the interaction forces since the droplet is still in the limit where surface tension dominates.

Most importantly, using MEMS-based force sensor, it is possible to detect the vibration of the droplet during the sliding on micropillar array. The frequencies of this vibration distribute over a range of several to ten kHz. Droplet volume and sliding velocity do not affect the range of this vibration which suggests that the vibration is caused by the detachment of each liquid leg adhered to a micropillar at the receding of the droplet. This suggestion is supported by the result that the frequency range of the vibration shifts toward lower region if the interval of the micropillar increases. Viscosity also shows an effect to lower the frequency of the vibration due to the damping. From the experimental result, it was shown that the viscosity of the droplet can be estimated by integrating the frequency spectrum of the vibration.

Interaction force distribution during the vibration of droplets

Using an array of piezoresistive cantilevers, the normal force between a vibrating droplet and a micropillar array is studied. It is shown that the normal force between the droplet and a micropillar during vibration greatly depends on the location of the micropillar. Measurement results for a 3 μL water droplet demonstrate that the amplitude of the normal force change at a micropillar on the peripheral of the contact is more than 100 times larger than that at a micropillar close to the center of the contact area. The cantilever array is also used to investigate the frequency and damping factor of the droplet vibration. As one of the

applications, the proposed cantilever array was shown to be able to measure the viscosity of small droplet (3 μL) based on the attenuation rate of the cantilever output.

Finally, a demonstration on the measurement of the tapping induced vibration was provided. In fact, just by tapping the substrate, we could obtain the resonant vibrations of the droplet, which indicates that the actual sensing devices based on droplet vibration can be very simple since an external vibrator might not be needed.

Appendix

Appendix 1 Experimental results

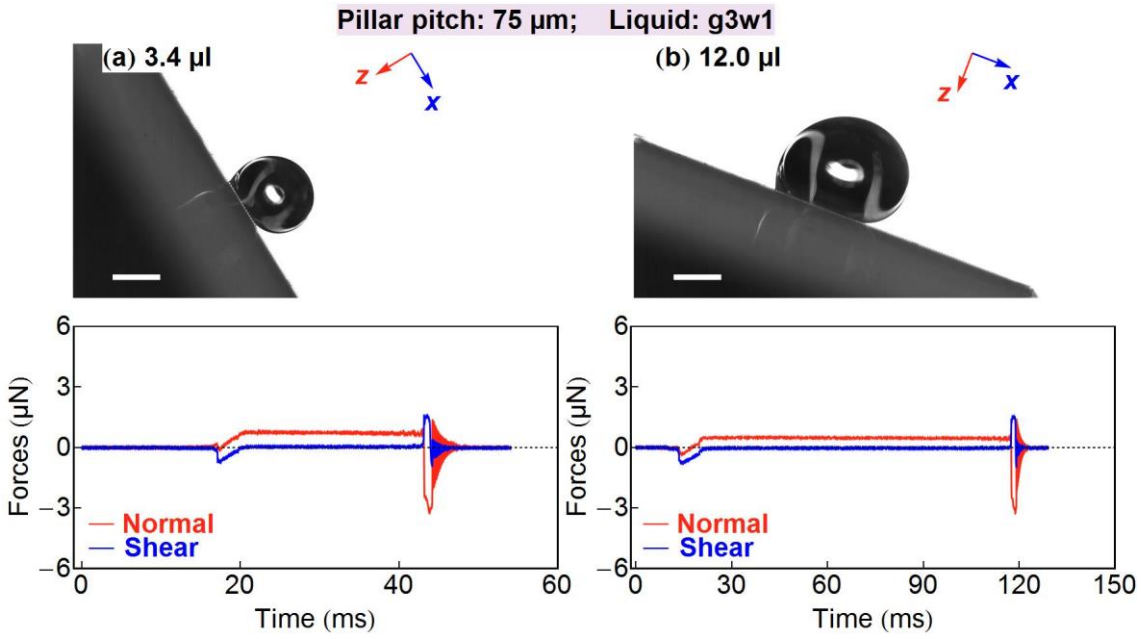

Fig. A. 1 Interaction forces during the sliding of a 3.4 μL G3W1 droplet and 12 μL G3W1 droplet on the sensor with a 75 μm pitch micro pillar array.

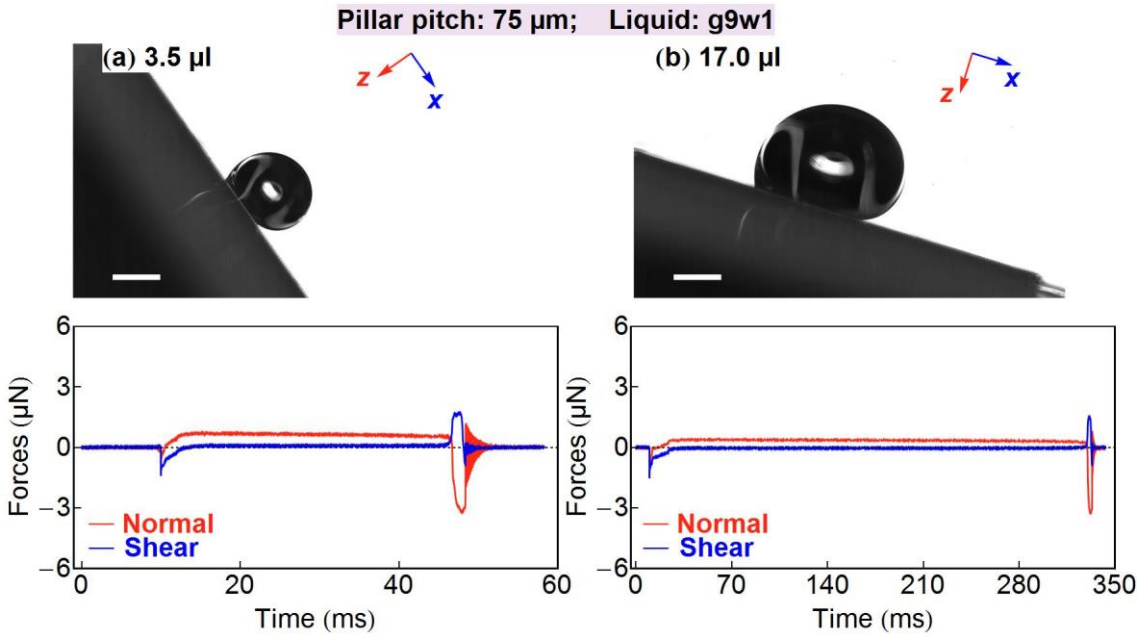

Fig. A. 2 Interaction forces during the sliding of a 3.5 μL G1W1 droplet and 17 μL G1W1 droplet on the sensor with a 75 μm pitch micro pillar array.

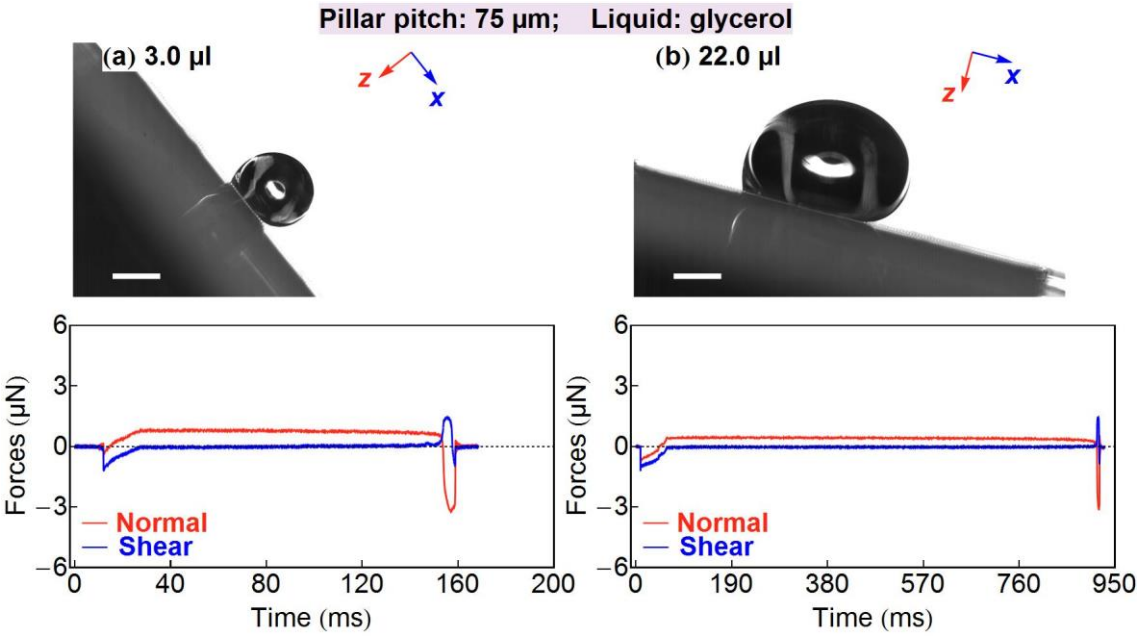

Fig. A. 3 Interaction forces during the sliding of a 3.0 μL glycerol droplet and 22 μL glycerol droplet on the sensor with a 75 μm- pitch micro pillar array.

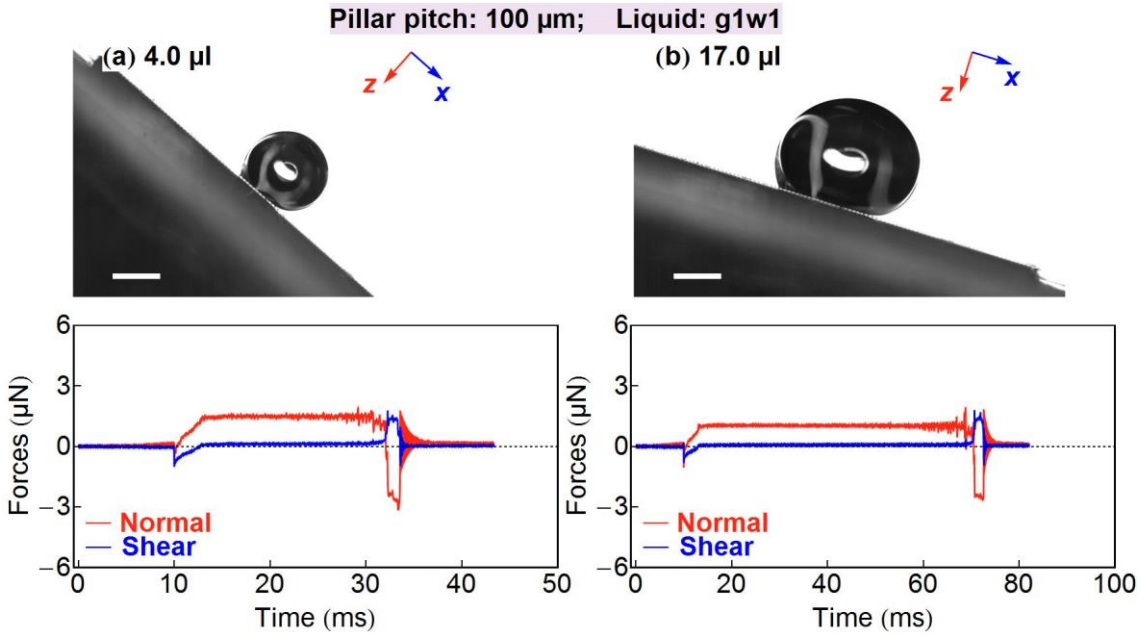

Fig. A. 4 Interaction forces during the sliding of a 4.0 μL G1W1 droplet and 17 μL G1W1 droplet on the sensor with a 100 μm pitch micro pillar array..

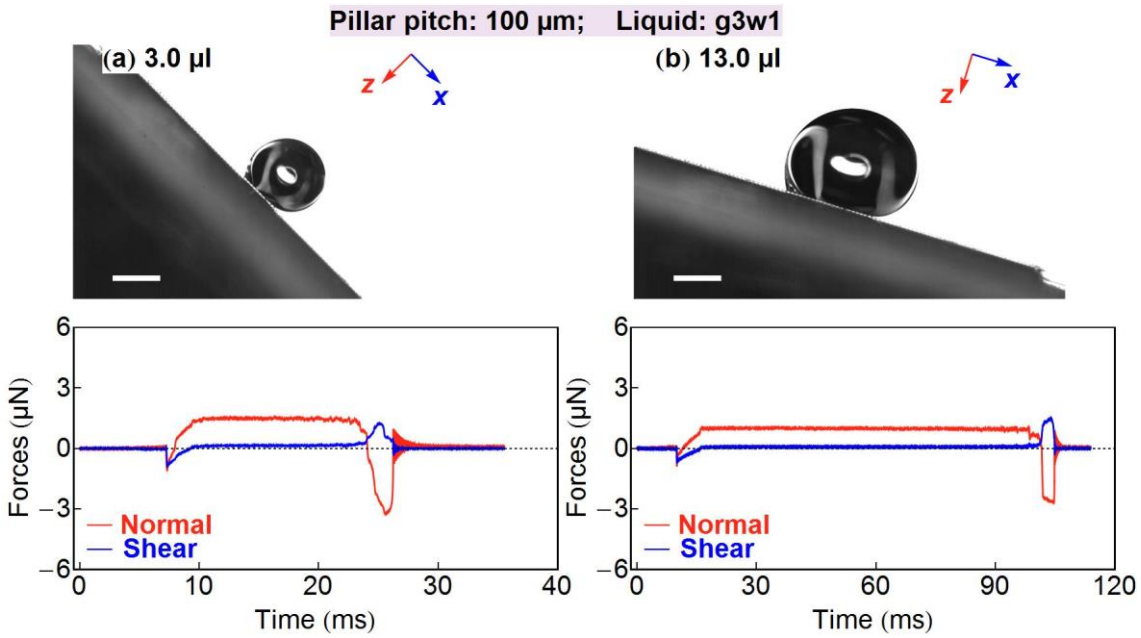

Fig. A. 5 Interaction forces during the sliding of a 3.0 μL G3W1 droplet and 13 G3W1 water droplet on the sensor with a 100 μm pitch micro pillar array.

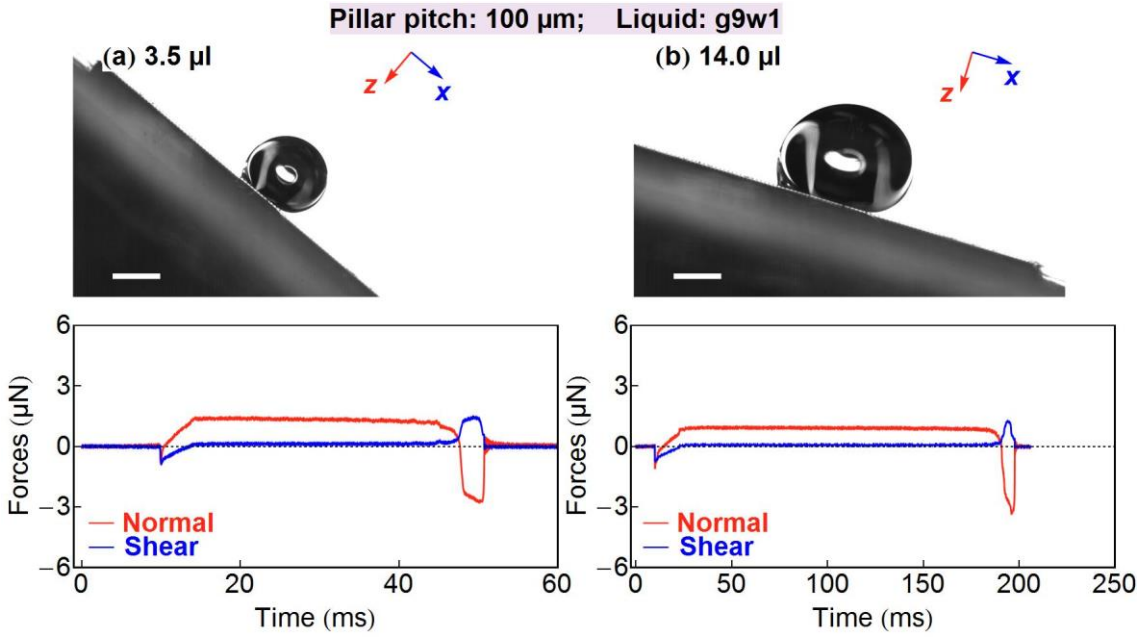

Fig. A. 6 Interaction forces during the sliding of a 3.5 μL G9W1 droplet and 14 μL G9W1 droplet on the sensor with a 100 μm pitch micro pillar array.

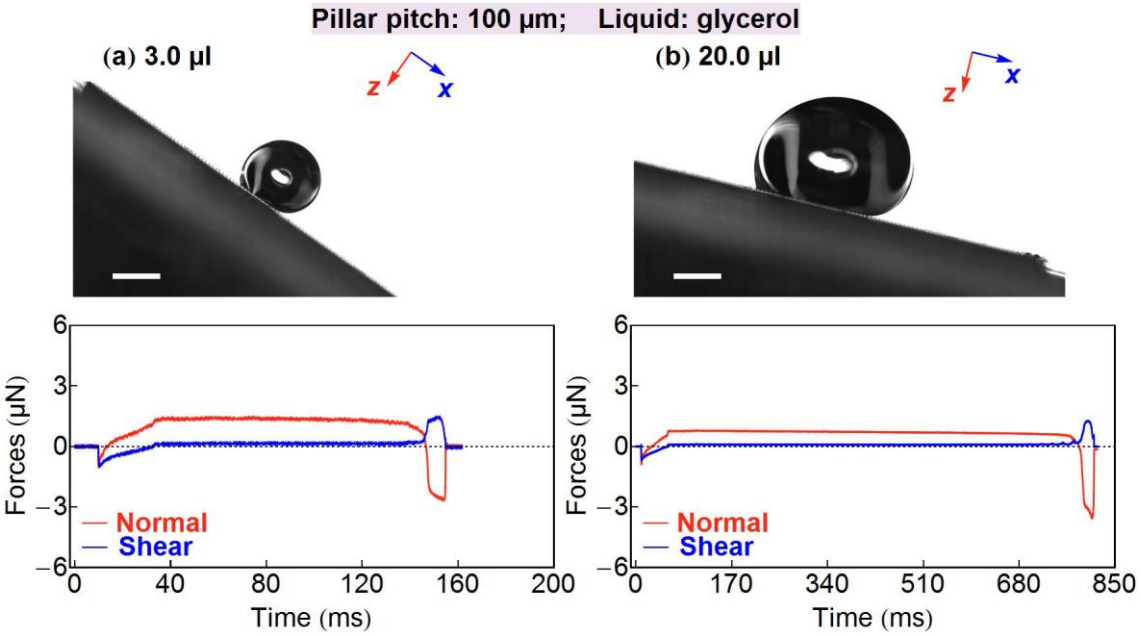

Fig. A. 7 Interaction forces during the sliding of a 3.0 μL glycerol droplet and 20 μL glycerol droplet on the sensor with a 100 μm pitch micro pillar array.

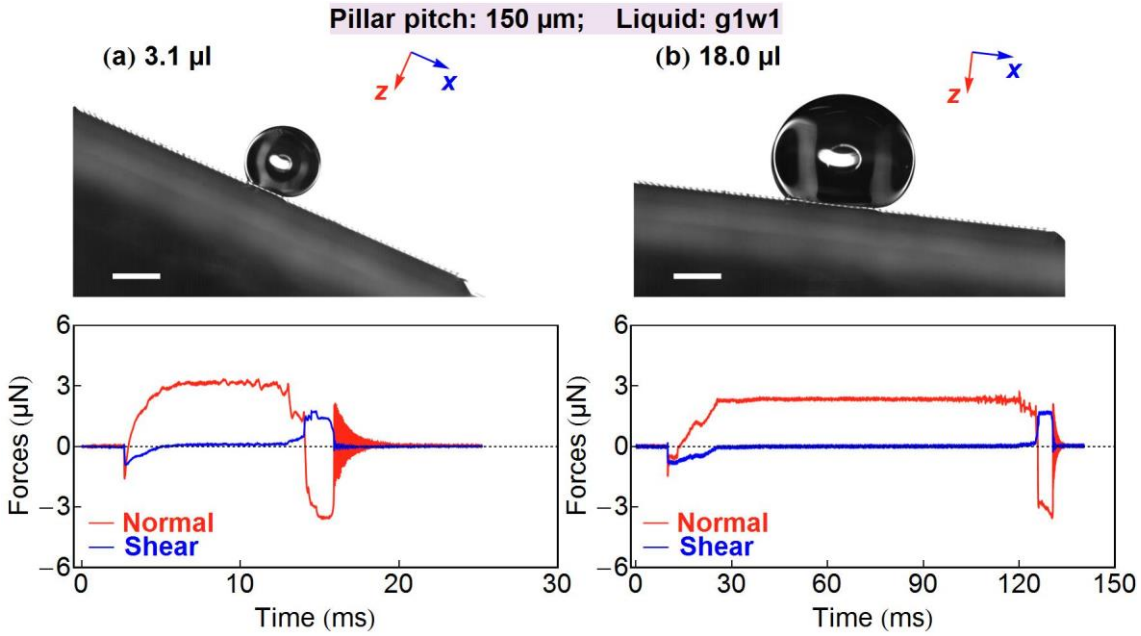

Fig. A. 8 Interaction forces during the sliding of a 3.1 μL G1W1 droplet and 18 μL G1W1 droplet on the sensor with a 150 μm pitch micro pillar array.

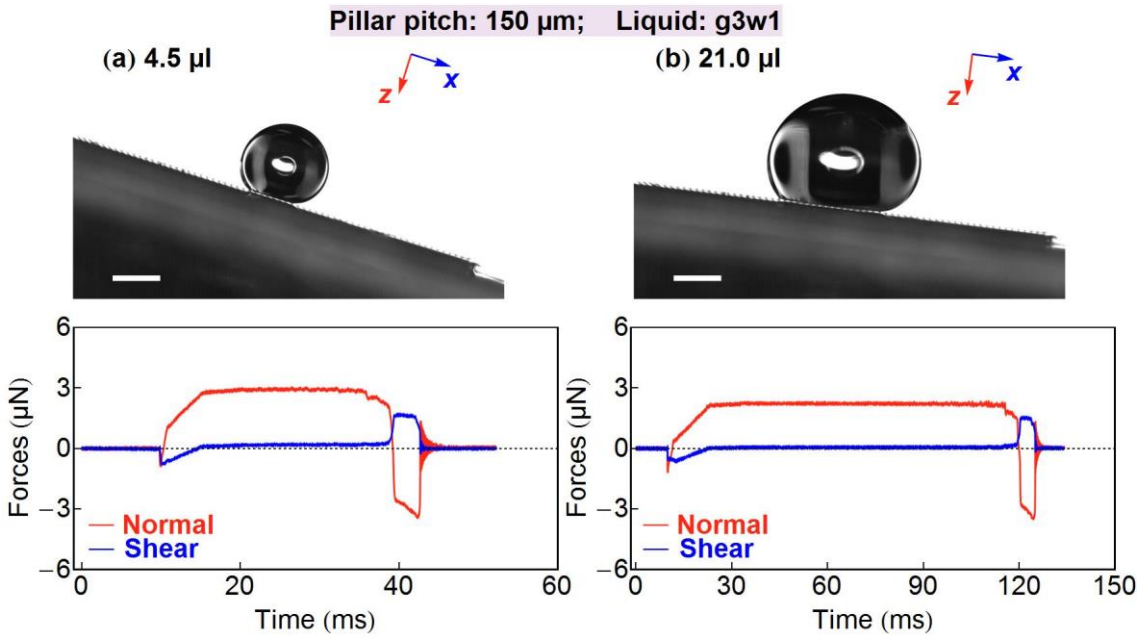

Fig. A. 9 Interaction forces during the sliding of a 4.5 μL G3W1 droplet and 21 μL G3W1 droplet on the sensor with a 150 μm pitch micro pillar array.

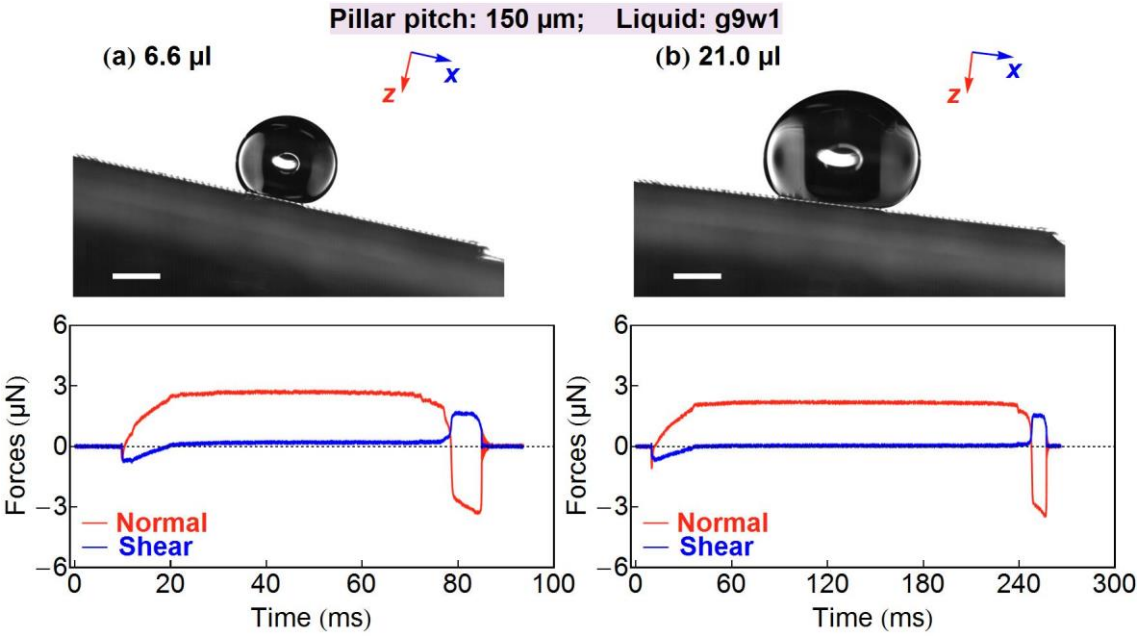

Fig. A. 10 Interaction forces during the sliding of a 6.6 μL G9W1 droplet and 21 μL G9W1 droplet on the sensor with a 125 μm pitch micro pillar array.

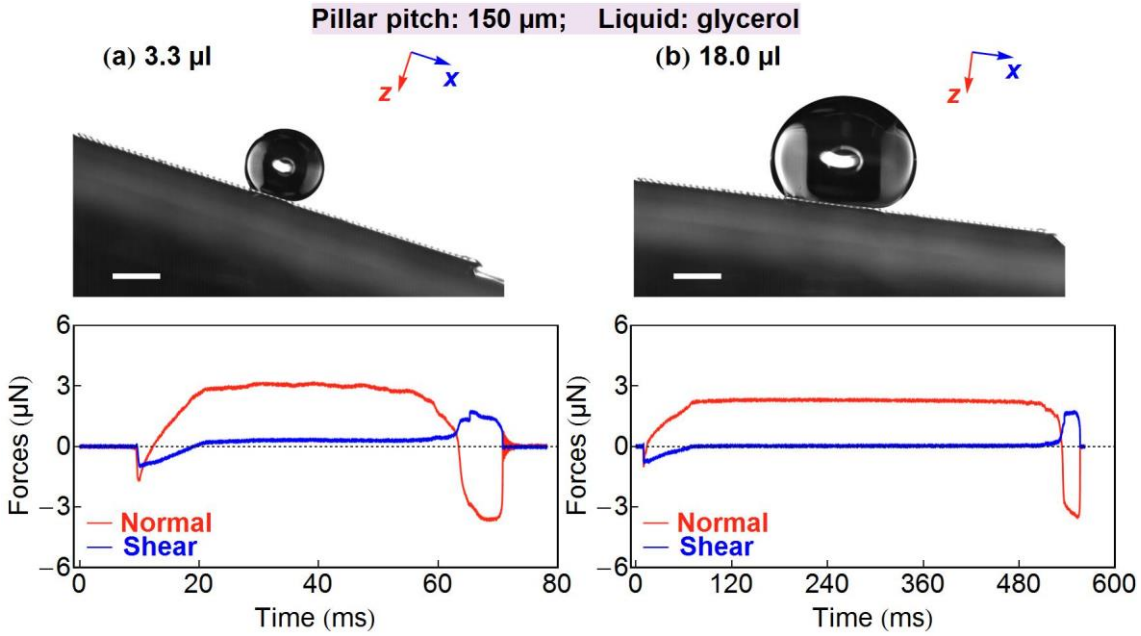

Fig. A. 11 Interaction forces during the sliding of a 3.3 μL glycerol droplet and 18 μL glycerol droplet on the sensor with a 125 μm pitch micro pillar array.

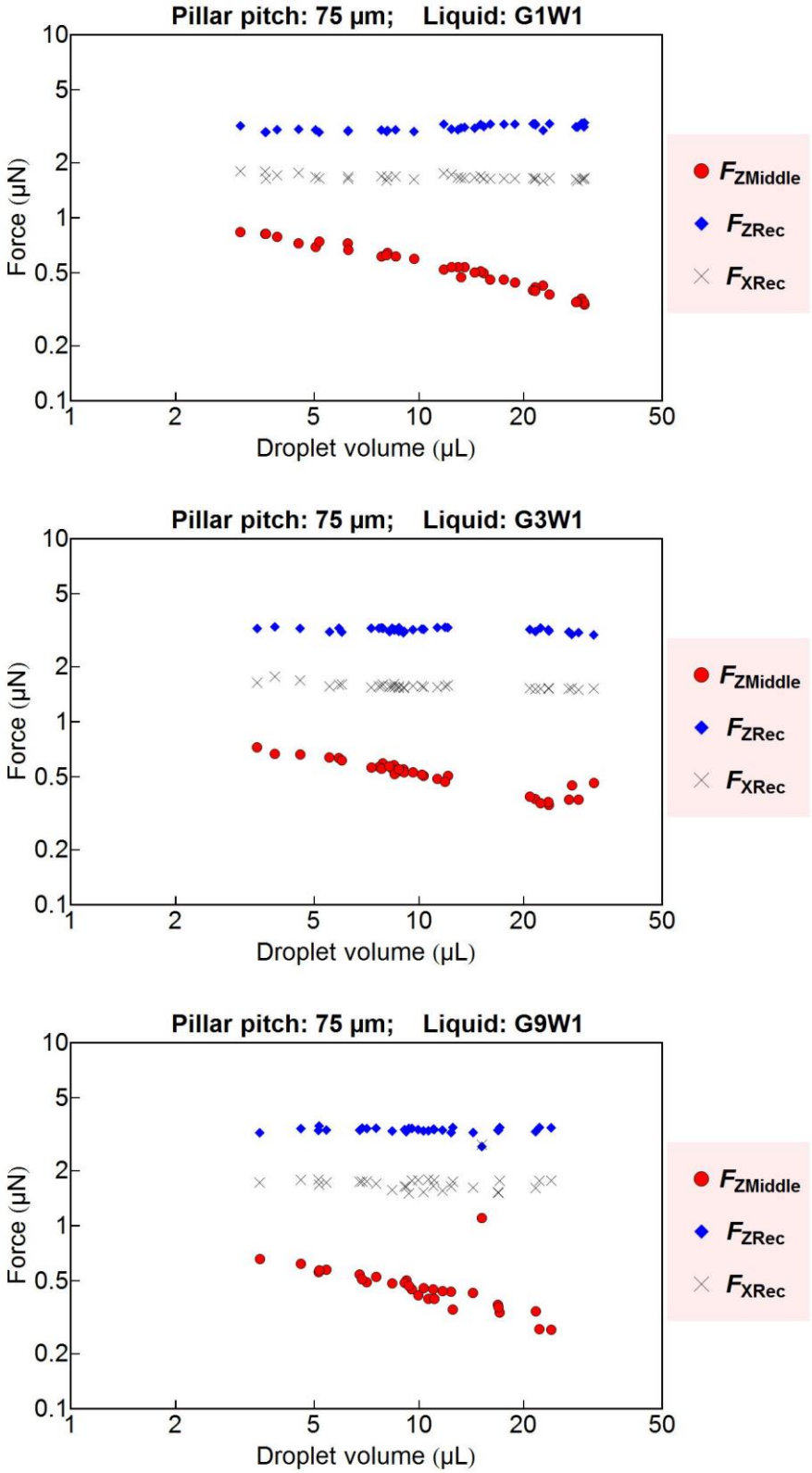

Fig. A. 12 Effect of droplet volume on the interaction forces.

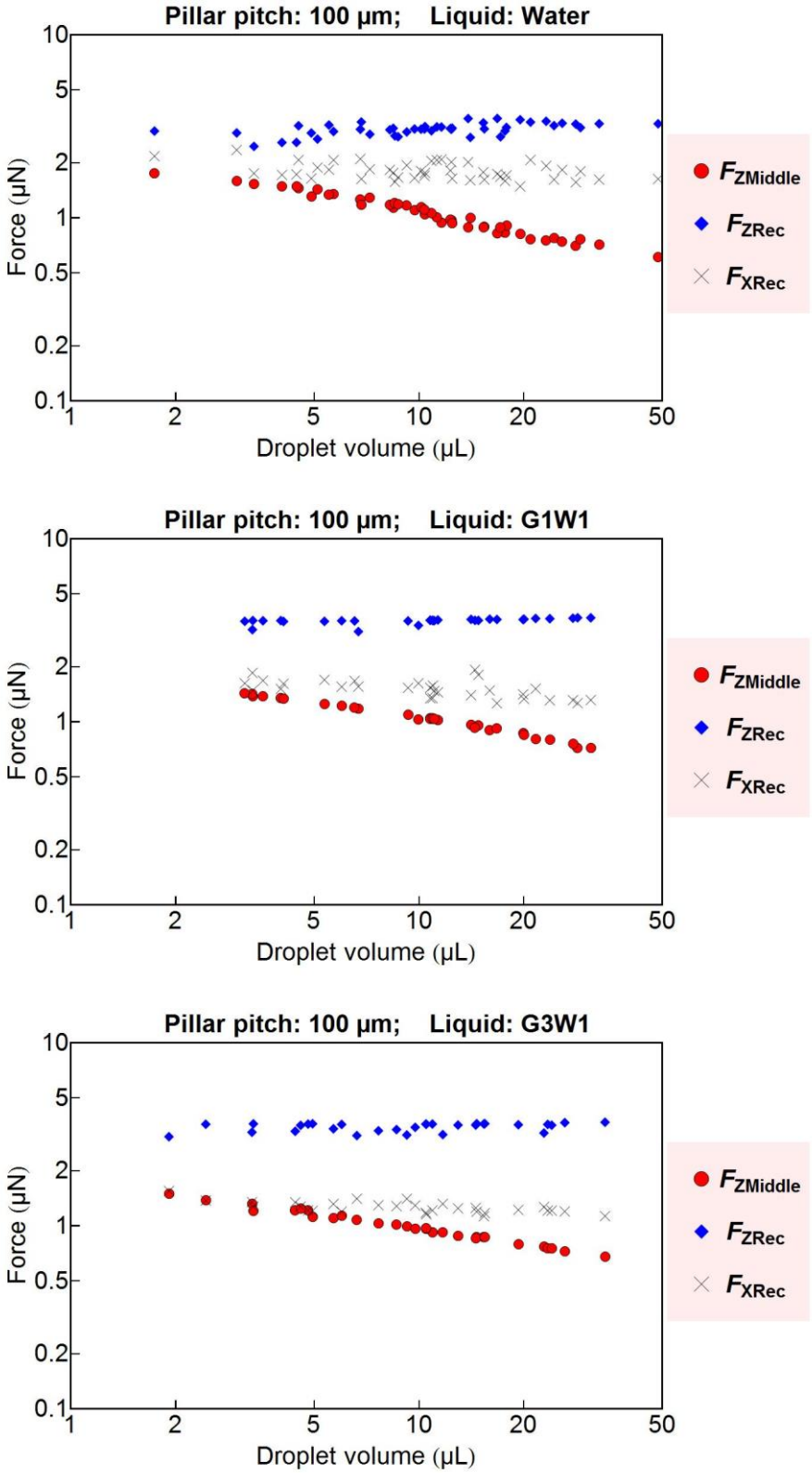

Fig. A. 13 Effect of droplet volume on the interaction forces (continued).

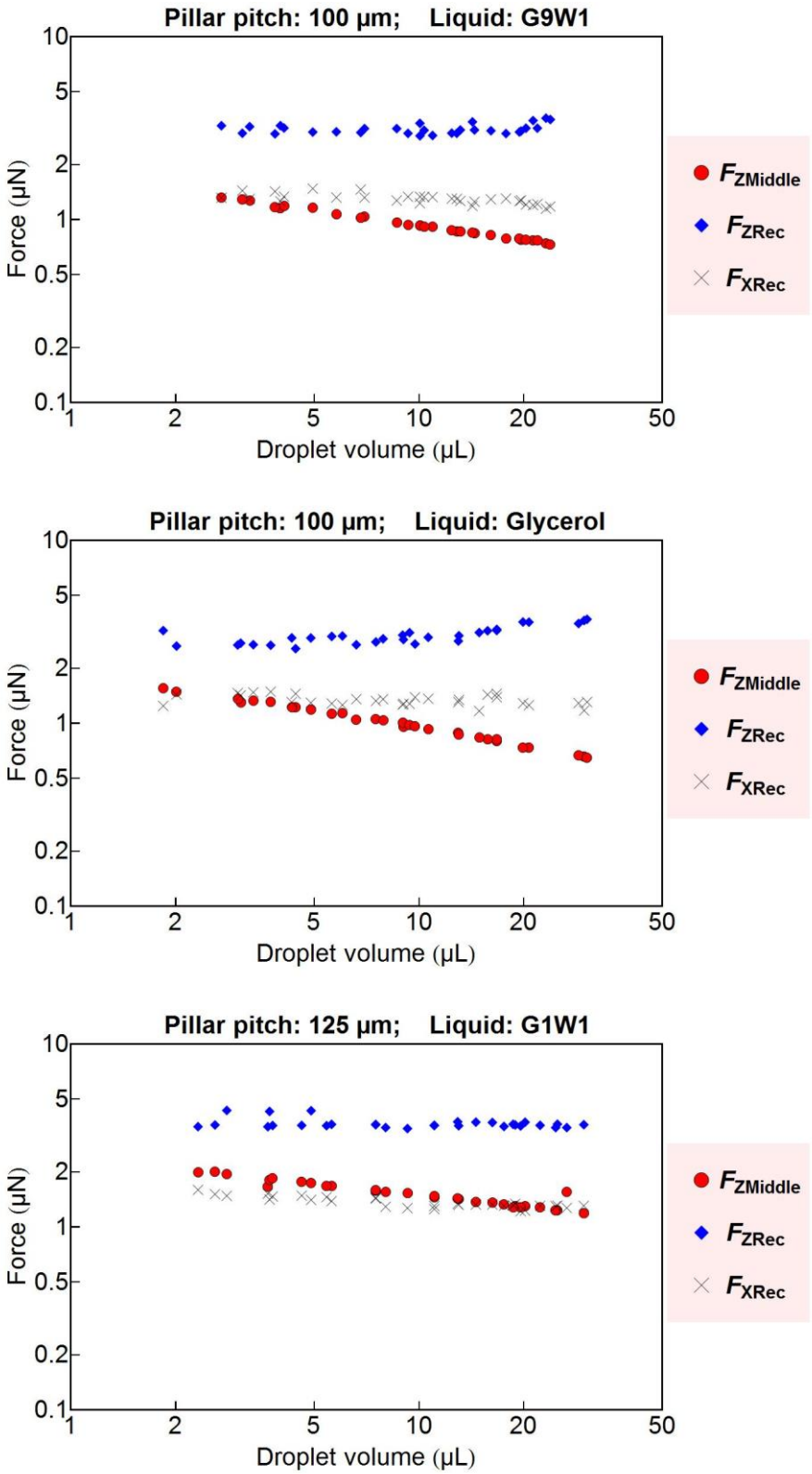

Fig. A. 14 Effect of droplet volume on the interaction forces (continued).

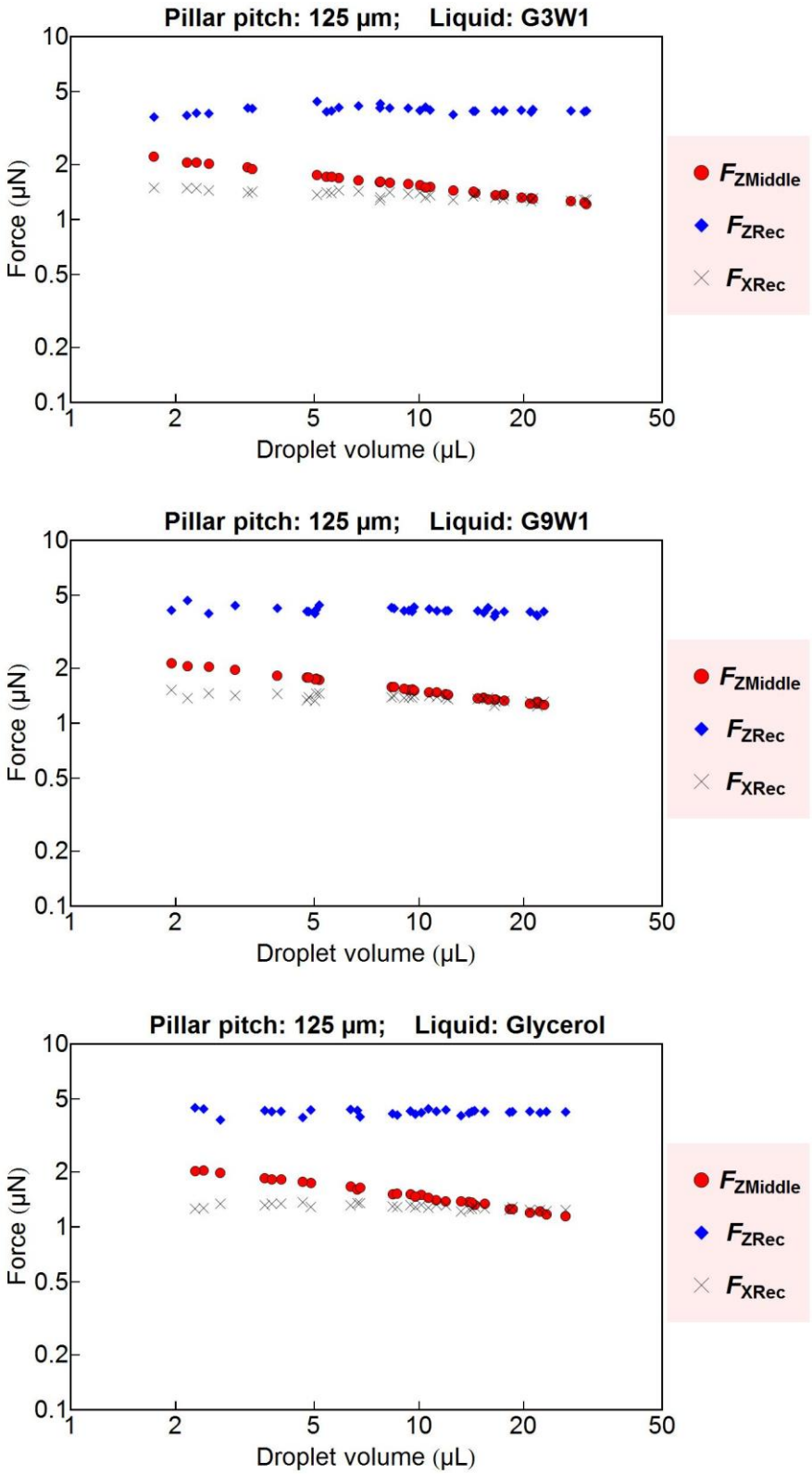

Fig. A. 15 Effect of droplet volume on the interaction forces (continued).

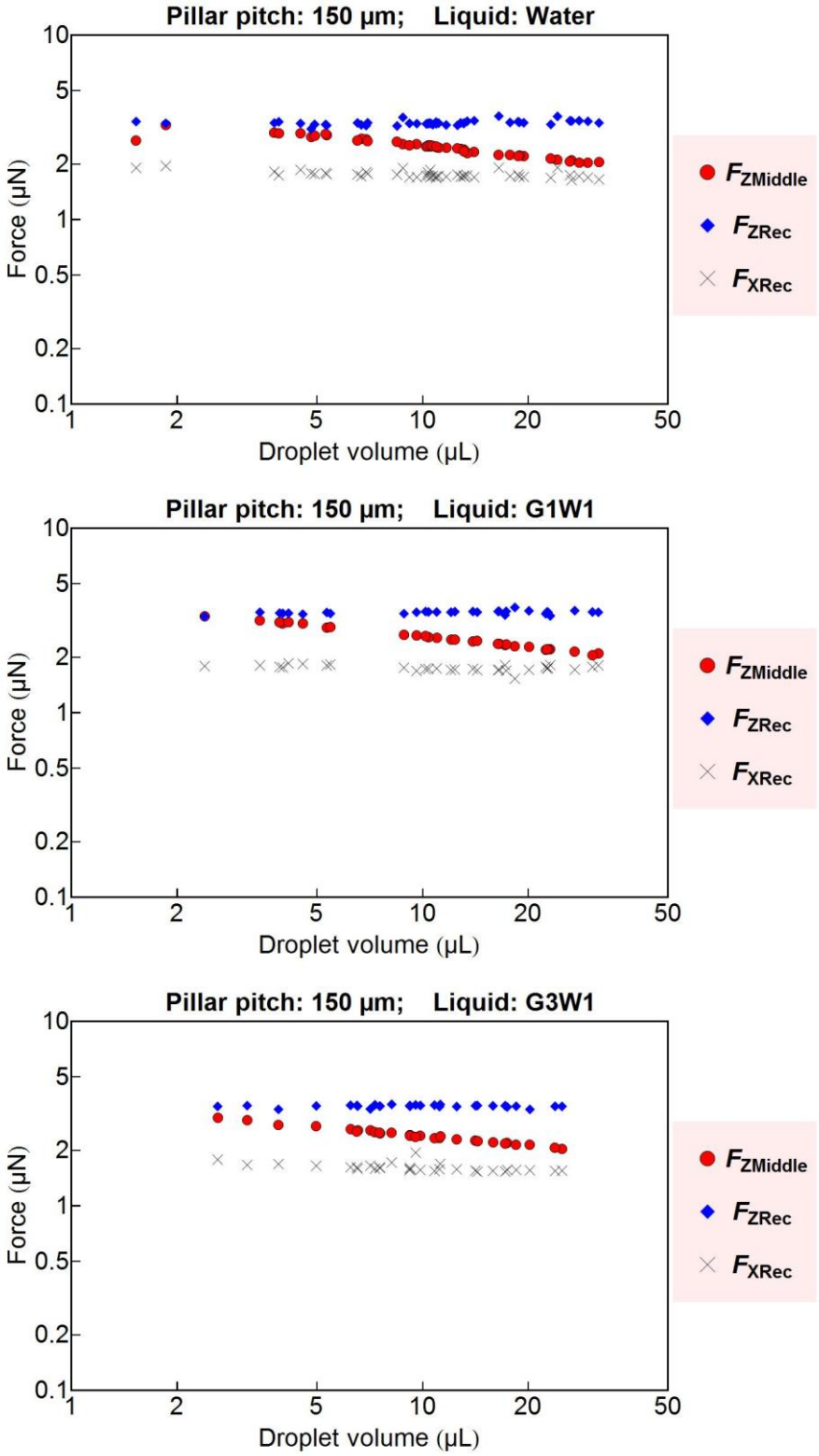

Fig. A. 16 Effect of droplet volume on the interaction forces (continued).

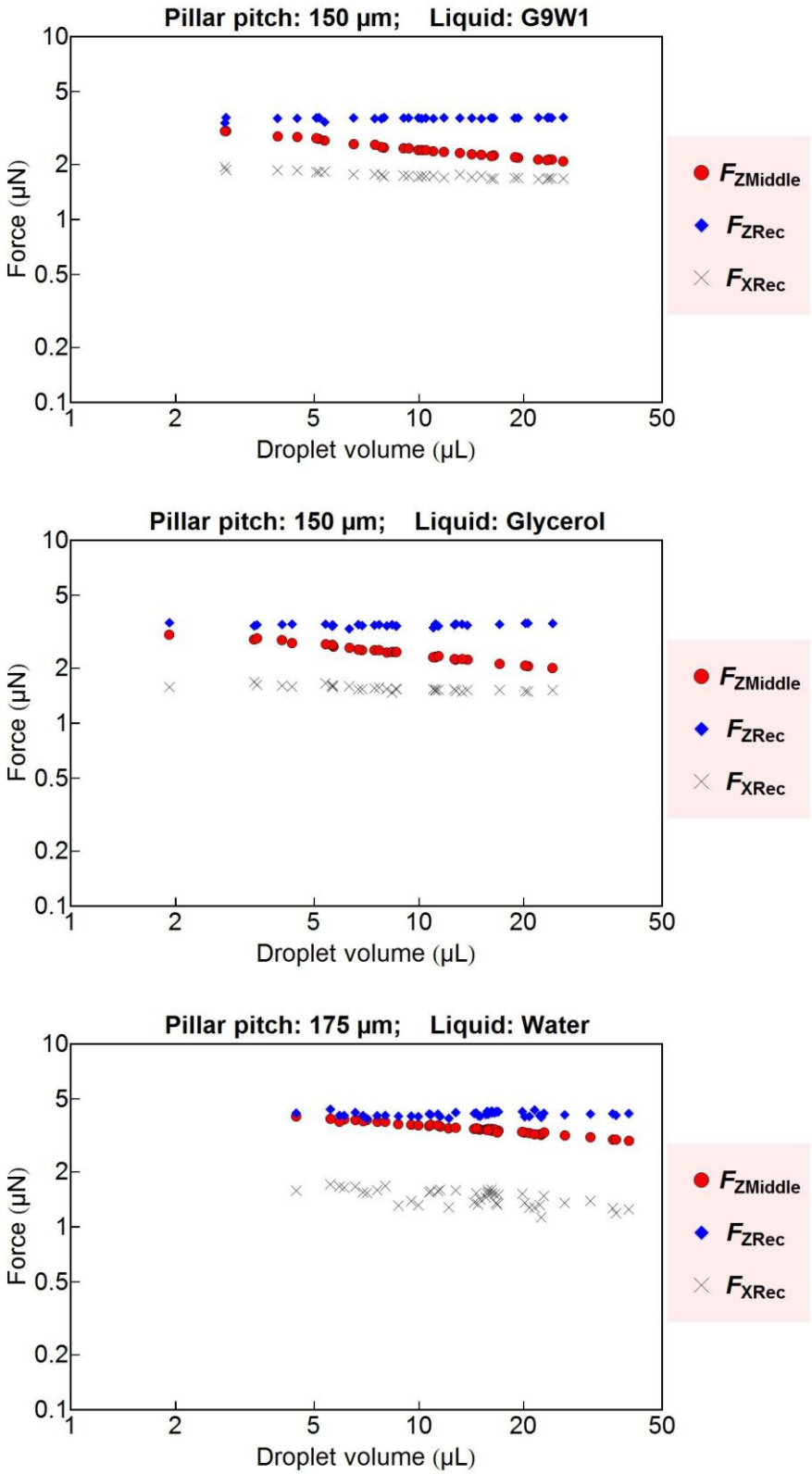

Fig. A. 17 Effect of droplet volume on the interaction forces (continued).

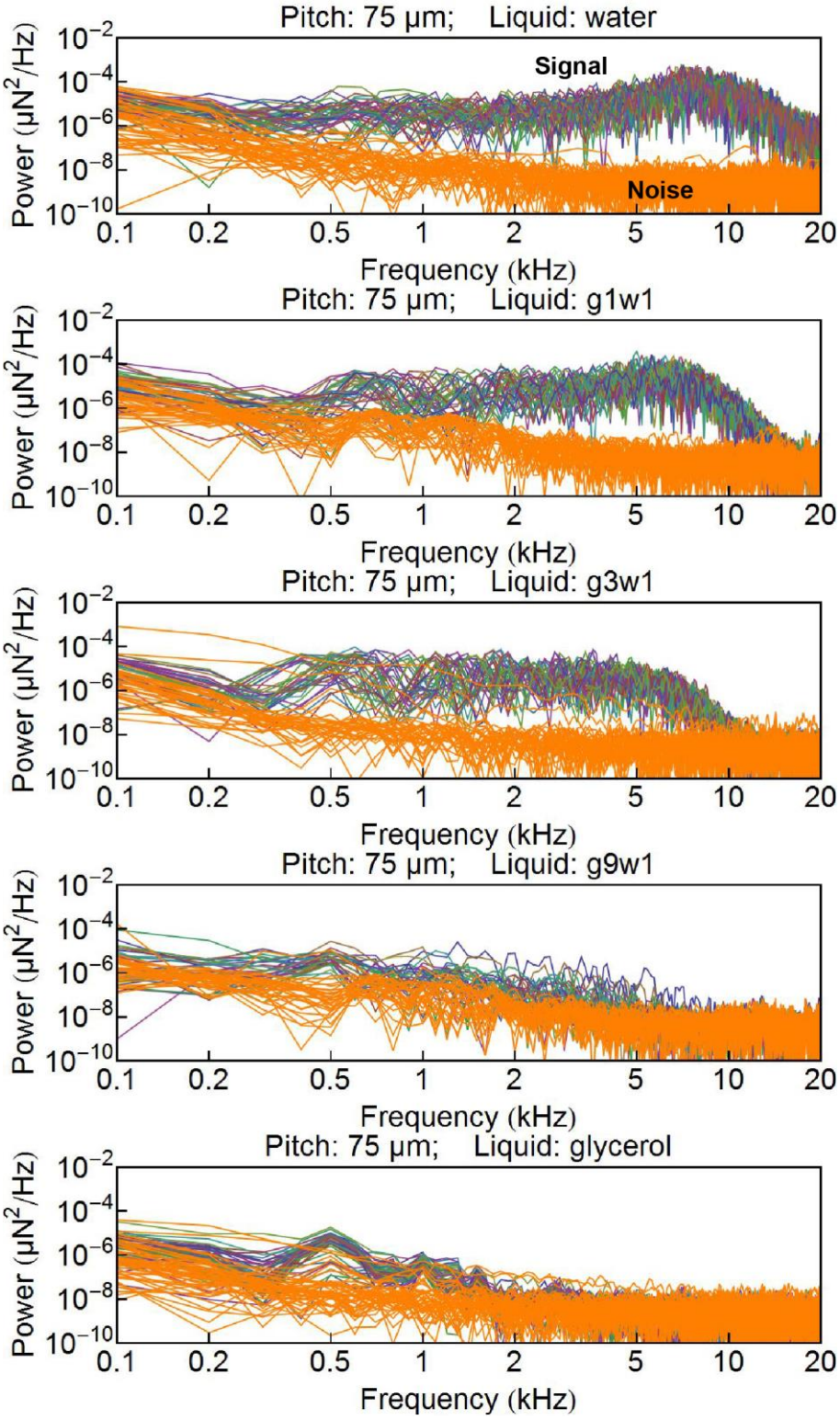

Fig. A. 18 Spectrums of the normal force during the sliding of the droplet on 75 μm-pitch micropillar array.

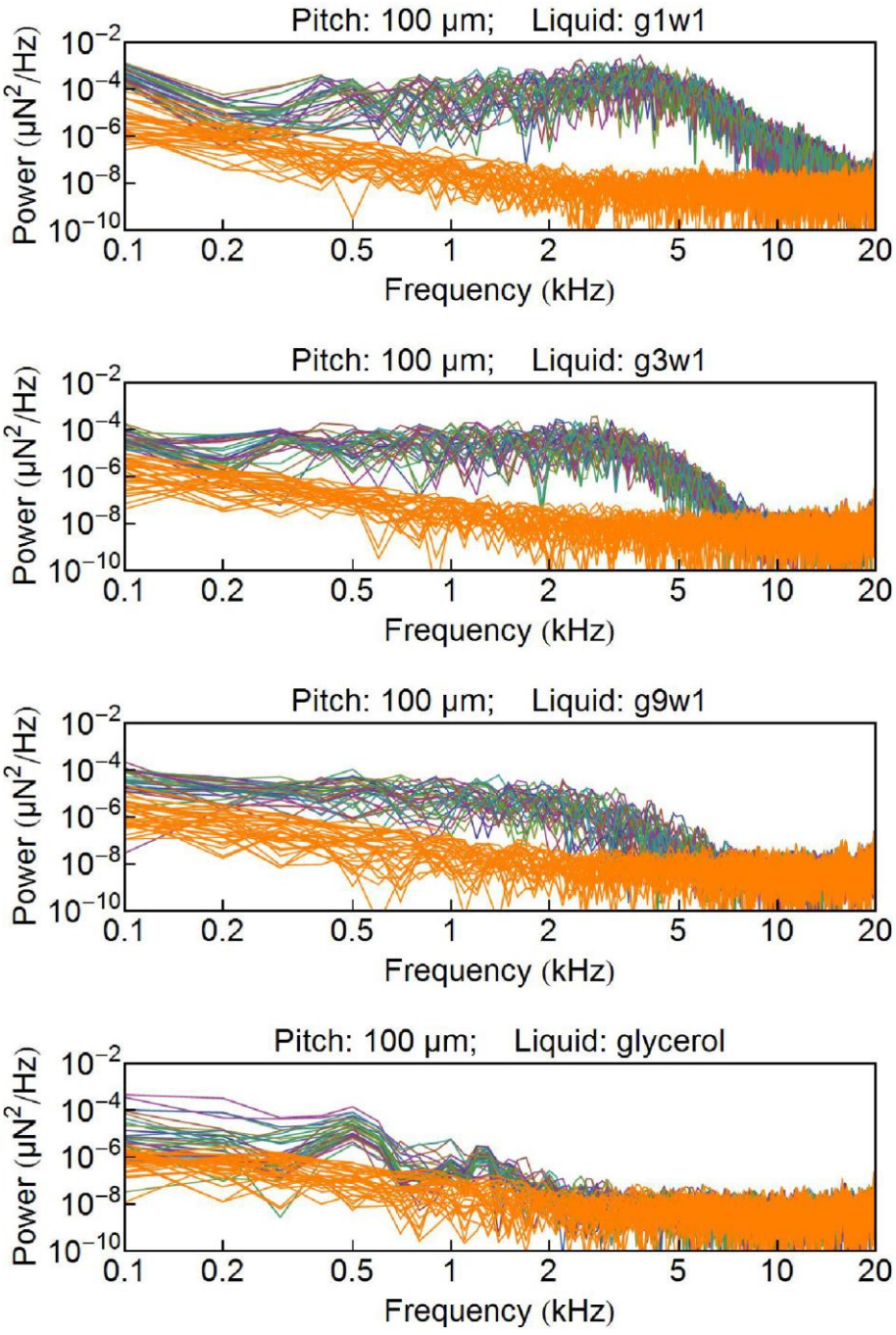

Fig. A. 19 Spectrums of the normal force during the sliding of the droplets on 100 μm-pitch micropillar array.

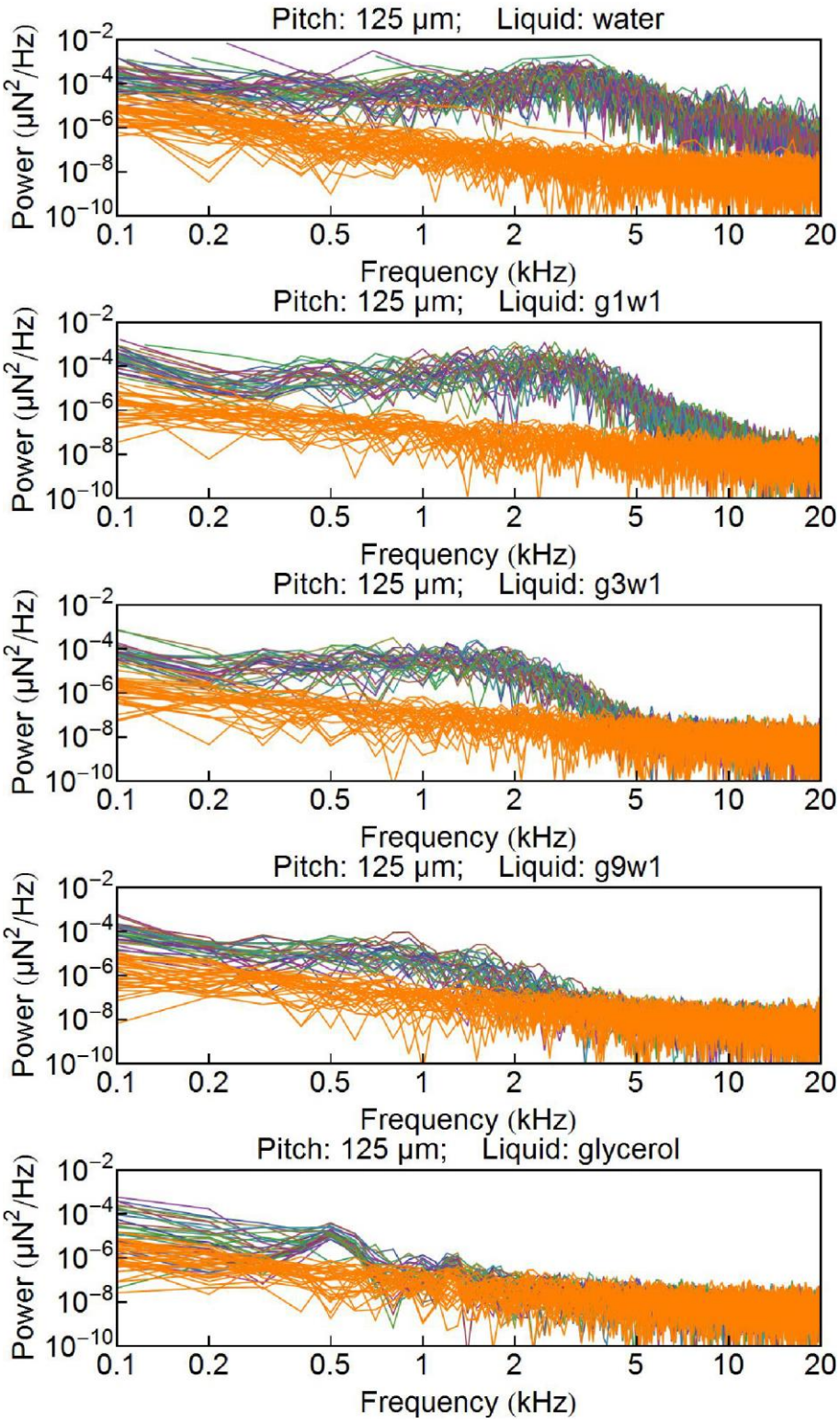

Fig. A. 20 Spectrums of the normal force during the sliding of the droplets on 125 μm-pitch micropillar array.

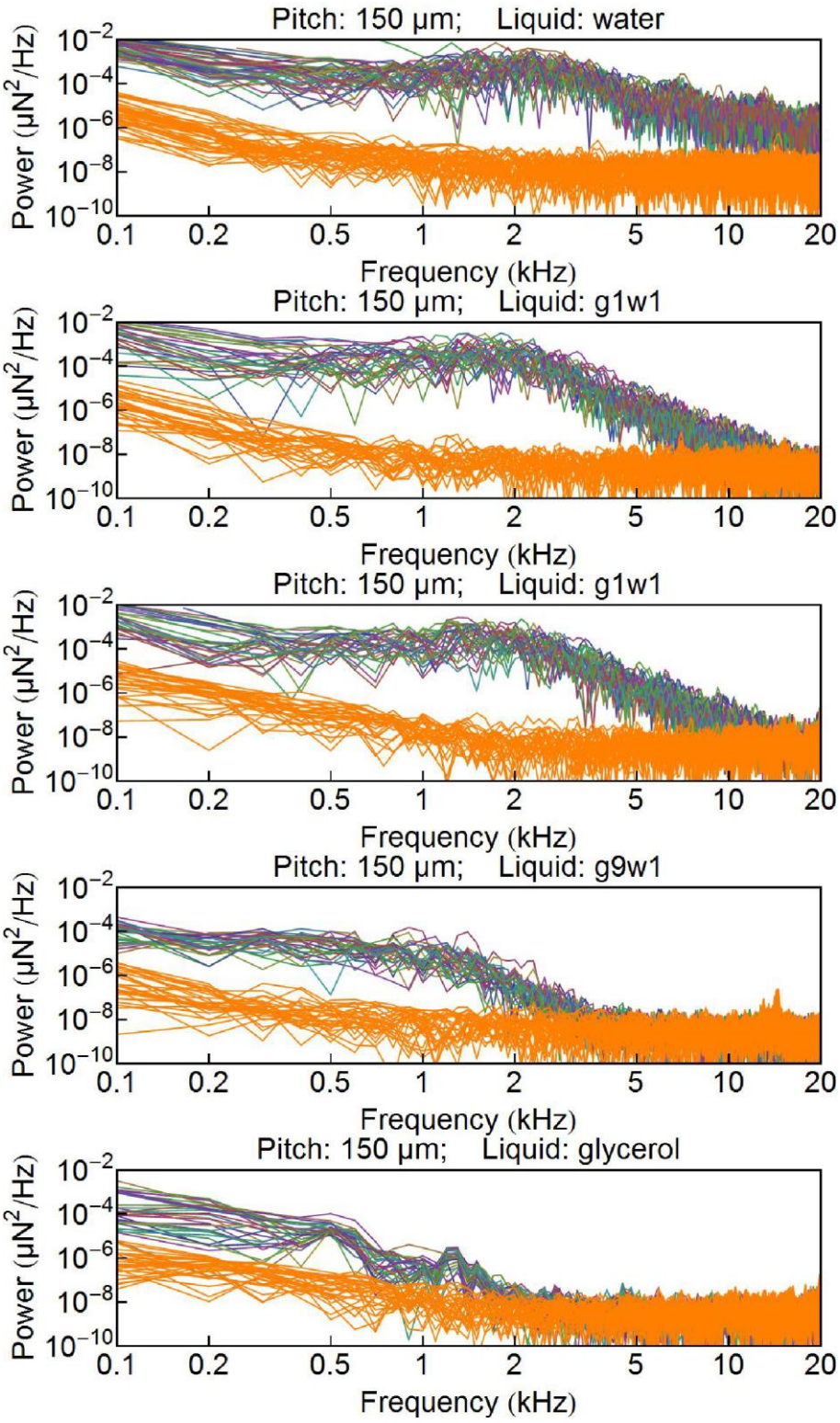

Fig. A. 21 Spectrums of the normal force during the sliding of the droplets on 125 μm-pitch micropillar array.

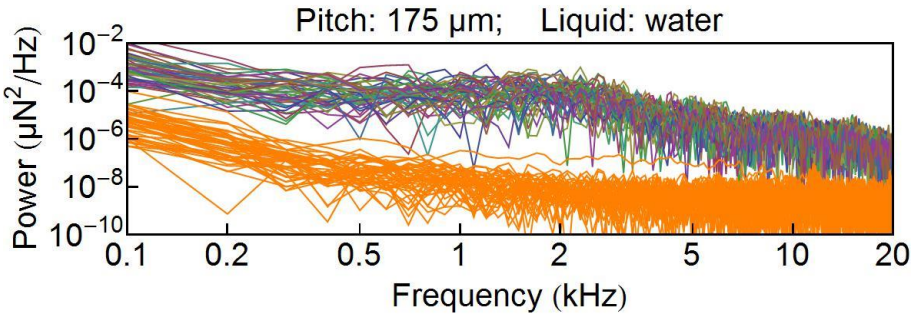

Fig. A. 22 Spectrums of the normal force during the sliding of water droplets on 175 μm-pitch micropillar array.

Comparison of the normal force during the vibration of droplet

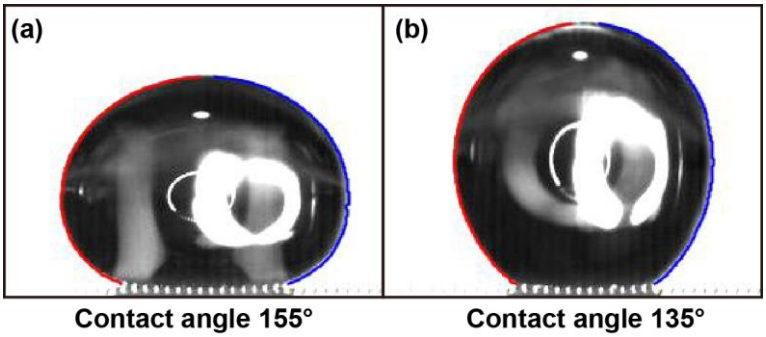

Fig. A. 23 Maximum and minimum contact angle during the vibration of the droplet.

During the vibration of the droplet described in **Fig. 5.5**, the maximum and minimum of the contact angle can be obtained optically by extracting the profile of the droplet as shown in **Fig. A. 23**. During the vibration of the droplet, the maximum and minimum contact angle were 155°and 135°, respectively.

Moreover, from the contact angle, the amplitude of the normal force change at the edge of the contact area can be estimated as followed:

$$\Delta F = 4w\gamma(\sin 135° - \sin 155°) \qquad \textbf{(A.1)}$$

where w = 30 μm is the width of the pillar; γ = 72 mN/m is the surface tension of water.

Thus, we obtain ΔF = 2.46 μN, which is the almost the same with the amplitude of the normal force change measured by the sensor S1 (2.51 μN).

Result on the tapping induced vibration of a G1W1 droplet

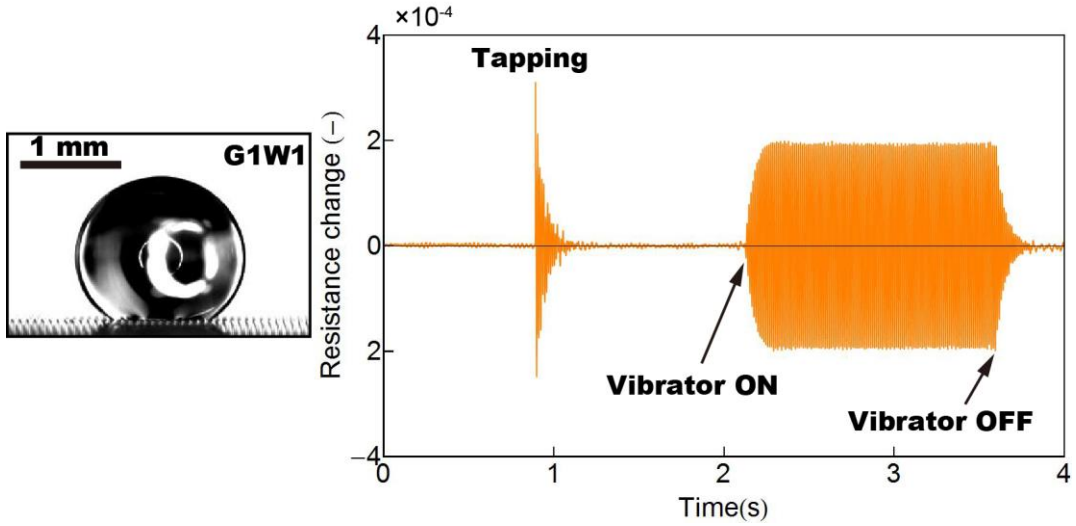

Fig. A. 24 Output of the cantilever when tapping the substrate and when shaking the substrate.

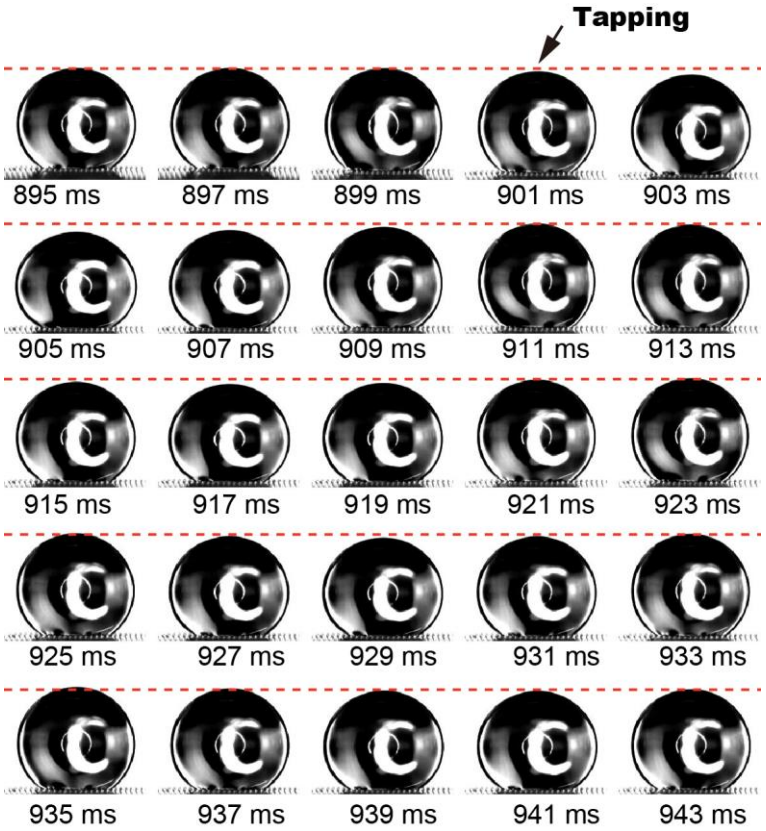

Fig. A. 25 Snapshots of the high speed camera showing the motion of the droplet when tapping is induced.

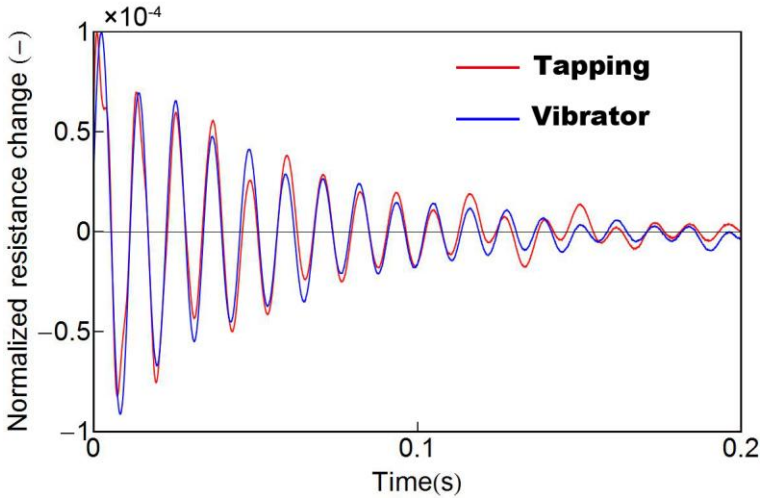

Fig. A. 26 Attenuation rate of the two vibrations.

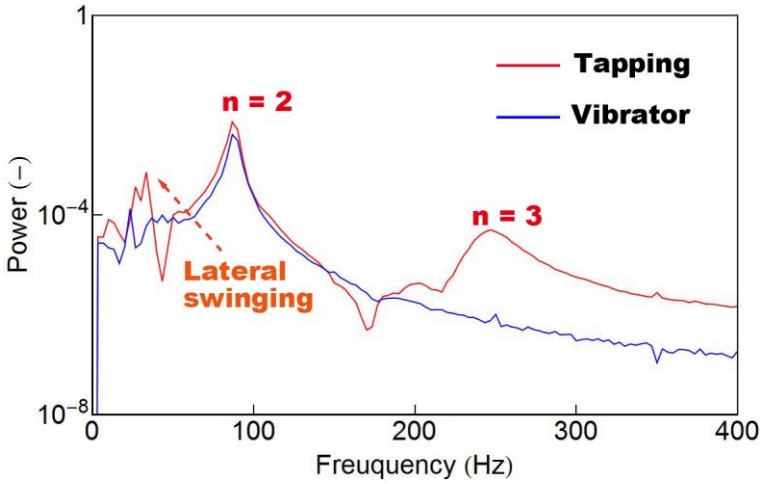

Fig. A. 27 Frequency spectrum of the tapping induced vibration and the forced vibration of the droplet.

Vibration mode of the droplet

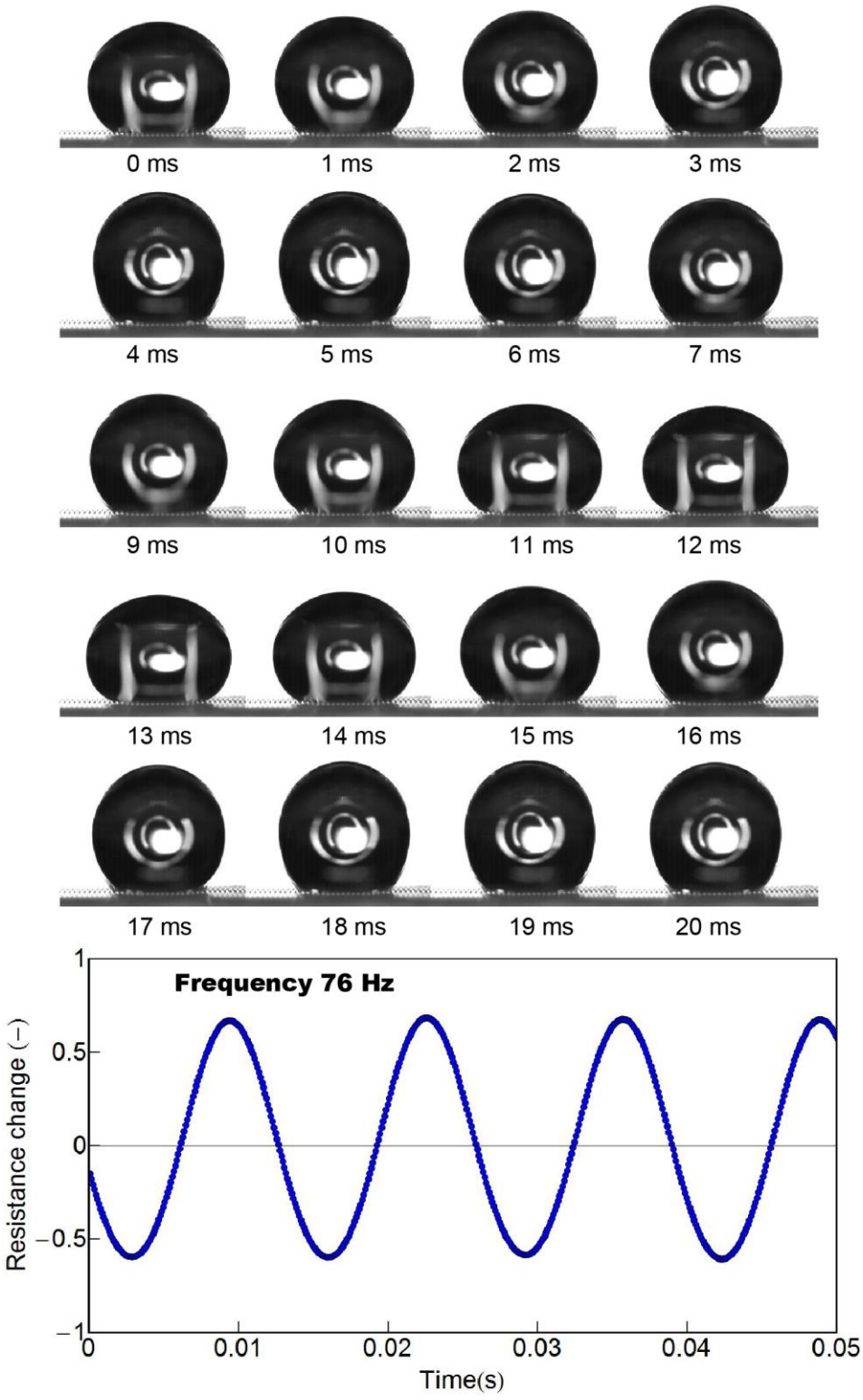

Fig. A. 28 Vibration mode $n = 2$

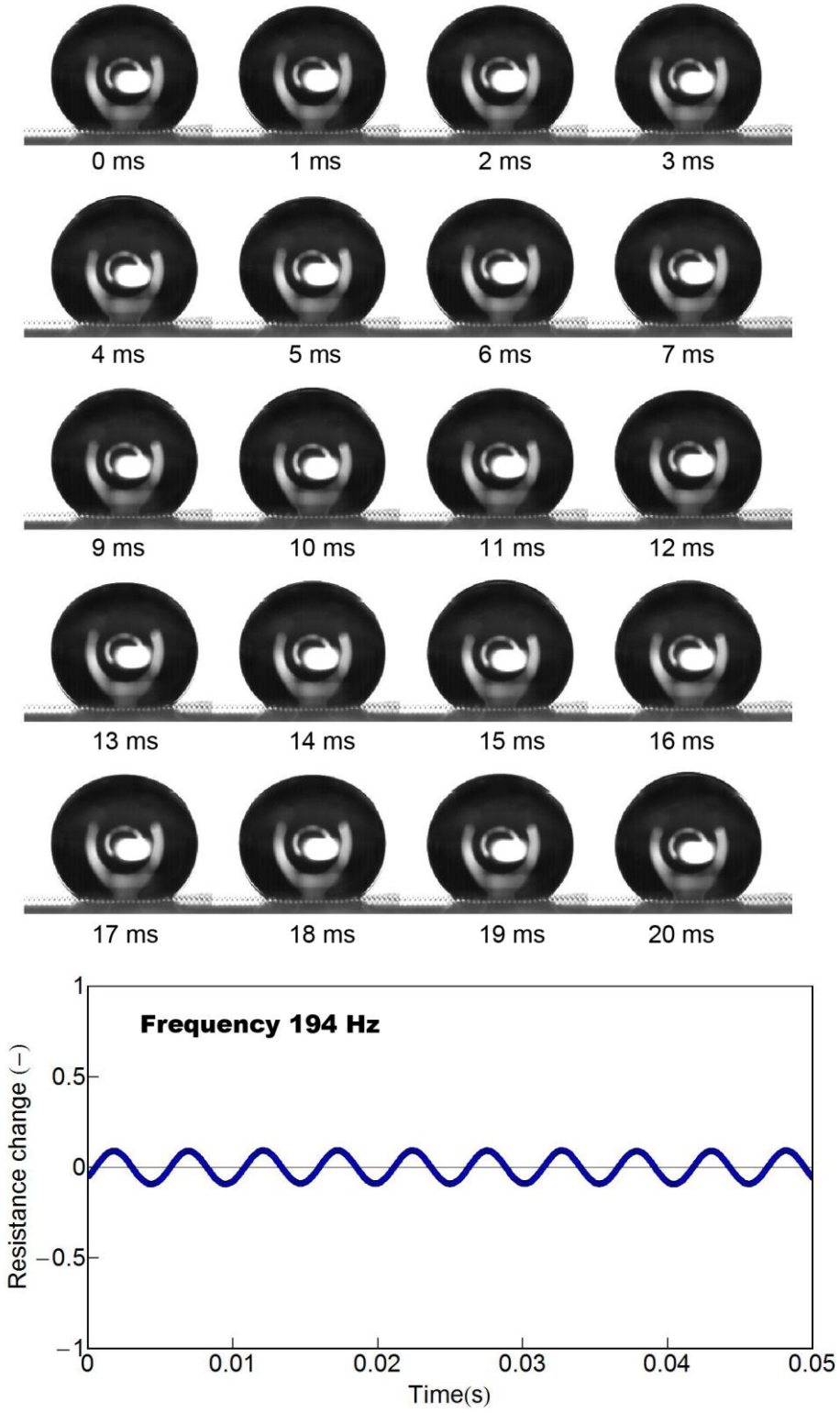

Fig. A. 29 Vibration mode n = 3

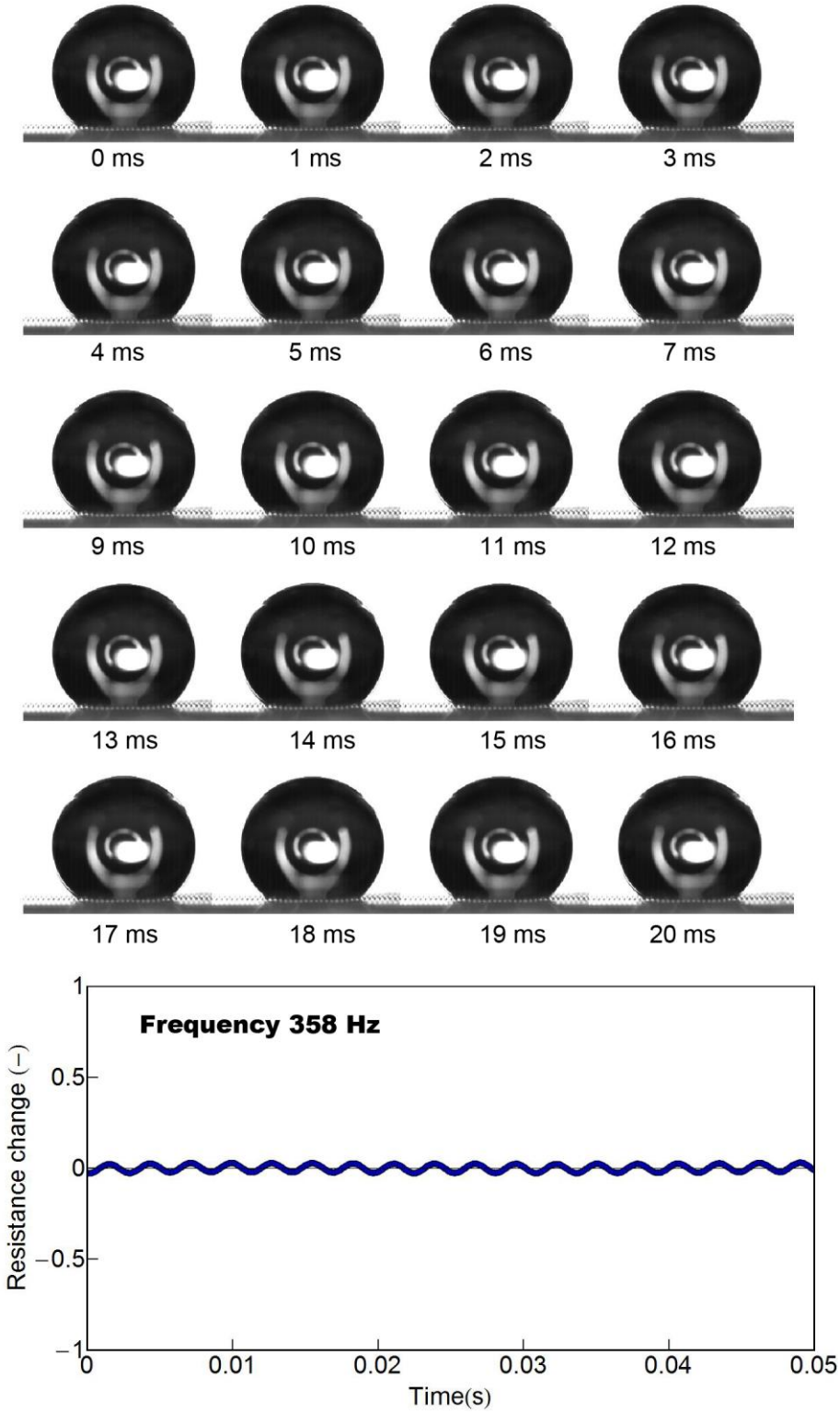

Fig. A. 30 Vibration mode $n = 4$

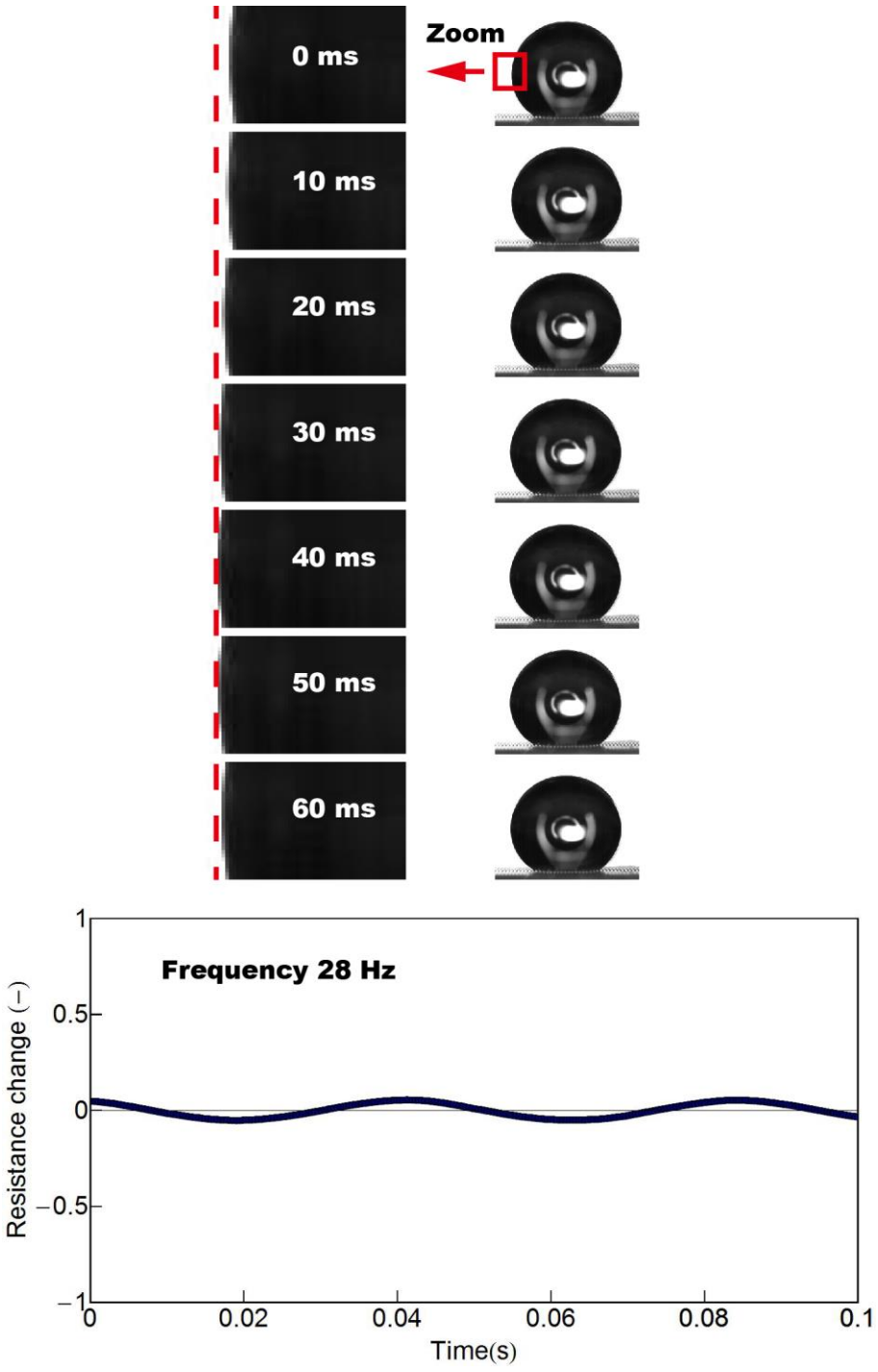

Fig. A. 31 Lateral swinging of the droplet.

Rolling motion of a glycerol droplet

Rolling motion of a glycerol droplet can be observed by tracking a bubble trapped inside the droplet as shown in the following snapshot series of the high speed camera.

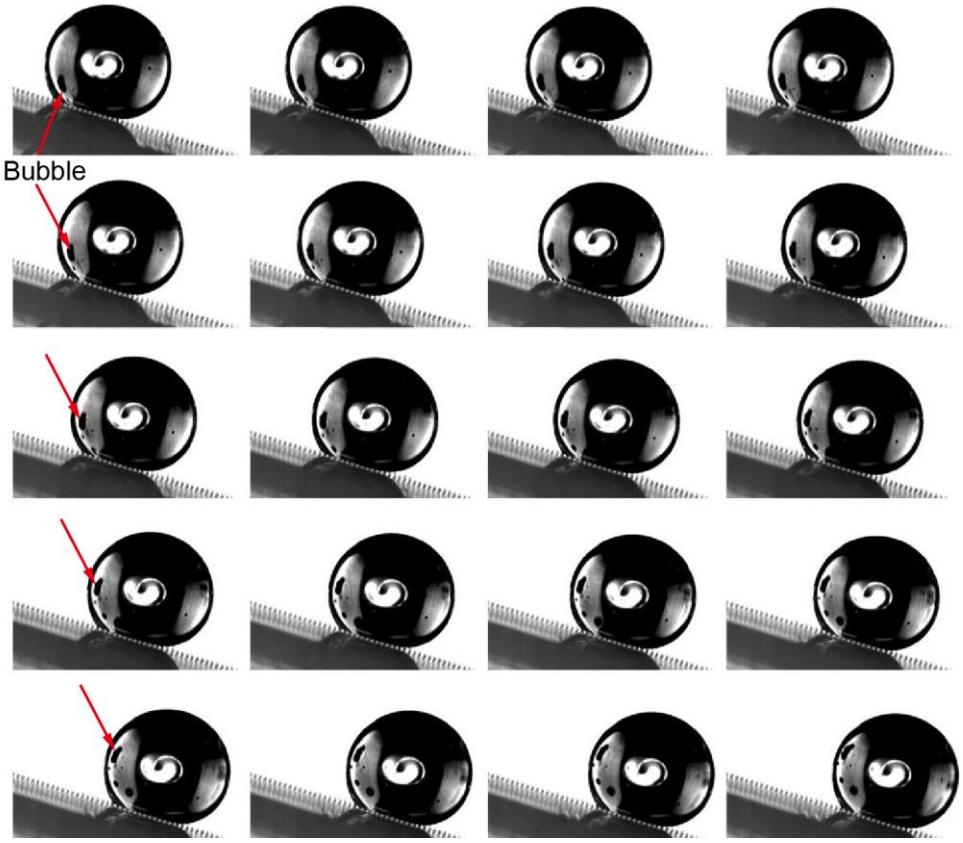

Fig. A. 32 Snapshots of the high speed camera showing the rolling motion of a glycerol droplet

Appendix 2 Chemicals

Table B. 1 Chemicals used in this study

Chemicals	Producers	Usage
OFPR-800LB 23cp	Tokyo Ohka Kogyo Co.	Pattern silicon
KMPR-1035	MicroChem Co.	Form the micropillar
AZP-4620	MicroChem Co.	Cover layer when etching the device silicon layer
NMD-3 (TMAH 2.38%)	Tokyo Ohka Kogyo Co.	Develop photoresist
OAP	Tokyo Ohka Kogyo Co.	Adhesive layer for photoresist coating
Acetone (CH3COCH3, 99.5%)	Wako Pure Chemical Industries, Ltd.	Remove photoresist and vacuum oil
IPA (CH3CH(OH)CH3, 99.7%)	Wako Pure Chemical Industries, Ltd.	Remove photoresist and vacuum oil
Ethanol (CH3CH2OH, 99.5%)	Wako Pure Chemical Industries, Ltd.	Remove photoresist and vacuum oil
Hydrofluoric acid (HF, 46%)	Wako Pure Chemical Industries, Ltd.	Etching box layer of an SOI wafer
Glycerol ($C_3H_3(OH)_3$, 99%)	Wako Pure Chemical Industries, Ltd	Experiment

References

[1] B. Bhushan, "Biomimetics: lessons from nature: An overview," *Philosophical Transactions of the Royal Society A: Mathematical, Physical and Engineering Sciences,* vol. 367, pp. 1445-1486, 2009.

[2] R. Blossey, "Self-cleaning surfaces - virtual realities," *Nat Mater,* vol. 2, pp. 301-306, 2003.

[3] Z. Guo, W. Liu, and B.-L. Su, "Superhydrophobic surfaces: From natural to biomimetic to functional," *Journal of Colloid and Interface Science,* vol. 353, pp. 335-355, 2011.

[4] W. Barthlott and C. Neinhuis, "Purity of the sacred lotus, or escape from contamination in biological surfaces," *Planta,* vol. 202, pp. 1-8, 1997.

[5] K. Liu, X. Yao, and L. Jiang, "Recent developments in bio-inspired special wettability," *Chemical Society Reviews,* vol. 39, pp. 3240-3255, 2010.

[6] C. NEINHUIS and W. BARTHLOTT, "Characterization and Distribution of Water-repellent, Self-cleaning Plant Surfaces," *Annals of Botany,* vol. 79, pp. 667-677, 1997.

[7] D. Quere, "Wetting and roughness," *Annual Review of Materials Research,* vol. 38, pp. 71-99, 2008.

[8] B. Bhushan and Y. C. Jung, "Natural and biomimetic artificial surfaces for superhydrophobicity, self-cleaning, low adhesion, and drag reduction," *Progress in Materials Science,* vol. 56, pp. 1-108, 2011.

[9] Y. Y. Yan, N. Gao, and W. Barthlott, "Mimicking natural superhydrophobic surfaces and grasping the wetting process: A review on recent progress in preparing superhydrophobic surfaces," *Advances in Colloid and Interface Science,* vol. 169, pp. 80-105, 2011.

[10] J. Ou, B. Perot, and J. P. Rothstein, "Laminar drag reduction in microchannels using ultrahydrophobic surfaces," *Physics of Fluids,* vol. 16, pp. 4635-4643, Dec 2004.

[11] O. I. Vinogradova and A. L. Dubov, "Superhydrophobic Textures for Microfluidics," *Mendeleev Communications,* vol. 22, pp. 229-236, 2012.

[12] T. Wu and Y. Suzuki, "Engineering superlyophobic surfaces as the microfluidic platform for droplet manipulation," *Lab on a Chip,* vol. 11, pp. 3121-3129, 2011.

[13] M. Washizu, "Electrostatic actuation of liquid droplets for micro-reactor applications," *Industry Applications, IEEE Transactions on,* vol. 34, pp. 732-737, 1998.

[14] H. Gau, S. Herminghaus, P. Lenz, and R. Lipowsky, "Liquid Morphologies on Structured Surfaces: From Microchannels to Microchips," *Science,* vol. 283, pp. 46-49, 1999.

[15] A. Nakajima, "Design of hydrophobic surfaces for liquid droplet control," *NPG Asia Mater,* vol. 3, pp. 49-56, 2011.

[16] G. McHale, M. I. Newton, and N. J. Shirtcliffe, "Immersed superhydrophobic surfaces: Gas exchange, slip and drag reduction properties," *Soft Matter,* vol. 6, pp. 714-719, 2010.

[17] Y. Sumino, N. Magome, T. Hamada, and K. Yoshikawa, "Self-Running Droplet: Emergence of Regular Motion from Nonequilibrium Noise," *Physical Review Letters,* vol. 94, p. 068301, 02/14/ 2005.

[18] P. Guo, Y. Zheng, C. Liu, J. Ju, and L. Jiang, "Directional shedding-off of water on

natural/bio-mimetic taper-ratchet array surfaces," *Soft Matter,* vol. 8, pp. 1770-1775, 2012.

[19] C. Lv and P. Hao, "Driving Droplet by Scale Effect on Microstructured Hydrophobic Surfaces," *Langmuir,* vol. 28, pp. 16958-16965, 2012.

[20] M. Reyssat, F. Pardo, and D. Quere, "Drops onto gradients of texture," *EPL,* vol. 87, Aug 2009.

[21] T. A. Duncombe, E. Y. Erdem, A. Shastry, R. Baskaran, and K. F. Böhringer, "Controlling Liquid Drops with Texture Ratchets," *Advanced Materials,* vol. 24, pp. 1545-1550, 2012.

[22] C.-M. Chen and S. Yang, "Directed Water Shedding on High-Aspect-Ratio Shape Memory Polymer Micropillar Arrays," *Advanced Materials,* vol. 26, pp. 1283-1288, 2014.

[23] M. J. Hancock, K. Sekeroglu, and M. C. Demirel, "Bioinspired Directional Surfaces for Adhesion, Wetting, and Transport," *Advanced Functional Materials,* vol. 22, pp. 2223-2234, 2012.

[24] A. Shastry, M. J. Case, and K. F. Böhringer, "Directing Droplets Using Microstructured Surfaces†," *Langmuir,* vol. 22, pp. 6161-6167, 2006.

[25] D. t Mannetje, S. Ghosh, R. Lagraauw, S. Otten, A. Pit, C. Berendsen, *et al.*, "Trapping of drops by wetting defects," *Nat Commun,* vol. 5, 04/11/online 2014.

[26] N. Tretyakov and M. Muller, "Directed transport of polymer drops on vibrating superhydrophobic substrates: a molecular dynamics study," *Soft Matter,* 2014.

[27] S. P. Thampi, R. Adhikari, and R. Govindarajan, "Do Liquid Drops Roll or Slide on Inclined Surfaces?," *Langmuir,* vol. 29, pp. 3339-3346, Mar 12 2013.

[28] B. M. Mognetti, H. Kusumaatmaja, and J. M. Yeomans, "Drop dynamics on hydrophobic and superhydrophobic surfaces," *Faraday Discussions,* vol. 146, pp. 153-165, 2010.

[29] J. Hyvaluoma, A. Koponen, P. Raiskinmaki, and J. Timonen, "Droplets on inclined rough surfaces," *European Physical Journal E,* vol. 23, pp. 289-293, Jul 2007.

[30] C. W. Extrand, "Model for contact angles and hysteresis on rough and ultraphobic surfaces," *Langmuir,* vol. 18, pp. 7991-7999, Oct 15 2002.

[31] B. M. Mognetti and J. M. Yeomans, "Modeling Receding Contact Lines on Superhydrophobic Surfaces," *Langmuir,* vol. 26, pp. 18162-18168, Dec 7 2010.

[32] N. Savva and S. Kalliadasis, "Droplet motion on inclined heterogeneous substrates," *Journal of Fluid Mechanics,* vol. 725, pp. 462-491, Jun 2013.

[33] L. Mahadevan and Y. Pomeau, "Rolling droplets," *Physics of Fluids (1994-present),* vol. 11, pp. 2449-2453, 1999.

[34] P. G. Degennes, "Wetting - Statics and Dynamics," *Reviews of Modern Physics,* vol. 57, pp. 827-863, 1985.

[35] J. F. Joanny and P. G. Degennes, "A Model for Contact-Angle Hysteresis," *Journal of Chemical Physics,* vol. 81, pp. 552-562, 1984.

[36] G. Fang, W. Li, X. Wang, and G. Qiao, "Droplet Motion on Designed Microtextured Superhydrophobic Surfaces with Tunable Wettability," *Langmuir,* vol. 24, pp. 11651-11660, 2013/09/15 2008.

[37] G. McHale, M. I. Newton, and N. J. Shirtcliffe, "Dynamic wetting and spreading and the role of

topography," *Journal of Physics-Condensed Matter,* vol. 21, Nov 18 2009.

[38] J. D. Smith, R. Dhiman, S. Anand, E. Reza-Garduno, R. E. Cohen, G. H. McKinley, *et al.*, "Droplet mobility on lubricant-impregnated surfaces," *Soft Matter,* vol. 9, pp. 1772-1780, 2013.

[39] A. Dupuis and J. M. Yeomans, "Dynamics of sliding drops on superhydrophobic surfaces," *Europhysics Letters,* vol. 75, pp. 105-111, Jul 2006.

[40] N. Le Grand, A. Daerr, and L. Limat, "Shape and motion of drops sliding down an inclined plane," *Journal of Fluid Mechanics,* vol. 541, pp. 293-315, Oct 25 2005.

[41] U. Thiele and E. Knobloch, "Driven drops on heterogeneous substrates: Onset of sliding motion," *Physical Review Letters,* vol. 97, Nov 17 2006.

[42] P. G. de Gennes, F. Brochard, and D. Quere, *Capillarity and Wetting Phenomena Drops, Bubbles, Pearls, Waves*: Springer, 2003.

[43] R. Raj, R. Enright, Y. Zhu, S. Adera, and E. N. Wang, "Unified Model for Contact Angle Hysteresis on Heterogeneous and Superhydrophobic Surfaces," *Langmuir,* vol. 28, pp. 15777-15788, 2012.

[44] E. Raphaël and P. G. de Gennes, "Dynamics of wetting with nonideal surfaces. The single defect problem," *The Journal of Chemical Physics,* vol. 90, pp. 7577-7584, 1989.

[45] M. Reyssat and D. Quere, "Contact Angle Hysteresis Generated by Strong Dilute Defects," *Journal of Physical Chemistry B,* vol. 113, pp. 3906-3909, Mar 26 2009.

[46] P. Hao, C. Lv, and Z. Yao, "Droplet Detachment by Air Flow for Microstructured Superhydrophobic Surfaces," *Langmuir,* vol. 29, pp. 5160-5166, 2013.

[47] M. Reyssat, D. Richard, C. Clanet, and D. Quere, "Dynamical superhydrophobicity," *Faraday Discussions,* vol. 146, pp. 19-33, 2010.

[48] A. T. Paxson and K. K. Varanasi, "Self-similarity of contact line depinning from textured surfaces," *Nat Commun,* vol. 4, p. 1492, 2013.

[49] P. F. Hao, C. J. Lv, Z. H. Yao, and F. He, "Sliding behavior of water droplet on superhydrophobic surface," *EPL,* vol. 90, Jun 2010.

[50] T. Furuta, M. Sakai, T. Isobe, S. Matsushita, and A. Nakajima, "Sliding of Water Droplets on Hydrophobic Surfaces with Various Hydrophilic Region Sizes," *Langmuir,* vol. 27, pp. 7307-7313, 2011.

[51] C. Lv, C. Yang, P. Hao, F. He, and Q. Zheng, "Sliding of Water Droplets on Microstructured Hydrophobic Surfaces," *Langmuir,* vol. 26, pp. 8704-8708, 2010.

[52] A. Nakajima, Y. Nakagawa, T. Furuta, M. Sakai, T. Isobe, and S. Matsushita, "Sliding of Water Droplets on Smooth Hydrophobic Silane Coatings with Regular Triangle Hydrophilic Regions," *Langmuir,* vol. 29, pp. 9269-9275, 2013.

[53] K. M. Smyth, H.-M. Kwon, A. T. Paxson, and K. K. Varanasi, "Visualization of contact line motion on hydrophobic textures," *Surface Innovations,* vol. 1, pp. 84-91, 2013.

[54] P. Olin, S. B. Lindstrom, T. Pettersson, and L. Wagberg, "Water Drop Friction on Superhydrophobic Surfaces," *Langmuir,* vol. 29, pp. 9079-9089, 2013.

[55] J. Wu, R. Ma, Z. Wang, and S. Yao, "Do droplets always move following the wettability gradient?,"

Applied Physics Letters, vol. 98, pp. 204104-3, 2011.

[56] J. V. I. Timonen, M. Latikka, O. Ikkala, and R. H. A. Ras, "Free-decay and resonant methods for investigating the fundamental limit of superhydrophobicity," *Nat Commun,* vol. 4, 2013.

[57] Z. Yoshimitsu, A. Nakajima, T. Watanabe, and K. Hashimoto, "Effects of Surface Structure on the Hydrophobicity and Sliding Behavior of Water Droplets," *Langmuir,* vol. 18, pp. 5818-5822, 2002.

[58] D. W. Pilat, P. Papadopoulos, D. Schaeffel, D. Vollmer, R. Berger, and H. J. Butt, "Dynamic Measurement of the Force Required to Move a Liquid Drop on a Solid Surface," *Langmuir,* vol. 28, pp. 16812-16820, Dec 11 2012.

[59] D. Richard and D. Quere, "Viscous drops rolling on a tilted non-wettable solid," *Europhysics Letters,* vol. 48, pp. 286-291, Nov 1999.

[60] G. Lagubeau, M. Le Merrer, C. Clanet, and D. Quere, "Leidenfrost on a ratchet," *Nat Phys,* vol. 7, pp. 395-398, 2011.

[61] M. Sakai, H. Kono, A. Nakajima, X. Zhang, H. Sakai, M. Abe, *et al.*, "Sliding of Water Droplets on the Superhydrophobic Surface with ZnO Nanorods," *Langmuir,* vol. 25, pp. 14182-14186, 2009.

[62] A. D. Sommers, T. J. Brest, and K. F. Eid, "Topography-Based Surface Tension Gradients to Facilitate Water Droplet Movement on Laser-Etched Copper Substrates," *Langmuir,* vol. 29, pp. 12043-12050, 2013.

[63] D. Quere, M.-J. Azzopardi, and L. Delattre, "Drops at Rest on a Tilted Plane," *Langmuir,* vol. 14, pp. 2213-2216, 1998.

[64] W. Choi, A. Tuteja, J. M. Mabry, R. E. Cohen, and G. H. McKinley, "A modified Cassie-Baxter relationship to explain contact angle hysteresis and anisotropy on non-wetting textured surfaces," *Journal of Colloid and Interface Science,* vol. 339, pp. 208-216, Nov 1 2009.

[65] W. Xu and C.-H. Choi, "From Sticky to Slippery Droplets: Dynamics of Contact Line Depinning on Superhydrophobic Surfaces," *Physical Review Letters,* vol. 109, p. 024504, 2011.

[66] A. Gauthier, M. Rivetti, J. Teisseire, and E. Barthel, "Finite Size Effects on Textured Surfaces: Recovering Contact Angles from Vagarious Drop Edges," *Langmuir,* vol. 30, pp. 1544-1549, 2014.

[67] P. Papadopoulos, L. Mammen, X. Deng, D. Vollmer, and H.-J. Butt, "How superhydrophobicity breaks down," *Proceedings of the National Academy of Sciences,* vol. 110, pp. 3254-3258, 2013.

[68] T. Podgorski, J. M. Flesselles, and L. Limat, "Corners, Cusps, and Pearls in Running Drops," *Physical Review Letters,* vol. 87, p. 036102, 06/27/ 2001.

[69] M. Miwa, A. Nakajima, A. Fujishima, K. Hashimoto, and T. Watanabe, "Effects of the Surface Roughness on Sliding Angles of Water Droplets on Superhydrophobic Surfaces," *Langmuir,* vol. 16, pp. 5754-5760, 2000.

[70] R. Tadmor, P. Bahadur, A. Leh, H. E. N'guessan, R. Jaini, and L. Dang, "Measurement of Lateral Adhesion Forces at the Interface between a Liquid Drop and a Substrate," *Physical Review Letters,* vol. 103, p. 266101, 2009.

[71] L. Rayleigh, "On the Capillary Phenomena of Jets," *Proceedings of the Royal Society of London,* vol. 29, pp. 71-97, 1879.

[72] L. Dong, A. Chaudhury, and M. K. Chaudhury, "Lateral vibration of a water drop and its motion on a vibrating surface," *The European Physical Journal E,* vol. 21, pp. 231-242, 2006.

[73] S. Daniel, S. Sircar, J. Gliem, and M. K. Chaudhury, "Ratcheting Motion of Liquid Drops on Gradient Surfaces†," *Langmuir,* vol. 20, pp. 4085-4092, 2004.

[74] S. Mettu and M. K. Chaudhury, "Motion of Liquid Drops on Surfaces Induced by Asymmetric Vibration: Role of Contact Angle Hysteresis," *Langmuir,* vol. 27, pp. 10327-10333, 2011.

[75] S. Daniel, M. K. Chaudhury, and P. G. de Gennes, "Vibration-Actuated Drop Motion on Surfaces for Batch Microfluidic Processes," *Langmuir,* vol. 21, pp. 4240-4248, 2005.

[76] K. C. Chaudhary and T. Maxworthy, "The nonlinear capillary instability of a liquid jet. Part 2. Experiments on jet behaviour before droplet formation," *Journal of Fluid Mechanics,* vol. 96, pp. 275-286, 1980.

[77] S. Yamakita, Y. Matsui, and S. Shiokawa, "New method for measurement of contact angle (droplet free vibration frequency method)," *Japanese Journal of Applied Physics Part 1-Regular Papers Short Notes & Review Papers,* vol. 38, pp. 3127-3130, May 1999.

[78] A. J. JAMES, M. K. SMITH, and A. GLEZER, "Vibration-induced drop atomization and the numerical simulation of low-frequency single-droplet ejection," *Journal of Fluid Mechanics,* vol. 476, pp. 29-62, 2003.

[79] S. Mettu and M. K. Chaudhury, "Vibration Spectroscopy of a Sessile Drop and Its Contact Line," *Langmuir,* vol. 28, pp. 14100-14106, 2012.

[80] M. Perez, Y. Brechet, L. Salvo, M. Papoular, and M. Suery, "Oscillation of liquid drops under gravity: Influence of shape on the resonance frequency," *Europhysics Letters,* vol. 47, pp. 189-195, Jul 1999.

[81] N. Yoshiyasu, K. Matsuda, and R. Takaki, "Self-Induced Vibration of a Water Drop Placed on an Oscillating Plate," *Journal of the Physical Society of Japan,* vol. 65, pp. 2068-2071, 1996/07/15 1996.

[82] F. Celestini and R. Kofman, "Vibration of submillimeter-size supported droplets," *Physical Review E,* vol. 73, p. 041602, 04/07/ 2006.

[83] P. M. McGuiggan, D. A. Grave, J. S. Wallace, S. Cheng, A. Prosperetti, and M. O. Robbins, "Dynamics of a Disturbed Sessile Drop Measured by Atomic Force Microscopy (AFM)," *Langmuir,* vol. 27, pp. 11966-11972, 2011.

[84] J. S. Sharp, "Resonant properties of sessile droplets; contact angle dependence of the resonant frequency and width in glycerol/water mixtures," *Soft Matter,* vol. 8, pp. 399-407, 2012.

[85] X. Noblin, A. Buguin, and F. Brochard-Wyart, "Vibrated sessile drops: Transition between pinned and mobile contact line oscillations," *The European Physical Journal E,* vol. 14, pp. 395-404, 2004.

[86] F. Mugele, A. Staicu, R. Bakker, and D. van den Ende, "Capillary Stokes drift: a new driving mechanism for mixing in AC-electrowetting," *Lab on a Chip,* vol. 11, pp. 2011-2016, 2011.

[87] M. Nosonovsky and B. Bhushan, "Hierarchical roughness optimization for biomimetic superhydrophobic surfaces," *Ultramicroscopy,* vol. 107, pp. 969-979, 2007.

[88] A. B. D. Cassie and S. Baxter, "Wettability of porous surfaces," *Transactions of the Faraday Society,* vol. 40, pp. 546-551, 1944.

[89] G. McHale, S. J. Elliott, M. I. Newton, D. L. Herbertson, and K. Esmer, "Levitation-Free Vibrated Droplets: Resonant Oscillations of Liquid Marbles," *Langmuir,* vol. 25, pp. 529-533, 2009.

[90] R. J. A. Hill and L. Eaves, "Vibrations of a diamagnetically levitated water droplet," *Physical Review E,* vol. 81, p. 056312, 05/13/ 2010.

[91] Y. Kanda, "A graphical representation of the piezoresistance coefficients in silicon," *Electron Devices, IEEE Transactions on,* vol. 29, pp. 64-70, 1982.

[92] C. S. Smith, "Piezoresistance Effect in Germanium and Silicon," *Physical Review,* vol. 94, pp. 42-49, 04/01/ 1954.

[93] N. Thanh-Vinh, H. Takahashi, K. Matsumoto, and I. Shimoyama, "Two-axis MEMS-based force sensor for measuring the interaction forces during the sliding of a droplet on a micropillar array," *Sensors and Actuators A: Physical,* 2014.

[94] H. Takahashi, N. M. Dung, K. Matsumoto, and I. Shimoyama, "Differential pressure sensor using a piezoresistive cantilever," *Journal of Micromechanics and Microengineering,* vol. 22, May 2012.

[95] M. Gel and I. Shimoyama, "Force sensing submicrometer thick cantilevers with ultra-thin piezoresistors by rapid thermal diffusion," *Journal of Micromechanics and Microengineering,* vol. 14, pp. 423-428, Mar 2004.

[96] H. Takahashi, A. Nakai, N. Thanh-Vinh, K. Matsumoto, and I. Shimoyama, "A triaxial tactile sensor without crosstalk using pairs of piezoresistive beams with sidewall doping," *Sensors and Actuators A: Physical,* vol. 199, pp. 43-48, 2013.

Publications

Journal papers

[1] **Nguyen Thanh-Vinh**, Hidetoshi Takahashi, Kiyoshi Matsumoto, and Isao Shimoyama, "Two-axis MEMS-based Force Sensor for Measuring the Interaction Forces during the Sliding of a Droplet on a Micropillar Array," *Sensors and Actuators A: Physical*, 2014. (Accepted)

[2] **Nguyen Thanh-Vinh**, Nguyen Binh-Khiem, Hidetoshi Takahashi, Kiyoshi Matsumoto, and Isao Shimoyama, "High-sensitivity Triaxial Tactile Sensor with Elastic Microstructures Pressing on Piezoresistive Cantilevers", *Sensors and Actuators: A. Physicals*, vol. 215, pp. 167-175, 2014.

[3] Hidetoshi Takahashi, **Nguyen Thanh-Vinh**, Uijin G. Jung, Kiyoshi Matsumoto, and Isao Shimoyama, "MEMS two-axis force plate array used to measure the ground reaction forces during the running motion of an ant," *Journal of Micromechanics and Microengineering*, vol. 24, no. 6, article no. 065014, 2014.

[4] Hidetoshi Takahashi, Akihito Nakai, **Nguyen Thanh-Vinh**, Kiyoshi Matsumoto, Isao Shimoyama, "A triaxial tactile sensor without crosstalk using pairs of piezoresistive beams with sidewall doping,", *Sensors & Actuators: A. Physical*, vol. 199, pp. 43-48, 2013.

Conference Proceedings

[1] **Nguyen Thanh-Vinh**, Nguyen Binh-Khiem, Kiyoshi Matsumoto, and Isao Shimoyama, "High Sensitive 3D Tactile Sensor With The Structure Of Elastic Pyramids On Piezoresistive Cantilevers," *The 26th IEEE International Conference on Micro Electro Mechanical Systems (MEMS 2013)*, pp. 41-44, Taipei, Taiwan, 20-24 January, 2013.

[2] **Nguyen Thanh-Vinh**, Hidetoshi Takahashi, Tetsuo Kan, Kentaro Noda, Kiyoshi Matsumoto, Isao Shimoyama, "Micro suction cup array for wet/dry adhesion," *IEEE 24th International Conference on Micro Electro Mechanical Systems (MEMS2011)*, Cancun, Mexico, pp. 284-287, Jan. 23-27, 2011.

[3] **Nguyen Thanh-Vinh**, Hidetoshi Takahashi, Nguyen Binh-Khiem, Kiyoshi Matsumoto, and Isao Shimoyama, "Measurement of the Pressure Distribution During the Onset of Slip," *IEEE Sensors 2012*, pp. 966-969, Taipei, Taiwan, 28-31 October, 2012.

[4] **Nguyen Thanh-Vinh**, Kiyoshi Matsumoto, and Isao Shimoyama, " Highly Sensitive Pressure Sensor Using A Gold-Coated Elastic Pyramid Array Pressing On A Resistor," *The 26th IEEE International Conference on Micro Electro Mechanical Systems (MEMS 2013)*, pp. 596-599, Taipei, Taiwan, 20-24 January, 2013.

[5] Nguyen Binh-Khiem, **Nguyen Thanh-Vinh**, Kiyoshi Matsumoto, and Isao Shimoyama, "Three dimensional microfluidic design with spincoated micrometer-thin elastomer multilayer," *The 25th IEEE International Conference on Micro Electro Mechanical Systems (MEMS 2012)*, pp. 1109 - 1112, Paris, France, 29 January-2 February, 2012.

[6] **Nguyen Thanh-Vinh**, Kiyoshi Matsumoto, Isao Shimoyama, "Local slip detection using MEMS force sensor array," *59th Meetings of The Japan Society of Applied Physics and Related Societies*, Waseda University, Tokyo, pp.01-010, March. 15-18, 2012.

[7] **Nguyen Thanh-Vinh**, Kiyoshi Matsumoto, Isao Shimoyama, "Local slip detection using MEMS force sensor array," *30th Sensors Micromachine and Applied Systems Symposium, Sendai International Center*, Sendai, Nov. 5-7, 2013.

[8] **Nguyen Thanh-Vinh**, Hidetoshi Takahashi, Kiyoshi Matsumoto, and Isao Shimoyama, "Interaction Forces during the Sliding of a Water Droplet on a Textured Surface," *The 27th IEEE International Conference on Micro Electro Mechanical Systems (MEMS 2014)*, San Francisco, pp. 979-982, 26-30 January, 2014.

[9] Dinh Hoang-Giang, **Nguyen Thanh-Vinh**, Kentaro Noda, Phan Hoang-Phuong, Nguyen Binh-Khiem, Kiyoshi Matsumoto, and Isao Shimoyama, "Micro Liquid-Based Thermo-Acoustic Transmitter for Emitting Ultrasound in Liquid Medium," *The 27th IEEE International Conference on Micro Electro Mechanical Systems (MEMS 2014)*, San Francisco, pp. 849-852, 26-30 January, 2014.

[10] **Nguyen Thanh-Vinh**, Hidetoshi Takahashi, Kiyoshi Matsumoto, Isao Shimoyama, "Direct measurement of the interaction forces during the sliding of a water droplet on a pillar-typed superhydrophobic surface", *67th Annual Meeting of the APS Division of Fluid Dynamics*, 23-25 November, 2014.

[11] **Nguyen Thanh-Vinh**, Kiyoshi Matsumoto, Isao Shimoyama, "A viscometer based on the vibration of the droplets on a piezoresistive cantilever array", *The 28th IEEE International Conference on Micro Electro Mechanical Systems (MEMS 2015)*, Estoril, Portugal.

[12] Nguyen Minh-Dung, Pham Quang-Khang, **Nguyen Thanh-Vinh**, Kiyoshi Matsumoto, Isao Shimoyama, "Measurement of SAW propagation using a piezo-resistive cantilever array", *The 28th IEEE International Conference on Micro Electro Mechanical Systems (MEMS 2015)*, Estoril, Portugal.

[13] Ryo Aoki, **Nguyen Thanh-Vinh**, Kentaro Noda, Tomoyuki Takahata, Kiyoshi Matsumoto, Isao Shimoyama, "Sound Focusing in Liquid Using a Varifocal Acoustic Lens", *The 28th IEEE International Conference on Micro Electro Mechanical Systems (MEMS 2015)*, Estoril, Portugal.

Acknowledgment

I am deeply grateful to my adviser, Professor Isao Shimoyama who has guided me through the whole PhD course. I would like to express my special appreciation and thanks to Professor Shimoyama for his guidance and the opportunity to do my research in a top-class research environment. His encouragement and advice have always been the inspiration that help me in all the difficult times.

I thank Professor Hiroyuki Fujita, Professor Yoshihiko Nakamura, Professor Yuji Suzuki, Professor Shu Takagi and Professor Shoji Takeuchi for serving as the committee members of my PhD defense. Their invaluable advice and suggestions greatly improved the research of this thesis. I am deeply grateful to Professor Shu Takagi for his insightful comments on the very first results of my research.

I am grateful to Professor Kiyoshi Matsumoto for his useful technical advice especially on measurement techniques and signal analysis.

I would like to thank Professor Keiji Sakai, Dr. Taichi Hirano and Dr. Yuji Shimokawa for the viscosity measurement of the liquid samples using EMS Viscometer. I thank Dr. Atsushi Takei for the fruitful discussions on the topic of wetting.

I also thank all the senior members of Shimoyama Lab for their help and supports during the last 6 years. I particularly thank Dr. Hidetoshi Takahashi and Dr. Kentaro Noda for their advice on sensor fabrication and measurement technique. I thank Dr. Nguyen Binh Khiem and Dr. Nguyen Minh Dung for their supports and useful comments on my research. I am grateful to Dr. Tomoyuki Takahata for sharing his advice on both research and personal life. I thank Dr. Yasutaka Ichikawa and Mr. Toru Nakakubo for the useful discussions on the physics of droplets. I am grateful to Dr. Tetsuo Kan for teaching me about soft lithography and anisotropic Si etching. I thank Dr. Akihito Nakai and Dr. Yusuke Takei for the advice on tactile sensors. I also would like to thank Dr. Akira Inaba, Dr. Akihiro Isozaki, Dr. Uijin Jung, Dr. Takanori Usami for their useful information in writing thesis. I thank Mr. Takuya Tsukagoshi for being so kind to me and for the fruitful discussions on the topic of cells, soft matter and sensing technique. I also want to thank Dr. Kayoko Hirayama for her advice in droplet deposition on a superhydrophobic surface using a glass tube.

Finally, I would like to thank my parents, my sisters and all the members of my family who have always supported and encouraged me to pursuit a PhD degree. Especially, I would like to thank my wife, Nguyen Thi Ngoc Anh for her supports, day after day. She had been taking care of our daughter so that I could go to school and do my research. She was always there to encourage me every single time I failed an experiment. Without her supports, this thesis would not have been completed.